Analysis and modelling of the dislocation response during non-isothermal creep in Ni-SX superalloys

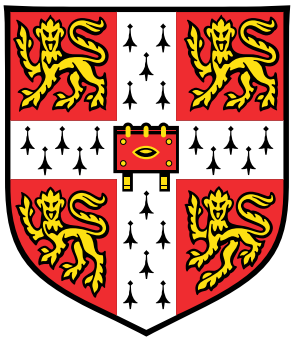

Caspar Wilhelm Michael Schwalbe

Department of Materials Science and Metallurgy
University of Cambridge

This dissertation is submitted for the degree of
Doctor of Philosophy

Wolfson College

May 2019

Declaration

This dissertation is submitted for the degree of Doctor of Philosophy at the University of Cambridge. It describes the research carried out in the Department of Materials Science and Metallurgy between October 2014 and October 2018 under the supervision of Professor Catherine M.F. Rae and Dr. Enrique Galindo-Nava, and the work carried out on leave to work away at Institut P' - Département de Physique et Mécanique des Matériaux, ISAE-ENSMA under the supervision of Dr. MdC Jonathan Cormier. Except where reference is made to the work of others, the contents of this dissertation are original and have not been the result of collaboration. No part of the work described here has been submitted for the purpose of gaining academic qualification at this or any other institute of higher learning. This dissertation does not exceed 60,000 words in length and has fewer than 150 figures.

Parts of this dissertation have been presented at:

Creep parameter determination based upon element segregation in Ni-SX superalloys. C. Schwalbe, E. Galindo-Nava, N. Jones, C.M.F. Rae. Creep 2017, St. Petersburg, Russia, 19-21 June 2017.

Investigating the Dislocation-Driven Micro-mechanical Response Under Non-isothermal Creep Conditions in Single-Crystal Superalloys. Schwalbe, C., Cormier, J., Jones, C. N., Galindo-Nava, E., & Rae, C. M. F. Euro Superalloys 2018, Oxford, United Kingdom, 9-13 September 2018.

Parts of this dissertation have been published in:

[100] Jones, R. D., Di Gioacchino, F., Lim, H., Edwards, T. E. J., Schwalbe, C., Battaile, C. C., & Clegg, W. J. (2018). Reduced partitioning of plastic strain for strong and yet ductile precipitate-strengthened alloys. *Scientific Reports*, 8(1), 361. http://doi.org/10.1038/s41598-018-26917-0

[179] Schwalbe, C., Cormier, J., Jones, C. N., Galindo-Nava, E., & Rae, C. M. F. (2018). Investigating the Dislocation-Driven Micro-mechanical Response Under Non-isothermal Creep Conditions in Single-Crystal Superalloys. *Metallurgical and Materials Transactions A*, 1-15. http://doi.org/10.1007/s11661-018-4764-3

[180] Schwalbe, C., Jacques, A., Galindo-Nava, E., Jones, C. N., Rae, C. M. F. & Cormier, J., (2018). *In Situ* Measurement of the Precipitate Volume Fraction and Interfacial Lattice Misfit during Non-isothermal Creep in the Superalloy CMSX-4. *Materials Science and Engineering: A*, 740-741. http://doi:10.1016/j.msea.2018.10.033

Caspar Wilhelm Michael Schwalbe
May 2019

Acknowledgements

This project would not have been possible without the generous support and expert advice of my supervisor Professor C.M.F. Rae and the financial support received from the EPSRC and Rolls-Royce plc. The numerous discussions with Dr. E. Galindo-Nava inspired me to develop my modelling skills further and his advice and support in modelling were extremely valuable in the development of numerous models in this thesis. Chapter five of this thesis would have looked very different if it would not have been for the help and support from Professor J. Cormier who allowed me to use his lab facilities, provided material and shared his vast experience and knowledge in the field with me. Rolls-Royce plc. and my industrial supervisor C.N. Jones in particular are gratefully acknowledged for providing me material and funding as well as valuable insights and understanding into the commercial side of this project.

Further I would like to thank various people in the Department of Materials Science and Metallurgy Cambridge for taking the time to train me on various instruments used during this project: S. Griggs (SEM), D. Nicol (FiB), C.T. Dolan (TEM), A.J. Moss (XRD), Dr. M.E. Vickers (XRD) as well as the workshop.

I am grateful for the training received by Dr. J. Barnard, Dr. O.M.D.M. Messé, Dr. H.T. Pang, M. Wang-Koh and Dr. G. Divitini on the TEMs used in this project. Furthermore, I would like to thank Professor C.M.F. Rae and Dr. H.T. Pang for their input and review of the image analysis.

I am grateful for the discussions with Dr. M. Scervini on the use of thermocouples, as quantifying and controlling the error in thermal measurement proved to be a key part of this project.

Dr. C. Hayward is gratefully acknowledged for obtaining the EPMA element maps at the University of Edinburgh.

The micro-pillar project outlined in this project is built on the experience and knowledge acquired by Dr. R. Jones whom I thank for sharing his expertise.

Working with the software ThermoCalc, it was invaluable to learn from and discuss feasibilities and errors with Dr. C. Goddard, Dr. K.A. Christofidou and S. Jin.

Further, I would like to thank various other members of the RR-UTC in Cambridge: A. J. Goodfellow, E. Hildyard, C. Kienl, F.D. León Cázares, S. Llewelyn, J. Moffat, Dr. L. Owen, R. Schlütter, Dr. A.Wilson as well as Dr. Di Gioacchino who helped me with various questions throughout the project and provided support.

Importantly, I would like to thank and dedicate this work to my family and friends. Their love and support helped me through ups and downs of this project and helped me not lose sight of life outside "the bubble": Margot, Hubertus and Birgit; Joshua, Ulrike, Franz-Michael, Harriet, Marc, Niklas, Julia, Ursula, Thomas, Ulrike, Petra, Martin, Marlies, Bong-Youn, Itco, Birco, Franz-Friedrich, Anna, Daniel, Maren, Peter, David, Jingyuan, Andrea, Detlev, Gesine, Hasso, Penny and Rex; Joshua, Jonathan, Leonas and Carlotta. Vielen Dank e muito obrigado!

Lastly, I would like to thank all the teachers who taught, inspired and supported me and the taxpayers who financed twenty years of primary, secondary and tertiary education.

Abstract

Nickel-based single-crystal superalloys are commonly used as the material of choice for turbine blades in modern aircrafts. The temperatures and stresses in the turbine are subject to continuous change during in-flight operation. The deformation rates of the turbine blades during operation are currently approximated based on isothermal creep tests.

This dissertation seeks to understand how the high temperature creep response of the single-crystal nickel-based superalloys CMSX-4 and CMSX-10 changes when subjected to a non-isothermal test cycle varying between the tertiary and rafting creep regimes. For this purpose, creep tests cycling between a base temperature of 900 °C and a peak temperature of 1050 °C under a constant load ($\sigma = 200$ MPa) were carried out and the samples were subsequently analyzed using TEM dislocation analysis. The creep results displayed significantly faster non-isothermal strain rates than would be expected when adding up the isothermal strain rates at each temperature. By studying tests interrupted at different stages of creep, it is argued that the faster strain accumulation results from a higher dislocation activity compared to isothermal studies which are driven by the non-isothermal evolution of the interfacial lattice misfit. Furthermore, the thermal cycling creep rate under these conditions depends on the creation of interfacial dislocation networks that can take two shapes (a classical edge-type network, or one in which the dislocations are paired) and their disintegration by the γ'-shear of dissimilar Burgers vector pairs.

The experimental findings were used to create a non-isothermal creep model to better understand the dislocation-based creep response. In particular, the role of γ'-shear and dislocation glide and climb in the γ-phase on the overall creep resistance of the alloys were examined with the model. Furthermore, the rate of non-isothermal micro-structural transformation (via rafting and coarsening) and its impact on the creep response was examined. The non-isothermal creep model is based on the evolution of key creep parameters during thermal cycling. These parameters include the effective γ-interdiffusivity, the γ-Orowan resistance, the interfacial lattice misfit, the anti-phase boundary energy, the γ'-critical resolved shear stress and the solid solution hardening in both phases. The computation of the key creep parameters was based on an *in situ* measured phase fraction evolution of the alloy CMSX-4.

Table of contents

List of figures

List of tables

Nomenclature

Roman Symbols

a_γ	Lattice parameter in γ-phase [m]
$a_{\gamma'}$	Lattice parameter in γ'-phase [m]
b	Burgers vector [m]
C_{ijkl}	Stiffness tensor
d	Dislocation spacing [m]
D	Diffusion coefficient of nickel
E	Energy of the system
$\bar{e}_{11}$	Elastic deformation in x direction
$f_{\gamma'}$	Volume fraction of γ'-phase [m/Pas]
G	Shear modulus [Pa]
$h_{x,y,z}$	Channel width in x,y,z dimension [m]
k	Boltzmann constant= 1.38064852×10^{-23}[J/K]
$L_{x,y,z}$	Precipitate length in x,y,z dimension [m]
l_{111}	Particle shear length [m]
m_K	Schmid factor tensor
n	Exponent in the Orowan equation for γ-glide and γ'-shear
N_A	Avogadro's number

p Jog distance [m]

Q Precipitation activation energy $[kJ/mol]$

r Particle radius [m]

T Temperature [K]

V_γ Volume of matrix channels in simulated cell

$V_{\gamma'}$ Volume of precipitate in simulated cell

w Fitting parameter for strongly coupled dislocations

$\check{w}$ Fitting parameter for strongly coupled dislocations

w_i Element weight fraction

W_1 Fitting parameter for dislocation glide [m/Pas]

W_2 Fitting parameter for dislocation shearing [m/Pas]

Greek Symbols

α Proportionality scaling factor used for solid-solution hardening

β Avrami exponent

γ Interfacial energy $[\frac{J}{m^2}]$

γ Disordered FCC matrix phase

γ' $L1_2$-ordered precipitate phase

γ_{APB} Antiphase boundary energy $[\frac{J}{m^2}]$

$\dot{\gamma}_K$ Slip rate on glide plane

γ_{max} Maximum shear strain on slip plane

γ_{xy} Strain components in xy-plane

δ Interfacial lattice misfit

δ_{cpcm} Unconstrained interfacial lattice misfit

δ_{cpcp} Constrained interfacial lattice misfit

δ_{eff} Effective interfacial lattice misfit

$\dot{\varepsilon}_{pl}$ Plastic deformation / strain [/]

$\bar{\varepsilon}_{xx}$ Elastic deformation in x-direction

ε_L Atomic interaction parameter in solid-solution hardening model

η' Dielastic interaction parameter

λ Shear length on active slip plane

ν Velocity of a dislocation [m/s]

ξ Scaling factor for microstructural transformation (i.e. coarsening and rafting)

ρ_0 Initial dislocation density $[m^{-2}]$

$\rho^{D_{inc}}$ Dislocation density enabled to form Eggeler-pairs $[m^{-2}]$

ρ_K Interfacial dislocation density on slip plane $[m^{-2}]$

ρ_m Density of mobile dislocations $[m^{-2}]$

ρ_{max} Dislocation density required to reach an unconstrained interfacial misfit $[m^{-2}]$

σ_{ij} Normal stress tensor [Pa]

$\sigma_{ij,P}$ Stress in particle [Pa]

σ_{Int} Interfacial energy $[\frac{J}{m^2}]$

τ_K Shear stress [Pa]

$\tau_{K,0}$ Resistance to dislocation glide [Pa]

τ_{cut} Critical particle shear stress for weakly or strongly coupled dislocations [Pa]

τ_{SSH} Resistance to glide due to solid-solution hardening [Pa]

τ_{Or} Resistance to glide due to Orowan hardening [Pa]

ϕ Parelastic interaction constant used in solid-solution hardening

χ	Stacking fault energy $[\frac{J}{m^2}]$
Ψ	Diffusion length required to reach experimentally observed creep minimum
Ω	Atomic radius [m]

Chapter 1

Introduction

With more than three billion air passengers each year [1], today's global economy is facilitated by secure, efficient and affordable mobility provided by jet engines. The efficiency of a jet engine (see Figure 1.1) is largely driven by the turbine, where the kinetic energy released from the combustion of the gas mixture is transformed into mechanical energy that powers the compressor and fan blades at the front of the engine.

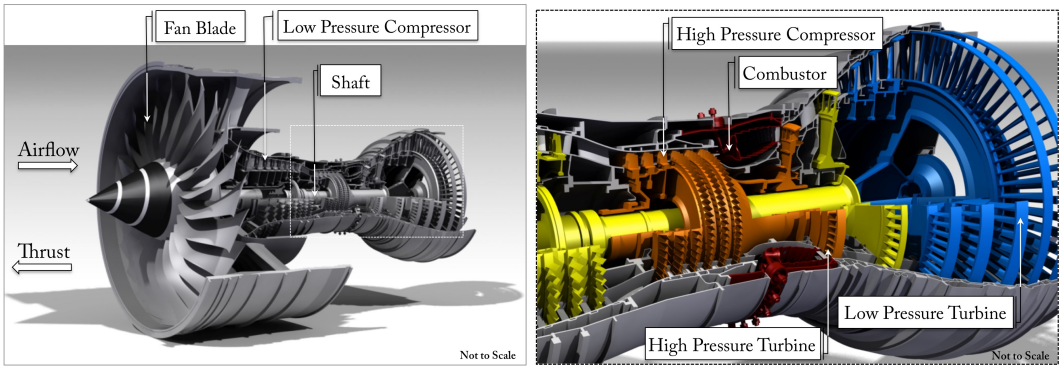

(a) Overview of Engine (b) View of the Turbine Section

Fig. 1.1 Impression of a Trent 900 Turbofan.
[3]

The turbine is a region of high temperature and rotating components experience considerable load, therefore materials selected for this region have to exhibit high stability and strength at high temperatures, together with high resistance to corrosion, a low density and good producibility. The finished product also has to meet a competitive price point [167, 25]. These design criteria are currently best met by the nickel-base superalloys.

1.1 Introduction to the alloy system

Superalloys consist of a number of different major and minor alloying elements (see Figure 1.2 and 1.3).

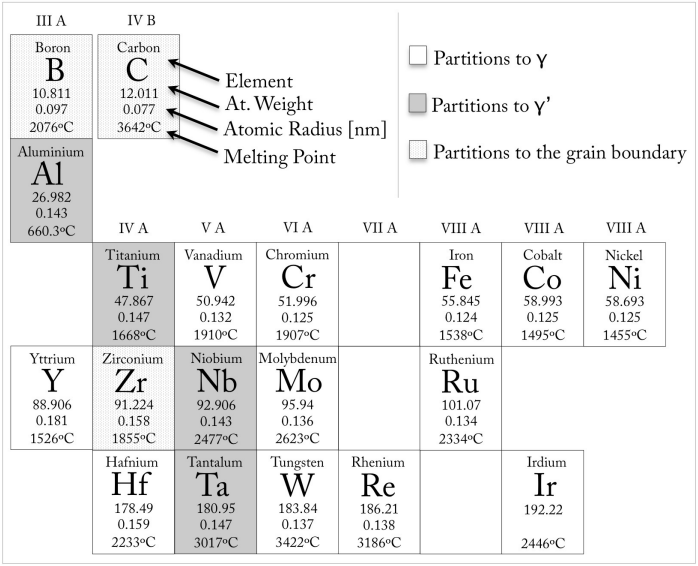

Fig. 1.2 Key alloy elements in superalloys with their position in the periodic table [164].

Nickel-base superalloy components for turbine applications feature either a polycrystalline or single-crystal grain structure. Due to different operating conditions in the turbine, grain boundaries can enhance strength or indeed, limit life (see [164] p.18f & p.130). Forged polycrystalline superalloys are used for cooler discs, whilst single crystals are used for the hotter turbine blades where creep is the critical damage process. The comparatively higher temperature capability of single crystals is a result of absent grain boundaries, which eliminates grain boundary slip, porosity associated with grain boundaries and negative effects associated with the alloying of grain boundary stabilisers (such as a lower melting point and a smaller heat-treatment window) [164] p.20f [25]. Additionally, as single crystal blades are cast in a similar crystal orientation, the entire turbine array becomes more predictable with regards to component lifetime.

Commercial single-crystal superalloys contain up to 14 different alloying elements (Figure 1.3). The elements vary significantly in their properties, such as atomic radius, melting point, atomic weight (see Figure 1.2) and elastic modulus. The chemical interaction (i.e. changes in bonding length resulting in the formation of an $L1_2$-ordered phase described in detail later) and the combination of their individual properties dictate the mechanical properties and give superalloys their superior performance at high temperatures. The overall

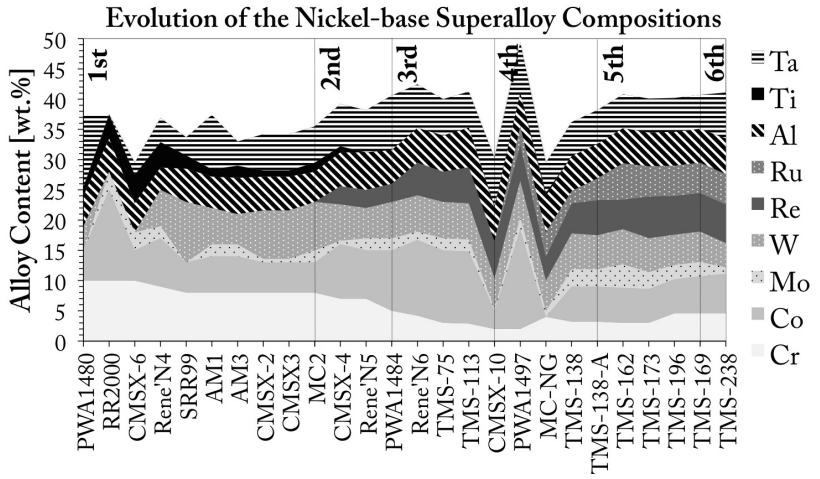

Fig. 1.3 Change of element content with each generation of nickel-superalloys (adapted from [164]).

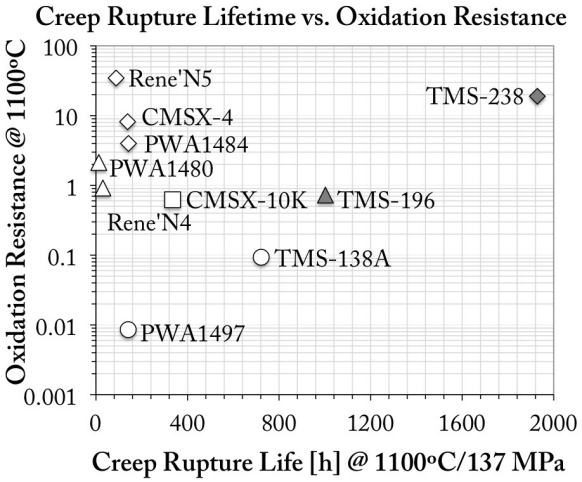

Fig. 1.4 Graph comparing the performance of selected alloys in terms of creep rupture life at 1100 °C and 137 MPa (x-axis) against the oxidation resistance at 1100 °C (adapted from [107]). In the cited paper the oxidation resistance parameter is a logarithmic combination of isothermal mass increase and cyclic mass decrease.

alloy mixture has been optimised for performance under turbine conditions and in the process underwent a series of alterations (see Figure 1.3). The objective of changing the alloy compositions was to improve key lifetime parameters, such as creep rupture life and oxidation resistance of an alloy simultaneously, so that the improved alloys occupy the top right corner of Figure 1.4.

To study the creep resistance of current alloy compositions and to model and optimise these compositions further the conventional approach has been to study alloys at constant

high temperature and below yield stress conditions (isothermal creep). The optimisation achieved under such isothermal condition is illustrated in Figure 1.4.

However, during in-flight operation the temperature and stress conditions vary considerably in the turbine (non-isothermal creep). This thesis studies the micro-mechanical response shown by two conventional single-crystal superalloys under non-isothermal creep. The main objective of this thesis is to understand which parameters and to what extent, drive the creep deformation under conditions that relate to in-flight turbine conditions. Ultimately, by modelling the micro-mechanical response under non-isothermal conditions and comparing it to the conventional isothermal creep approach, this thesis addresses how current models can be improved in order to estimate the creep response during in-flight conditions.

1.2 Overview of the thesis structure

This thesis is structured into seven chapters which will be briefly described. Chapter 2 reviews the relevant research on the micro-structure of nickel-base single crystal superalloys, presents in service turbine data and then reviews the literature on creep damage mechanisms and the models which best describe the material deformation during isothermal and in-flight operation of the turbine.

In Chapter 3 the different experimental set-ups as well as analysis instruments used in the scope of this thesis are introduced.

In Chapter 4 experimental and theoretical work is presented that estimates the deformation parameters across a single alloy and during non-isothermal creep testing.

Chapter 5 offers an in-depth analysis of the micro-mechanical response during non-isothermal testing investigated using electron microscopy.

Based upon the parameters calculated in Chapter 4 and the mechanisms observed to be actively contributing to the material deformation in Chapter 5, a non-isothermal creep model is presented in Chapter 6.

The final chapter summarises and describes conclusions based on the key results presented within this thesis.

Chapter 2

Deformation Mechanisms

This chapter is divided into four sections. In the first section, the microstructure of cast nickel superalloys is reviewed. The second section presents in-service turbine data, such that these conditions can be related to non-isothermal creep tests. The third section reviews mechanisms and parameters driving high-temperature isothermal creep. The phenomena resulting from non-isothermal high temperature creep are then reviewed in the fourth section.

2.1 Nickel-based single crystal superalloys

2.1.1 The two phase microstructure

The unique high temperature capabilities of nickel-based superalloys is in part due to their bi-phasic microstructure that consists of a disordered FCC γ-matrix phase into which harder γ'-precipitates of a L_{12}-ordered intermetallic phase are coherently embedded. In the ordered phase consisting mainly of Ni_3Al, the nickel atoms predominantly occupy the $(0, \frac{1}{2}, \frac{1}{2})$-sites, whilst aluminium and tantalum occupy the $(0,0,0)$-sites. In the disordered matrix phase all atoms are presumed to occupy any lattice position with the same probability. However, due to preferential partitioning a number of elements are overall more likely to be found in the matrix than the precipitate. The preferential partitioning of all major alloying elements is summarised in Figures 1.2 and 2.1(left).

Different quantities of alloying elements are added, such that their beneficial properties prevail under multiple operating conditions. Beside the γ'-phase formation (aluminium) and γ-stabilisation (cobalt), properties such as castability (tantalum), oxidation resistance (chromium, aluminium), solid-solution hardening (tantalum, rhenium), slow diffusivity (rhenium, tungsten), increasing the lattice misfit (molybdenum, rhenium) and counteracting

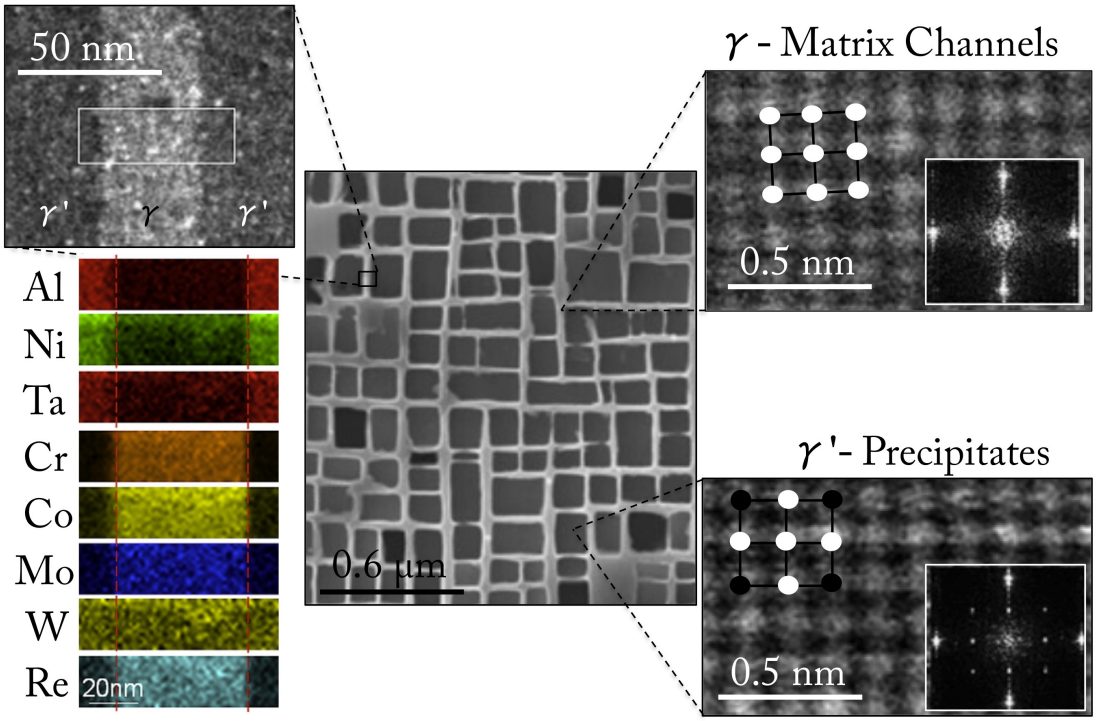

Fig. 2.1 [Left] HAADF image of a γ-channel between γ' (top left) with corresponding element mapping in the marked area (below) [76];
[Center] SEM-image of a nickel-base superalloy microstructure [132]; [Right] HAADF images with corresponding diffractogram insets [75]

TCP-formation (cobalt, ruthenium) are improved through the addition of the cited elements [99]. The two alloys investigated in this thesis are commercially known as CMSX-4 and CMSX-10K which are registered trademarks of the Cannon Muskegon Corporation. The nominal chemical composition of both alloys is presented in Table 2.1.

Table 2.1 The chemical composition of the alloys studied in this thesis (weight %) from [208].

Alloys	Cr	Co	Mo	W	Al	Ti	Ta	Re	Hf	Ni
CMSX-4	6.5	9	0.6	6.5	5.6	1.0	6.5	3.0	0.1	Bal.
CMSX-10K	2	3	0.4	5	5.7	0.2	6	6.3	0.03	Bal.
CMSX-10N	1.5	3	0.4	5	5.8	0.1	8	7	0.03	Bal.

At room temperature, the precipitate phase usually makes up around 62.5 - 75 Vol.%, but decreases gradually with increasing temperature. This is due to changing element solubilities in the ordered γ'-phase with increasing temperatures [164].

As the $L1_2$-phase is the ordered variant of the FCC phase, both phases have compatible structures and are generally coherent. A small difference between the lattice parameters arises from the preferential partitioning of alloying elements with different atomic diameters to the two phases. With generally larger elements partitioning to the γ-phase, the resulting lattice parameter in the creep regime is slightly larger than that in the γ'-phase [147, 17, 23, 96]. As a result, a negative mismatch (misfit) exists at the interfaces, that can be quantified by Equation 2.1.

$$\delta = \frac{2 * (a_{\gamma'} - a_{\gamma})}{(a_{\gamma'} + a_{\gamma})} \tag{2.1}$$

The misfit is a function of the local lattice environment and as such, it will change with temperature as a result of the lattice dilation and element solubility [147, 21, 54, 149, 22].

In addition to the compositional difference across interfaces (nano-scale), the element concentration also varies across the micron-scale due to dendritic solidification in the casting process. These heterogeneities are resolved for all but the slowest diffusing elements after a standard γ'-solution heat treatment (see Figure 2.2).

2.1.2 Impact of the dendritic structure

Superalloys solidify by forming dendrites, that grow in a conifer-like structure into the melt (see Figure 2.2). The direction of solidification has a direct impact on the creep properties of

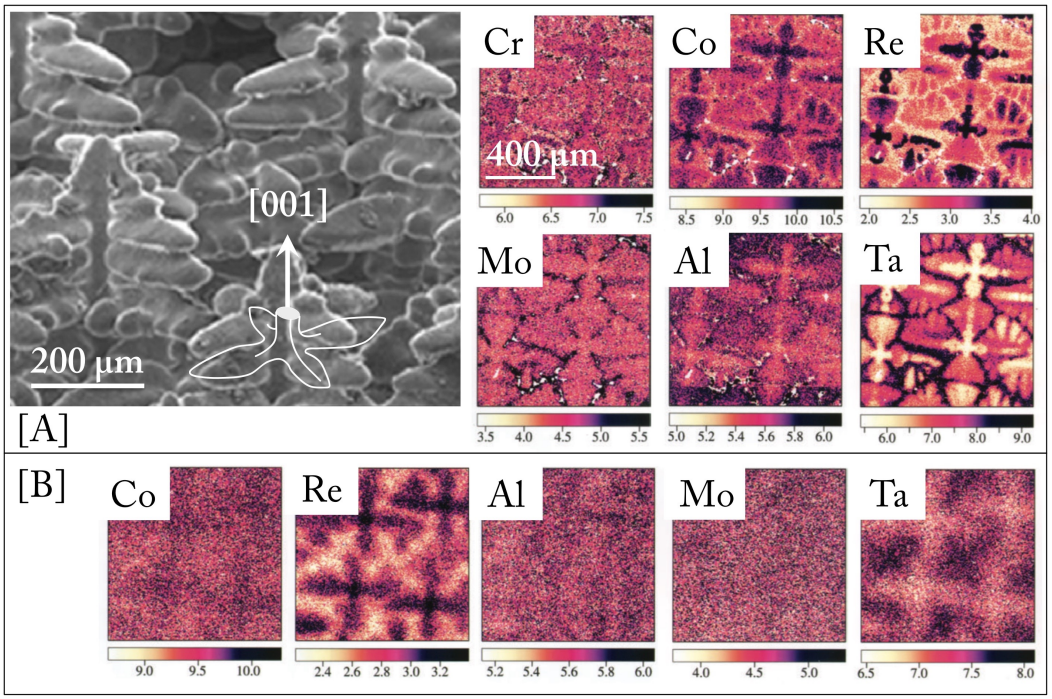

Fig. 2.2 SEM-image of an etched dendritic microstructure growing in [001]-direction [94]; [A] As-cast alloy EPMA-maps, [001]-direction is normal to imaging plane; [B] Post heat-treatment alloy EPMA-maps [105]

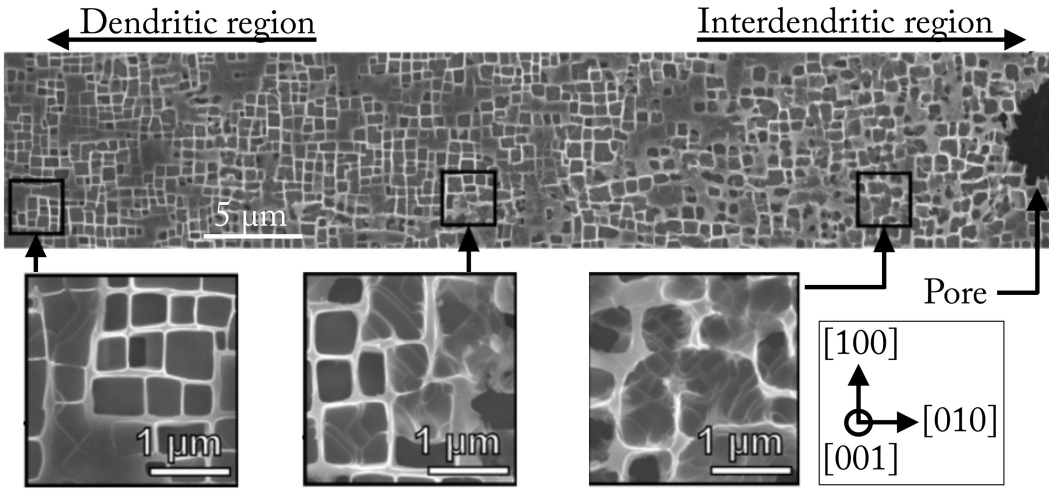

Fig. 2.3 SEM images after exposure of 1293K and 160MPa for 9h in [001] tensile creep by [6]; The [Left] Side closer to prior dendritic region. [Right] End of the image contains a casting pore located in prior interdendritic region

the alloy and has been extensively studied (see [183, 28, 138]). These studies have concluded that the most beneficial crystal orientation for high temperature creep under a centrifugal force is a crystal growth in [001]-direction. This is because this direction exhibits the lowest modulus which reduces stresses during rapid temperature change. In the dendritic structure, the Primary-Dendrite-Arm (PDA) (also called Dendrite Core (DC)) solidifies first, forming a continuous trunk structure along the casting direction, whilst the Secondary-Dendrite-Arms (SDA) grow from the PDA in a branched pattern [59, 98, 134, 223]. Ultimately, the surrounding Interdendritic Region (IR) solidifies. The spacing of the dendrites and their size depends on the alloy mixture, the casting rate and structure of the casting form [220, 142]. For example, a slower withdrawal rate and thermal gradient result in a bigger dendrite arm spacing and lower dendrite misorientation [98].

The porosity in the Interdendritic-Region is inversely proportional to the withdrawal rate [153, 160]. However subsequent heat-treatments increase the porosity in the interdendritic-region to a greater extent than the effect of the withdrawal rate [98].

Driven by the different solidus and liquidus segregation of the elements upon solidification [89], the elemental concentration in the as-cast microstructure varies throughout the dendritic structure (shown by the electron probe microanalysis (EPMA) maps in Figure 2.2). As a result of this elemental scatter, the dendrite cores are more deformable, due to the elemental composition in this region resulting in a higher γ-volume fraction and thus wider γ-channels in comparison to the inter-dendritic regions [59]. To homogenise the alloys, superalloys are subsequently heat-treated for several hours [164]. However, substantial differences in element distribution remain after heat-treatment (see Figure 2.2) [94, 105]. In the alloy CMSX-4, the difference in element concentration between the PDA and IR for the slow diffusing element rhenium can be as high as a factor of two [59] even after heat-treatment. This highlights that rhenium is seen as a key γ-partitioning element, that drives the misfit towards a more negative value [20, 56]. On a microscopic scale the interfacial lattice misfit along with the effects of the elastic anisotropy of the material, drive the precipitate shape [169]. As a result, the precipitate shape varies with the interfacial misfit from a spherical shape (low misfit) in the interdendritic region, towards a cuboidal shape in the dendrite cores (high misfit). This is shown in Figure 2.3 [6, 157].

2.2 Conditions in the turbine during in-flight operation

The temperature and stress conditions that turbine blades are exposed to change during a flight cycle. The stress and temperature conditions of a given flight cycle can be divided into three different flight segments (see p.5 [164]). Firstly the take-off, followed by a number of climb and descents to change between flight corridors and finally the approach and landing segment. The most significant temperature rise in the turbine entry (or inlet) temperature (TET) occurs during take-off and climb (see Figure 2.4). Each new climb phase leads to a brief jump in the engine temperature, whilst during the approach of the aircraft the engine temperature drops significantly. A final brief temperature rise is seen, when the aircraft lands and the reverse thrust is applied.

In commercial jet engines the exhaust-gas temperature (EGT) is routinely acquired in operation by a thermocouple attached to the exhaust gas stream of the turbine (see Figure 2.5). For every engine type the respective manufacturer is required to publish classifications used as guidelines for pilots during routine operations (see Table 2.2,[5]). The table offers insight into the length scale of routine take-off and climb segments. Without knowledge of the specific engine architecture, the EGT temperature used in the classification table cannot be related to the magnitude of the temperatures of prior blade stages, such as the Turbine Inlet Temperature (TIT), or the Interstage Turbine Temperature (ITT).

Table 2.2 Exhaust gas temperature limits for engine classifications

Temperatures [°C]	Start-up	Continuous	Take-Off [5min.]	Over Temp. [20sec.]
Long-haul [5]	700	850	900	920

However, the datasets in Figure 2.4 and Table 2.2 give valuable information about the exposure times to different temperature regimes, as well as the approximate heating and cooling rates of the different phases in a flight cycle. Using this data, non-isothermal test conditions can be devised that are based on the temperature evolution and gradients during in-flight operation of a turbine blade.

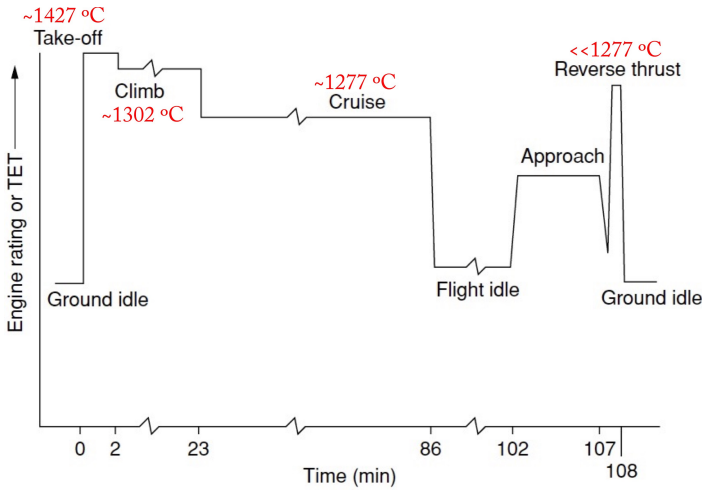

Fig. 2.4 Sketch of the in-flight turbine entry temperature evolution for a civil aircraft. Figure taken from p.5 [164] and adapted with the turbine entry temperatures (displayed in red for the take-off, top of climb and start of the cruise segment) published on p.55 of [42]

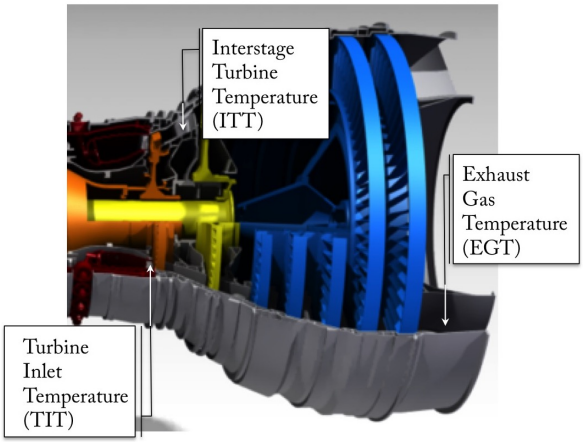

Fig. 2.5 Impression of a Trent 900 turbine [3] with relevant stations named that carry thermocouples in test-runs [4]

2.2.1 Temperatures across a single turbine blade

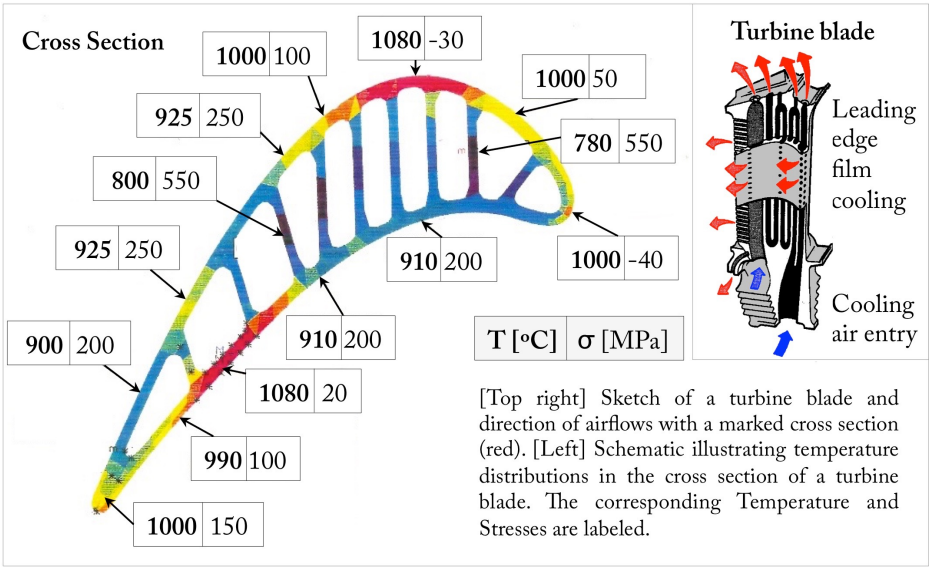

Fig. 2.6 [Left] Temperature and stress distribution across a first stage turbine blade [51]; [Right] Sketch of a cooled turbine blade [83]

The magnitude of the temperature and stress during operation depends on the turbine blade stage as well as the blade geometry. The gas temperature decreases with each additional turbine stage following the combustor (see Figure 1.1). In the first turbine stage (HPT) the gas temperature can reach above the melting point of the superalloys used, dropping to the level of the exhaust gas temperature (∼700 °C, see Figure 2.4) in the last low pressure turbine stage (LPT) [2]. These drastically different temperature regimes require blade designs that are specifically tailored to the HPT and LPT-stages.

The HPT-stage blades are cooled with air that is fed through a number of channels in the blades (see Figure 2.6). In addition the blades are coated with a thin layer of yttrium-stabilised-zirconia acting as a Thermal Barrier Coating to the blade. These two measures effectively cool the superalloy blade. Figure 2.6 shows a cross section through a model HPT blade along with the temperatures and stresses associated with each individual section of the blade. Whilst large sections of the blade remain under 900 °C and thus stay 'cool', the leading and trailing edge are exposed to the hottest temperatures of the order of 1100 °C [207, 51].

The gas temperatures during take-off on the first LPT-stage, are roughly in the same order of magnitude as the colder parts of the HPT-blade. As this temperature is sufficiently low, the LPT-stage is commonly not cooled or coated.

2.3 Isothermal creep effects

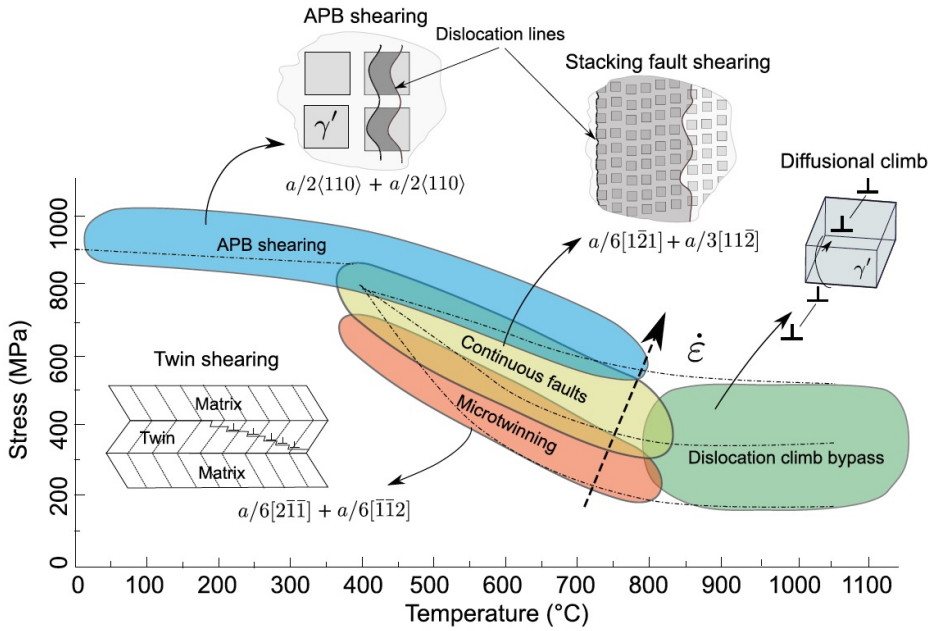

Fig. 2.7 Deformation map for a single crystal superalloy illustrating the dependence on stress, temperature and strain rate. From [15, 187]

The deformation in single crystal superalloys is temperature and stress dependent, as the deformation map adapted by Barba *et al.* [15] in Figure 2.7 highlights. As shown in the figure, each deformation mechanism is driven by a specific interaction between the mobile dislocations and the microstructure. The relevant dislocation mechanisms in the high temperature (>850 °C) creep regime will be reviewed in Section 2.3.1. The resulting dislocation interactions are discussed in Section 2.3.2. Depending on the active deformation mechanisms, the plastic strain response of a given superalloy changes. The different responses have been categorised into creep regimes and creep stages, which will be further discussed in Section 2.3.3.

2.3.1 Dislocation motions in high temperature creep

Dislocations will move by the energetically most favourable mechanism under the applied temperature and stresses. Four different dislocation motions (glide, shear, climb and cross-slip) have been observed in single-crystal superalloy samples in the high-temperature creep regime. Whilst the bulk of the deformation in this regime is generally due to dislocation

glide and climb, the contributions of the other mechanisms depend on parameters such as dislocation density as well as alloy mixture and homogeneity (Section 2.1.2).

Dislocation glide

Dislocation glide (also referred to as slip, shown in Figures 2.10 and 2.12) is the primary method of deformation in the γ-matrix of superalloys [92, 229]. Dislocation glide is localised to the twelve $\{111\}\langle 110\rangle$-type slip planes in an FCC-crystal. The shear stress (τ_K), acting on each slip plane can be calculated with the Schmid factor equation. Slip systems with the highest Schmid factor will deform first and subsequently carry the deformation motion (see [92]). The overall plastic deformation accumulated by the slip of dislocations was described by Orowan with Equation 2.2.

$$\dot{\varepsilon}_{pl} = b \cdot \rho_m \cdot v(\tau) \tag{2.2}$$

$$v(\tau) \propto (\tau_K - \tau_{K_0})^n \tag{2.3}$$

Where ρ_m refers to the density of mobile dislocations that can glide in the material, and v to the dislocation velocity. The velocity of slip at high temperatures is only weakly related to the ambient temperature [33]. A much stronger, linear proportionality exists between the acting stress and the dislocation velocity (see Figure 3.12 in [92]). Svoboda and Lukáš [198] argued, using linear thermodynamics of irreversible processes, that the slip velocity can be expressed as a function of the acting shear stress on the respective glide plane (τ) (see Equation 2.3).

Dislocation shear

The dislocation glide in the γ'-precipitate phase is generally referred to as shear. In the high temperature creep regime, dislocations can shear the γ'-phase by creating an Anti-phase boundary (APB). The passing of dislocations across the coherent interface into the $L1_2$-ordered precipitate disrupts the bonding arrangement between atoms by bringing energetically unfavourable atoms into nearest-neighbour relationships, creating a planar stacking fault known as an Anti-phase boundary (APB). Dislocation shear is facilitated by $\frac{a}{2}\langle 1\bar{1}0\rangle\{111\}$-dislocations, formed in the softer γ-matrix that exhibit sufficient energy to pass across the coherent interface into the $L1_2$-ordered precipitates [162]. To cross the interface, the action of the shear stress on the dislocation must generate energy of the order of the planar defect it

creates upon shearing. As the Anti-phase-boundary energy (APBE) is in the order of 250 $[\frac{mJ}{m^2}]$ [164], the γ'-interfaces cannot easily be passed by a single dislocation, and hence act as obstacles to dislocation motion. The energy embedded in the APB-fault is balanced by the repulsive forces between the two dislocations such that through the pile-up stresses the dislocation at the front of the pile-up has enough energy to generate an APB-fault [125, 40]. The trailing dislocation can then follow into the phase without an additional energy barrier (restoring the lattice as it shears through γ'). Thus γ'-shearing is observed as two closely spaced dislocations (i.e. a $a[110]$-Superdislocation) that requires sufficient dislocation density to form and thus only occurs after the accumulation of substantial strain deformation [6, 7].

As implied in Figure 2.7, the APB shearing regime is related to the yield strength of an alloy and thus becomes operative for lower applied stresses with increasing temperatures as the APBE falls.

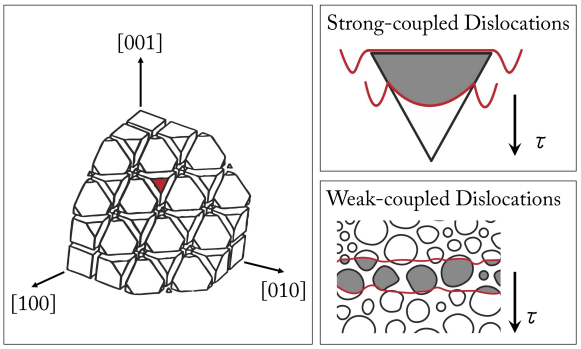

Fig. 2.8 [Left] 3D-(111) cross section of the γ'-cuboids; [Right,Top] Sketch of a γ'-particle cut by strong-pair coupling, leaving an APB (highlighted in grey); [Right,Bottom] Sketch of γ'-tertiary precipitates cut by weak-pair coupling [164, 40]

Assuming a constant applied stress, the shearing of the γ'-precipitates depends on the APB-formation Energy, the size, distribution, shape and volume fraction. The APB-Energy [46, 212] and the γ'-volume fraction [145] are contingent on the local element distribution in the region (IR, SDA, PDA). Whilst the γ'-size, distribution and shape depend on the heat treatment and subsequent temperature exposure [82, 229].

To estimate the shear stress required to enter a γ'-precipitate, two equations have been proposed that cover the different γ'-sizes. For higher γ'-volume fractions and γ'-sizes, as in the case of primary γ'-particles, the dislocation spacing (between leading and trailing dislocations) is comparable to the particle diameter (see Figure 2.8). Therefore a given particle will contain one dislocation pair in a $\{111\}$-slip plane, that is then *strong-coupled* [164]. Huther and Reppich proposed the following formula for this case ([164] p.78f).

$$\tau_{cut,strong} = \breve{w}\left(\frac{Gb}{r}\right)\sqrt{f}\frac{w}{\sqrt{\pi^3}}\left(\frac{2\pi\gamma_{APB}r}{wGb^2} - 1\right)^{1/2} \tag{2.4}$$

The variables are defined as follows: f as the volume fraction of γ', r-particle radius, γ_{APB}-Anti-phase-boundary energy, G the γ'-shear modulus, with w and $\breve{w}$ as fitting-parameters.

$$\tau_{cut,weak} = \frac{\gamma_{APB}}{2b}\left[\left(\frac{12\gamma_{APB}fr}{\pi Gb^2}\right)^{1/2} - f\right] \tag{2.5}$$

Smaller particles at lower volume fractions, such as secondary and tertiary γ'-particles, then contain *weak-coupled* dislocation pairs, that span across a number of particles (see Figure 2.8). According to Ardell this case can be described by Equation 2.5 [9]. Under isothermal creep conditions the critical resolved shear stress (CRSS) is then calculated for a given precipitate size distribution (PSD), as shown in Figure 2.9 by [34].

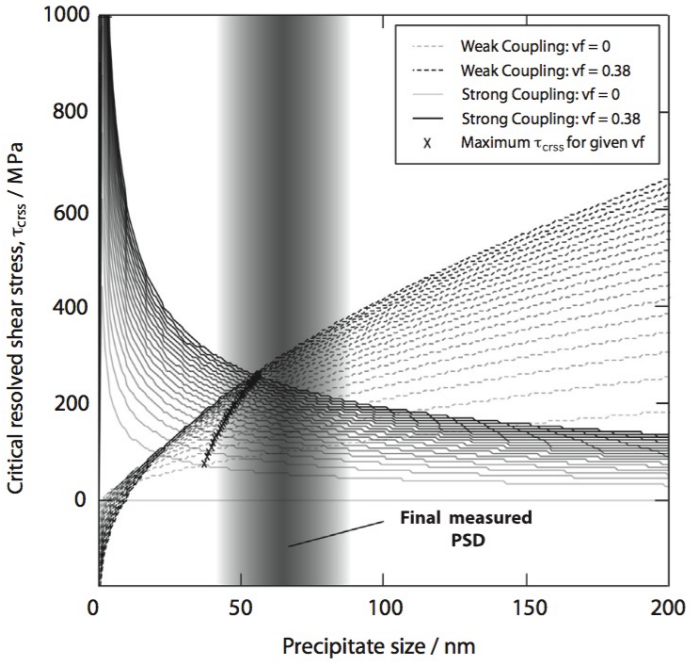

Fig. 2.9 Calculated values of the critical resolved shear stress (CRSS) at 700°C assuming weak and strong dislocation coupling; The measured PSD and ideal precipitate sizes are highlighted [Alloy: RR1000]; [34]

Dislocation cross-slip

Dislocation cross-slip describes the conservative motion of a screw dislocation from a {111}-type plane onto a free, intersecting slip plane that also contains the direction of the Burgers vector (see Figure 2.11). This occurs if a back-stress (i.e. from a dislocation pile-up) hinders further dislocation motion along the plane [92].

Svoboda and Lukáš [199] have included the effect of cross slipping by allowing dislocations of intersecting slip systems with a common Burgers vector direction to interact.

Dislocation climb

Dislocation climb is the upward or downward movement of dislocation loops along the interfaces of the $L1_2$-phase (see Figure 2.12). Climb is facilitated by vacancies that diffuse (individually or in small clusters) to the dislocation core, resulting in the creation of two steps called jogs [92]. These further act as vacancy sinks and sources, and have an edge character. Jogs then enable edge components of dislocations to climb onto a new slip plane [92]. With climb, the volume changes locally (resulting in a non-conservative motion). Importantly, the climbing of a dislocation, away from its original slip plane, onto a new one allows additional glide in the original $\langle 101 \rangle$slip plane and can result in the annihilation of the climbed dislocation in the new slip plane. As climb is dependent on the concentration and mobility of vacancies (correlated to diffusion), the process is temperature dependent [92].

Different approaches to the modelling of dislocation climb have been published. Svoboda proposed modelling the resulting reduction in dislocation density and change in volume [199]. Fedelich modelled the plastic deformation resulting independently from climb [63]. Whilst Dyson coupled the climb and glide mechanisms, to model the resulting plastic deformation [52]. Furthermore, all models assume the contribution of dislocation climb to the total deformation in the high temperature creep regime to be different.

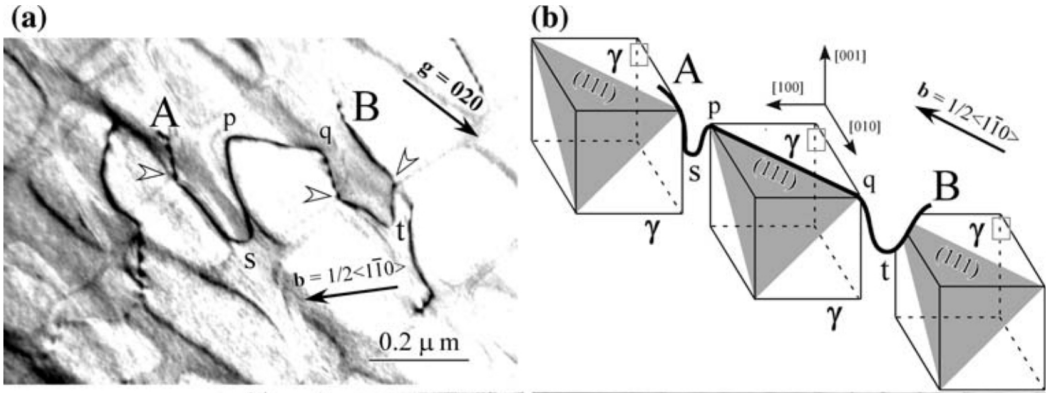

Fig. 2.10 (a) A screw dislocation AB gliding in a (111) plane in the matrix channels, with its segments pq attached to the upper surface of a cuboidal precipitate and its other parts bowing into the channels at sites s and t. Beam//[001]. (b) A schematic illustration to show the stereoscopic configuration of the dislocation AB in (a). [227]

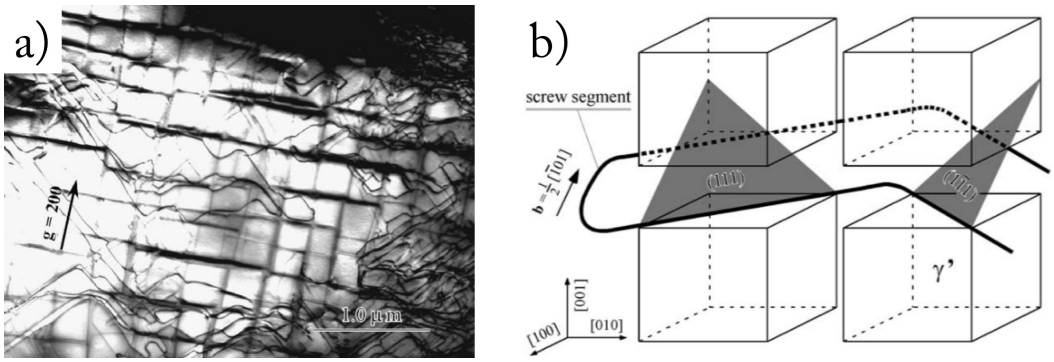

Fig. 2.11 (a) A screw dislocation cross-slipping in a (111) plane in the matrix channels, TMS-138 after 2h of creep (1100°C, 137 MPa). (b) A schematic illustration to show the cross-slip motion observed in (a). [226]

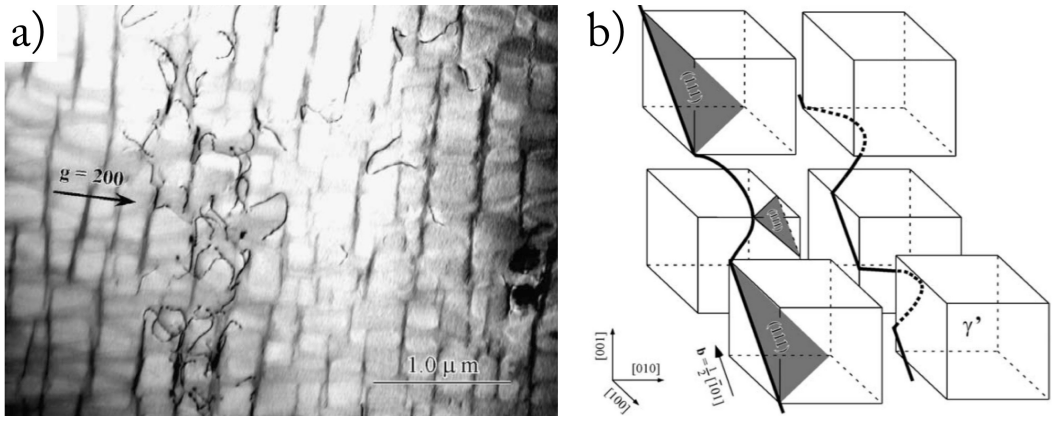

Fig. 2.12 (a) A dislocation gliding and in a (111) plane and climbing along the edges of the precipitates in the matrix channels, TMS-75(+Ru) after 2h of creep (1100°C, 137 MPa). (b) A schematic illustration to show the motion observed in (a). [226]

2.3.2 Interactions between defects

Interaction between point defects and dislocations

Provided the diffusion speeds of alloying atoms soluble in the γ-matrix are below the dislocation line velocity, these exert a pinning force on the edge dislocation. This is generally referred to as solid-solution hardening. The effect is related to the atomic size misfit and bonding strength between alloying elements (included through the effect on the modulus) and has been quantified in terms of its influence on the lattice parameter, shear modulus and flow stress of the alloy for B-subgroup alloying elements in nickel, by Mishima *et al.* [143, 144]. The contribution to the resistance of dislocation glide has further been approximated by a number of models [85, 170, 230] and will be modelled in Section 4.1.1.

Interactions between dislocations

Dislocations interact through their elastic fields by either repulsing, annihilating or reacting with each other. If the stress field around the dislocation cores is equal and opposite the dislocation lines annihilate. An annihilation event will lead to local relaxation (i.e. softening) due to the locally decreased dislocation density (and associated stress fields). Repulsion of dislocations due to equal stress fields results in a pile-up in front of impenetrable interfaces and leads to dislocation hardening [25]. Two opposite type dislocations have to be on the same slip plane, to annihilate each other, whereas repulsive forces can even be exerted across slip planes [12]. The resistance to γ'-glide (τ_{K_0}) according to the calculations laid out in the appendix of [199] by Svoboda, can be approximated on the condition that the energy released by slip is equal to the increase of the energy of dislocations deposited on the γ/γ'-interfaces and thus depends on the energy of deposited γ/γ'-interfacial dislocations (ρ_K), divided by the average channel width h (with G as the Shear-modulus) (see Equation 2.6). The multiplication factor (2.2×10^{-8}) results from approximating the line energies of screw and mixed dislocation (see appendix of [199] for an in-depth discussion).

$$\tau_{K_0} = \sqrt{\frac{2}{3}}\frac{Gb}{h}(1 + 2.2 \times 10^{-8} \cdot \rho_K) \tag{2.6}$$

The model by Tinga *et al.* has expanded this equation to include dislocation hardening on every slip-system [204]. The dislocation interactions will be further considered in the creep modelling presented in Sections 6.2.3, 6.3.4 and 6.2.5.

Interfacial dislocation networks

Beside repulsion and annihilation, dislocations can interact to form interfacial dislocation networks.

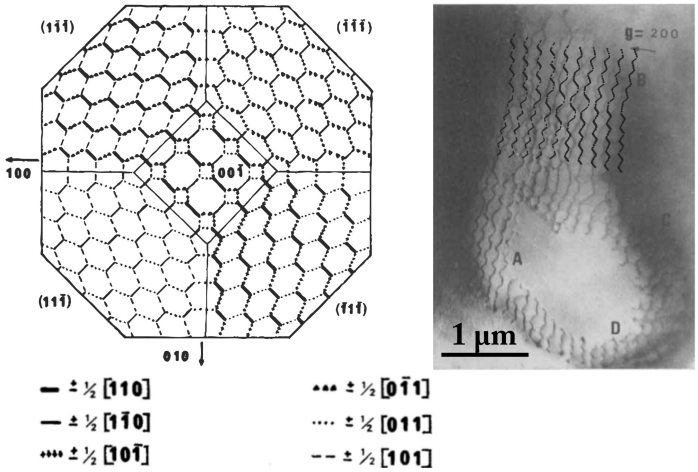

Fig. 2.13 [Left] General view of the three dimensional pure edge dislocation network covering four {111}-faces; [Right] Micrograph of a γ'-interfacial dislocation network with a schematic network insert. From Lasalmonie *et al.* [114].

Interfacial dislocation networks form largely due to two factors, interfacial stresses and the anti-phase boundary energy. Where single dislocations do not have the energy required to shear the γ'-precipitate phase by creating an APB-fault, they become trapped at the interfaces. The interfacial deposition of edge dislocations can be energetically favourable, where the interaction between the stress field from the dislocation and the interfacial lattice misfit leads to an overall reduction of the stress fields [67, 30, 123, 217]. As the dislocation density increases with test time, further dislocations are deposited around the interfaces with an ever decreasing distance between them, eventually these distances are so low that neighbouring dislocations will interact in an energetically favourable configuration, eventually forming interfacial dislocation networks [30, 62, 193].

As shown in Figure 2.14, the networks begin to form during the first stages of high temperature creep, forming $\frac{a}{2}\langle 110\rangle$-edge dislocation interfacial networks [114]. The reactions are laid out in detail by Field *et al.* [67]. With the onset of the second stage of creep, the interfacial dislocation networks are fully established and are shown in their three dimensional structure in Figure 2.13. The established dislocation networks can further be characterised by their regularity and mesh density which Figure 2.14 indicates depends on the alloying content. In particular the content of high partitioning elements like rhenium (that maximise

lattice misfit [148]) result in a closer network spacing. The average network dislocation spacing can be approximated by Equation 2.7 [30].

$$d = \frac{|b|}{|\delta|} \tag{2.7}$$

The higher the misfit, the higher the resulting driving force for dislocations to bow into the γ-channels. As a result, dislocations create more regular and denser interfacial networks, with higher misfit [147, 108, 228, 226, 227]. Conversely, a lower misfit will lead to less dislocation motion in the matrix channels, less regular and wider dislocation networks linked to a higher minimum creep rate [226, 227] and a shorter creep life [228].

The established dislocation networks will interact with every new dislocation in its proximity. Most importantly they will act as an additional barrier, preventing further dislocations from entering the γ'-phase by interacting with them [213, 214].

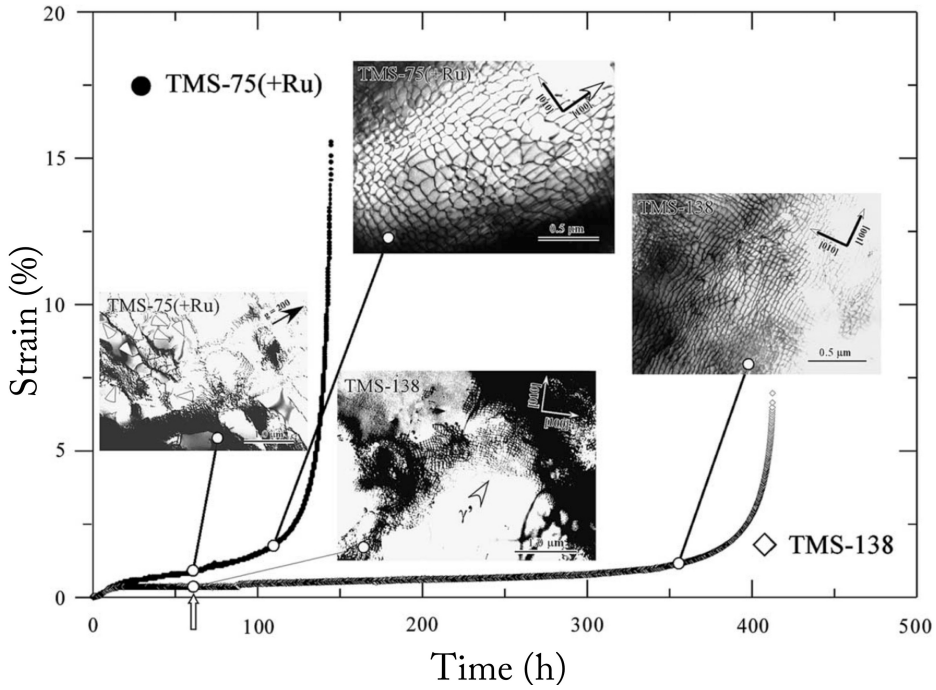

Fig. 2.14 Creep curves (1100°C, 137 MPa) for two alloys (TMS-75+Ru;TMS-138) with SEM micrograph inserts corresponding to the creep stage marked [226].

2.3.3 Creep regimes

The isothermal creep response of a given superalloy changes according to the number and kind of dislocation mechanisms activated under the applied temperature and stress. These

different creep responses have been categorised into three distinctive different creep regimes according to Reed *et al.* [164]: primary, tertiary (also referred to as intermediate) and rafting. Additionally the creep response over the test time is commonly characterised into three distinctive creep stages: primary, secondary (also referred to as intermediate) and tertiary. The terminology chosen for the creep regime and test stages hints at similarities in the shape of the creep curves. However, the creep regimes are narrowly defined by the principal deformation mechanisms carrying the principal deformation activity, whilst the terms to describe test stages describe distinctly different sections of the creep curve.

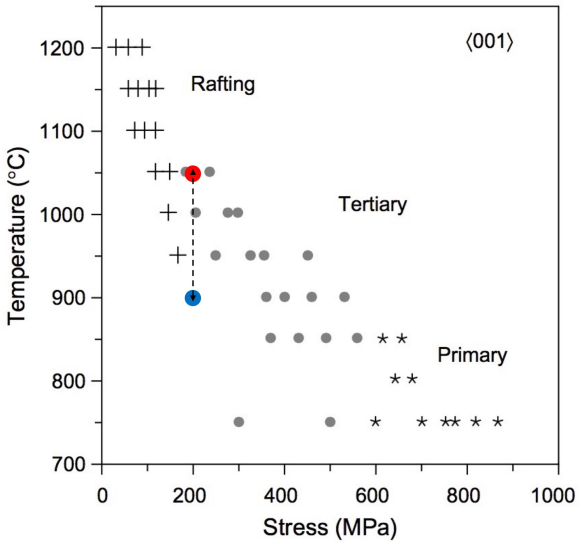

Fig. 2.15 Plot of temperature vs. applied stress, indicating the conditions where in the case of alloy CMSX-4 different creep deformation regimes operate [164]; The blue and red dot on the dashed black line correspond to the base and high temperature condition the experiments of the non-isothermal study conducted in this study were cycled between.

Matan *et al.* [164] plotted the defining creep mechanisms for the alloy CMSX-4 as a function of the applied stress and temperature for a [001]-oriented crystal in Figure 2.15. The primary creep regime occupies the low temperature high stress regime and governs above a threshold stress of 500 ($\pm$50) MPa and temperatures below 850 °C. The creep curve in this regime is characterised by a rapid initial strain accumulation that then turns into slightly slower yet continuous strain accumulation. As pointed out in Figure 2.7, this regime is dominated by the stacking-fault shear of $a\langle 11\bar{2}\rangle$ net Burgers vector dislocations. The interested reader is referred to Rae and Reed [162] for an in-depth analysis of the configurations of stacking faults between two partial dislocations.

On the high temperature (> 950 °C) low stress (< 200 MPa) side, the isothermal creep deformation is driven by the rafting regime, with dislocation glide and climb the principal

mode of deformation (see Figure 2.7). Rafting refers to a transformation of the microstructure from γ'-cuboids into rafts. This process and its driving forces are described in subsection 2.3.4. Tests in the rafting regime exhibit a long plateau of low creep strain accumulation (see creep curve for TMS-138 in Figure 2.14). Material failure in the rafting regime is commonly triggered by voids forming at topologically closed packed phases (TCP). Further information on the formation mechanism and role of TCPs can be found with Reed and Rae in [161].

For pressures and temperatures between the rafting and primary, the tertiary regime governs. Figure 2.7 indicates that this region is similarly governed by dislocation glide and climb in the γ-matrix without undergoing a micro-structural transformation of the microstructure (rafting). The strain accumulation in this regime results in an exponentially rising creep curve. Due to the comparably lower temperatures, dislocation climb of edge dislocations is less pronounced. On the low temperature end dislocation cross-slip of screw dislocation becomes important [164].

Creep stages

The two creep curves shown in Figure 2.14 can be subdivided into three distinct stages over their lifetime. The primary creep stage sees an initial increase in strain. Thereafter, the strain only marginally increases (leading to a nearly constant strain rate), called the intermediate or secondary creep stage. Ultimately the strain continuously increases in the tertiary creep stage.

Crucially, the creep deformation for these two tests performed at 1100 °C and 137 MPa exhibit no stacking-fault shear in the primary stage, as would be common in the primary creep regime. Instead, the dislocation activity is limited to the γ-matrix. Following an initial incubation stage, wherein the dislocation density homogenises throughout the sample [151, 226] the primary deformation stage is characterised by an increasing dislocation density that seeks to compensate the interfacial misfit stresses [136].

The intermediate (or secondary) creep stage that is particularly prominent for the alloy TMS-138 in Figure 2.14 is characteristic for the rafting regime [177, 129, 202, 151]. An extended steady state stage secondary creep regime has been linked to the recovery softening by dislocation climb and strain hardening mechanisms by dislocation hardening reaching an equilibrium stage [202]. Reaching a steady state regime under certain test conditions thus requires a specific rate of diffusion to balance out the strain deformation. As mentioned in Section 2.3.2, Zhang *et al.* have further linked the prominence of a secondary creep stage to the establishment of interfacial dislocation networks and their effectiveness against γ'-shearing [226].

During the tertiary creep stage in the high temperature creep regime dislocations enter the γ'-precipitates by APB-shear, unlike in the tertiary creep regime [108, 226, 153, 53, 135]. In the tertiary creep stage the shearing of primary γ'-particles by a[110]-superdislocations [202, 229, 164] becomes the dominant mechanism of the mechanical deformation [6, 7] whilst the shearing of smaller γ'-precipitates is not seen as lifetime dependent [222].

2.3.4 Morphological transformation of the microstructure

In the high temperature creep regime the two-phase microstructure transforms due to two overlapping mechanisms, isotropic coarsening and rafting.

Rafting

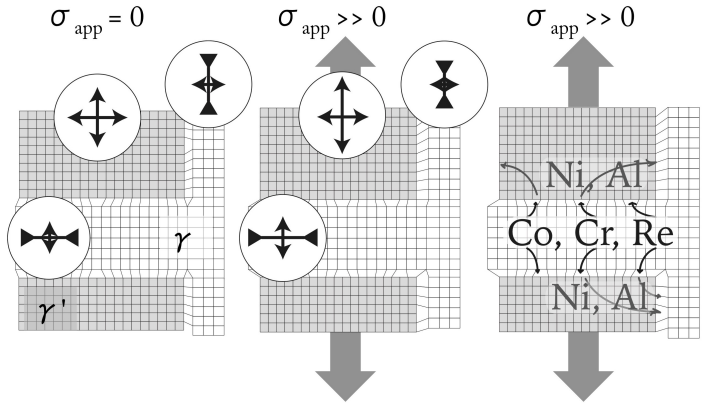

Fig. 2.16 [left] Internal stress fields; [centre] Superimposed external stress fields leading to [right] atomic reordering; based on [104, 112].

Rafting refers to a microstructural transformation, in which the γ' evolves from the initial cuboidal microstructure to long plates (Figure 2.17) called rafts. Matan *et al.* [140] have found, that rafting occurs above an initial threshold strain of $\sim 0.7 \pm 0.3\%$ (in the region of 1050 - 1200°C) and $\geq$900°C, and results from the atomic reordering around the stress-fields of interfacial dislocations. The atomic reordering is triggered by the coupling of diffusion processes with local stress fields (resulting from the superposition of external and internal stresses) (see Figure 2.16).

The microstructure will contain initial stress fields (Figure 2.16 left) due to the lattice misfit, these are superimposed on the local stress fields, once an external load is applied (Figure 2.16 centre). As a result of the net stress fields, negative misfit alloy exposed to a tensile load, will carry more dislocation activity at the horizontal channel interfaces [152].

The horizontal channels then attract larger alloying elements (Co, Cr, Re), in order to relax the compressively stressed dislocation cores whilst comparatively smaller atoms (Al, Ni) diffuse to more relaxed fields, i.e. the vertical channels [24, 76]. The opposite distribution and subsequent evolution holds for a positive misfit, or an applied compressive load, producing rods parallel to the tensile axis [131, 152, 32].

As aluminium and nickel form the γ'-phase (Ni_3Al), the developing rafts will lie perpendicular to the applied tensile stress (Figure 2.17). The speed of rafting depends on the applied stress, the misfit stress [123, 172] and the diffusion processes activated at the exposed temperature [166, 165]. Subsequently, regions of high misfit (i.e. DC) experience a faster transformation towards a rafted structure (Figure 2.17) [165, 141].

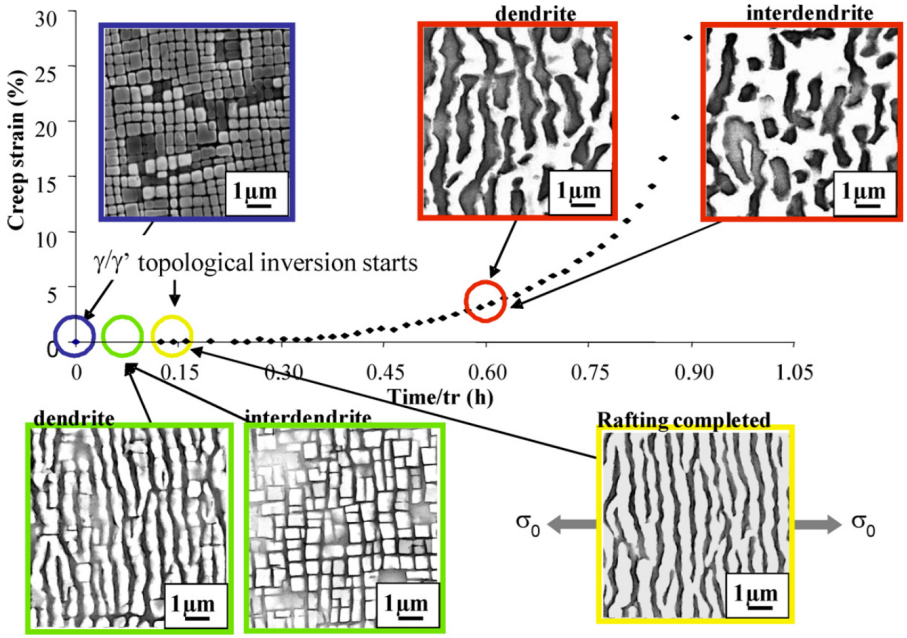

Fig. 2.17 Creep behaviour with normalised creep time depicting the microstructural evolution in the dendritic and interdendritic region of the sample (Alloy MCNG); [141].

The rafting process is completed with the onset of secondary creep, and the effect of creep hardening then accounts for a visible minimum strain rate [166] (Figure 2.17). A rafted structure (defined by the closure of most vertical channels) is seen as contributing to strain hardening, as the extensive rafts impede dislocation climb and increase dislocation interaction lengths across γ-channels [166]. In the three dimensional microstructure (Figure 2.18) many γ'-particles are in reality interconnected, and as a result the distribution of local stress fields becomes more complex than described above.

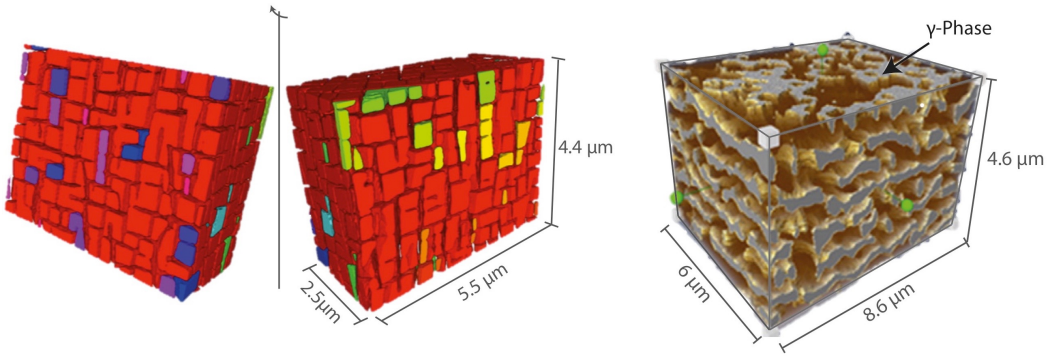

Fig. 2.18 [Left] FiB-tomography reconstruction showing interconnected γ'-particles in the same colour (alloy: PWA1497); [Right] Creep ruptured 3D FiB-tomography reconstruction with the applied stress normal to the cubes' top, showing the topological inversion (alloy: PWA1497); [232]

$\gamma' - coarsening$

Isotropic coarsening due to Ostwald ripening does not require an applied load and will occur simultaneously with rafting should the latter process be activated [57, 31]. Coarsening characterises the growth of larger γ'-particles at the cost of smaller ones. The diffusion of the slowest elements, with the greatest γ-partitioning tendency (i.e. rhenium) are thought to be rate dependent on the coarsening rate [113]. Isotropic growth is most pronounced alongside the rafting process and decreases significantly, once the horizontal γ-channels have reached about three times their original size [57].

Towards the end of the lifetime in the rafting regime, the microstructure will have drastically coarsened (see Figure 2.18 right), leading to an inverted microstructure in which the γ-phase is now embedded in a γ'-matrix (topological inversion) [60]. The irregularity of the rafts and the topological inversion is thought to be generally more pronounced in the interdendritic region (Figure 2.17). Upon inversion, the γ'-phase ultimately becomes the carrier of deformation activity by shearing resulting in further acceleration of the strain rate and ultimately material failure [7].

2.4 Non-isothermal creep phenomena

2.4.1 Non-isothermal and constant stress conditions

Non-isothermal creep conditions are designed to mimic certain in-flight stress and temperature conditions in order to better understand the micro-mechanical response of the tested alloy during in-flight operation. Specifically, tests reported in the literature are designed to alternate between a lower base temperature and short high-temperature exposures (e.g. to mimic a one engine inoperative scenario in a helicopter engine in the case of the highest temperature studies by Cormier *et al.*[36]). The temperature steps trigger the microstructure to adjust towards a new thermo-stress equilibrium. Depending on the magnitude and duration of the high-temperature step, different dislocation mechanisms are activated. The creep lifetime under non-isothermal conditions then depends, on the temperature, exposure time, heating and cooling rate, cycling times and alloy composition. The observations and trends summarised in the following, were taken from experiments, using predominantly the alloys AM1 and MC2, performed by Cormier *et al.* with a test-rig described in [36], that allows over-heating events up to 1200 °C.

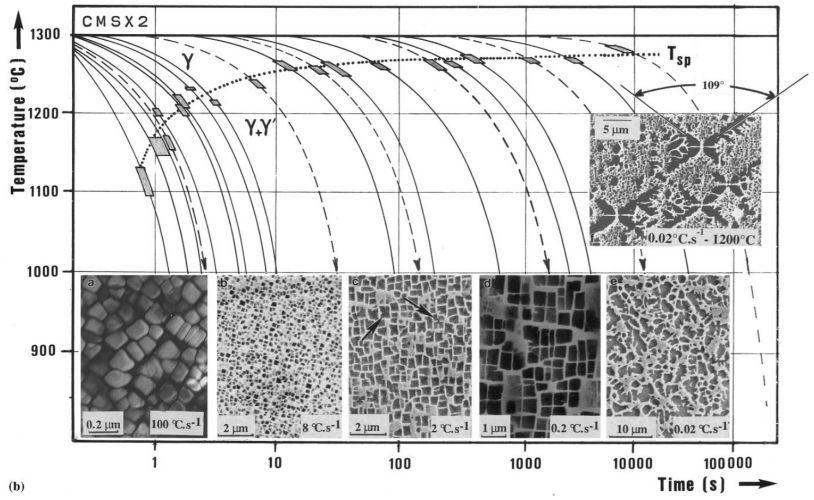

Fig. 2.19 CCT curve determined by dilatometry with the corresponding micrographs of the developed microstructures for various cooling rates [Alloy H3hr CMSX-2]; [82]

Short high-temperature exposures (see Figure 2.21), result in an increase in the magnitude of the interfacial lattice misfit (see Figure 2.23), subsequently inducing new dislocation activity into the interfacial microstructure [119]. Simultaneously, the γ'-volume fraction decreases with temperature, due to the subsequent higher solubility of γ'-partitioning elements in the γ (Figure 2.22). The γ'-edges then dissolve first into the γ-phase (see Figure 2.20) [37].

When varying the overheating length by 30, 90 and 150 seconds, Cormier *et al.* found, that the longest exposure resulted in the longest creep lifetime [38]. The authors related this to the longer high-temperature exposures resulting in more stable interfacial dislocation networks, that subsequently protected the γ'-particles against dislocation shearing [39].

The cooling rate affects the particle size and distribution (see Figure 2.19) [82]. A higher cooling rate, leads to the re-precipitation of secondary γ'-particles into the matrix channels (see Figure 2.20), which effectively reduces the dislocation motion in the γ [102, 103]. This results in a lower strain rate and longer creep life [192, 38], until the γ'-seconday particles redissolve into the γ'-primary due to Ostwald ripening [118].

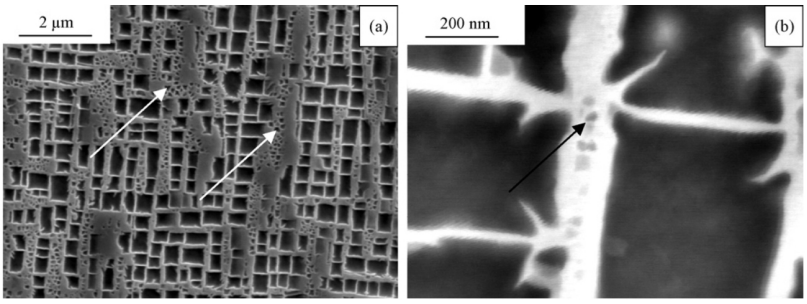

Fig. 2.20 Microstructure after an 180s 1200°C overheating [a] arrows indicate reprecipitation of secondary γ'-precipitates into the matrix channels; [b] magnification of the interphase region; [Alloy MC2]; [118]

The shorter and more frequent overheating events showed higher plastic strain accumulation during the exposure (see Figure 2.21), resulting in a substantially shorter lifetime [77]. The additional strain accumulated during an overheating event is thought to result, in part, from the actual overheating and is largely due to a post-high-temperature exposure strain that accumulates just after the sample has cooled back down to the base temperature condition [115]. The extent of post-high-temperature creep strain added impacts the post-overheating creep life, in that a slower creep rate and longer primary creep stage extends residual life [115].

The interfacial dislocation networks generated under non-isothermal creep conditions have been shown to be less regular and wider spaced (see Hantercherli *et al.* [87]). This indicates, that the average network spacing and its regularity is a function of the underlying interface topography (which changes due to γ'-dissolution and re-precipitation).

Lastly, the microstructure is a dominant factor in creep life under non-isothermal conditions. The microstructure differs with alloy composition, as well as external parameters (e.g. loading paths) [77]. Samples deformed in compression (resulting in rafts parallel to the stress axis, called P-Type) previous to the overheating under a tensile stress, displayed a longer

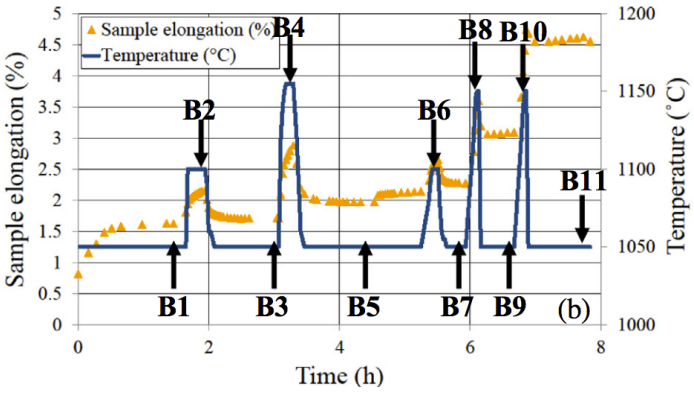

Fig. 2.21 Non-isothermal Creep Test *in situ* analysed with XRD-synchrotron radiation, exposed to five temperature steps at 120MPa plotted with the corresponding elongation measurement [alloy: AM1]; [120]

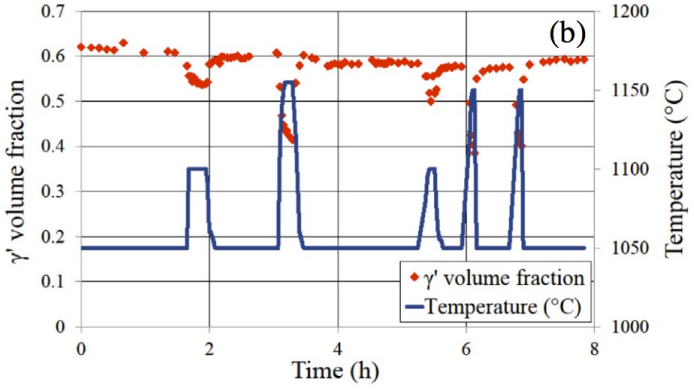

Fig. 2.22 γ'-volume fraction analysis to test in Figure 2.21; [120]

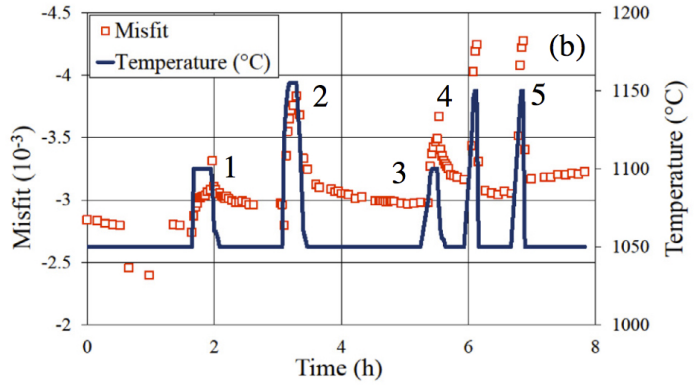

Fig. 2.23 Misfit analysis to test in Figure 2.21; [120]

creep lifetime under very high temperature heating cycles [77] whilst a 1170 h tensile-stress pre-rafted and coarsened (N-Type) microstructure resulted in a shorter creep life [77]. This has been linked to the formation of a 'labyrinth' like microstructure, that a P-Type structure develops under tensile stress [101, 77], that is thought to effectively block further dislocation motion.

To conclude, an overheating event reduces the remaining creep lifetime, by increasing the creep strain rate [163], and increasing the porosity along the slip planes [101] whilst the residual creep lifetime seems to strongly depend on the microstructure prior to the overheating [115].

2.4.2 Isothermal and varying stress conditions

Dirand *et al.* [48] as well as Schenk *et al.* [176] stepped the applied stress under constant high temperature creep conditions. They reported, that stepping the stress results in a decrease in misfit, similar to the effect of a temperature step. However the jump in lattice misfit is here caused by an increase in the von Mises stress, without a change of the γ'-volume fraction [176]. Furthermore they found that the plastic strain rate increased rapidly, approaching the yield point of the alloy [176]. Results for simultaneous temperature and stress stepping, termed the creep-fatigue regime are published with [116].

Chapter 3

Creep Testing and Analysis

3.1 Micro-pillar deformation at room temperature

3.1.1 Micro-pillar preparation

The micro-pillars in this study were created from fully heat-treated (8h at 1314 °C, 4h at 1140 °C and 16 h at 870 °C) samples of CMSX-4, supplied by Rolls-Royce plc. Square section pillars with a side length of 5 μm and an aspect ratio of approximately 1:3 were milled at the edge of each sample, using a *Helios Nanolab, FEI, USA* focussed ion beam scanning electron microscope (FIB SEM). The pillar was positioned 5 μm from the edge of the sample to avoid any overhang. Initially, the material was milled rapidly, at a current of 9 nA and an accelerating voltage of 30 kV, to shape the pillar and remove surrounding material. The final step involved a cleaning cross-section at 0.43 nA and a 2° offset from the vertical to remove any taper. The face on which the pattern was to be deposited was milled last, at a current of 0.23 nA, to reduce Ga^+ implantation and re-deposition from the FIB milling. Finally, the sample was oriented so that the top of the pillar could be milled, to ensure it was flat and normal to the pillar axis. The above milling sequence helps minimise the effect that tapering and ion damage have on the observed strain hardening, an effect which is nevertheless expected to be negligible for the relatively large pillars tested here [100].

3.1.2 Speckle patterning

With the sample oriented so that the face for Pt-deposition was normal to the electron beam, the speckle pattern was reproduced from the bitmap image provided in Di Gioacchino and

Clegg [45]. The pattern, containing 4000 speckles of 3×3 pixels, was deposited at the top of the pillar over an area of 4×8 μm^2. The deposition was completed in a single pass to avoid the spreading of deposited material that follows possible shifts in beam position due to sample charging. The amount of material deposited per point was controlled by the dwell time (1200 μs) and was chosen to produce speckles of approximately 40 nm in diameter. The deposition was done at 15 kV, 1.4 nA at a beam size of 13.3 nm for 43 s.

3.1.3 Micropillar testing

Prior to compression an image was acquired at 15 kV, 1.4 nA, with a 6.1 min scan time and a 4 mm working distance at 5 nm resolution of the finished pillar. Subsequently, micro-compression was carried out with an *in situ* nano-indenter using a 10 μm *Alemnis, CH* flat punch in a field emission gun scanning electron microscope (FEG SEM) *Cross beam, Zeiss, GE*. The punch was brought into proximity with the pillar and the latter compressed to 0.1 strain with a nominal rate of 5×10^{-3} s^{-1}. An image of the deformed pillar was taken in the original FIB-SEM microscope under the same conditions for the digital image correlation.

3.1.4 Digital image correlation and strain mapping

Digital image correlation was carried out using the software *DaVis, LaVision, Germany*, using subsets (S) down to 16×16 pixels giving a spatial resolution of up to 80×80 nm^2, with a window overlap of 50%. The image of the deformed pillar was correlated with the undeformed pillar image to obtain the 2D displacement field on the xy-plane of investigation. This was used to calculate the maximum shear strain, γ_{max} at each subset:

$$\gamma_{max}(S) = 2\sqrt{(\frac{\varepsilon_{xx} - \varepsilon_{yy}}{2})^2 + (\frac{\gamma_{xy}}{2})^2} \tag{3.1}$$

where ε_{xx}, ε_{yy} and $\gamma_{xy} = 2\varepsilon_{xx} = 2\varepsilon_{yy}$ are the strain components in the xy plane. The Equation 3.1 was used as it compensates for the lack of out-of-plane displacement data as outlined further in Jones *et al.* [100].

Two images of the same speckle pattern acquired at the conditions used for testing were correlated to characterise the spatial distortion associated with irregularities in the SEM scan. The correlation produced a bundle of horizontal bands of ~ 0.04 strain in the γ_{max} map. Therefore, each individual value had an error of $\zeta = \pm 0.04$.

Images of the pillars used for DIC also displayed compositional contrast, as shown in Figure 4.44. This enabled the positions of the precipitates to be identified and outlined

directly on the maps of maximum shear strain. The outlining was done by eye inspection and thresholding using the software *ImageJ, National Institute of Health, USA*. The value of $\langle \gamma'_{max} \rangle$ was determined by summing the maximum shear strain values obtained for the precipitate phase (γ') using Equation 3.1 and dividing by the number of data points, N^P:

$$\langle \gamma'_{max} \rangle = \sum_{S \varepsilon \gamma'} \gamma_{max}(S)/N^P \tag{3.2}$$

The same approach was taken to estimate the matrix parameters.

The standard error in the mean shear strain was then calculated as $S.E. = \zeta/\sqrt{n}$, where n is the number of shear strain values used to calculate the mean. For each phase, the mean shear strain was calculated from a large number of shear strain values (> 2000) and therefore the corresponding error was relatively small < 0.0008. Despite this uncertainty, it is important to note that the sign of the calculated $p_{plastic}$ remains unaffected.

3.2 Non-isothermal creep testing

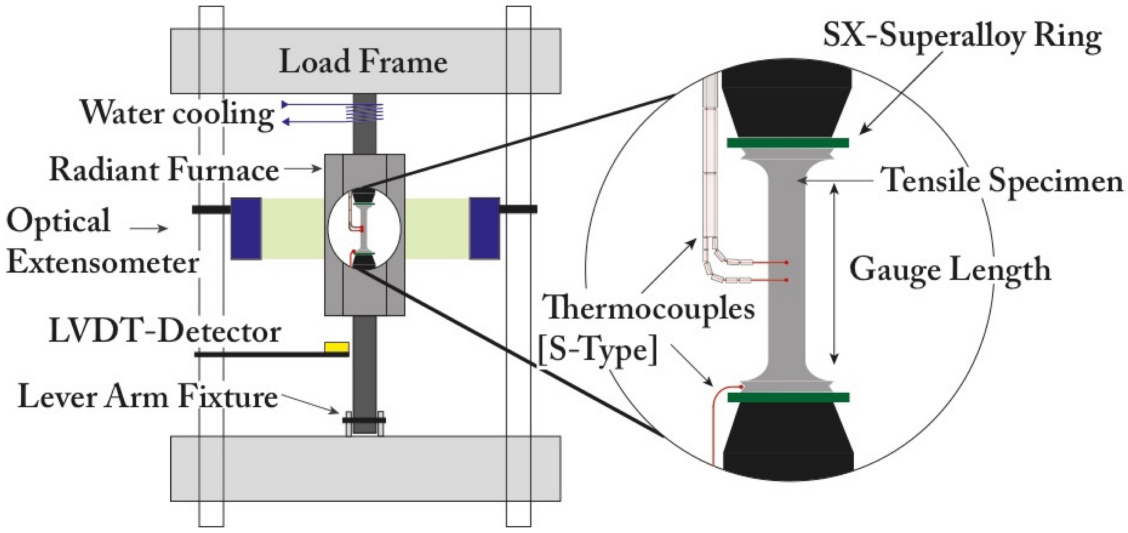

Fig. 3.1 Sketch of the used test set-up on the creep rig.

The non-isothermal creep tests were performed on a *Lever Arm Setra SF 2400* creep frame using a calibrated deadweight, equipped with a radiant furnace controlled by a *Eurotherm 2408* controller with extension measured by a *Keyence LS7070T* optical extensometer (see

Figure 3.1). The temperature was controlled by an S-type thermocouple spot welded to the centre of the gauge length. The calibrated offset measured by the thermocouple at peak temperature was ±0.85°C. The load was held at an initial applied stress of 200 MPa, only decreasing during the high temperature exposure by 4 MPa.

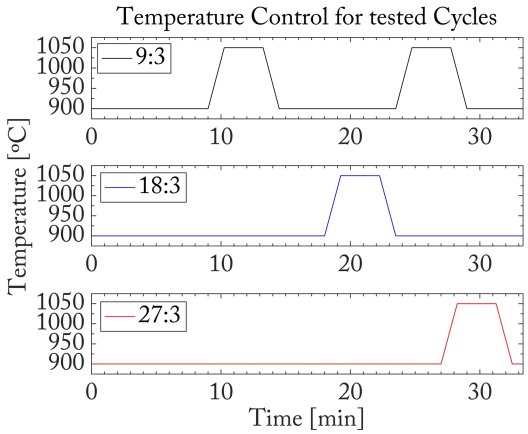

Fig. 3.2 Non-isothermal temperature control for the three different cycle times tested (9-3, 18-3 and 27-3 top to bottom).

The non-isothermal creep tests performed in this thesis consisted of a continuous four segment temperature cycle of a variable holding time at the base temperature, a heating segment, a three-minute hold at high temperature and cooling to base temperature (see Figure 3.2). Hence the three cycle times differed only by the holding time at the base temperature, which were 9, 18 and 27 minutes, corresponding to the black, blue and red line in Figure 3.2 respectively. The heating and cooling rates were kept constant at 120 $[\frac{K}{min}]$ and the resulting overshoot at the high temperature hold and base temperature was +3 K and -4 K respectively. Each cycle type was interrupted at four stages of creep life: just after the first heating cycle, and after heating cycles corresponding to 0.5%, 1% and 2% plastic strain. The test was stopped each time once the sample had just cooled back down to 900 °C. The final cooling rate was 163 $[\frac{K}{min}]$ until 700 °C, 112 $[\frac{K}{min}]$ until 500 °C and 55.5 $[\frac{K}{min}]$ thereafter. The load was removed once the sample had cooled down to 500 °C.

3.3 Post-creep metallographic analysis

3.3.1 Scanning Electron Microscopy

The SEM images for the alloy test series of CMSX-4 were taken using a *Zeiss Gemini 300* microscope, imaging at 5 kV using the In-Lens detector. For the alloy CMSX-10K the

Backscatter Detector was used at 5kV. The specimens were cut and mounted in a conductive bakelite and then polished to 0.06 μm with diamond suspensions and ultimately a 1:5 Opus solution of colloidal silica.

3.3.2 Transmission Electron Microscopy

The deformation accumulation was investigated with a *JEOL 200CX* Transmission Electron Microscope (TEM) at 200 kV, using a double tilt holder. Blank discs were cut with a thickness of 200 μm with approximately <001> and <111> surface normal. From these blank discs, foils were made by twin-jet electro-polishing in a solution of 6% perchloric acid in methanol cooled to -5 °C. In order to improve resolution in comparison to bright field imaging (BF) weak beam dark field (WBDF) micrographs were recorded in regions of interest.

To determine the Burgers vectors of selected dislocations the foils were tilted towards the different two-beam conditions that surround the (111) and (100)-zone axes. The orientation of the acquired films in relation to the acquired diffraction patterns from a given region were then corrected according to a rotation calibration acquired with a MoO_3 sample. The visibility of the dislocations in a given region using different two beam conditions (and thus different g-vectors) were then compared and their respective Burgers vectors were determined according to the visibility table (see Table 3.1).

Table 3.1 (x) Invisible, (○) weak and (●) strong contrast of a dislocation of the specified Burgers vector under the indicated g vectors

g / b	$[01\bar{1}]$	$[10\bar{1}]$	$[1\bar{1}0]$	[110]	[101]	[011]
$(1\bar{1}1)$	○	x	○	x	○	x
$(\bar{1}11)$	x	○	○	x	x	○
$(11\bar{1})$	○	○	x	○	x	x
$(\bar{2}02)$	○	●	○	○	x	○
$(02\bar{2})$	●	○	○	○	○	x
$(\bar{2}20)$	○	○	●	x	○	○

3.3.3 Electron Probe Microanalysis

To measure the chemical composition across the dendritic microstructure, fully heat treated samples of the tested alloys were cut with approximately <001>-normals, mounted in a conductive bakelite and subsequently polished to 0.25 μm. The samples were analysed in a *Cameca SX100* microscope at 20 kV and 100 nA with a dwell time of 0.04 seconds per

5 μm step for a 1250×1250 μm^2 grid. The wavelength dispersive spectrometers (WDS) were equipped with crystals of TAP, LLiF, LPET, LiF and LPET. X-ray counts were recorded in two passes according to the radiations in the two columns in Table 3.2.

To verify the analysis the datasets were compared against identical alloy compositions exposed to longer dwell times.

Table 3.2 Crystal and radiation set-up for the two passes performed at each data acquisition point.* was only performed for the CMSX-10N alloy. Crystal acronyms: TAP -Thallium acid phthalate, LiF - Lithium fluoride, PET - Pentaerythitol; L - large.

Pass /Crystal	TAP	LLiF	LPET	LiF	LPET
1	Al Kα	Cr Kα	Re Mβ	Ni Kα	Ti Kα
2	Ta Mα	W Lα	Nb Lα^*	Co Kα	Mo Lα

3.3.4 In-situ X-ray diffraction

In situ non-isothermal creep experiments were performed by Alain Jacques *et al.* together with the datasets for the alloy AM1 published in [120]. The previously unpublished dataset for CMSX-4 was acquired with a triple crystal diffractometer (TCD) on the high energy XRD beamline (BW5) at the HASYLAB (DESY) [126, 194], using a 120 keV energy (k = 0.0103 nm). The setup and the data analysis are extensively described by Jacques and Bastie [96]. Within the TCD, the incident X-ray beam is successively diffracted by a (3 1 1) Laue Si monochromator ($2\Theta = 3.60°$), the specimen ((2 0 0) reflection, $2\Theta = 3.33°$ at high temperature), and a second (311) Laue Si-monochromator (analyser) in a non-dispersive (+,-,+) geometry. Different zones of the specimen in the Bragg condition diffract the monochromatised beam into slightly different directions, according to their local interplanar distance, and one of those directions is selected by the analyser, which sends the beam to an energy-sensitive Ge point detector. A rotation of the specimen (omega scan) probes the local orientation of the diffracting zones, and a rotation of the analyser crystal (alpha scan) probes the distribution of the beams diffracted by the specimen, i.e. through the lattice parameters. The size (100 μm wide, 500 μm high) of the beam transmitted through the specimen is large enough to get a statistically significant sampling of local misorientations and chemical inhomogeneities related to the dendritic solidification of the alloy. The typical full width at half maximum of an omega scan and an alpha scan are respectively 0.1° and less than 50". The instrumental width of the peaks is better than 1" [126], and it was checked that their shape profiles did not depend on the omega position. A full analyser scan (typically 200 steps of 1 second at 1" from each other) in transmission through a whole specimen having

a 3.6 mm gauge diameter can be recorded within 5 min [126] with a peak to background ratio better than 10^4. Faster scans (90 s) were required during positive thermal jumps in which the plastic strain evolved rapidly and these were recorded with reduced spans and counting times. The (200) γ and γ' peaks are clearly distinct, with a background lower than 200 counts s^{-1} (cps) for a peak maximum larger than 10^4 cps, and have a non-Gaussian shape. The TCD profiles were fitted using three ad-hoc exponential functions [96] (γ and γ' peaks as well as tails) and a specific procedure allowing a direct determination of the γ and γ' volume fractions (respectively f_γ and $f_{\gamma'}$) from the areas of the main two peaks (assuming kinematical diffraction conditions) and the constrained lattice misfit of the γ/γ'-interface plane (δ_{eff}) [47] using:

$$\delta_{eff} = \Delta\alpha \times \cot(\Theta_B) \tag{3.3}$$

where δ_{eff} is the distance between the γ and γ' peaks and is known with a precision better than 0.1" after the fitting. The relative volume fractions of both phases were directly deduced from the peak areas. The scattering amplitude of the different atomic sites of the FCC γ-phase and the ordered Ni_3Al γ'-phase, taking into account the real composition of the alloy and the distribution of the different elements among possible sites, was found to be identical within a few percent. The coherent tertiary precipitates and the surrounding matrix have a lattice parameter different to the rafts and the channels and as such do not contribute to the peaks nor appear in the volume fraction.

3.3.5 Back-Laue X-ray diffraction

To measure the crystals' offset from the [001]-direction films were acquired using a back reflection Laue set-up with an unfiltered Molybdenum radiation source at 20 kV and 40 mA for 2 hours per film with a 3 cm screen distance. The acquired diffraction patterns were then analysed and the offset quantified using the software SingleCrystal 3.0 (a Trademark of CrystalMaker Software Ltd.).

Chapter 4

Estimation of Creep Parameters

One of the motivations of this study is to develop a non-isothermal physically based creep model. The parameters needed for such a model (e.g. phase fractions and APB-energy) are alloy and temperature dependent and, as such, require individual computing routines to be quantified correctly. This chapter will lay out the approach taken toward estimating the key creep parameters required for a non-isothermal model.

Firstly in Section 4.1, the effect of temperature on key creep parameters is quantified using nominal alloy compositions. Secondly in Section 4.2, the scatter created using nominal and actual composition based parameters is quantified in order to understand how much the creep parameters would vary in a specific alloy. Finally, using an *in situ* X-ray analysed dataset, the γ'-phase fraction evolution during non-isothermal high temperature creep exposure is estimated (Section 4.3) laying the foundation for the remaining creep parameter calculations presented in Section 4.4.

The last section of this chapter (4.5) presents a study that is aimed at investigating the effects of the overall microstructure in predicting the location of dislocation glide. For this purpose the plastic response in micro-pillars was examined. The results acquired however, did not prove suitable for use in the model presented but are interesting in themselves and form the basis of a joint publication by Jones *et al.* [100].

4.1 Equilibrium creep parameters

In the high temperature creep regime investigated, the microstructural deformation is driven by the evolution of a number of key parameters. These are solid-solution hardening, Orowan backstress, the effective diffusivity in the γ-matrix, anti-phase boundary energy in the γ'-phase, phase fractions and interfacial misfit stresses (see Chapter 2 and 3 in [167]). These

alloy and temperature dependent parameters were estimated for the creep conditions tested in order to understand how these parameters contribute to the non-isothermal creep deformation.

With increasing temperature, the equilibrium phase fraction shifts to a lower γ'-phase fraction, resulting in a gradual γ'-dissolution with temperature. Using the Thermodynamic Software *Thermo-Calc* and the *TCNi7* database, the equilibrium element concentration between 800 and 1220 °C was estimated for the γ (Figure 4.1a) and γ'-phase (Figure 4.1e). This data was further used to quantify the temperature dependence of the solid-solution hardening (SSH) resistance in the γ-matrix.

4.1.1 Estimating the solid-solution hardening contribution

The solid-solution model by Labusch *et al.* [85] has been shown to give a good estimate of the contribution to the overall shear stress (τ_{SSH}) (see Toda-Caraballo *et al.*[209]). To capture the temperature dependence of this parameter, the change in lattice parameter (a), shear modulus (G) and alloy element concentration (c) was considered at each temperature step. The critical shear strength in the γ-matrix is estimated by Labusch according to Equation 4.1, where ε_L is the atomic interaction parameter laid out further in Equation 4.2.

$$\tau_{SSH} = \frac{1}{550} \cdot G \cdot \varepsilon_L^{\frac{4}{3}} \cdot c^{\frac{2}{3}} \tag{4.1}$$

$$\varepsilon_L = \sqrt{\eta'^2 + \alpha^2 \cdot \phi^2} \tag{4.2}$$

The parameter ε_L then summates the parelastic interaction (ϕ) and the dielastic interaction (η') according to Equations 4.3 and 4.4 respectively. With a proportionality factor (α) assessing the interaction between parelastic and dielastic effects, taking a value between 3 and 16 for screw and above 16 for edge dislocations [209]. To account for both types a value of $\alpha = 16$ was used.

$$\phi = \frac{1}{a} \cdot \frac{da}{dc} \tag{4.3}$$

The parelastic interaction describes the change in γ-lattice constant with a changing composition (c). The atomic concentration at each temperature step was estimated using the *Thermo-Calc* database *TCNi7* and then used to estimate the lattice constant with the coefficients published by Caron [27].

$$\eta' = \frac{\eta}{1 + \frac{1}{2}|\eta|} \quad | \quad with \quad \eta = \frac{1}{G} \cdot \frac{dG}{dc} \tag{4.4}$$

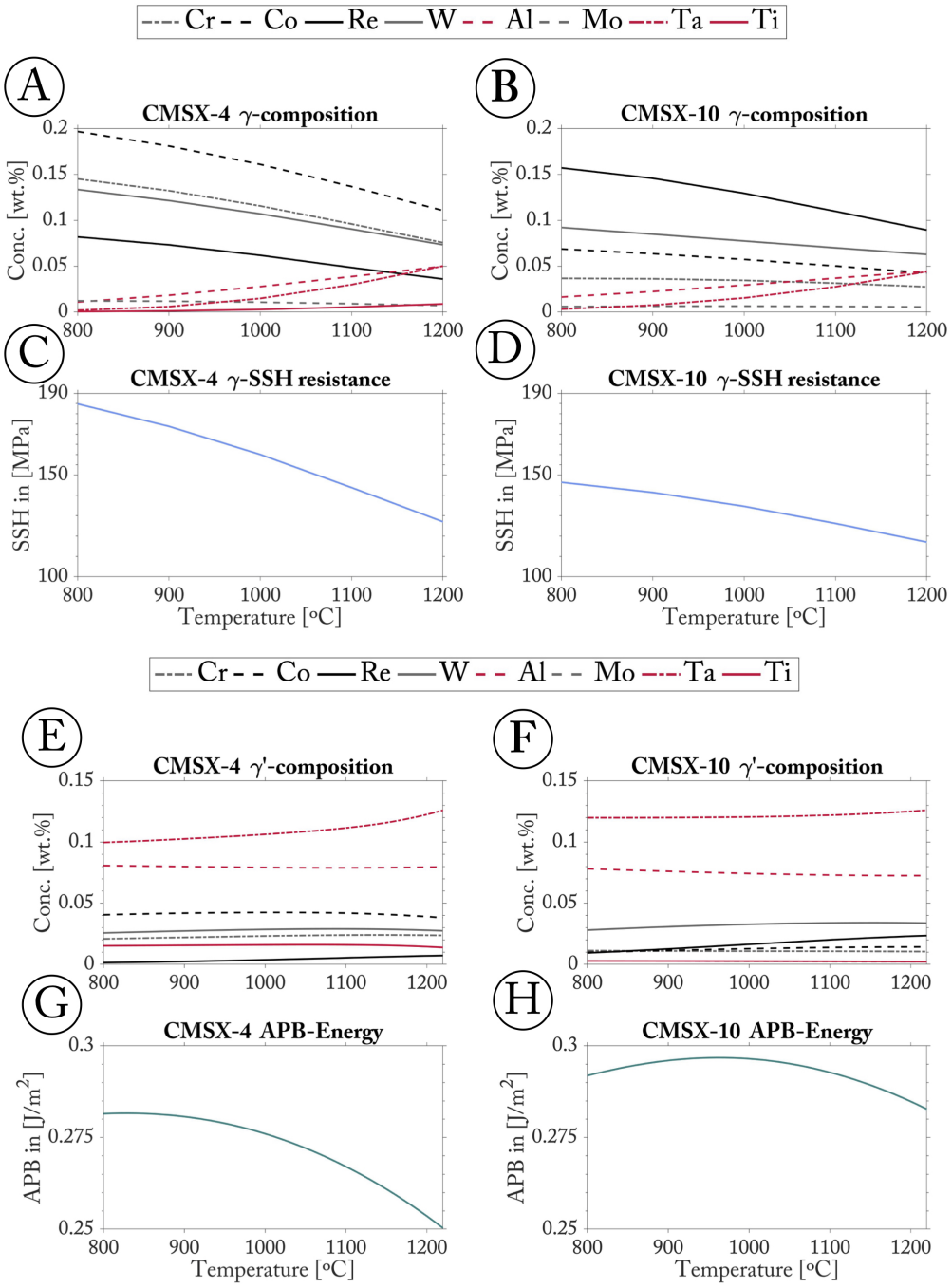

Fig. 4.1 Parameters estimated for the alloy CMSX-4 (a,c & e,g) and CMSX-10 (b,d & f,h): a/b) Temperature dependent element concentration of the γ-matrix and e/f) of the γ'-precipitate phase; c/d) Estimated solid-solution hardening (SSH)-resistance in γ-matrix; g/h) Modelled anti-phase boundary energy (APB) at the γ/γ'-interface

The dielastic parameter (η') estimates the change in local bonding energy between the solute atoms in the γ-matrix resulting from a change in the shear modulus with composition. The shear modulus change was estimated using a linear rule of mixture of the weight fraction compositions estimated with *Thermo-Calc* and the specific modulus of each element taken from Section 15-1 of [71]. The referenced element input parameters are listed in Table A.2.

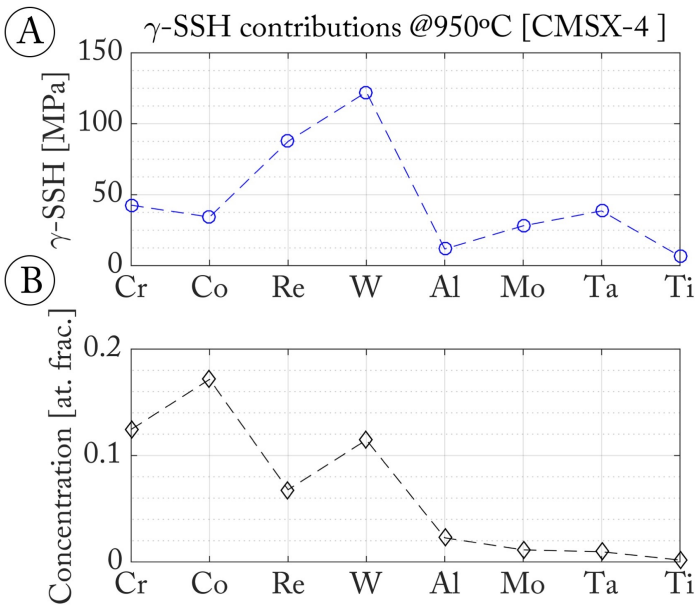

Fig. 4.2 γ-solid solution hardening contributions of each alloying element in CMSX-4 (A) estimated for the γ-matrix composition (B) at 950 °C

The solid-solution hardening contributions of each alloying element in the γ-phase were calculated at each temperature step and are shown for the alloy CMSX-4 at 950 °C in Figure 4.2. Comparing the atomic concentration of each alloying element to the element specific hardening contribution in the figure reveals the efficiency of the heavy and dense atoms, rhenium and tungsten to the solid-solution resistance of the alloy.

These individual element contributions were then added up, resulting in the temperature specific solid-solution hardening resistance of each phase. The temperature specific solid-solution resistance in the γ-phase of the alloy is shown in Figure 4.1c and 4.1d, and indicates a drop of 18 and 7 MPa for the alloys CMSX-4 and CMSX-10, respectively between 900 °C and 1050 °C. The estimated value is the resistance a dislocation will experience on the slip plane and would have to be multiplied with the Taylor factor in order to estimate the solid-solution hardening contribution to the yield strength of the alloys (see Kozar *et al.* [111] for an outline of this approach).

4.1.2 Anti-phase boundary energy

In the high temperature and low stress creep regime, dislocations have to overcome an anti-phase boundary energy (APB) barrier at the interfaces [7]. The *Thermo-Calc* based approach published by Crudden *et al.* [41] which adapted the work by Inden [95] for thermodynamic database calculations was used. The thermally dependent ordering energy was calculated using the alloy compositions at each temperature step to estimate the overall temperature dependence of the APB-energy.

The short-range ordering correction factor introduced by Crudden *et al.* to the H_{mix}^{FCC} data (i.e. the calculated data was reduced by 10%) was not used in this study. Instead the updated *TCNi7* database was used which incorporates more datapoints and overall higher accuracies for model alloys, replacing the *TTNi7* database used by Crudden *et al.*.

To date, the APB-energy has only been measured experimentally using TEM-dislocation imaging [88, 14]. Due to the temperature restrictions of this measurement technique, no experimental values are published for elevated temperatures. The model used is thus based on the assumption that the temperature effect can be adequately captured by using the temperature dependent enthalpy and solute content. The temperature dependence is presented in Figure 4.1g and 4.1h, and shows a drop of 8.6 and 0.9 $[\frac{mJ}{m^2}]$ between 900 and 1050 °C for the alloy CMSX-4 and CMSX-10 respectively.

When comparing the APB-estimates to the experimental and modelled data assembled in [212, 41], two key findings seem to have been adequately captured. Firstly, the APB-energy decreases with increasing tantalum content. Secondly, small additions of titanium (see CMSX-10) have a strong hardening influence on the APB-energy. Looking at the efficency of different alloying elements on the APB-energy with Crudden *et al.* [41], the high temperature stability (and modest increase) of the APB-energy in CMSX-10 can further be attributed to the addition of niobium.

4.1.3 Effective interdiffusivity

Interdiffusion in the ordered $L1_2$-phase is up to three orders of magnitude lower than in the disordered γ-phase [44]. Therefore the prior mode of interdiffusion is ignored in this model and only the interdiffusion through the disordered phase is considered.

The effective γ-interdiffusivity of alloying element atoms is of particular interest during high temperature creep. This is not only due to the high temperatures reached in the operating regimes (see Figure 2.6) but also due to the number of alloying elements used in most conventional superalloys (see Figure 1.3) and their very different diffusivities.

Goswami *et al.* [81] studied to what extent small additions of slow-diffusing solute atoms result in a reduction in vacancy diffusion and effective diffusion coefficients. Using density functional theory calculations Goswami *et al.* found that small additions of rhenium resulted in a small reduction in the vacancy diffusion coefficient [81]. Fu *et al.* argued that this reduction is not due to a size misfit effect between the alloy elements but is instead caused by the dense electronic structure and bonding arrangements of incompressible Ni-Re and Ni-Ru bonds, which do not favour solute-vacancy exchanges [69].

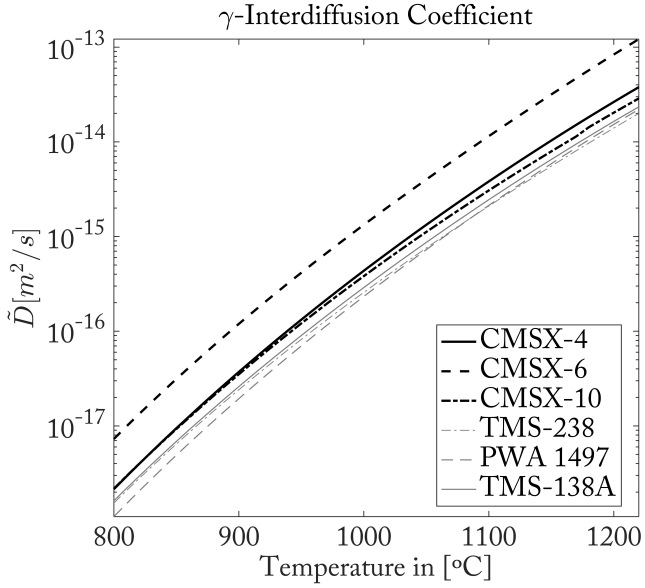

Fig. 4.3 Effective interdiffusivites for selected alloy compositions, see text for further details

To estimate the simultaneous diffusion of different alloying elements through the disordered lattice without the need for extensive processing power a simplification had to be made. The binary (Ni-X) mobilities had been experimentally measured by Campbell *et al.* [26] and Karunaratne *et al.* [106].

A careful study of the concentration profiles by Epishin *et al.* clarified that the kinetics of the diffusion of the γ-stabilising elements, such as Cr, Co, W, and Re, in a multicomponent system is similar to that observed in the binary alloys of these elements with Ni [61]. As a result, the effective interdiffusivity of an alloy was approximated from the binary interdiffusivities according to the approach published by Zhu *et al.* [231] displayed in Equation 4.5. The temperature dependent evolution of the effective interdiffusivity in the γ-phase ($\tilde{D}_{eff}$) was estimated by calculating the harmonic mean of all alloying element diffusivities in nickel ($D_0^{m,Ni}$). These binary diffusivities were estimated by using the *TCNi7* database in *Thermo-Calc*, that in turn largely depends on the databases in [26, 106].

$$\tilde{D}_{eff} = \frac{1}{\sum_m \frac{x_m}{D_0^{m,Ni}}} \tag{4.5}$$

The effective interdiffusivities for six selected alloys are shown in Figure 4.3. These alloys perform very differently under high temperature creep conditions (see Figure 1.4) and have very different alloy compositions (see Figure 1.3 or alloy composition table in the appendix). Yet, as pointed out by Goswami *et al.* [81], these stark differences in creep performance are not directly reflected in their effective interdiffusivities. Whilst the first generation alloy CMSX-6 exhibits a 5× and 5.3× higher effective diffusivity at 900 °C and 1050 °C, respectively, compared to the sixth generation alloy TMS-238, the second generation alloy CMSX-4 displays only a minor increase in diffusivity of 1.05× and 1.2× at 900 °C and 1050 °C to the third generation CMSX-10 alloy.

In the high temperature creep regime, diffusion assisted dislocation climb has been shown to be the dominant mechanism (see Figure 2.7 in Section 2.3). One would thus expect that the creep performance in this regime is correlated to the atomic inter-diffusivity. However, comparison the high temperature creep performance of the alloys CMSX-4 and CMSX-10 in Figure 1.4 of Section 1.1 indicates that the latter alloy exhibits a substantially longer creep rupture life ($\sim 2\times$ longer).

This comparison further highlights that if one wants to capture the proper high temperature creep response of a given alloy, one has to model all major contributing alloy dependent parameters.

4.2 Quantifying the elemental scatter in the alloys on creep parameters

Creep experiments of a given alloy performed under the same conditions are subject to a considerable amount of scatter (see Figure 2 in [166]). This has been linked to the effect of misorientation [139] and the chemical segregation remaining after the γ'-solution heat-treatment (see Section 2.1.2 on the role of dendrites). The impact of micro-structural inhomogeneity on the creep deformation rates in the alloy CMSX-10 has been shown experimentally by Tabrizi [201].

This section seeks to quantify how the key creep parameters differ across different regions of the microstructure in order ultimately to be able to account and model the scatter in creep data resulting from the compositional segregation.

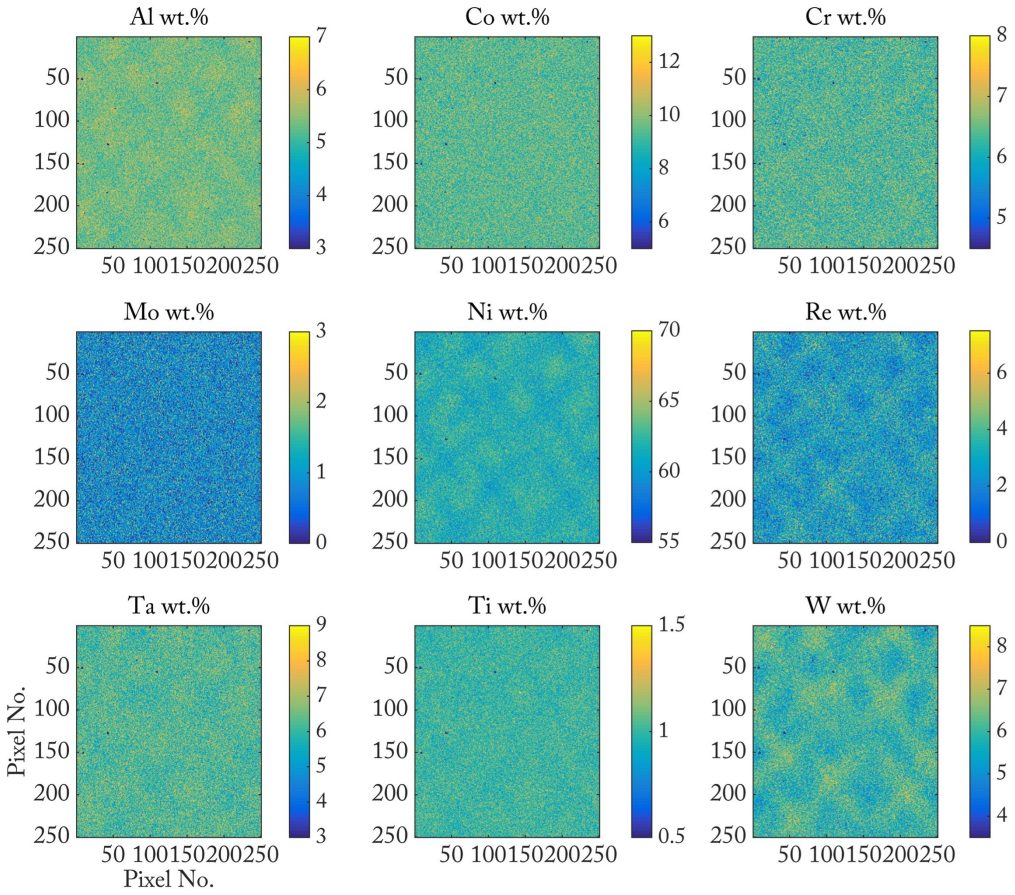

Fig. 4.4 Compositional distribution (wt.%) of all major alloying elements in the alloy CMSX-4, acquired with a 5μm-spacing between pixels using EPMA

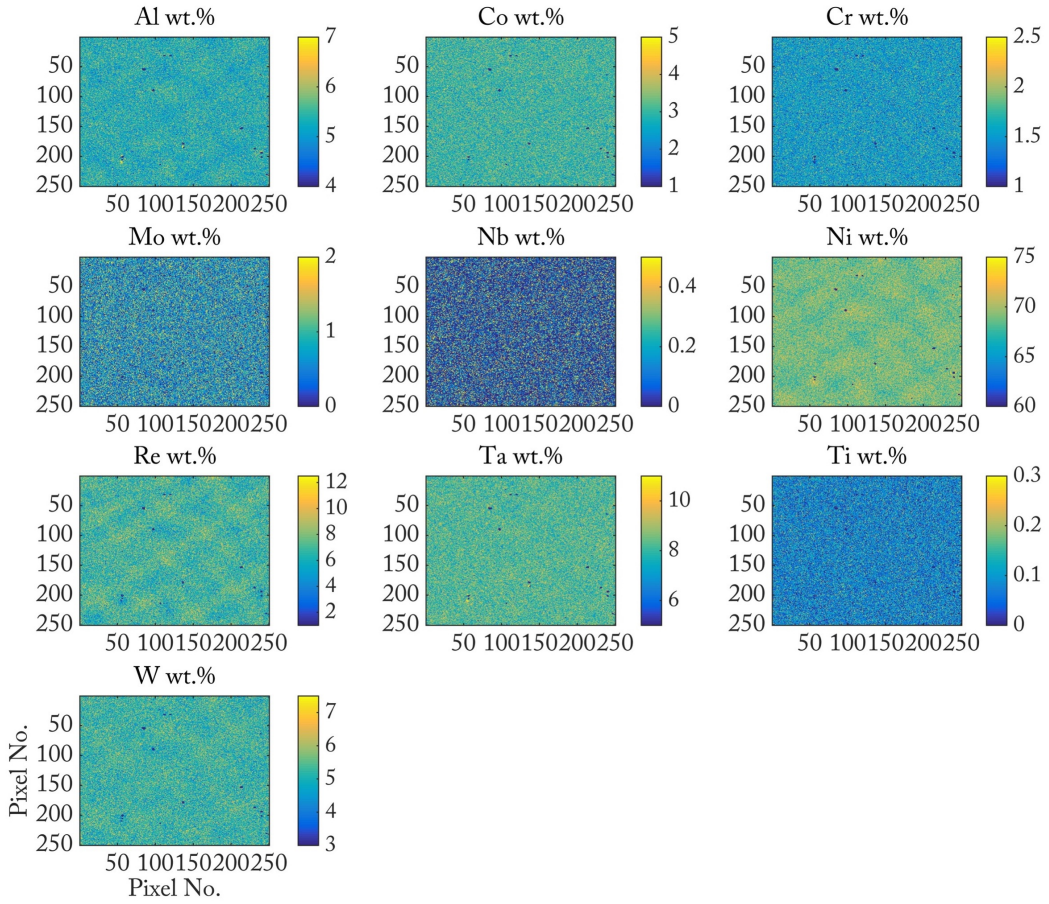

Fig. 4.5 Compositional distribution (wt.%) of all major alloying elements in the alloy CMSX-10N, acquired with a 5μm-spacing between pixels using EPMA

Section 3.3.3 described the set-up and apparatus used to acquire the EPMA maps for the two alloys investigated, CMSX-4 and CMSX-10N (CMSX-10N is a variant of the alloy CMSX-10K see Table 2.1). The sample area measured 1250 μm^2 and contained a number of dendrite traces, which can be seen in the maps of the slowest diffusing elements (Re,W) in Figure 4.4 and 4.5 for CMSX-4 and CMSX-10 respectively. The overall mean composition and its scatter was calculated from all acquired measuring points and compared to the nominal composition (published in [164, 208]) in Figure 4.6. Despite the short acquisition time, highlighted in Section 3.3.3, good agreement between mean and nominal composition was found and thus the regions selected for these datasets are considered representative of the two alloys studied.

Tracing the remnants of dendrites with Re-variants

Using the superalloy CMSX-4 Brueckner *et al.* [20] showed that the remnants of dendrites could be accurately traced from the rhenium composition maps for the fully heat-treated samples. Using this approach for the alloy CMSX-4, the acquired rhenium composition was divided into 15 bins of equal compositional width, where the rhenium content (wt.%) of the bins is proportional to the bin number (Figure 4.16) such that, the lowest acquired compositions are in bin number one and the highest in bin number 15. To account for the greater variation in rhenium the CMSX-10N maps were divided into 17 equally spaced bins.

The overall element composition of each alloy variant was then calculated based on the rhenium binning. Using the bin number of each rhenium pixel and its location in the data-matrix, the remaining alloy elemental maps were sorted into the corresponding bins. The mean composition of each alloying element was calculated and the resulting overall composition of all alloy variants is shown in Figure 4.7 for both alloys.

The frequency of each alloy variant (bin) in the EPMA map was further estimated for both alloys and is shown in Figure 4.8. The resulting distributions show, that the most frequent variant number is 7 and 10 for CMSX-4 and CMSX-10N respectively. To better compare the size of the interdendritic and dendritic regions in both alloys, both alloys were binned into 15 variants and the most frequent variant numbers were 7 and 8 for CMSX-4 and CMSX-10 respectively. This indicates, that the alloy CMSX-4 has more area corresponding to lower variants (interdendritic regions) compared to CMSX-10N but that the compositional difference between the alloy variants is much more pronounced for CMSX-10N.

To confirm that the binning based on the rhenium content was able to capture the dendritic arrangement the nearest neighbour environment of the data-points on the rhenium map was investigated. The nine neighbouring cells of each data-matrix entry were analysed for the

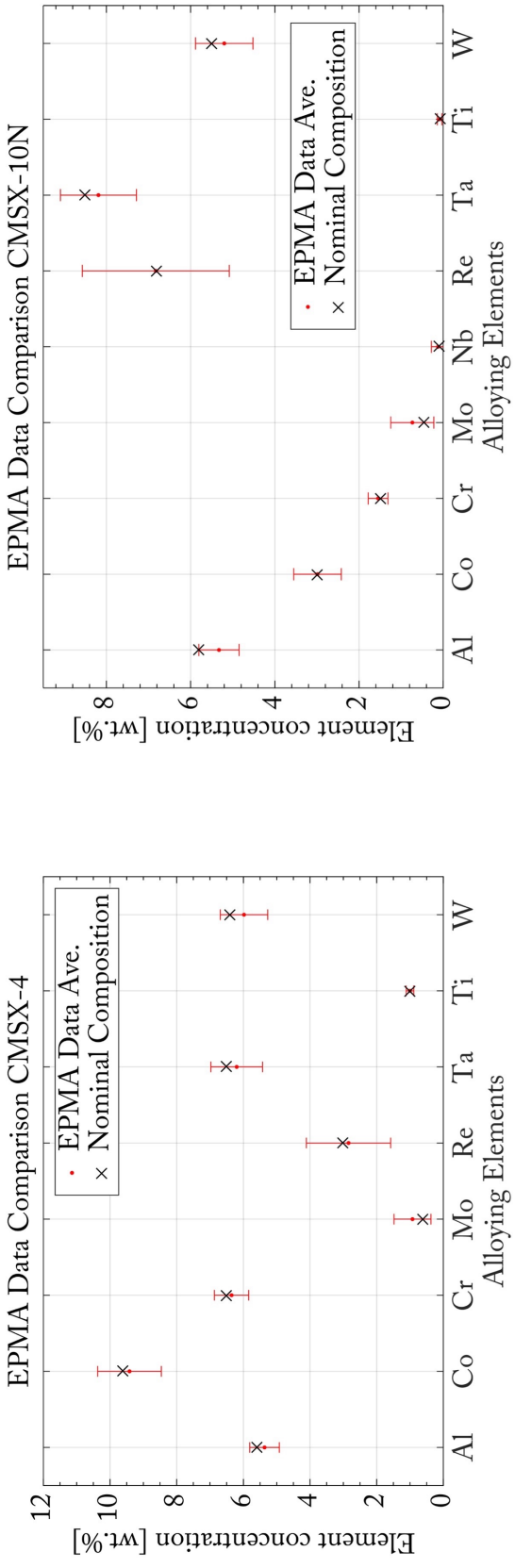

Fig. 4.6 Experimentally acquired mean composition (red dot) and scatter (red line) compared to the published nominal composition (x-markers) for the investigated alloys CMSX-4 (bottom) and CMSX-10N (top)

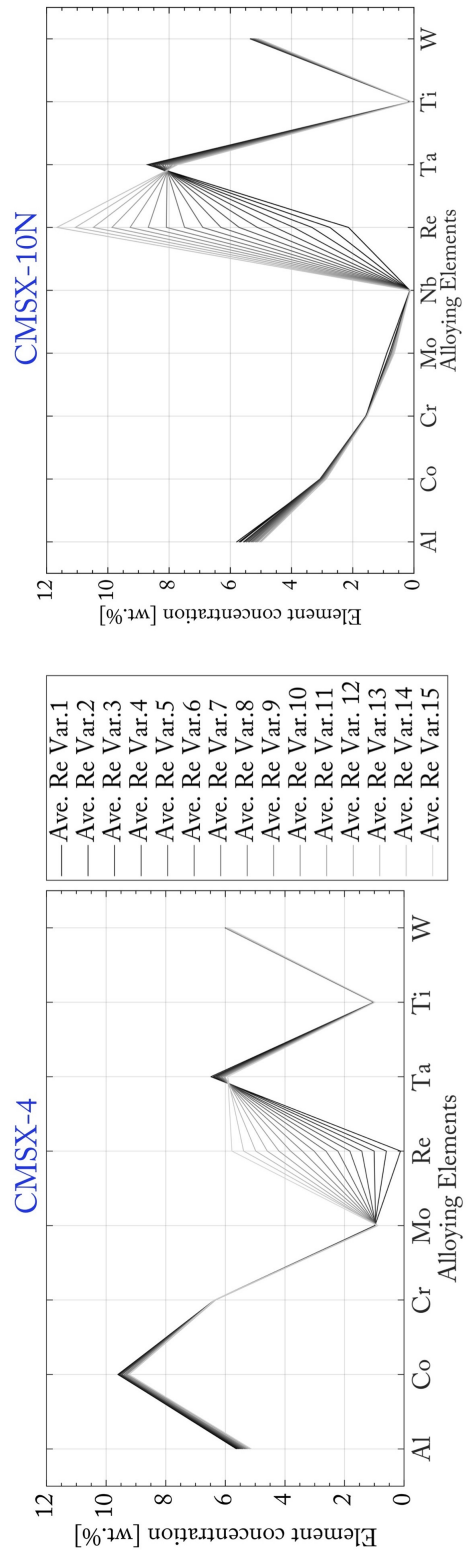

Fig. 4.7 Calculated compositions in the 15 different alloy variants based on the rhenium segregation for CMSX-4 (bottom) and 17 different alloy variants in CMSX-10N (top)

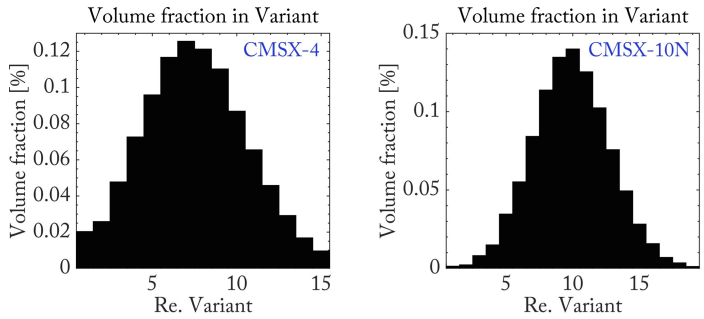

Fig. 4.8 The calculated frequencies of different rhenium bin numbers (alloy variants) in the alloys CMSX-4 (left) and CMSX-10N (right).

five lowest, medium and highest rhenium bin numbers, according to their assigned bin numbers and plotted in Figure 4.9. The graph reveals that the neighbouring cells around a low bin number tend to also be lower. This arrangement is in line with the nearest neighbour environment expected for dendritic remnants thereby correctly reflecting the compositional arrangements in the alloys.

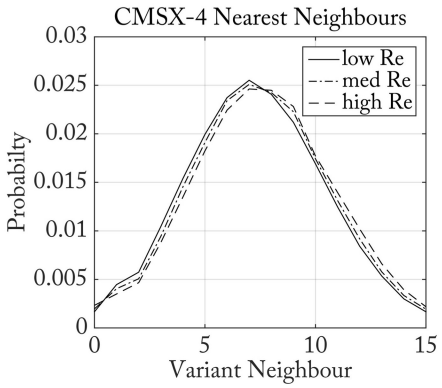

Fig. 4.9 The nearest neighbour environment around each alloy variant neighbour for the alloy CMSX-4, plotted for the lowest, medium and highest five bin numbers.

Phase composition and phase fractions

Using the calculated alloy variant compositions in Figure 4.7 and the *TCNi7* database in *ThermoCalc*, the respective γ and γ'-phase fractions were estimated and are plotted in Figure 4.10. The phase fractions of the first variant (interdendritic region) are plotted in black with the lightness continuously increasing to the phase fraction curve of variant 15 (dendrite core). The mean alloy composition is plotted as a red curve throughout the variant plots and corresponds to the equilibrium calculations for the respective parameters.

The modelled γ'-phase fractions in the dendritic and interdendritic regions correctly reflect the trends in the published literature (see Section 2.1.2). The highest γ'-phase fractions can be found in the interdendritic region and the lowest in the dendritic cores. Further, due to the higher rhenium variation in the alloy CMSX-10N, a greater difference exists between the lowest γ'-phase fractions in the interdendritic region (variant 15) and the dendritic cores (variant 1). According to Figure 4.10, the alloy CMSX-10N exhibits a higher and more stable γ'-phase fraction at higher temperatures compared to CMSX-4. Between 900 °C and 1050 °C the γ'-phase fraction drops from 0.63 to 0.56 and from 0.60 to 0.47 for the mean alloys compositions of CMSX-10N and CMSX-4 respectively.

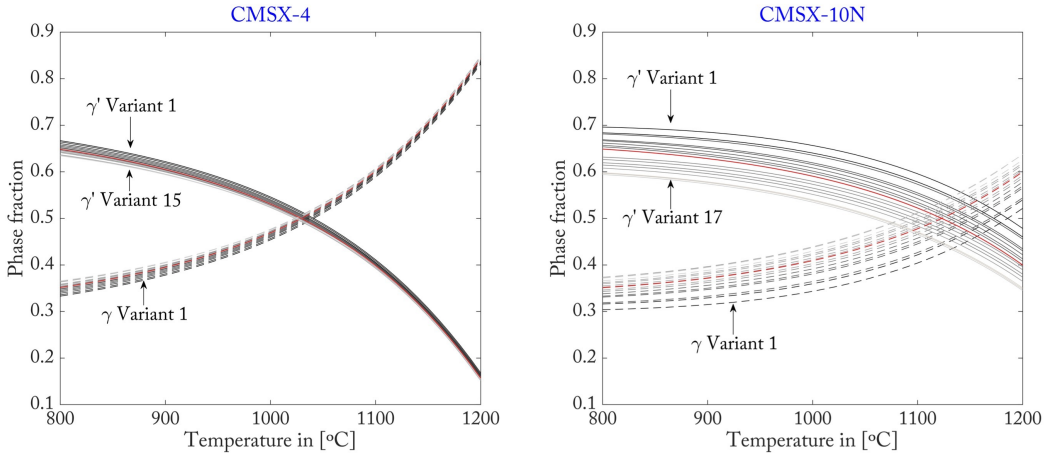

Fig. 4.10 Phase fractions at different temperatures based on the alloy variants in CMSX-4 (left) and CMSX-10N (right) for the γ'-phase (solid lines) and γ-matrix (dashed lines) with the respective fractions based on the mean alloy compositions in red

Effective interdiffusivity

The effective interdiffusion of each alloy variant was calculated according to the routine outlined in Section 4.1.3 and the results are plotted in Figure 4.11. The inflexion points in both graphs result from insufficient data points in the *ThermoCalc* database. The associated uncertainty in the calculated value is particularly pronounced for the variant 1 in CMSX-4, where the values change by more than one order of magnitude within a few degrees of temperature.

Comparing the two alloys and their respective variants it becomes apparent that the difference between variants is comparable to the difference between the alloys. The mean composition of CMSX-4 amounts to roughly the same diffusivity as the alloy variant 1 in CMSX-10N. This is further illustrated in Figure 4.12, where the alloy variants in CMSX-10N

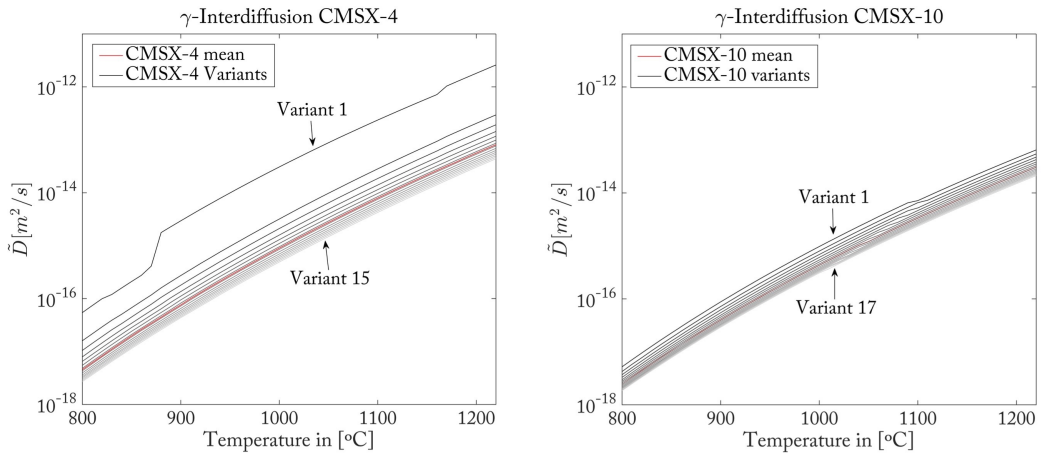

Fig. 4.11 Effective interdiffusion coefficients over temperature of the respective alloy variants for the alloy CMSX-4 (left) and CMSX-10N (right)

from Figure 4.11(right) are plotted together with the mean diffusivities calculated for the alloys TMS-238 and CMSX-6 from Figure 4.3. It can be concluded, that the inter-diffusion in the first few variants of CMSX-10N would overlap with the last variants in CMSX-6 and the opposite would be true for CMSX-10N and TMS-238.

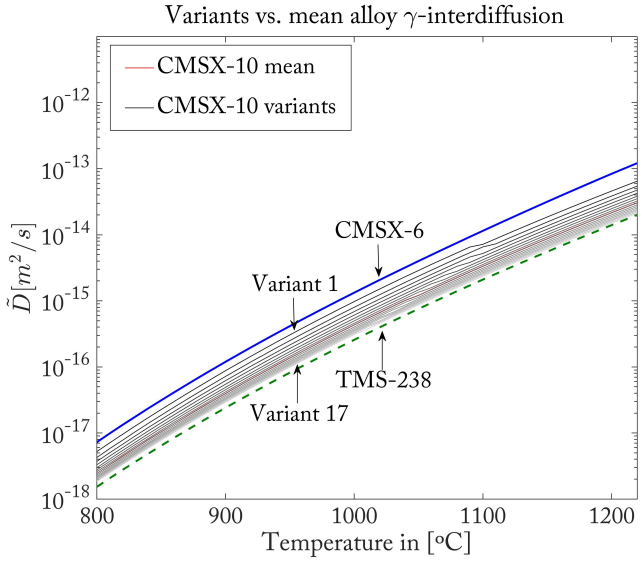

Fig. 4.12 Comparing the alloy variants in CMSX-10N against the mean alloy effective interdiffusivities of CMSX-6 (solid blue line) and TMS-238 (dashed green line)

Anti-phase boundary energy

Following the approach in Section 4.1.2, the APB-energy was calculated for all alloy variants and plotted in Figure 4.13. In line with the findings in Section 4.1.2, the modelled APB-energy for the alloy variants in CMSX-10N was more stable at higher temperatures and resulted in a higher APB-energy for the mean composition when compared to the alloy CMSX-4.

Modelling shows the resistance to APB-shearing is lower in the dendritic cores (highest variant numbers) of an alloy than in the interdendritic region. The estimated mean alloy APB-energies are overall lower than those calculated using nominal alloy compositions in Figure 4.1, highlighting that with the current approach small alloy compositional differences can result in a significant difference in the resulting APB-energy.

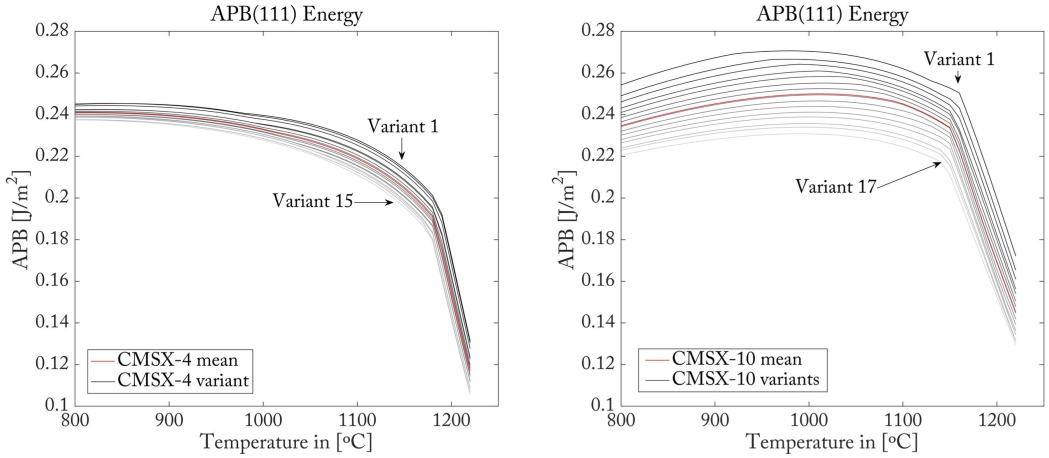

Fig. 4.13 APB-energy over temperature of the respective alloy variants in CMSX-4 (left) and CMSX-10N (right)

Solid-solution hardening

Using the same calculation routine as outlined in Section 4.1.1, the solid-solution hardening contribution to the γ-phase for each of the alloy variants was estimated and is plotted in Figure 4.14. The parameter has not been divided by the Taylor factor in this instance (as done in Section 4.1.1), to show the yield strength contribution of this parameter.

The resistance to solid-solution hardening in the different alloy variants shows a strong variation between the dendritic cores and the interdendritic region. In the alloy CMSX-10N, the modelled resistance towards dislocation bowing in the γ-matrix is 73.6 MPa (24.5 MPa on the slip plane) higher in alloy variant 17 than in variant 1 at 900°C. This difference decreases

for higher temperatures in both alloys, such that in CMSX-10N the difference amounts to 64.9 MPa (21.6 MPa on the slip plane) at 1050 °C (see Figure 4.14).

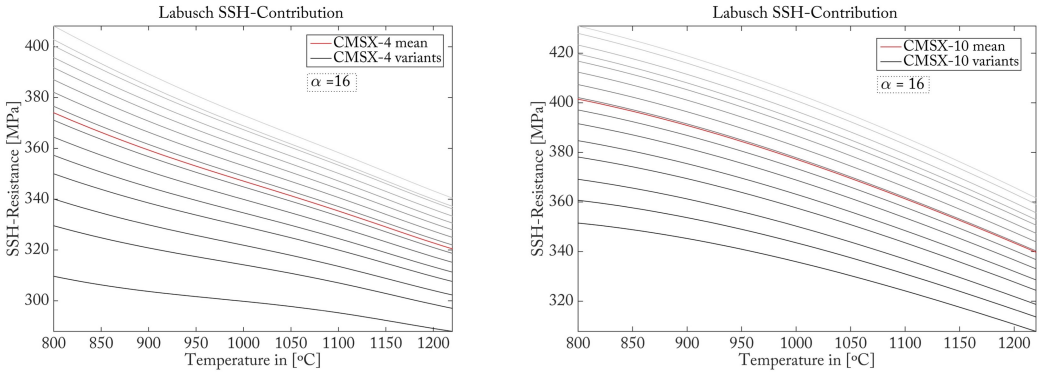

Fig. 4.14 Solid-solution hardening (SSH) resistance over temperature modelled for the respective alloy variants in CMSX-4 (left) and CMSX-10N (right)

Interfacial energy

The interfacial free energy of the particle-matrix interfaces is commonly used in the particle coarsening theory [133, 8] and to estimate the stacking fault energy for dislocation climb by kinks and jogs [11].

The interfacial energy on the (100)-interfaces was estimated using the nearest-neighbour broken-bond approach published by Sonderegger and Kozeschnik [188] as this approach had been specifically compared to experimental data in the Ni-Al alloying system. The approach allows coupling with thermodynamic data, such as the *TCNi7* database in *ThermoCalc* used in this study. The interfacial energy (Υ) then results from Equation 4.6 as outlined in [188]. Where the parameter N_A is the Avogadro constant, n_S the number of atoms per unit area of the interface (estimated with $4^{2/3}/a^2$ for fcc-lattices), z_L as the coordination number (estimated at 14442) and z_S as the number of nearest neighbor broken bonds (estimated at 4751). Instead of the solution enthalpy of the γ'-phase used in the paper, the ordering energy ΔE_{Ord} was used in this approach. The latter parameter is thought to better describe the physical basis of this parameter, as the interfacial energy on these coherent interfaces results from the order/disorder transition between the $L1_2$ and FCC phase transition.

$$\Upsilon = \frac{n_S \cdot z_s \cdot |\Delta E_{Ord}|}{N_A \cdot z_L} \quad | \quad with \quad \Delta E_{Ord} = \Delta E_{L1_2} - \Delta E_{FCC} \tag{4.6}$$

The temperature dependence of the interfacial energy for the different alloy variants is plotted in Figure 4.15. According to the graphs, the interfacial energy is initially higher for the

CMSX-4 alloy and then decreases faster with higher temperatures compared to the CMSX-10N alloy. This temperature sensitivity and high temperature decrease of the interfacial energy has been previously published by Ardell [10]. As for the other alloy dependent parameters plotted in this chapter, the difference between alloy variants in CMSX-10N is greater compared to CMSX-4. The interfacial energy decreases only 4.2 $[\frac{mJ}{m^2}]$ compared to 7.4 $[\frac{mJ}{m^2}]$ between 900 °C and 1050 °C for CMSX-10N compared to CMSX-4. The higher interfacial energy estimated for CMSX-4 can be attributed principally to the higher alloying concentration of titanium, which has been reported to significantly strengthen the interfaces even for small additions (see Ardell [10]).

The magnitude of the interfacial energy calculated for the alloy CMSX-4 was compared to the linear combination approach that uses the alloy compositions calculated with ThermoCalc (see Figure 4.1), outlined by Liu *et al.* [127] (see Equation 3 in publication) and others [225, 184]. The resulting interfacial energies amount to 32.6 and 30.8 $[mJ/m^2]$ at 900 °C and 1050 °C respectively (so a factor of three lower than estimated here) using the constants published by Liu *et al.* but the calculations are of the same order of magnitude using the constants by Shang *et al.* [225, 184]. Due to this large difference in published results and the low overall thermal effect on this parameter, the interfacial energy was not further used for the non-isothermal model. Instead the particle coarsening and dislocation climb dynamic were fitted to experimental datasets.

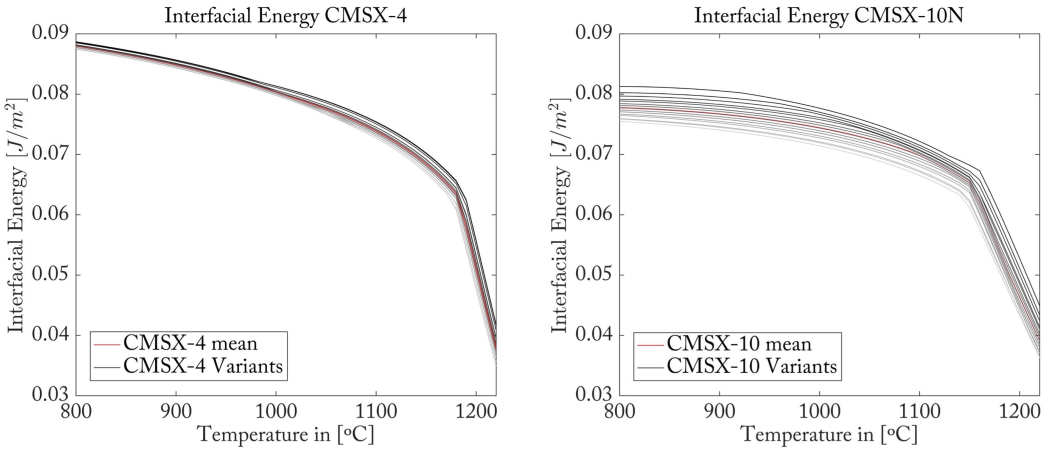

Fig. 4.15 Interfacial energy at different modelled temperatures for the respective alloy variants of the alloys CMSX-4 (left) and CMSX-10N (right)

Conclusion and further work in modelling the alloy element scatter

Estimating the elemental scatter within fully heat-treated alloys enables modelling the creep parameters driving the deformation mechanisms in every region of the alloy respectively. Quantifying these parameters for the different regions revealed that every alloy has a unique distribution of elements in each region of the microstructure (a function of alloy composition and heat treatments). Crucially, the parameter distribution within an alloy can amount to a difference in creep parameters as pronounced as that between the mean parameters of different alloy series. The volume fraction and APB-energy are lower and the solid-solution hardening is higher in the dendritic cores of the alloys CMSX-10 and CMSX-4 than in the inter-dendritic regions. As the plastic response in the γ'-phase depends on the volume fraction and APB-energy (Equations 2.4 and 2.5 in Section 2.3.1) a lower critical shear stress of the γ'-precipitates in the dendritic cores is expected (see Section 4.4.5 for a detailed analysis of this parameter). The plastic response in the γ-matrix on the other hand depends on the volume fraction (higher in the dendritic cores) and solid-solution hardening (lower in the dendritic cores). To infer from these trends the creep response in both phases requires the rhenium based variant parameters to be entered into a creep deformation model. Such a model would help to explain why the dendritic core regions deform overall much faster than the interdendritic regions as observed experimentally by Milhet *et al.* [141] (see Figure 2.17).

Furthermore, such a model could assess the effectiveness of heat treatments and alloying element additions on the creep response of alloys. The theoretical approach to include the variant based parameters in a creep model is outlined in Figure 4.16. The key assumption is described in Figure 4.16d, explaining that the creep model depends on the exchange of dislocations between bordering alloy variant domains. The number and difference between alloy variants decrease for high temperature tests over the test time due to further chemical homogenisation assisted by γ-interdiffusion.

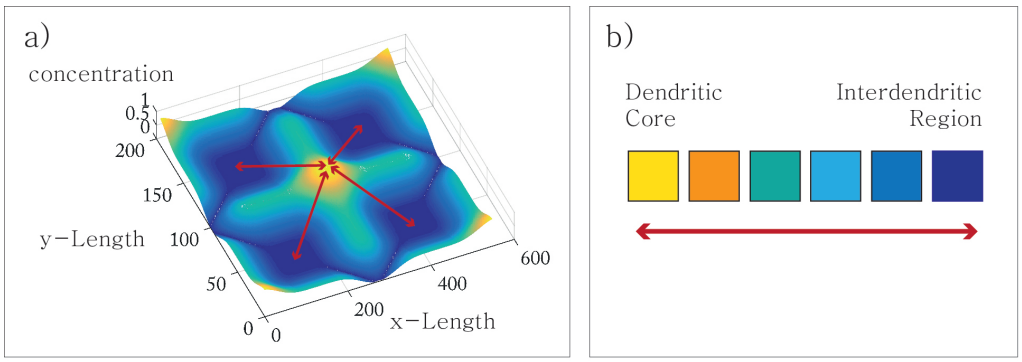

[a] Model dendritic cell highlighted by the concentration distribution of a precipitate partitioning element. Indicated is the 4−fold symmetry of the cell. [b] Due to this symmetry one can reduce the number of modelled cells to one multi−cellular array of gradually decreasing precipitate content.

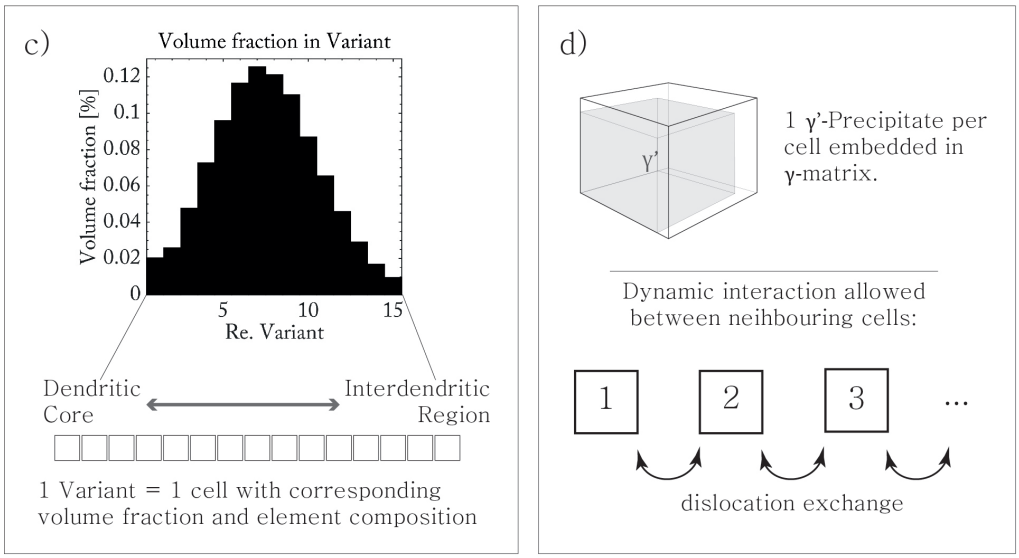

[c] Overall volume fractions of 15 calculated Re−variants in the alloy. Each variant composition and frequency is used to model a unit cell of corresponding composition. [d] Each modelled cell has a single γ'-precipitate; a dislocation exchange is only permitted amongst nearest neighbouring cells.

Fig. 4.16 Theoretical approach to implement the alloy compositional scatter in a dislocation based model to study the influence of homogenisation heat treatments on the overall creep response

4.3 Modelling non-equilibrium creep parameters

The previous chapters calculated the creep parameter evolution based on the premise that the element composition of each phase was equal to the equilibrium composition at that temperature. However, when modelling non-isothermal creep, the compositions can have insufficient time to equilibrate. As a result the chemical compositions in both phases do not correspond to the applied temperature cycle. The non-isothermal compositions however result in metastable phase fractions which can in turn be measured experimentally and ultimately modelled. For this reason a previously unpublished dataset was acquired from Cormier and Jacques (see the test set-up outlined in Section 3.3.4) and was further analysed by the author in the following sections.

Following an initial thermal correction on the dataset outlined in Section 4.3.1, the non-isothermal γ'-phase fraction evolution was estimated. The model approach is outlined in Section 4.3.2. Calculations to establish the feasibility of the models' results are displayed in Section 4.3.3. The capabilities of the model are compared to those of the software *Dictra* in Section 4.3.4. The micro-structural response following the non-isothermal testing is then outlined in Section 4.3.5.

Experimental data acquired using *in situ* X-ray synchrotron radiation

Following the experimental set-up described in Section 3.3.4 an experimental dataset was obtained by A. Jacques and J. Cormier using XRD-synchrotron radiation (Figure 4.17). After an 8 h isothermal pre-rafting at 1050 °C and 118 MPa, the non-isothermal creep experiment consisting of three heating and cooling cycles at a constant stress of 118 MPa was performed (highlighted by the grey background in Figure 4.17). Failure occurred in the fourth heating cycle marked by a cross. Black arrows indicate the back-fitted nominal temperatures for each non-isothermal segment.

The evolution of the effective lattice misfit (blue line and left axis in Figure 4.17) and the simultaneous evolution of the γ'-phase fraction (red line) was acquired. The dataset outlined in this section has been published in [180]. Following reviewers comments the phase-fraction model presented here was changed to a more physical-based derivation which is presented in Appendix B. The model presented in this section was used to estimate the phase fraction evolution for the subsequent analysis and creep modelling.

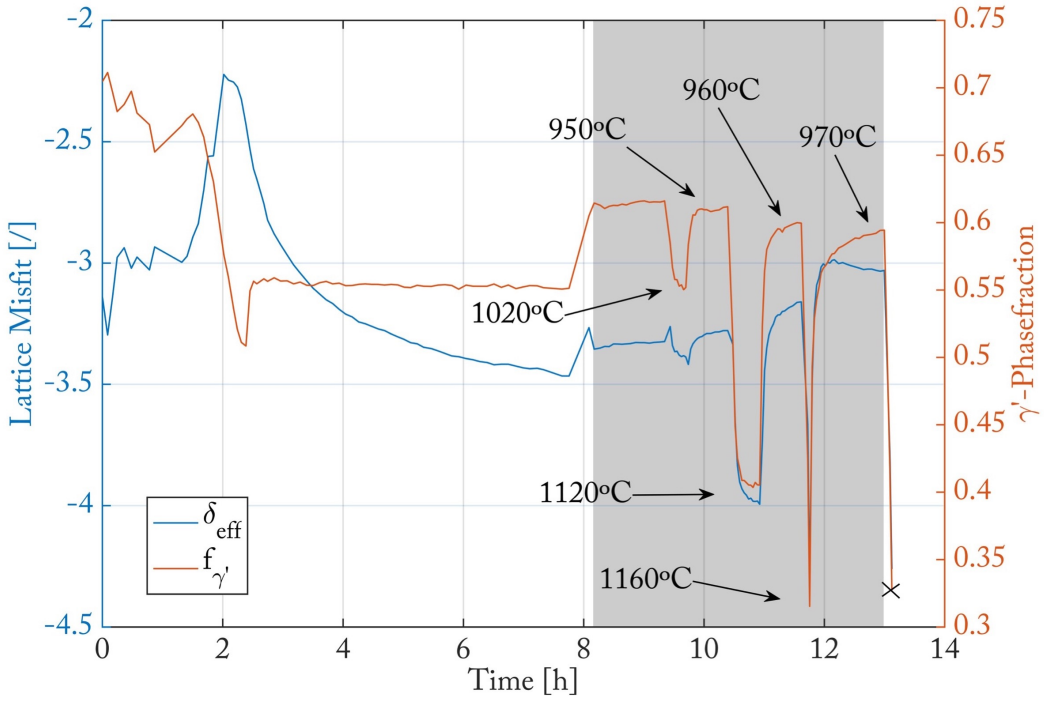

Fig. 4.17 Experimental dataset obtained using XRD-synchrotron. Blue line and left axis display the effective lattice misfit evolution and red line and right axis show the simultaneous evolution of the γ'-phase fraction. The grey background highlights the analysed non-isothermal regime of three heating and cooling cycles at 118 MPa. The prior segment is an isothermal pre-rafting performed at 1050 °C and 118 MPa. Failure occurred in the fourth heating cycle marked by a cross. Black arrows indicate the back-fitted nominal temperatures for each non-isothermal segment

4.3.1 Temperature correction

The largest uncertainty in the acquired data was attributed to the temperature measurement. The temperature was passively recorded with a S-Type thermocouple attached to the shoulder of the specimen, whilst the radiant furnace temperature was controlled through the output power. The certified offset for this Class 1 S-Type thermocouple was $\pm 1.1K$ at the highest measured temperature. As a new thermocouple was used in the experiment a possible drift contribution is negligible due to the comparatively short exposure time (compare with [16] p.38). However, due to thermal fluctuations over the gauge length a notable discrepancy between the XRD-analysis volume and the recorded temperature arises. Therefore, the temperature was back-fitted by extracting stable XRD-measured phase fractions (marked in Figure 4.17) and finding the corresponding temperatures from the calculated equilibrium

phase fractions (see Section 4.1). The correlated temperatures to each non-isothermal regime are displayed in Figure 4.17.

4.3.2 Creating a model to estimate non-isothermal phase-fractions

The precipitate phase fraction evolution was modelled using the approach by Johnson-Mehl-Avrami (JMA) [154, 93, 13]. The resulting best JMA fit to the experimental dataset is given in Equation 4.7, describing the phase fraction evolution at a given time.

$$P(t) = P_{FE} + (P_{IE} - P_{FE}) \cdot e^{-\beta t^n} \tag{4.7}$$

The constant P_{FE} is given by the equilibrium phase fraction at the final temperature step. The multiplier is given by the difference between the initial equilibrium phase-fraction P_{IE} and the mentioned final equilibrium phase-fraction at the final holding temperature of the heating/cooling step. The fitted Avrami exponential coefficient β [1/s] is further outlined in Equation 4.8.

$$\beta = \beta_0 \cdot exp\left(\frac{Q}{RT}\right) \tag{4.8}$$

In Equation 4.8 R is the molar gas constant, T the absolute temperature at a time step and Q the activation energy. An Avrami exponent of $n = 1$ was used and the factor $\beta_0 = 2.38 \cdot 10^{-7} s^{-1}$ was obtained by fitting to the dataset. The other parameters were determined by first subdividing the experimental dataset into its respective heating and cooling segments. Each dataset was fitted with the software *Igor Pro* to an exponential function. The activation energy (Q) for the phase dissolution and re-precipitation as well as the pre-exponential factor (β_0) were estimated using the fitted exponential coefficients. The activation energy for dissolution (heating events) was estimated at $111 kJ/mol$ and $101 kJ/mol$ for re-precipitation (cooling events). The values are significantly below the self-diffusion activation energy for pure Nickel ($279.7 kJ/mol$ [8]). This indicates that the γ'-phase dissolution and re-precipitation process is presumably more interfacial than diffusion-controlled. The Avrami exponent was therefore set at $n = 1$, to model a site saturated case with continuous platelet shaped (1-D) rafts that facilitate interface exchange (see p.190 [93]). The precipitate phase fraction evolution depends on the nucleation, growth and dissolution of γ'-tertiaries as well as the growth and dissolution of the rafts. Considering that the specimen was pre-rafted under an applied load, it is assumed that the number of nucleation sites (i.e. dislocations) is sufficiently saturated upon starting the non-isothermal excursions. The role of γ'-tertiaries as

a share of the phase dissolution and re-precipitation is assumed to increase with each heating cycle, due to the increasing heating temperatures (see Figure 4.18) [192, 82, 35]. The higher activation energy required for dissolution is thought to result from the added interfacial area.

The influence of the applied stress on the phase fraction dissolution and re-precipitation gradients can be neglected as the applied stress was held constant and the phase fraction model was only applied to the pre-rafted dataset (see Giraud *et al.* [78]).

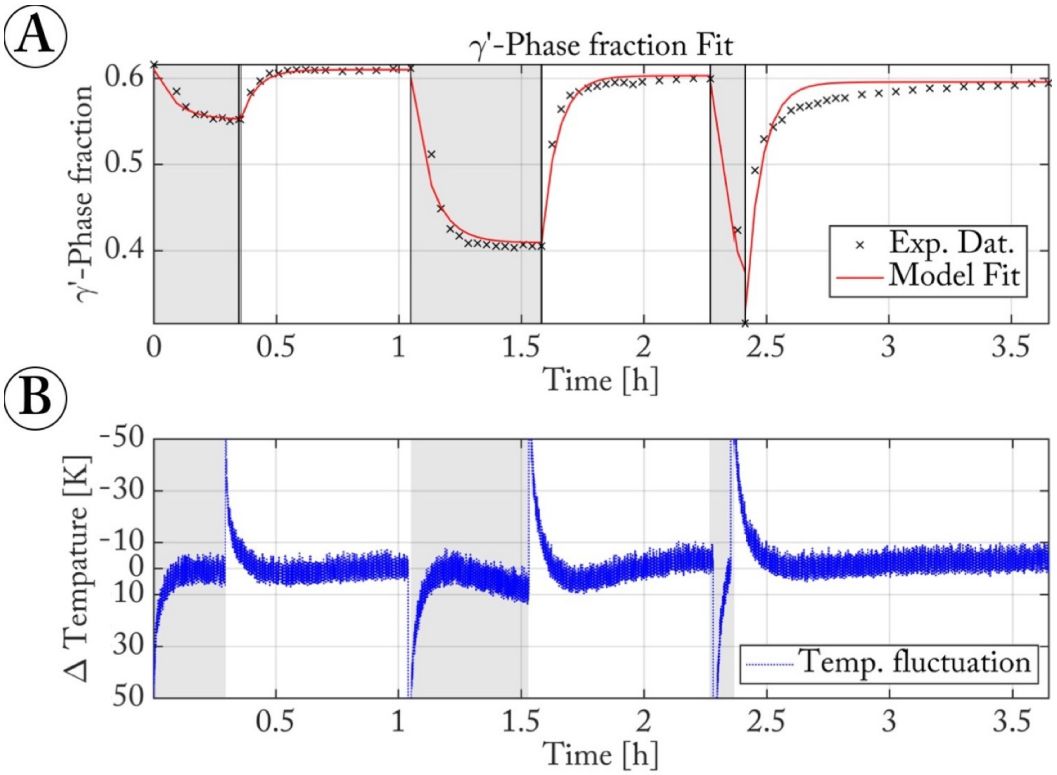

Fig. 4.18 (A) Comparison of the experimentally measure γ'-phase fraction during heating and cooling regimes (black crosses) against the *Thermo-Calc* based model fit (red line). (B) Experimentally measured temperature deviation from the target temperature in the sample (blue dots). Grey shaded areas highlight heating regimes, whilst areas of white background correspond to the cooling regimes (compare to Figure 4.17)

The resulting phase-fraction function is plotted in Figure 4.18a (red line) and is compared against the experimental synchrotron dataset (black x-data points). The three heating segments fitted to a higher activation energy are highlighted with a grey background. Figure 4.18b then displays the experimentally measured temperature deviation over the test time in the test piece measured by a thermocouple attached to the shoulder of the sample. The comparison between model-fit and temperature deviation indicates an overestimate in the re-precipitation speed for the second and third cooling segment in particular. For the heating

segments the solution speed is overestimated in the first and underestimated in the second and third cycle. In addition to the temperature deviation, the shift in precipitation dynamics toward γ'-tertiary re-precipitation and dissolution is thought to contribute to the high temperature inaccuracies of the model fit. Further work has to be done in order to determine the dependence of the activation energy on the state of rafting, applied load and temperature excursion. As sample failure occurred during the fourth heating step, the γ'-tertiary size distribution and number density during the third temperature segment is unclear and could not be used to optimise the model fit. The primary shortcoming of the proposed model in its current state in comparison to the Polystar model [37] is thus that there is no subdivision between the re-precipitation into large (primary) and small (tertiary) γ'-precipitates.

4.3.3 Adapting the phase fraction model temperature cycling

The model outlined was used to compute the phase fraction evolution for a non-isothermal creep experiment of 30 mins at a base temperature of 900 °C followed by a heating of 150 °C to a 3-minute high temperature hold with a constant heating and cooling rate of 250 K/s (see Figure 4.19a). The blue line shows the simulated temperature control. The red line shows the resulting metastable phase fraction evolution under these conditions. The equilibrium γ'-phase fraction of 0.64 at base temperature (900 °C) is reached within 14 mins of cooling.

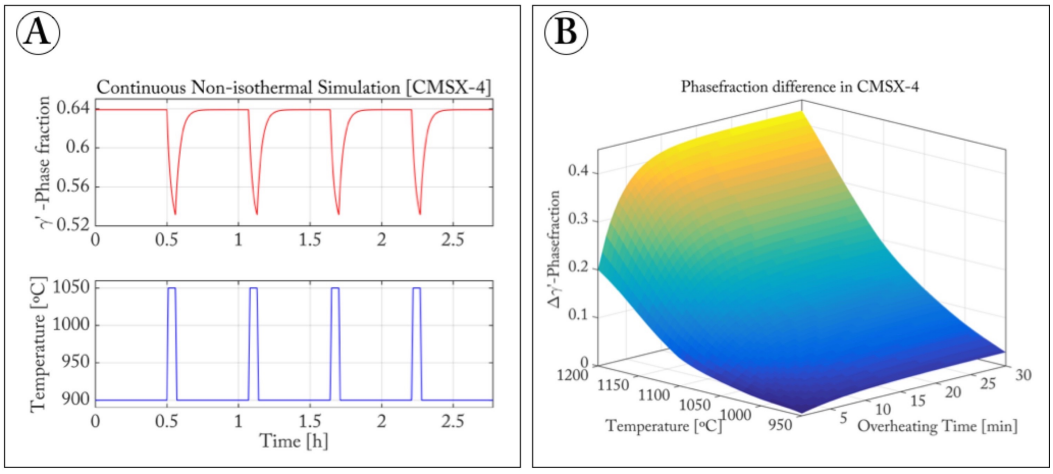

Fig. 4.19 (A) Blue line shows the simulated temperature control with a base temperature of 900 °C for 30 mins followed by a 150 °C heating for 3 mins at a heating and cooling rate of 250 K/s. The red line shows the resulting phase fraction evolution under these conditions. (B) Plot showing how the metastable difference between minimum and maximum phase fraction will develop when changing the heating time and temperature whilst keeping other conditions constant

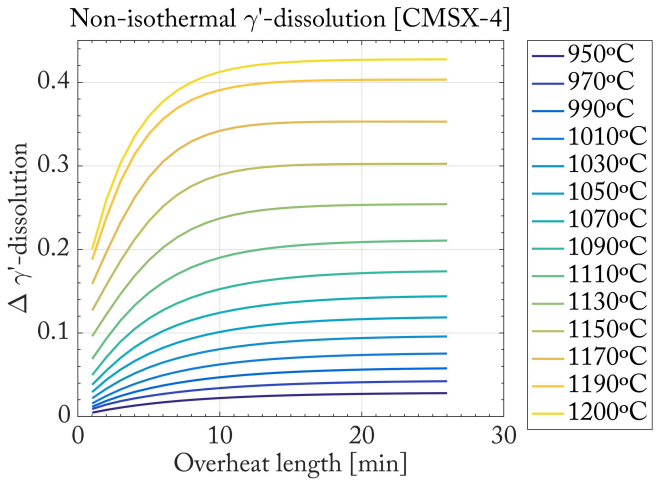

Fig. 4.20 Figure 4.19b rendered in a 2D-plot showing the γ'-dissolution rates for various non-isothermal heating temperatures.

The phase fraction evolution is thought to be influenced principally by the high temperature time and temperature. Keeping all other parameters constant (heating and cooling rate at 250 K/s and base condition with 30 min at 900 $°C$), the high temperature heating time and temperature were varied and the difference in γ'-phase fraction between the equilibrium at peak (base temperature) and metastable minimum (high temperature heating) was calculated and is plotted in Figure 4.19b. For further clarity Figure 4.19b was re-plotted as isothermal curves in Figure 4.20. The trends indicate that the phase fraction dissolution decreases exponentially with temperature. The high temperature time also increases γ'-phase fraction dissolution but follows a logarithmic dependency. With a high temperature regime of about 15 minutes, the non-isothermal phase fractions in the base temperature and high temperature regime continuously change between the equilibrium phase fraction in both regimes. This agrees well with the trends published by Cormier *et al.* [37] and Giraud *et al.* [78].

The modelled figures help to compare the dissolution rates between non-isothermal creep tests of different high temperatures or timeframes in the literature, or to design tests with a specific cyclic γ'-dissolution.

Ultimately, the phase fraction evolution and overall high temperature phase stability is also affected by the alloy chemistry. This was not investigated in this study.

4.3.4 Comparing the phase fraction model to Dictra

The *Thermo-Calc* software module *Dictra* was developed to simulate diffusion controlled reactions in multi-component alloy systems, by solving multi-component diffusion equations.

To compare the module capabilities in phase fraction estimation to the developed non-isothermal model outlined above a simple calculation using *Dictra* is presented.

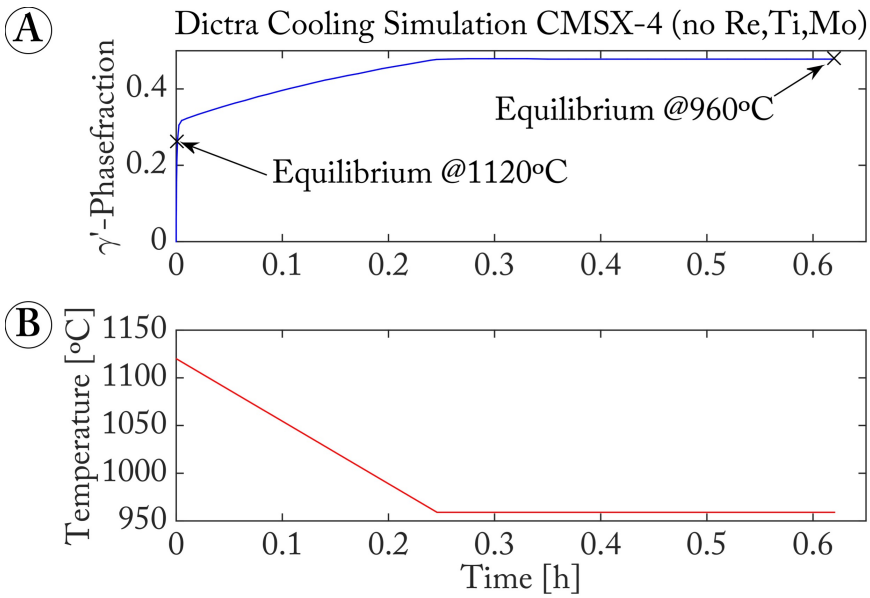

Fig. 4.21 *Dictra* simulation of 2nd cooldown using only six major alloying elements of CMSX-4. (A) Precipitate phase fraction over time; (B) Simulated temperature over time

The simulation is set to calculate a cooling from 1120 °C down to 960 °C with a linear gradient, approximated from the second cooling event in the synchrotron dataset (see Figure 4.19b). To simulate the second cooling step using *Dictra*, the thermodynamic database *TTNi8* was selected and only the main alloying elements of CMSX-4 were entered for computational efficiency (Cr, Co, W, Al, Ta, with a balance in nickel with compositions shown in Table 2.1). Including the other alloying elements (in particular rhenium) slowed the calculation down to unfeasible amounts. All phases except *FCC_A1* and *Gamma_prime* were rejected. Then the mobility database *mobni1* was appended with the previously defined elements and only the *FCC_A1* and *FCC_L12* phases set active. The simulated microstructure was entered as an active region of a 250 nm matrix-channel containing the *FCC_A1* lattice, whilst the precipitate region containing the *Gamma_prime* lattice was entered as inactive. As a result, no diffusion through the *Gamma_prime* lattice is possible, a reasonable assumption considering that the effective diffusion coefficients of matrix and precipitate phase are three orders of magnitude apart.

To simulate the phase fraction evolution, *Dictra* requires the user to adapt the atomic mobilities properly. Choosing the default mobility suggested to the user results in an overestimate of the precipitation process. As mentioned in Section 4.3.2 however, the phase

fraction dissolution and precipitation seems to be more interfacial-controlled than diffusion driven. As a result, the calculated phase fraction (Figure 4.21a) tracks the equilibrium phase fraction of the alloy at every time step (no metastable phase fraction state).

In addition to the overestimation of γ'-phase fraction evolution speeds, the extensive computation times (particularly for the actual 11-element alloy compositions) makes *Dictra* less suitable for a multiple iteration non-isothermal model application.

4.3.5 Plastic strain accumulation

.

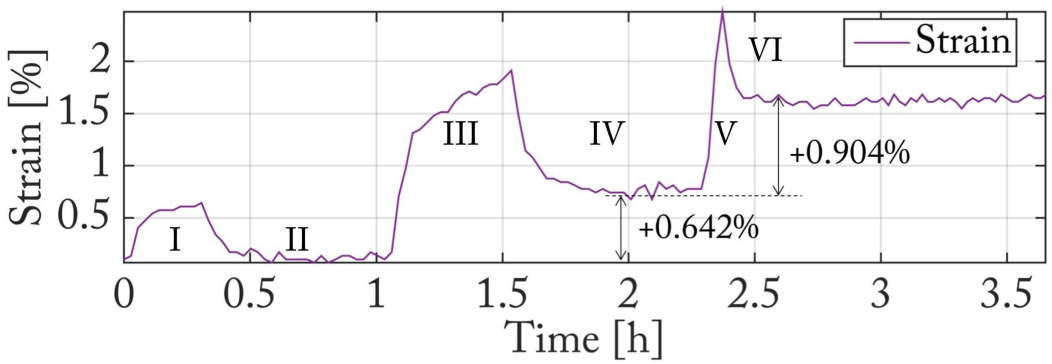

Fig. 4.22 Accumulated strain in the test specimen over the test time (purple). I,III and V highlight heating regimes, whilst II, IV and VI correspond to the cooling regimes (compare to Figure 4.17 and Figure 4.18)

The plastic strain accumulation was recorded during the non-isothermal creep deformation and was plotted in Figure 4.22. The net strain accumulation following each heating cycle is referenced in the figure. Following the second and third heating in Figure 4.22 a significant strain accumulation can be seen as compared to a negligible increase after the first heating cycle. Interestingly, once the effect of the high temperature exposure has tapered off, very little plastic deformation is added at the base temperature steps.

Evidence of the high level of plastic deformation is seen when examining the microstructure with an SEM. Figure 4.23 A-D depicts the microstructure after failure, which occurred in the fourth heating cycle. Images 4.23A and B show an inter-dendritic and dendritic region respectively, 5 mm away from the fracture surface, whereas images 4.23C and D display the microstructure observed 1 mm away from the fracture surface in the inter-dendritic and dendritic regions. Closer to the fracture surface the microstructure has evolved further, with a significant number of dislocations visible in the γ'-phase of both regions (see Position 1 in

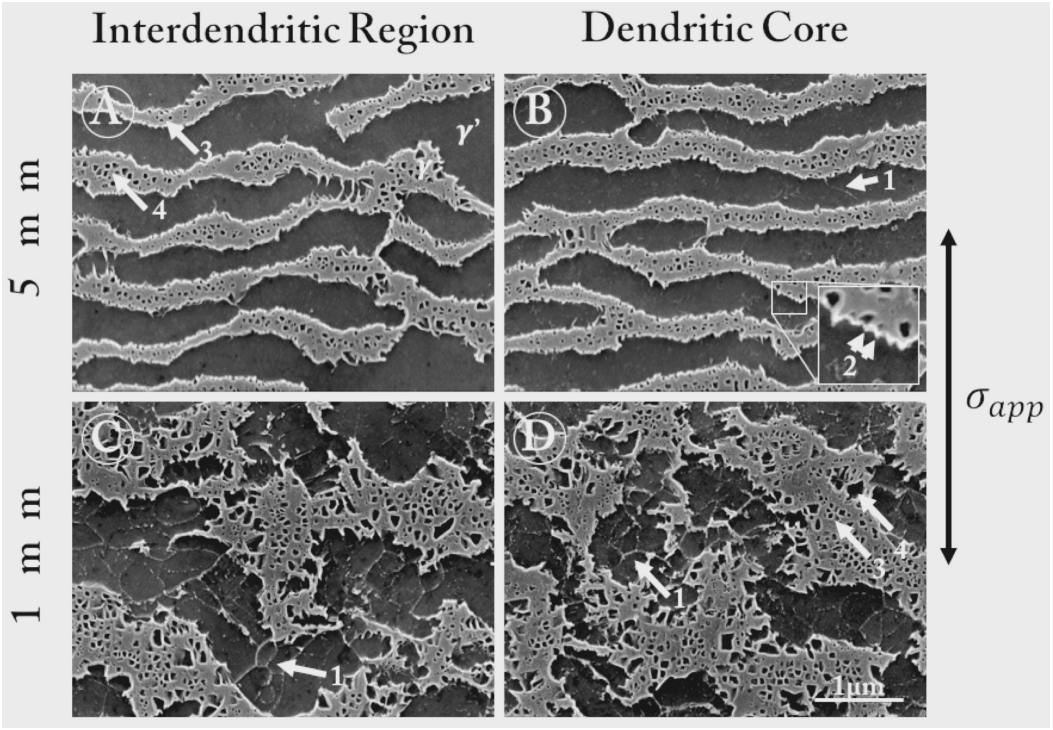

Fig. 4.23 SEM(SE)-micrographs (25 kV, 74 μA) of the [001] oriented CMSX-4 specimen cut longitudinally and imaged 5 mm (A and B) and 1 mm away from the fracture surface (C and D). Sample failure occurred in the fourth heating cycle (see Figure 4.17). The etch dissolved the γ'-phase which appears in dark grey, with bright grey areas as γ-phase. Images A and C show the microstructure in the interdendritic region and B and D in the dendritic cores. Position 1 marks dislocation remnants in the -phase. Position 2 highlights serrations on the interfaces, which are the remnants of the interfacial dislocation networks. Positions 3 and 4 highlight small and large γ'-tertiaries respectively. Imaged by J. Cormier

Figure 4.23), whereas 5 mm from the fracture surface, the difference between dislocation density in the γ'-phase in the inter-dendritic and dendritic region is more apparent with the latter region exhibiting more. The visible dislocations originate from the γ-phase, most likely via precipitate shearing of mixed dislocations [7] and vacancy assisted dislocation climb of edge dislocations [124, 58]. The latter mechanism is driven by dislocations escaping the interfacial dislocation networks [87, 186]. The dislocation networks are visible as protrusions on the interfaces indicated by Position marker number 2 in Figure 4.23 (the interested reader is referred to [90, 62] for a detailed analysis of these protrusions). Dislocation glide in the γ-phase and vacancy assisted dislocation climb [86, 11] cannot be captured with the imaging technique used, but are generally accepted to be operative under these conditions. As discussed in Section 4.3.3, the γ'-phase fraction is subject to dissolution

and re-precipitation under non-isothermal conditions. As a result, γ'-tertiaries can exhibit a bimodal size distribution, as highlighted by Positions 3 and 4 in Figure 4.23.

4.4 Parameters estimated with metastable compositions

The phase fraction variation does not precisely track the temperature profile due to the different diffusivities of the alloying elements [26, 106]. Instead, as seen using *in situ* synchrotron X-ray radiation, the γ'-dissolution lags behind the temperature profiles depending on exposed temperature and thermal gradient [120].

In the previous section, the γ'-dissolution was approximated with an Avrami-equation fitted to an experimental dataset of CMSX-4 thermally cycled under constant load and investigated *in situ* using X-ray synchrotron radiation [182]. The phase fraction evolution was modelled for three test conditions outlined in Section 3.2. These tests all exhibited a constant heating and cooling rate of 120 $[\frac{K}{min}]$ and four temperature segments of a variable holding time at the base temperature, a heating segment, a three-minute hold at high temperature and cooling to base temperature (see Figure 3.2). Thus, the three cycle times differed only by the holding time at the base temperature, which were 9, 18 and 27 minutes.

The non-isothermal γ'-phase fraction evolution is shown for these three test conditions in Figure 4.24, starting with heating up to the three-minute high temperature exposure. The line colours correspond to the test cycles displayed in Figure 3.2 (9, 18 and 27 minutes, corresponding to the black, blue and red line respectively).

4.4.1 Non-isothermal phase fraction modelling

The phase fraction model suggests that the γ' in the 14.5 minutes long 9:3 cycle is in a metastable state throughout the test for the alloy CMSX-4. At the end of a cycle, the γ'-phase fraction roughly reaches its original value. This is in contrast to the phase fraction evolution of the 18:3 and 27:3 cycling condition, which end in a section of 9 and 18 minutes respectively, where the equilibrium phase fraction is fully re-established. These sections are assumed to be similar to the isothermal creep conditions, in that the above simulated equilibrium model parameters are re-established at the base temperature. Before this point however, the interfacial compositions are effectively in a metastable state. The impact of this metastable composition on the interfacial lattice misfit and subsequent interfacial dislocation activity will be examined further in Section 5.3.

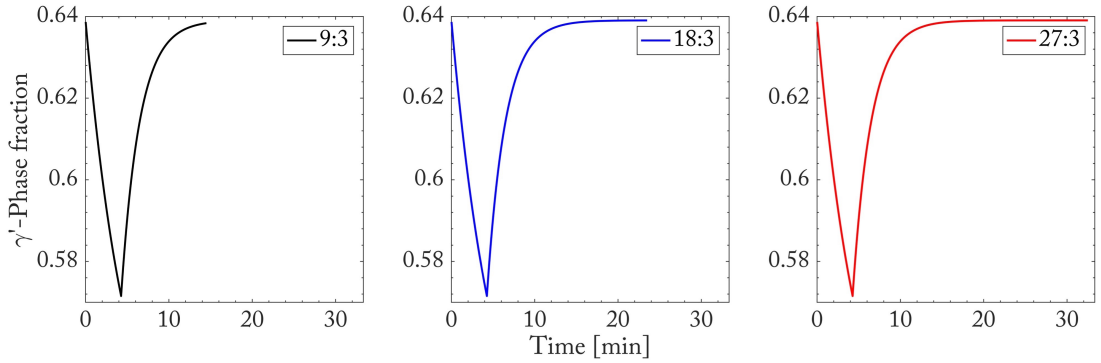

Fig. 4.24 Modelled γ'-phase fraction evolution of a single heating and subsequent base temperature cycle for the three test types of the CMSX-4 series: 9:3, 18:3 and 27:3 (from left to right)

4.4.2 Non-isothermal simulated cell evolution

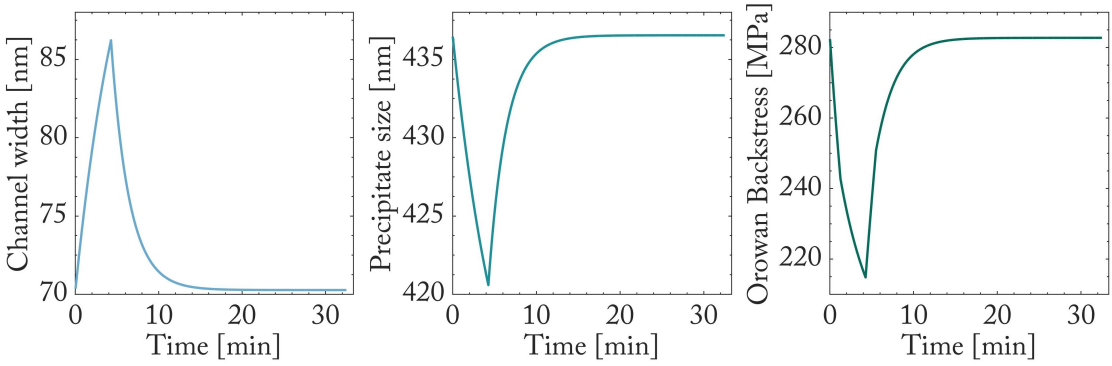

Fig. 4.25 (from left to right) a) Modelled evolution of CMSX-4 for the 27:3 test condition of the γ-channel width, b) γ'-precipitate length and c) resulting Orowan backstress in the γ-channel

The phase fraction data presented above for the 27:3 test condition was used to estimate the channel and precipitate length evolution during a single cycle, shown in Figure 4.25a and b respectively. For this simulation, an average sized simulated cell of one cubic γ'-particle of 450 nm edge length with a 50 nm γ-channel length (h) was assumed (see Figure 6.2). The effect of γ'-tertiary precipitation and dissolution on the effective channel lengths upon cooling was not considered in this model. The γ'-dissolution in this simulated simulated cell is estimated to result in an expansion of the γ-channels by 16 nm in each direction (from Figure 4.25a). Using the γ'-evolution, the Orowan backstress in a dislocation-free channel was calculated using Equation 4.9 (adapted from [199]). The shear modulus (G) data for the

corresponding temperatures was taken from Sieboerger *et al.* [185] and the Burgers vector (b) was estimated at 2.5 Å.

$$\tau_{Or} = \frac{\sqrt{2}G \cdot b}{\sqrt{3}h} \tag{4.9}$$

The evolution of the Orowan backstress is displayed in Figure 4.25c and shows a reduction by 65 MPa. However, the stress field driving the dislocations through the microstructure cannot be directly related to the applied stress alone. The true three-dimensional stress field acting in a given simulated cell is largely a function of the interfacial lattice misfit from the coherent γ/γ'-interfaces (see [151, 55, 156]). As the interfacial lattice misfit increases in magnitude with temperature [147, 149, 22], the stress field in the microstructure also increases. The increase in interfacial lattice dislocation density is attributed to the increase in lattice misfit (see Zhang *et al.* [226]). The effect and evolution of the lattice misfit will be further discussed in Section 4.4.7.

4.4.3 Non-isothermal diffusion based parameter evolution

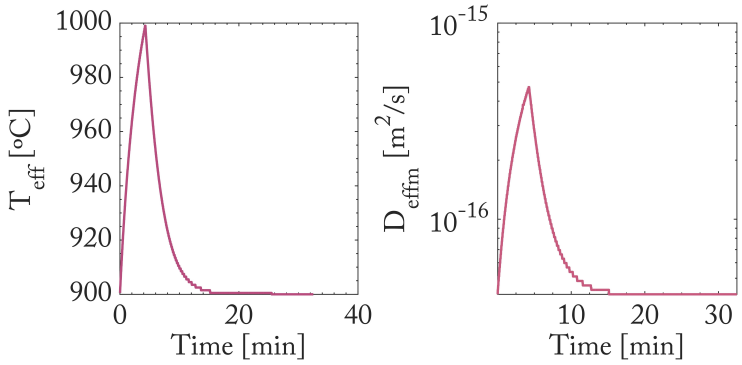

Fig. 4.26 (from left to right) a) Modelled evolution of the alloy CMSX-4 for a single 27:3 cycle of the effective temperature (T_{eff}) and b) effective mean diffusivity for CMSX-4

To estimate the energetic and compositional state of the material at each time step, the calculated γ'-phase fraction (Figure 4.24) was chosen over the temperature control cycle (Figure 3.2). As phase composition drives the parameter evolution, the metastable evolution of the remaining creep parameters was calculated by correlating the metastable phase fraction evolution at each time step to the corresponding equilibrium phase fraction estimated using the *TCNi7* database in *Thermo-Calc*. This corresponding temperature is termed the effective temperature T_{eff} (see Figure 4.26a). The effective temperature peaks at 1000°C indicating,

that the 3 min high temperature regime effectively establishes an atomic composition similar to this temperature. To calculate the metastable evolution of the effective γ-interdiffusivity (D_{effm}) the previously calculated equilibrium interdiffusivity (see Section 4.1.3) is correlated to each time/temperature step of the effective temperature, such that the peak D_{effm} is equal to equilibrium value at 1000°C.

4.4.4 Non-isothermal solid-solution hardening

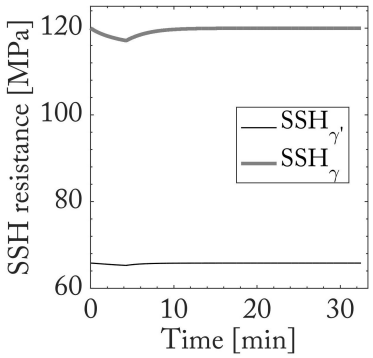

Fig. 4.27 Solid-solution hardening parameters estimated in CMSX-4 for the γ'-precipitate phase (left) and the γ-matrix phase (right)

The solid solution in the γ' and γ-phase is estimated and plotted in Figure 4.27. The equilibrium based calculation of these parameters was outlined in Section 4.1.1. Using the effective temperature approach outlined in the section above, from the equilibrium parameter values the non-isothermal evolution was calculated and the result divided by the Taylor factor to compute the effective resistance on each slip plane. Comparing the plotted results it is evident that the solid-solution resistance is higher in the γ-matrix and shows an overall small temperature dependence during non-isothermal cycling. The γ-matrix SSH-resistance decreases by 3 MPa upon heating from 900°C to 1050 °C, whilst the γ'-phase only decreases by 0.3 MPa for the same heating increment.

4.4.5 Critical particle shear strength estimation

The critical resolved shear stress (CRSS or also referred to as τ_P) required by a dislocation to enter the γ'-precipitates was first calculated as a function of the precipitate size using equilibrium parameters. The critical shear stress is dependent on the APB-energy (calculated in Section 4.1.2), the volume fraction and precipitate size and the result is plotted as a

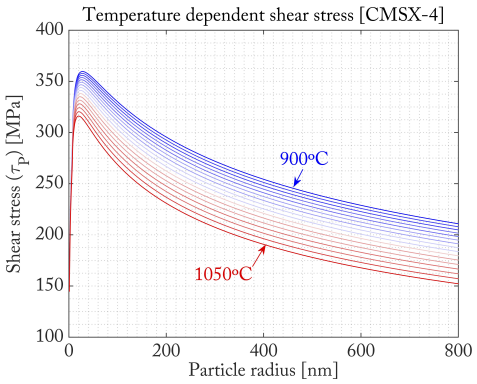

Fig. 4.28 Precipitate shear stress for the alloy CMSX-4 as a function of the precipitate radius plotted for thermal exposure in the experiments. The upper boundary in blue corresponds to the value at base temperature, the lower red curve plots the high temperature values.

function of the precipitate radius for the temperatures between 900°C and 1050°C in 10°C increments in Figure 4.28. The model used is a weak and strong coupled unified approach published by Galindo-Nava *et al.* in [72]. This approach describes the precipitate strength for multimodal particle distributions and was expanded for the case of cuboidal strong-coupled precipitates using Equations 4.10 and 4.11.

$$h = \frac{L}{f^{\gamma'}} - L \tag{4.10}$$

$$\lambda = \frac{2l_{111}}{\sqrt{3}} + \sqrt{2}h \tag{4.11}$$

Where h is the mean channel width, L the mean precipitate length and $f^{\gamma'}$ the precipitate equilibrium volume fraction. The shear length on the active slip plane in the precipitate is given by the parameter λ, which includes the precipitate length on the glide plane (l_{111}).

The model indicates a strong thermal dependence on the critical shear stress, with the γ'-resistance decreasing for higher temperatures. Using the effective temperature approach and the same heating cycles outlined in Section 4.4.3 (between 900°C and 1050°C) the non-isothermal evolution of the APB-energy and the critical resolved shear stress in the alloy CMSX-4 were calculated and are plotted in Figure 4.29.

Figure 4.29 indicates that, as a result of the high temperature exposure to 1050°C the APB-energy decreases by 6.5 $[\frac{mJ}{m^2}]$ (-2.7%). In the previous sections it was shown, that the γ'-precipitate size (Figure 4.25b) and volume fraction (Figure 4.24) decreased by 15.9 nm (-3.6%) and 0.07 (-10.5%) fractions respectively. These three main contributions to the

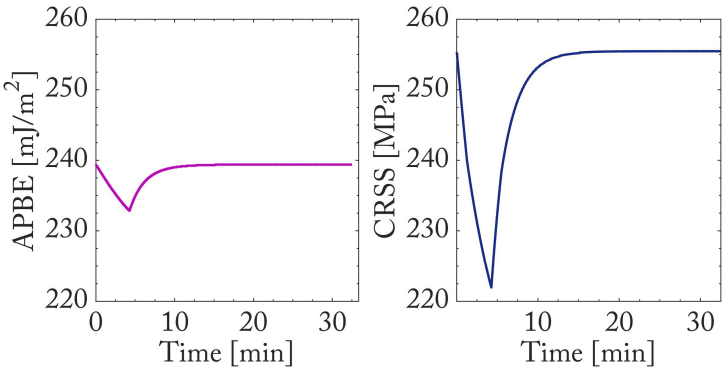

Fig. 4.29 Non-isothermal precipitate resistance parameters estimated for CMSX-4 (a) anti-phase boundary energy and (b) CRSS

critical resolved shear stress of the γ'-precipitates translate into a reduction of 33.3 [MPa] (-13 %) to the parameter.

4.4.6 Non-isothermal parameter estimation for CMSX-10K

For the alloy used in the experiment, CMSX-10K (an alloy variant of CMSX-10N, see Table 2.1) the parameter evolution was calculated. The modelling was based on the 18:3 experimental temperature profiles outlined in Section 3.2. The CMSX-10K tests consisted of a constant heating and cooling rate of 120 $[\frac{K}{min}]$ and four temperature segments. A 18-minute holding time at the base temperature (900 °C), a heating segment, a three-minute hold at high temperature (1050 °C) and cooling to base temperature (see Figure 3.2).

Each contributing non-isothermal creep parameter was calculated using the same approach outlined for the alloy CMSX-4 presented above. Central to this approach is the γ'-phase fraction evolution. As no XRD-synchrotron dataset for this alloy could be found by the author the same formula previously fitted to CMSX-4 was used. The calculated γ'-evolution was plotted in Figure 4.30a. The accuracy of the result was established by comparing data acquired from the laser triangulation sensor for the 18:3 CMSX-4 and CMSX-10 creep tests (the position of the detector is shown in Figure 3.1 as LVDT). The comparison indicated that the CMSX-10 volume decreased less and was re-established faster than for the alloy CMSX-4. The modelled CMSX-10 γ'-fraction only decreases to 0.62 and is re-established after 9 min and 20 sec resulting in a 14 min 10 sec regime where the base temperature equilibrium parameters are re-established (see Figure 4.30a). The resulting γ'-fraction evolution thus recuperates equilibrium faster, shows a smaller γ'-dissolution and exhibits an overall higher γ'-phase fraction than the CMSX-4 γ'-phase fraction.

Central to the calculation of the remaining non-isothermal creep parameters is the estimation of the effective temperature (T_{eff}) (see Figure 4.30b). In comparison to CMSX-4, the effective temperature for the identical thermal exposure is higher in CMSX-10. The resulting effective diffusivity for CMSX-10 is thus also slightly higher than in CMSX-4.

When comparing the impact of the high temperature dissolution on an ideal simulated cell (defined in Section 6.2.1 as one mean sized particle surrounded by a mean sized channel width on three sides), the CMSX-10 simulated cell is estimated to decrease by only 11.6 nm (compared to the 16 nm in CMSX-4), as a result the Orowan backstress is 33.3 MPa higher at peak γ'-dissolution compared to CMSX-4 (see Figure 4.31).

Interestingly, the higher Orowan resistance in the γ-matrix for CMSX-10 is coupled with a slightly lower γ-solid-solution resistance (-2.5 MPa) at peak effective temperature in comparison to CMSX-4. The resulting resistance against dislocation glide in the γ-phase of CMSX-10 is thus overall greater than in CMSX-4 at all temperatures.

The γ'-phase in CMSX-10 shows an equally consistently higher resistance against dislocation shear than the alloy CMSX-4. The three main contributions to this parameter are the γ'-fraction (which according to Figure 4.30a decreases less and is overall higher), the precipitate size (which also decreases less and is overall higher as shown in Figure 4.31b) and the APB-energy, that even increases in the heating regime as seen in Figure 4.32b. The resulting modelled CRSS for CMSX-10 displayed in Figure 4.32c estimates a 24.5 MPa higher resistance against γ'-shearing by APB-pairs.

From the modelled parameter evolution it can be concluded that the alloy CMSX-10 should show a higher non-isothermal creep resistance than the alloy CMSX-4. The following chapter will present experimental creep results that can be compared to the modelled parameters in order to understand the *in situ* dislocation response during non-isothermal testing.

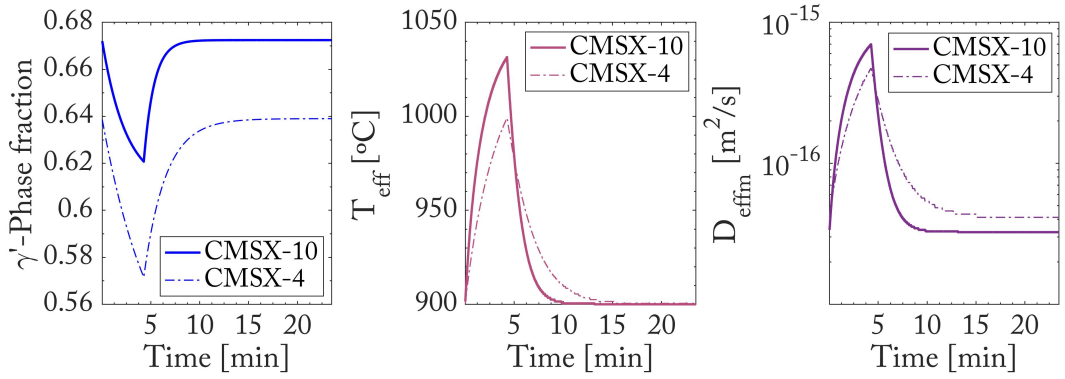

Fig. 4.30 Non-isothermal parameter evolution for CMSX-10 for a 18:3 cyclic test: (a) γ'-phase fraction, (b) effective temperature, (c) effective γ-diffusivity

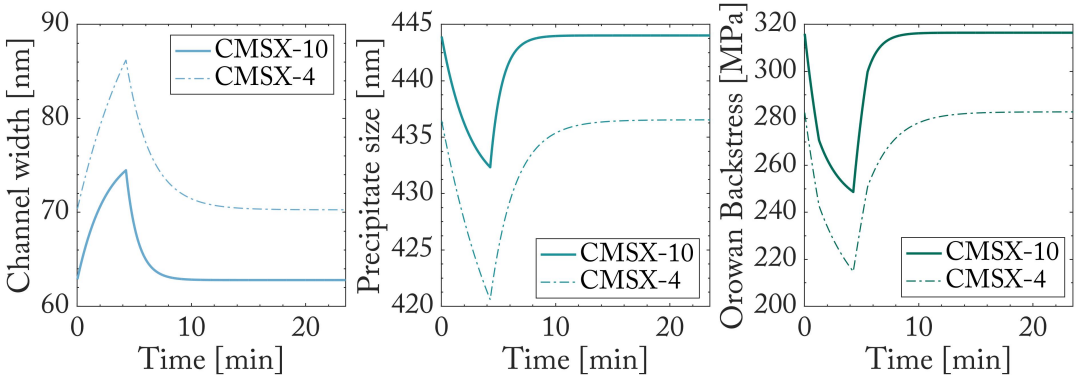

Fig. 4.31 Non-isothermal parameter evolution for CMSX-10 for a 18:3 cyclic test: (a) γ-channel width, (b) γ'-precipitate size, (c) Orowan backstress

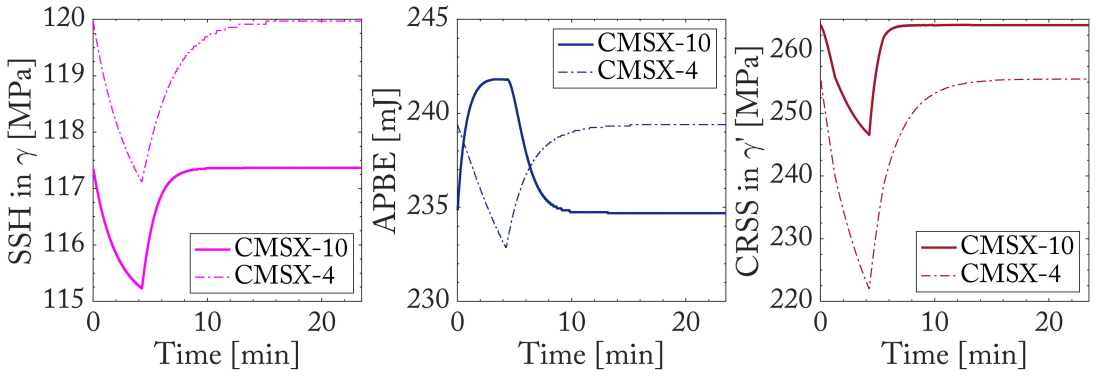

Fig. 4.32 Non-isothermal parameter evolution for CMSX-10 for a 18:3 cyclic test: (a) γ solid-solution hardening resistance, (b) APB-energy, (c) CRSS in the γ'-precipitate phase

4.4.7 Estimating the interfacial lattice misfit

To model the non-isothermal interfacial lattice misfit three different approaches were contemplated. Calculation with an empirical equation, with a concentration dependent model or using a thermodynamics based model. This section will lay out a novel approach using a thermodynamic model which currently has considerable limitations as it only works for the baseline alloy CMSX-4.

Overview of the different misfit parameters in the literature

In the literature three different measures of the interfacial lattice misfit are often used synonymously, adding to the problem of modelling the misfit correctly. The **unconstrained interfacial misfit** (δ_{cmcp}) is the parameter most commonly estimated using thermodynamical databases. It describes the size difference between the lattices of both phases without accounting for the effect of interface coherency. The γ/γ'-interfaces in superalloys are however coherent and are only assumed to lose coherency for very high dislocation densities deposited on the interfaces or as a result of long term high temperature exposures (over-ageing).

At the other end of the spectrum is the **inital constrained interfacial misfit** (δ_{cpcp}) which describes a coupled misfit that is created upon lattice creation, without any dislocations present. Interfacial dislocations are thought to relax the interfacial stresses and act as segregation sites (see Huang *et al.* [90] and Ge *et al.* [76] on the element segregation around dislocation cores), thereby altering the interfacial composition. The cross-influence between the interfacial composition, external applied stress and internal stress fields (i.e. from interfacial dislocations) means that the **effective interfacial misfit** (δ_{eff}) at any given time is directly related to the dislocation density contained at the respective time-step. The interested reader is referred to Dirand *et al.* for an analysis of these parameters [48].

During the synchrotron experiment the effective interfacial lattice mismatch was measured and is displayed in Figure 4.17.

Determining the different misfit parameters

To determine the unconstrained interfacial lattice misfit using *ThermoCalc*, the equilibrium concentration of both γ and γ'-phase were estimated (see Section 4.1). Using these compositions at each temperature, the molar volume (V_M) was estimated using the *ThermoCalc* database *TCNi7* at each temperature step. The lattice parameters of the γ (a_{γ}^{FCC}) and γ'-phase ($a_{\gamma'}^{L1_2}$) were then estimated, using Equations 4.12 and 4.13 respectively. The equations depend

on the molar Volumes and the Avogadro constant (N_A). The unconstrained lattice misfit (δ_{eq}) then results from Equation 4.14.

$$a_{\gamma}^{FCC} = (\frac{4 \cdot V_M^{\gamma,FCC}}{N_A})^{1/3} \tag{4.12}$$

$$a_{\gamma'}^{L1_2} = (\frac{4 \cdot V_M^{\gamma',L1_2}}{N_A})^{1/3} \tag{4.13}$$

$$\delta_{eq} = \frac{a_{\gamma'}^{L1_2} - a_{\gamma}^{FCC}}{2(a_{\gamma}^{FCC} + a_{\gamma'}^{L1_2})} \tag{4.14}$$

The calculated unconstrained lattice misfit for the alloy CMSX-4 over the high temperature range is displayed in Figure 4.33 as δ_{cpcm} (red dashed line). The unconstrained misfit rises with increasing temperature due to the increasing γ'-former soluted in the matrix thereby reducing the size difference between the phases (see Figure 4.1).

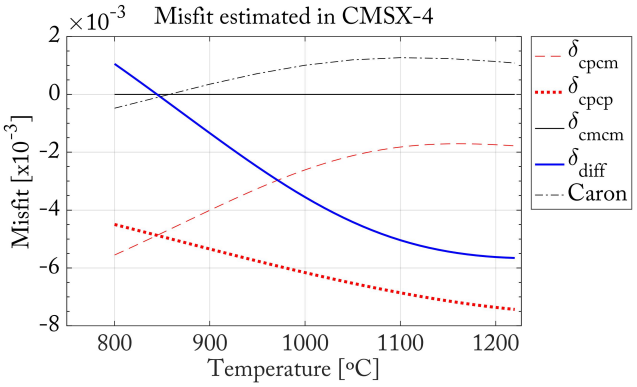

Fig. 4.33 Lattice misfit parameters compared for CMSX-4: (red dashed line) δ_{cpcm} - unconstrained misfit estimated using *ThermoCalc*, (red dotted line) δ_{cpcp} - initial constrained misfit estimated using *ThermoCalc*, (black dash-dot line) unconstrained misfit estimated according to Caron *et al.*, (black solid line) δ_{cmcm} - misfit estimated when using the matrix phase on both sides of the interface estimated using *ThermoCalc*, (blue solid line) δ_{diff} - differential misfit between δ_{cpcp} and δ_{cpcm};

The initial constrained interfacial misfit is a theoretical parameter that results from the chemical imbalance following strong thermal gradients. Under a strong thermal gradient the very different element mobilities determine not only the location of the interface but also its compositional gradient. This will be explored in detail using the thermodynamic software *Dictra* in Section 5.3. In the cited section it will be shown that strong thermal gradients do not allow for sufficient time for the diffusion of elements, other than aluminium, to keep

up with the interface. The conclusion is then, that the newly deposited γ'-phase region has a non-equilibrium composition, richer in W, Co, Cr and depleted in Ta. Nevertheless, the Al-enrichment in this region is sufficient to order the lattice into a $L1_2$ structure. The compositional difference however changes the misfit at the interface.

The element concentration to the left and right side of the interface will contain effectively an $L1_2$ structure that gradually dissolves (in the case of a heating) or gradually builds up (cooling). This highly unstable transient state is taken as the initial starting value, for the magnitude of a strained transient lattice misfit (the initial constrained misfit δ_{cpcp}).

To reflect the key assumption, that ordering precedes element concentration balance in a phase, the lattice structure was switched in *ThermoCalc*. Instead of calculating the matrix phase using the matrix composition and *FCC_A1* lattice the *FCC_L12* phase was selected. The computed constrained misfit is again plotted in Figure 4.33 as δ_{cpcp} (red dotted line). The constrained misfit decreases for higher temperatures due to the two coupled phases having a different thermal expansion.

Assuming no dislocation density (following a long term heat treatment), then the difference between the constrained and unconstrained misfit (δ_{diff}) is believed to be equal to the effective interfacial misfit at the specific temperature. The dislocation free effective interfacial lattice misfit is plotted as a blue line in Figure 4.33.

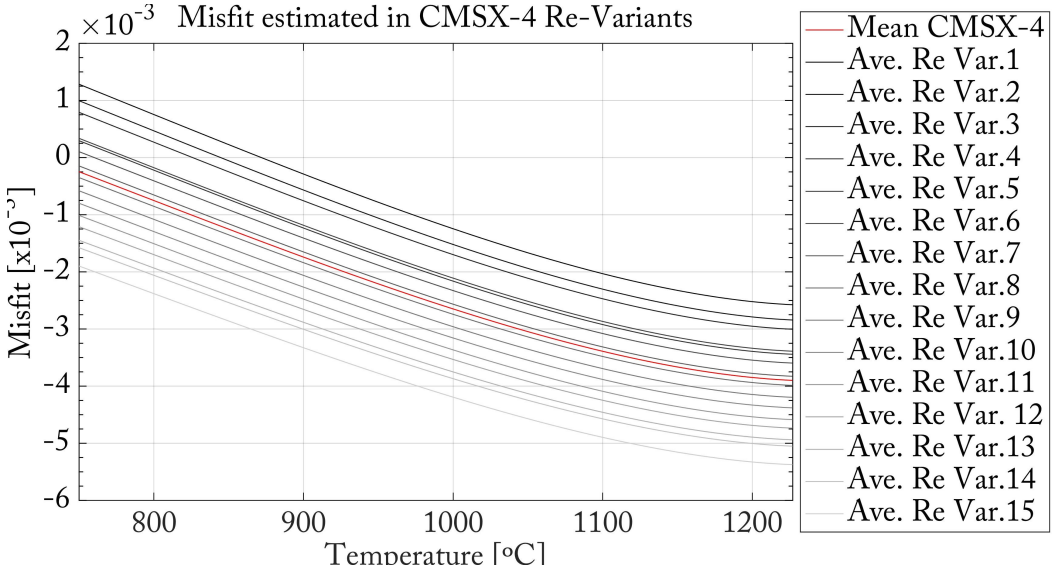

Fig. 4.34 Effective misfit calculated for the alloy based Re-variants over the high temperature regime in CMSX-4

This modelled effective interfacial lattice misfit was then plotted for the rhenium based alloy variants of the alloy CMSX-4 in Figure 4.34. For comparison, an experimental dataset

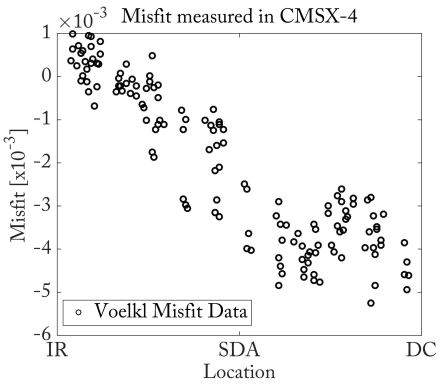

Fig. 4.35 Experimentally measured effective misfit by Voelkl *et al.* adapted from [217]

of the same alloy collected by Voelkl *et al.* [217] was reproduced in Figure 4.35. Voelkl *et al.* collected the dataset using a standard heat treated sample of CMSX-4 that was cooled down to -170 °C and analysed with convergent beam electron diffraction (CBED) [217]. In the study Voelkl *et al.* argue that the calculated effective interfacial lattice misfit is stable up to a temperature of 800 °C and can be compared to the modelled data at this temperature in Figure 4.34. The modelled effective misfit seems feasible as the trends between the inter-dendritic and dendritic values are correctly captured. The positive misfit in the inter-dendritic region is particularly well reproduced. The modelled values however fall within a narrower spread than seen experimentally by Voelkl *et al.* [217]. Furthermore, the thermal trends follow those seen experimentally using synchrotron radiation (Figure 4.17). The magnitude of the misfit measured there and computed here differ however, a result of the considerable dislocation density observed experimentally. No agreement can be observed between the experimental dataset and the formulated approach by Caron in [27] plotted in Figure 4.33 as a black dashed line. This approach had been used to estimate the lattice constants to quantify the parelastic interaction in Section 4.1.1 but is inadequate to estimate the resulting interfacial misfit.

To complete the range of misfit estimations possible using *ThermoCalc* the parameter δ_{cmcm} is shown in Figure 4.33. This parameter can be calculated using the disordered lattice (*FCC_A1*) for both phase compositions. The resulting misfit is zero for all temperatures as no site restrictions exist in this phase.

The *ThermoCalc* based approach outlined above however has significant limitations. An estimation of feasible δ_{cpcm} and δ_{cpcp} parameters was only possible for the alloy CMSX-4. Without a comprehensive further study of the databases used by *ThermoCalc* and their optimisation, the above outlined approach is merely showing the current complications in misfit estimation and a methodology for a future approach to estimate the different interfacial lattice misfits using a thermodynamic approach rather than individual fit-functions for the

different alloys. Nevertheless, as the computed trends correctly reflect the misfit variation with composition and temperature in the alloy CMSX-4 these are used for the non-isothermal creep model.

Estimating the non-isothermal misfit

Figure 4.36 shows the non-isothermal evolution of the initial constrained (δ_{cpcp}) and equilibrium unconstrained misfit (δ_{cpcm}) for the 27:3 heating test cycle. The datasets were calculated using the effective temperature approach and the resulting data is plotted in Figure 4.36 for the alloy CMSX-4 in black and CMSX-10 in red.

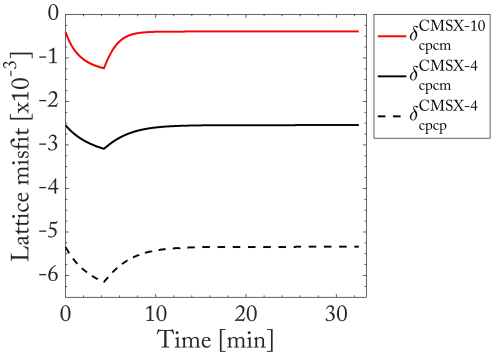

Fig. 4.36 The unconstrained (δ_{cpcm} - as solid lines) and constrained (δ_{cpcp} - as dashed line) misfit, plotted for the alloys CMSX-4 (black) and only the unconstrained misfit for CMSX-10 (red).

The constrained initial misfit could not be estimated for the alloy CMSX-10 and thus only the unconstrained estimate is plotted in Figure 4.36. As further calculations with low rhenium containing alloys were possible, the problems in calculating δ_{cpcp} are attributed to the high rhenium content of the alloy in the matrix (see Figure 4.1). As the δ_{cpcp} approach estimates the composition molar volume in an ordered lattice, it seems likely that such high rhenium contents are not contained in the *ThermoCalc* database. The unconstrained value for CMSX-10 indicates a lower magnitude of the unconstrained interfacial lattice misfit, which is linked to the loss of local coherency in the interface (see Schulze and Feller-Kniepmeier [178]). The cited study reported constrained bulk misfit values of -2.7×10^{-3} and $+1.2 \times 10^{-3}$ measured at -170 °C using CBED in the dendrite cores and inter-dendritic regions respectively. Further, the unconstrained misfit was modelled using FEM-calculations in the study amounting to -1.5×10^{-3} and $+0.6 \times 10^{-3}$ in the dendrite cores and inter-dendritic regions respectively.

Theoretical considerations implementing the thermodynamic misfit approach

Modelling the interfacial misfit using a thermodynamic approach with a constrained and unconstrained misfit leaves the question: how many interfacial edge dislocations would be required to change the effective interfacial lattice misfit from the former to the latter?

$$\rho_{max} = \left(\frac{\delta_{cmcp} - \delta_{cpcp}}{b} \right)^2 \tag{4.15}$$

Using Equation 4.15, the required dislocation density ρ_{max} is estimated and plotted in Figure 4.37(left). Using Brooks Equation [19], this results in an average dislocation separation of 82 nm. Dirand *et al.* in [48] measured the interfacial lattice misfit by measuring the interfacial dislocation network spacing using TEM, SEM and synchrotron analysis, reporting values for the dislocation spacing in this order of magnitude (∼70 nm) for heavily deformed tests using the alloy AM1.

Using the maximum number of dislocations, the precipitate length (L) and Equation 4.16, the required number of dislocations on the interfaces (DoP) was calculated and is plotted in Figure 4.37(right). This calculation takes into account how around an ideal cuboidal precipitate, the misfit and interfacial area change during a non-isothermal cycle.

$$DoP = \rho_{max} \cdot 6 \cdot L^2 \tag{4.16}$$

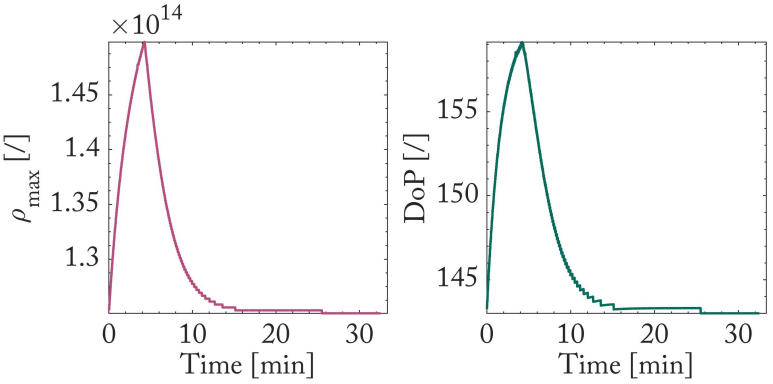

Fig. 4.37 Non-isothermal calculations for a 27:3 cycle of CMSX-4, (left) estimating the number of interfacial dislocations (ρ_{max}) required to relieve the initial constrained misfit to the level of the unconstrained misfit, (right) evolution of the number of ρ_{max} deposited on a cuboidal interface during non-isothermal cycling.

The result suggests that during a three minute high temperature segment, despite the loss of interfacial area (due to dissolution) an increase in the number of dislocations is required. The additional dislocations are required as the magnitude of the misfit increases during

heating. Thus an increase in the number of deposited dislocations is generally assumed to occur during the high temperature regimes.

4.4.8 Modelling of rafting and coarsening

As outlined in Section 2.3.4, the high temperature creep regime results in a morphological transformation from many small regular cuboidal precipitates towards a few long and thick rafts. Lifshitz and Slylov as well as Wagner (LSW) outlined in their works [122, 218] an approach to model the isotropic coarsening in polycrystalline superalloys due to Ostwald ripening (Equation 4.17).

$$[r^3 - r_0^3]^{1/3} = k \cdot t^{1/3} \tag{4.17}$$

The isotropic coarsening rate depends on a material coarsening constant k that is commonly estimated using Equation 4.18 (adapted from [121]), where D_{eff}^{iso} is the effective isothermal diffusion coefficient, σ_{Int} the precipitate-matrix interfacial energy per unit area, N_α the total equilibrium mole fraction of solute in the matrix, V_M the molar volume of the precipitate, R the gas constant and T the absolute temperature.

$$k = \left[\frac{8 \cdot D_{eff}^{iso} \cdot \sigma_{Int} \cdot N_\alpha \cdot V_M}{9 \cdot R \cdot T}\right]^{1/3} \tag{4.18}$$

For single crystal superalloys this approach was further expanded by Fedelich *et al.* [65] incorporating a distinction between isotropic coarsening and directional coarsening (rafting) based on experimental isothermal creep experiments at 1100°C using the alloy CMSX-4 (see Figure 4.38). The equations published by Fedelich *et al.* [65] however are not fitted to *ThermoCalc* based phase fractions and as such cannot be used for a non-isothermal model, where a phase fraction estimation error is particularly of relevance. Therefore, this study adapted and fitted the experimental dataset to LSW-theory. This approach also avoids using *ThermoCalc* estimated molar volumes (see previous section for a discussion of the limitations of *ThermoCalc* in this respect).

To model the non-isothermal morphological transformation of the microstructure as precisely as possible, from the displayed dataset by Fedelich *et al.* the isothermal material coarsening $\breve{k}$ was extracted (see Equation 4.19). $\breve{k}$ was adapted for the applied stress and divided by the effective isothermal diffusivity D_{eff}^{iso}. The resulting material constant is $\breve{k} = 1.3093 \cdot 10^{-11}[m]$.

$$\breve{k} = \frac{h_0}{D_{eff}^{iso}} \tag{4.19}$$

$$h_z = (\xi \cdot t \cdot \breve{k} \cdot D_{eff} + h_0^3)^{1/3} \tag{4.20}$$

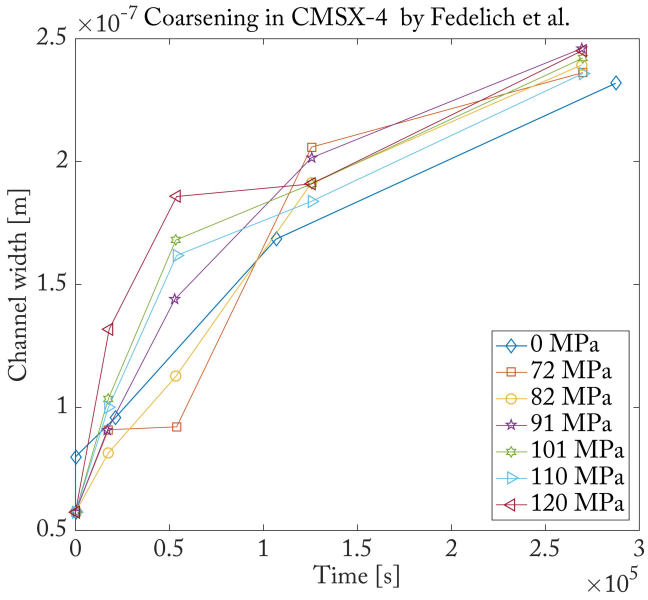

Fig. 4.38 Channel width during isothermal creep at 1100°C for various applied stresses (0-120 MPa), reproduced from [65].

The resulting morphological transformation of the channel length (h_z) then results from Equation 4.20 with D_{eff} as the non-isothermal effective γ-diffusivity and is plotted in Figure 4.39 as dash-dot lines in black, blue and red, corresponding to the effective diffusivities during the 9:3,18:3 and 27:3 non-isothermal cycles respectively (see Figure 3.2). The circle data points in Figure 4.39 correspond to the measured channel width in the dendritic core and the diamonds to the inter-dendritic regions following the interrupted tests (experimental test times shown in Figure 5.1). The experimental data points plotted in Figure 4.39 were calculated from SEM-micrographs, which were binarised in *ImageJ* and the channel widths and precipitate sizes were were fitted to a log-normal distribution and the most frequent channel width found using *Matlab, MathWorks Inc*.

Crucially, the channel width calculations based on the parameters extracted from the isothermal experiments by Fedelich *et al.* show a significantly slower micro-structural transformation than measured in the non-isothermal creep tests performed in this study. As a result, the modelled evolution was scaled (by a parameter ξ in Equation 4.20) to the non-isothermal data, using $\xi = 7.5$ and $\xi = 15$. The two scale parameters should then account for the micro-structural transformation in the growing (h_z-channel) and shrinking (h_x and h_y) channels respectively.

For the case of $\xi = 15$ the evolution was compared to the ideal raft and cuboids cases outlined by Fedelich *et al.* in [65] in Figure 4.40. The comparison between rafts and

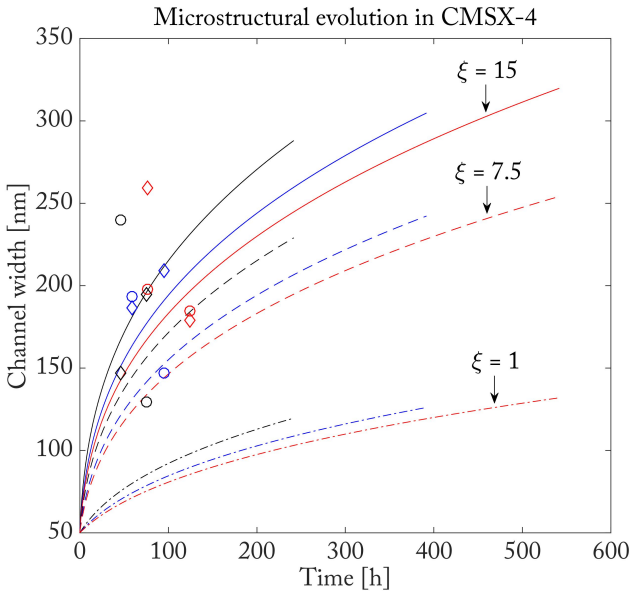

Fig. 4.39 Morphological transformation of the microstructure modelled for the alloy CMSX-4 using the Fedelich dataset (dash-dot lines), which is then further scaled by a parameter of $\xi = 7.5$ (dashed lines) and $\xi = 15$ (solid lines). The experimental data from the non-isothermal creep tests performed is plotted as circles for the dendrite cores and as diamonds for the inter-dendritic region. The black, blue and red colours correspond to the 9:3, 18:3 and 27:3 test cycles respectively.

cuboids is used by Fedelich *et al.* to determine the current state of rafting in a microstructure. Additionally the times to 1% and 2% plastic strain accumulation are plotted for the three test conditions (9:3, 18:3 and 27:3 in black, blue and red respectively).

The microstructure following the different non-isothermal cycles is shown and will be further discussed in the following Section 5.1.1. Comparing the modelled micro-structural evolution to the experimental times in Figure 4.40 one would expect to see strongly coarsening microstructures across all experimental cycles and fully completed rafts in the case of the 9:3 and 18:3 test cycles. As this finding will later be confirmed, this approach was thus implemented in the non-isothermal creep model.

The implementation of the combined effects of rafting and coarsening into the non-isothermal creep model for the alloy CMSX-4 is plotted in Figure 4.41a, with a close-up of the green box in Figure 4.41b. The calculation follows the methodology outlined in Section 4.4.2 for the γ-channel width of a single simulated cell now gradually increased at each base temperature step by modelled coarsening rate. The evolution for the three modelled test cycles shows a short spike in γ-channel width during the 3 minute heating cycles and

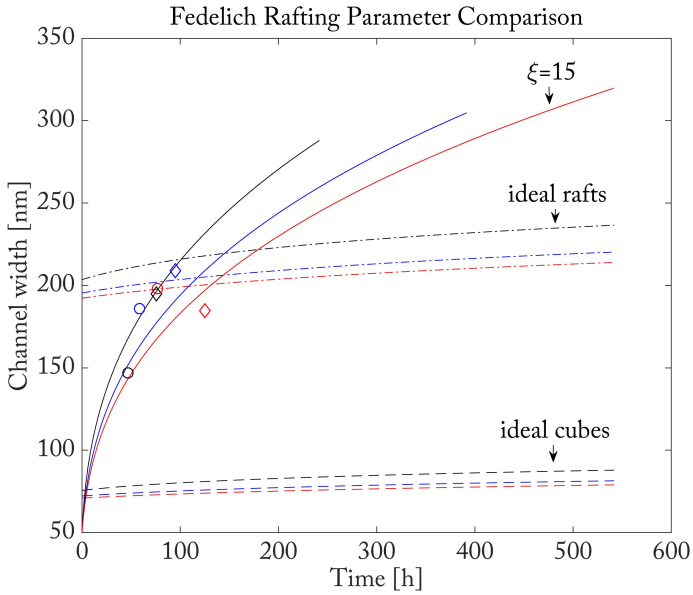

Fig. 4.40 Modelled non-isothermal γ-channel width evolution circles (solid lines) for the 9:3,18:3 and 27:3 test cycles in black, blue and red respectively. Correspondingly coloured is the experimental test data and times until 1% (circles) and 2% (diamonds) data plastic creep deformation. The dimensions for ideal fully rafted (dash-dot lines) and ideal cuboids (dashed lines) according to the formulas outlined by Fedelich *et al.* in [65] are shown.

decreasing upon cooling (see Figure 4.41b), whilst overall gradually increasing in γ-channel width with test time (see Figure 4.41a).

4.4.9 Conclusions on non-isothermal creep parameter modelling

Until the high temperature creep deformation can be observed *in situ* in superalloys, modelling this regime provides a valuable insight into the local micro-structural deformation mechanisms. Using established theory the key creep parameters have been estimated for non-isothermal creep cycling. This has been done by correlating the γ/γ' phase fraction evolution to the equilibrium phase fractions to estimate the theoretical effective temperature of the alloy at any given time during thermal cycling and then calculating the equilibrium creep parameter values of this theoretical temperature evolution.

As this approach is based on the thermal variation in equilibrium creep parameters, the magnitude of change in the parameters during non-isothermal cycling depends on the temperature dependence of the equilibrium parameters. As a result, solid-solution hardening (particularly in the γ'-phase) exhibits a very low non-isothermal variation, whereas γ-interdiffusion changes by one order of magnitude during the modelled thermal cycles.

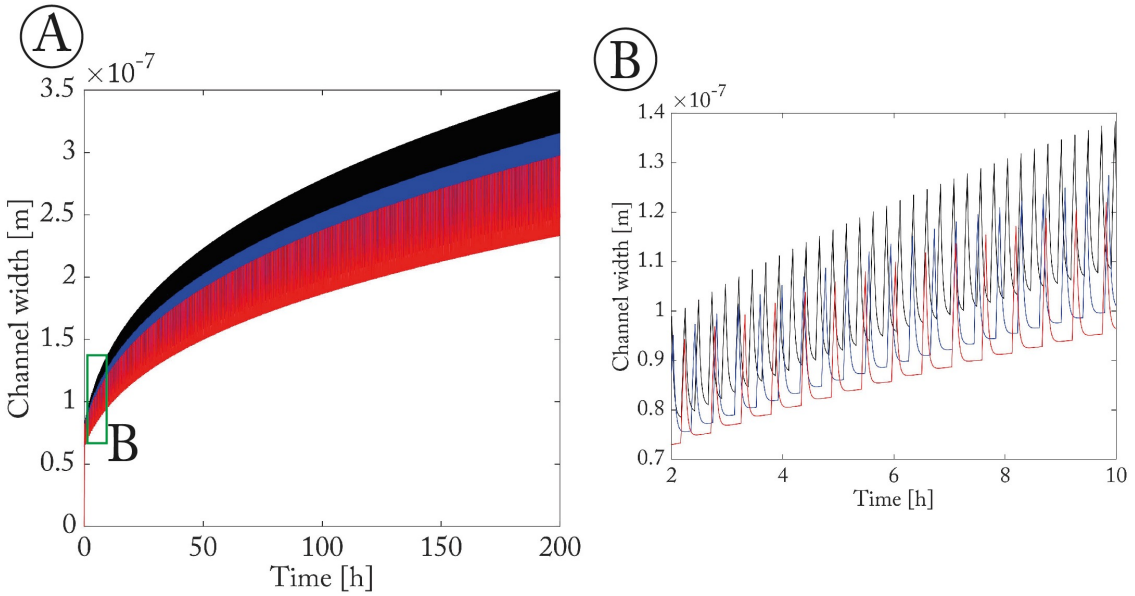

Fig. 4.41 Non-isothermal evolution of the CMSX-4 microstructure modelled for the 9:3, 18:3 and 27:3 test conditions plotted in black, blue and red respectively. Figure (B) is a close-up of the green box highlighted in (A) showing the microstructural evolution between individual cycles.

Comparing the two alloys investigated, CMSX-10 is estimated to have a lower phase fraction dissolution, a lower magnitude of interfacial lattice misfit, a higher Orowan backstress and higher γ'-critical resolved shear stress. Based on these trends, the dislocation activity in the γ/γ'-microstructure of the alloy CMSX-10 is projected to be considerably lower than in CMSX-4. Experimental results presented in Chapter 5 will investigate this claim.

4.5 Studying the location of dislocation glide

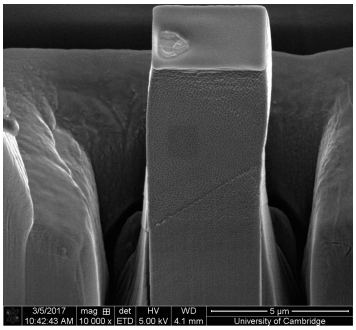

Fig. 4.42 Post-deformation SEM-micrograph of a micropillar with a deposited Pt-speckle pattern on its front face for DIC-analysis.

In an earlier study by the author (see [79]) it was argued that the arrangement of γ-channels to γ'-precipitates had an impact on the plastic response of the microstructure. Test samples were deformed under isothermal high temperature creep conditions (1050 °C and 150 MPa) and then examined using the SEM. The experimental data was then compared to simulations obtained with the isothermal creep model by Svoboda and Lukáš [195–199]. The study came to the conclusion that a wider γ-channel bordering on a narrower γ'-precipitate would likely result in the local plastic yielding of the latter phase.

In order to investigate this further and quantify the influence that the local γ/γ'-microstructure arrangement has on the overall plastic response, micro-pillars were manufactured, deformed and subsequently analysed using TEM, SEM and FIB-Tomography. During the study limitations in the analysis and testing became apparent such that the results obtained and presented in the following section cannot be used for the non-isothermal high temperature creep model in its current form. However, the results have been published in a joint publication with Jones *et al.* [100].

The micro-pillars were produced on a *Helios FIB-SEM* with the settings and procedure outlined in Chapter 3.1.3. The two pillars investigated were spaced 50 μm apart from each other and milled from a sample of fully heat treated CMSX-4. The distance between the pillars was large enough so that neither pillar influenced the plastic response of the other, whilst still being in the same dendrite region (considering a dendrite arm spacing of over 300 μm for this sample, see Figure 4.4). The sample had been cut within 2° certainty from the [001]-pole measured using X-ray Back-Laue reflection. The pillars were compressed at room temperature with the stress-strain response shown in Figure 4.43. The *Helios* pillar was further analysed to investigate the role of strain partitioning between the phases and its

three dimensional microstructure investigated using FIB-tomography. The *TEM* micro pillar was subsequently imaged and analysed using a TEM.

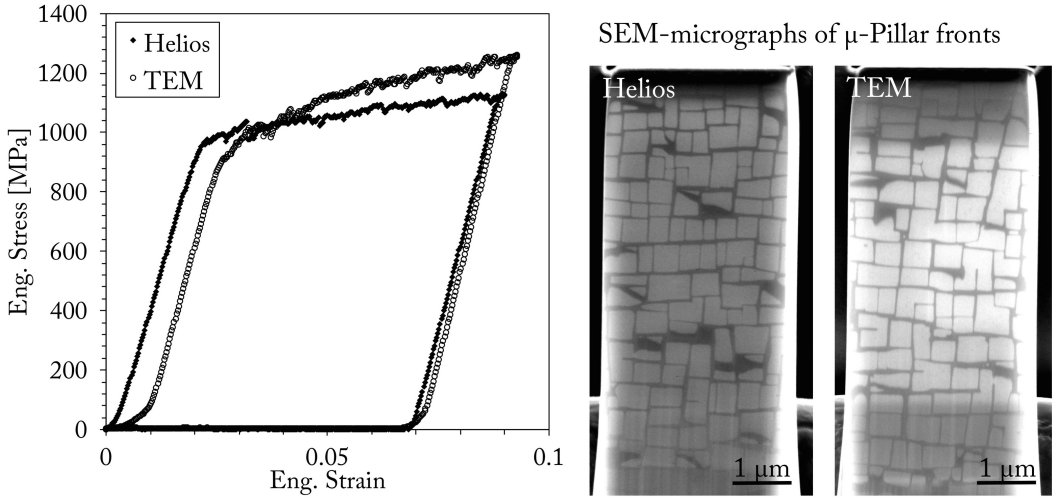

Fig. 4.43 Engineering stress vs. engineering strain curves plotted for the Helios and TEM analysed micropillars with their respective microstructures on the front face prior to deformation.

Plastic strain partitioning

The strain partitioning calculation published in this section was performed in collaboration with Jones to keep the analysis consistent with the other micro-pillars analysed in the joint publication [100]. The engineering stress versus engineering strain of the two pillars analysed in Figure 4.43 shows an identical elastic gradient for both pillars with a yield stress of 970 MPa. This result is $\sim$ 50 MPa above the quoted compressive yield stress and comparable to the tensile yield stress published by Tsuno *et al.* [211]. The cited study used conventional test equipment to investigate the asymmetry in compressive and tensile yield and found that these were comparable from room temperature up to the maximum investigated temperature of 750 °C.

A visible difference exists however, between the plastic response gradients of each pillar, resulting in a stress 151 MPa higher for the TEM-pillar at the point of unloading.

Following the digital image correlation laid out in Section 3.1.3 the resulting strain map is shown on the right of Figure 4.44. The colourmap corresponds to the maximum strain estimated (γ_{max}), showing distinctive slip bands across the top half of the pillar that align with the traces of the $\{111\} < 011 >$slip systems. The slip bands are spaced ~ 0.25 μm apart (more finely spaced than the precipitate size of 0.45 μm) and the slip band and direction

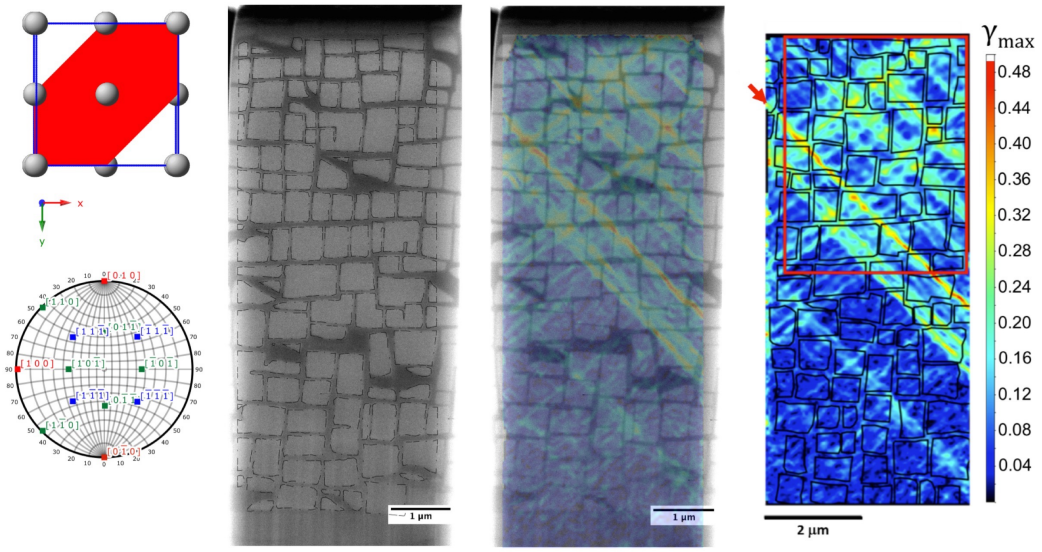

Fig. 4.44 [From left to right] Crystal orientation of the *Helios* analysed micropillar and pole figure, SEM-micrograph of the microstructure prior to deformation, overlay of the DIC-strain data, image of the DIC strain data with an overlay of precipitate outlines in black, the red frame indicates the area used to estimate the plastic strain partitioning.

with the greatest accumulated shear is marked by a red arrow. The shear strain varies along the slip bands, for instance between 0.32 and 0.40 in the case of the marked band, with no apparent strain difference between the two phases.

Using the area within the red box in Figure 4.44 the degree of strain partitioning was estimated between the maximum shear strain in both phases according to Equation 4.21 (see Section 3.1.3 for the parameter description).

$$p_{plastic} = \langle \gamma_{max} \rangle - \langle \gamma'_{max} \rangle \tag{4.21}$$

The strain partitioning difference for this pillar was calculated at $p_{plastic} = -0.0032$, indicating that the precipitate phase has strained slightly more than the matrix phase. This value was compared to a <011> oriented micro pillar of CMSX-4, where a value of $p_{plastic} = -0.0028$ was estimated [100].

These results provide evidence in support of recent neutron diffraction measurements [43] showing that the precipitate phase of CMSX-4 is the softer phase at room temperature. Furthermore, the relatively small difference between the values from the two differently orientated pillars suggests that the loading direction has no major effect on the partitioning of plastic strain under the tested conditions [100]. The low ratio of strain partitioning further highlights the good stress/strain coupling at the coherent γ/γ'-interfaces.

Effect of dislocation slip

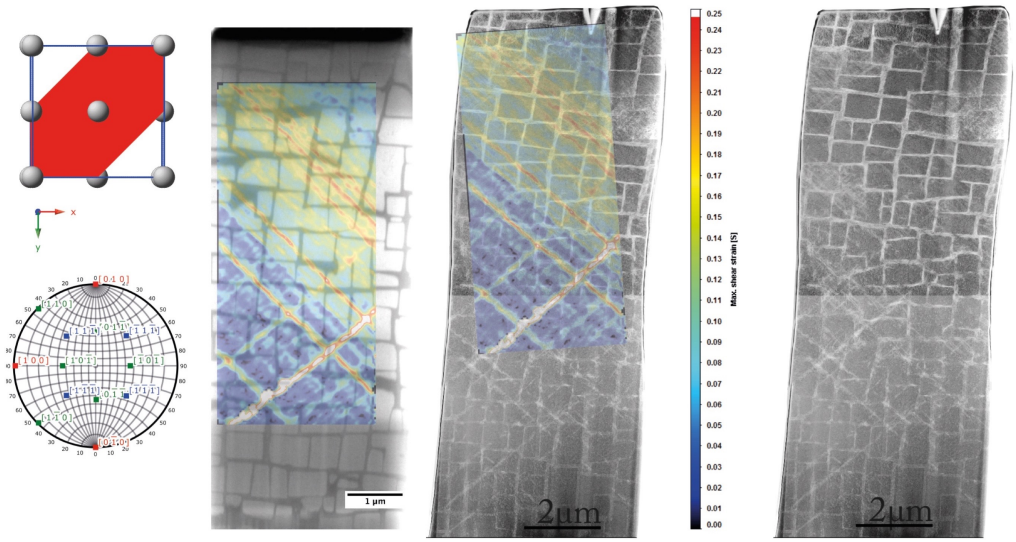

Fig. 4.45 [From left to right] Crystal orientation of the TEM analysed micropillar and pole figure; overlay of the DIC-strain data over the SEM-micrograph of the microstructure prior to deformation; overlay of the DIC-strain data over the TEM-micrograph of the microstructure post deformation; identical TEM-micrograph which was imaged using a [020] g-vector.

To assess the accuracy of the strain mapping technique, the *TEM* micro-pillars were prepared for further analysis using the FIB-SEM. The pillar was imaged and analysed using an *FEI Tecnai Osiris FEG* TEM (see Figure 4.45).

The TEM analysis displayed in Figure 4.45 shows a good agreement between the principal slip planes identified using DIC and those imaged using the TEM (see Figure 4.45 centre). In this temperature region Tsuno *et al.* [211] showed that the deformation of the alloy is caused by $\frac{a}{2} < 110 >$ dislocation pairs. This matched the orientation of the traces visible in Figures 4.44 and 4.45.

Looking more closely at the deformed pillar using TEM bright-field imaging (Figure 4.46) shows that the accumulated plastic deformation is macroscopically visible at positions such as site A marked in Figure 4.46. Furthermore, the dislocation density was proportional to the deformation activity in the particular region (compare region B and C respectively in Figure 4.46).

The subsequent TEM-EDX analysis of the pillar in Figure 4.47 compares two different regions of the microstructure. A region that has seen little deformation indicated by the DIC maps, located in the upper centre of the pillar and secondly, a region with significant

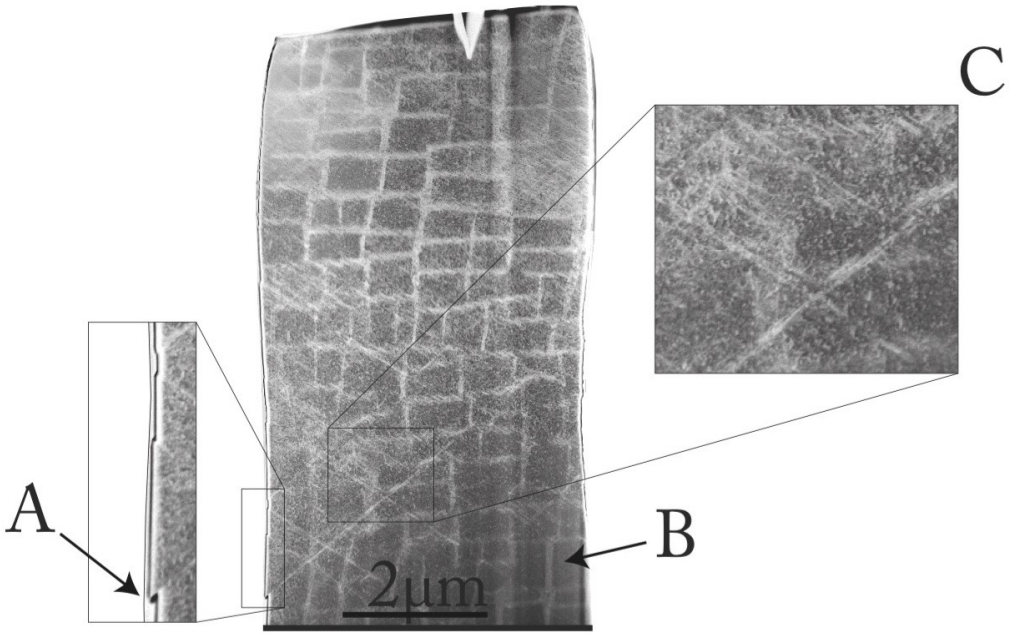

Fig. 4.46 TEM-micrograph of the micro-pillar imaged with a [111] g-vector indicating three regions of interest: (A) region of highest shear visible on the boundaries of the micro-pillar, (B) region of no dislocation activity, (C) shear bands passing through both phases of the microstructure without deflection.

deformation located in the left lower half of the pillar face. A qualitative comparison of key alloying elements (EDX-maps) is shown for both regions.

In the case of the lightly deformed region, well defined borders between the γ'-precipitate phase (rich in titanium, nickel and aluminium) and the γ-matrix (rich in chromium and cobalt) can be seen (see Figure 4.47 top), whereas for the highly deformed region a site of imbalance in the border is apparent in the composition plots. Located at the height of the horizontal γ-channel sloped at an angle of $\sim 45°$, a region of compositional imbalance caused by dislocation glide is seen. This region overlaps with a slip band that induced plastic deformation, displacing the pillar above the slip band slightly to the left in relation to the lower half of the pillar. The plastic deformation resulted in a layer of atoms in a ordered arrangement to be displaced beyond the borders of the precipitate interface prior to deformation. Due to the high strain rate and low diffusivity of the alloying elements at room temperature, atomic exchange via inter-diffusion can be ruled out. This chemical gradient induced into the microstructure is however assumed to be less important at high temperature creep conditions due to the high inter-diffusivity and low strain rates.

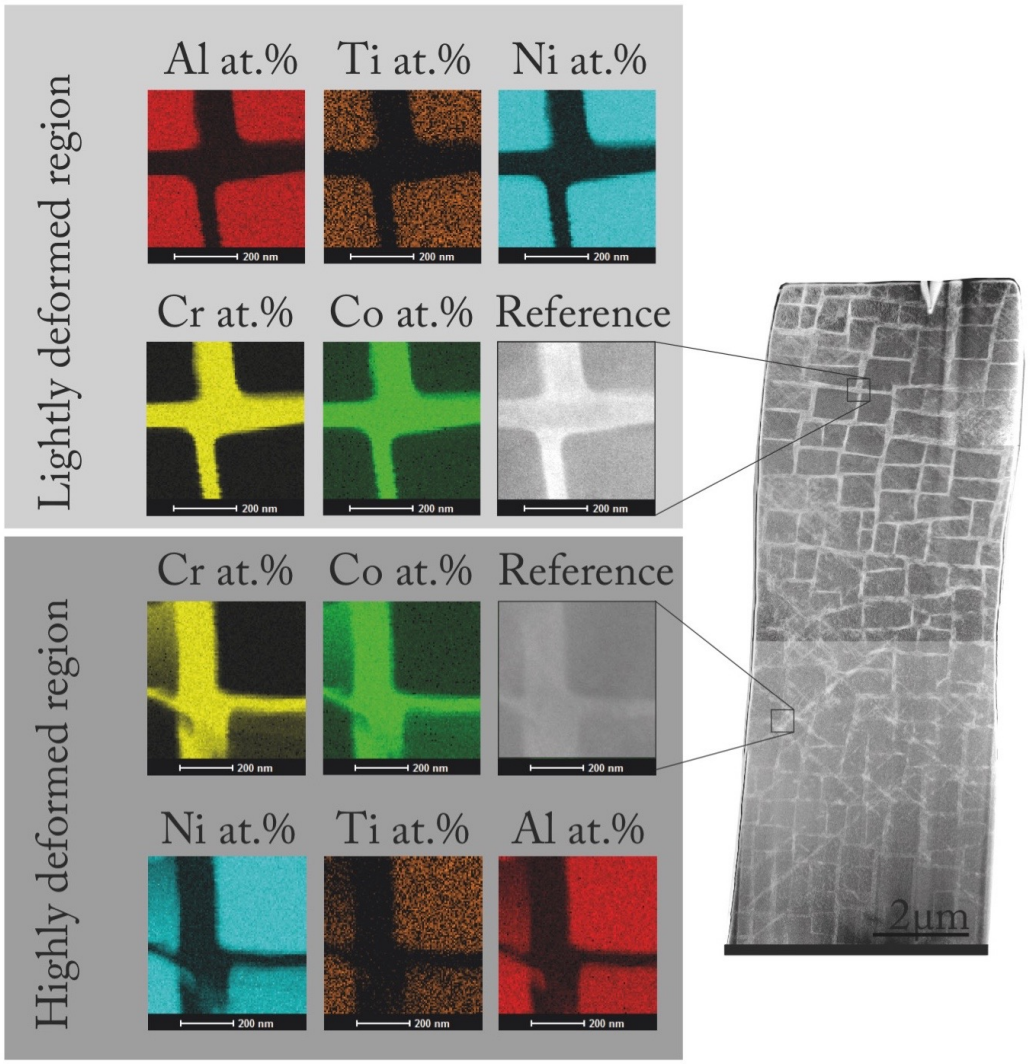

Fig. 4.47 TEM-micrograph from Figure 4.45 highlighting two regions deformed to different degrees with their respective qualitative EDX-analysis shown for five key alloying elements.

Influence of the microstructure on the dislocation slip

The *Helios* pillar was subsequently milled away in 50 nm slices and imaged after each milling step to generate a tomographic rendering of the three dimensional microstructure and its interconnectivity between γ'-precipitates. Earlier tomographic work [232] had studied the three dimensional connectivity between precipitates in the alloy PWA1497 (see Figure 2.18).

However, whilst the human eye can trace the interconnectivity between particles by comparing the slice numbers imaged in the same region by using the red reference line in Figure 4.48, it was not possible to enhance the dataset sufficiently to investigate it further

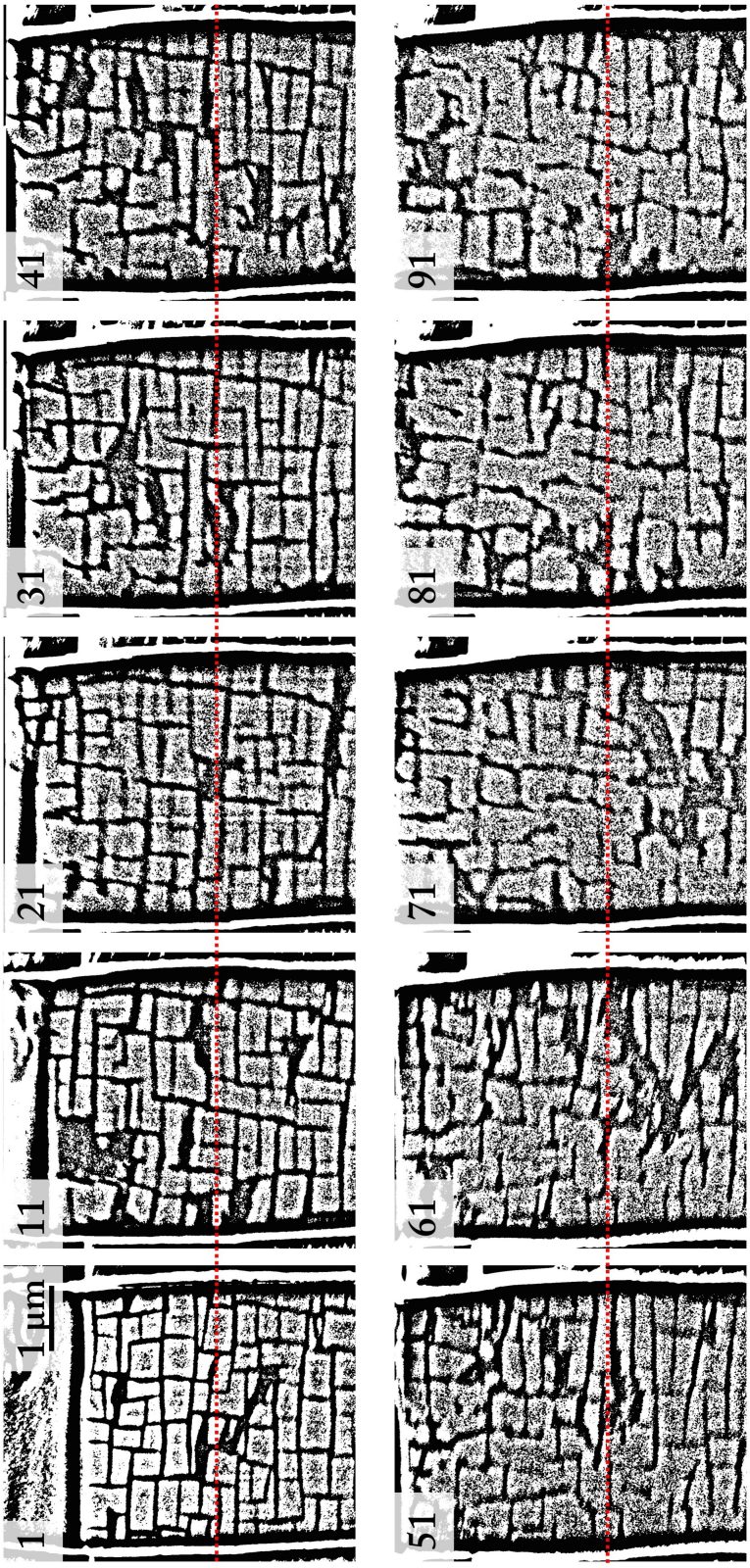

Fig. 4.48 Binarised SEM-micrographs of the micro-pillar front face during the tomographic slicing (slice numbers in top left corner and red horizontal line for reference).

using computer programming. In order to map the relation between slip bands and the 3D γ/γ'-microstructure, further work is required to enhance the signal to noise ratio after each milling step by including an additional low current cleaning step prior to the image acquisition.

Conclusion and further work to map the micro-structural influence on deformation

The observed difference in the stress-strain response between two micro-pillars indicates that the γ/γ' micro-structural arrangement impacts the spacing of slip bands and the dislocation deformation activity on them. Due to limitations in FIB-tomography rendering, the impact of the microstructure could not be quantified and the location of slip band formation could not be predicted from this dataset. Using DIC the local strain partitioning across the microstructure could be calculated for low temperature deformation and high strain rates. In this regime, no significant relationship between the loading direction and the ratio of strain partitioning could be found.

Chapter 5

Non-isothermal Creep Response

This chapter will lay out the results and analysis of the non-isothermal creep experiments performed. The discussion of these results builds on the parameter modelling described in the previous chapter and further provides the experimental verification required for the non-isothermal creep model laid out in Chapter 6.

The non-isothermal creep tests performed consisted of a continuous four segment temperature cycle of a variable holding time at the base temperature (900 °C), a heating segment, a three-minute hold at high temperature (1050 °C) and cooling to base temperature (see Figure 3.2). Hence the three cycle times differed only by the holding time at the base temperature, which were 9, 18 and 27 minutes.The three different test conditions are thus further referred to as 9:3, 18:3 and 27:3. The heating and cooling rates were kept constant at 120 $[\frac{K}{min}]$. Each cycle type was interrupted at four stages of creep life: just after the first heating cycle, and after heating cycles corresponding to 0.5%, 1% and 2% plastic strain. The test parameters, set-up and equipment are laid out in detail in Sections 3.2 and 3.3.

The chapter is structured into five sections. Firstly, the impact of different thermal cycling rates on the non-isothermal creep response in the alloy CMSX-4 is laid out. In the second section, the influence of the alloy composition is investigated by describing the creep response for the alloy CMSX-10K. In the third section the chemical composition gradients across the γ/γ'-interfaces resulting from the non-isothermal tests are investigated. The fourth section investigates the presence of tertiaries in both alloys studied. The final section then discusses the interdependence of these four parameters and their overall significance on the non-isothermal creep deformation.

5.1 The influence of different cycling rates on CMSX-4

To obtain plastic strain creep curves comparable to isothermal creep tests, only the base temperature strain data was extracted from the measured sample elongation (this approach has been outlined by Cormier *et al.* in [35]). The mean elongation per cycle step was then calculated and the dataset fitted to a best fitting polynomial function (see Figure B.1 in the appendix). The calculated accumulated creep strain over the test time for the 2% strained samples is plotted as curves in Figure 5.1a for the three different cycle times: black line corresponding to 9, blue to 18 and red to 27 minutes at base temperature. The end points for the interrupted tests (to 0.5% and 1% plastic strain) are also shown in the corresponding colour. Comparison between the three interrupted tests shows good agreement for the 9 minutes at the base temperature condition. The 18-minute test plotted to 2% strain deformed faster than the 0.5% and 1% tests. Similarly, for the 27-minute condition the 0.5% test deformed faster than the 1% and 2% tests.

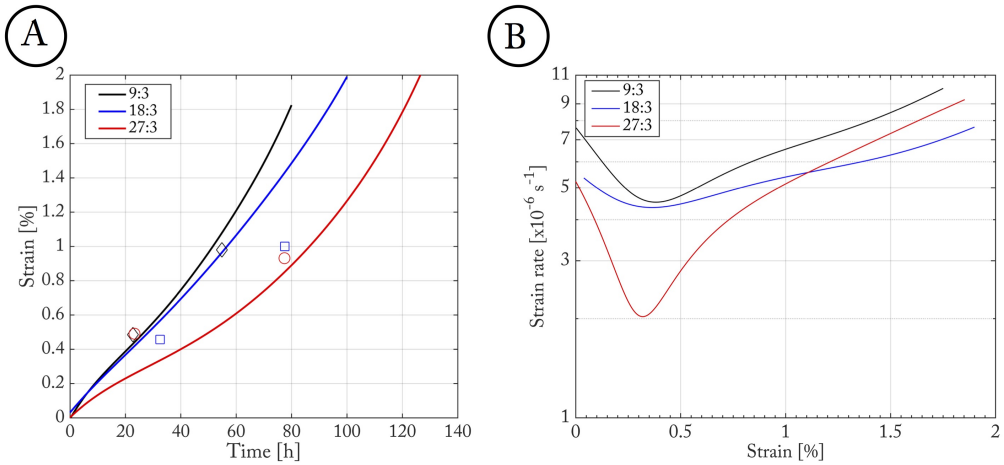

Fig. 5.1 (A) Plastic strain accumulated over time for the three non-isothermal test conditions presented in Figure 3.2: black (9:3), blue (18:3), red (27:3). Creep curves from experiments taken to 2% strain and end points taken from the interrupted tests in corresponding colour to the curves. (B) Logarithm of strain rate over strain derived from Figure 5.1(A).

Figure 5.1b shows the derived creep strain rate (s^{-1}) over the accumulated strain from the curves in Figure 5.1a. The overall strain rate decreases for longer cycle times. Further, Figure 5.1(b) indicates that the minimum strain rate across the non-isothermal tests is reached around 0.35% strain for all tests. This minimum strain rate is of the same order of magnitude as isothermal test data of CMSX-4 at 1050 °C and 170 MPa [166], if extrapolated to the load applied in this study and more than four orders of magnitude faster compared to isothermal data from 900 °C [166].

The remarkably high strain rate of the non-isothermal test cycles is further illustrated in Figure 5.2 where these tests are compared to isothermal data for CMSX-4 adapted from literature. Figure 5.2 plots isothermal data acquired by Cormier at 1050 °C and 200 MPa (inverted triangles) as well as isothermal data acquired by Matan *et al.* [166] at 1000 °C and 200 MPa (circles) and 950 °C and 185 MPa (squares). Considering that the mean temperatures for the 9:3, 18:3 and 27:3 test cycles, were 944 °C, 927 °C and 920 °C respectively, when using an average lifetime temperature approximation one would have expected these test cycles to be most similar to an isothermal test at 950 °C. A more realistic approximation is assuming that only the peak temperature regime contributes to the strain accumulation. As the 9:3 regime spends $\frac{1}{5}th$ and the 27:3 test $\frac{1}{10}th$ of their test times at 1050 °C, one would assume 1.5% strain to be reached after 200 h and 400 h for the 9:3 and 27:3 tests respectively. However, the non-isothermal tests are significantly faster than these models predicted, displaying strain rates that are slightly faster than the isothermal dataset at 1000 °C and slower than the dataset acquired at 1050 °C and 200 MPa. The strain rates are also much more similar between the three non-isothermal tests than the time at peak temperature ratio would suggest. Such strain rates are remarkable as the tests spent very little time at the peak temperature. The ratios between base and high temperature regimes for the different test cycles will be further illustrated below and in Table 5.1.

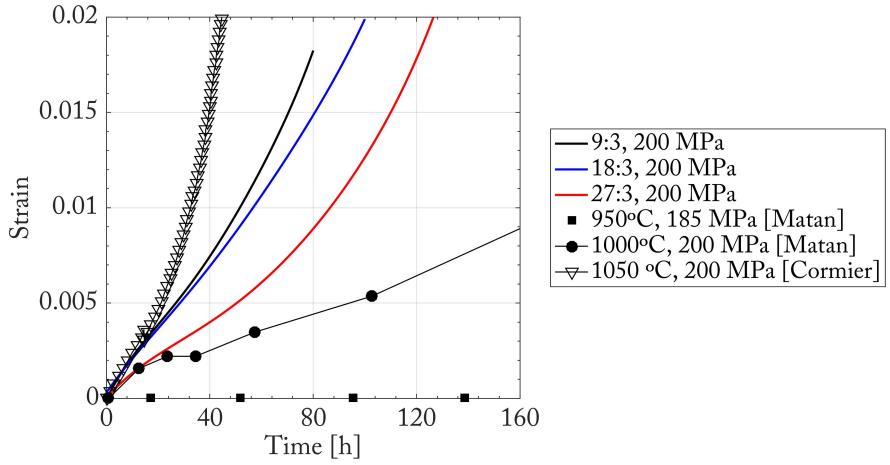

Fig. 5.2 Comparison of the non-isothermal creep curves from Figure 5.1a to isothermal data of CMSX-4. Isothermal data for 950 °C 185 MPa (squares) from Matan *et al.* [166], 1000 °C and 200 MPa (circles) from Matan *et al.* [166], and 1050 °C and 200 MPa (triangles) courtesy of J. Cormier.

Looking at 5.1a a degree of randomness is visible between the test results of the 18:3 and 27:3 series. Scatter in creep test data has been widely published (e.g. see Figure 2

in [166]) and is attributed to small offsets in single-crystal orientation as well as chemical composition and porosity originating from the casting process. The impact of the compositional variation on key creep parameters has been presented in Section 4.2. Due to the small sample dimensions used, these chemical variations have a bigger impact on the overall creep response.

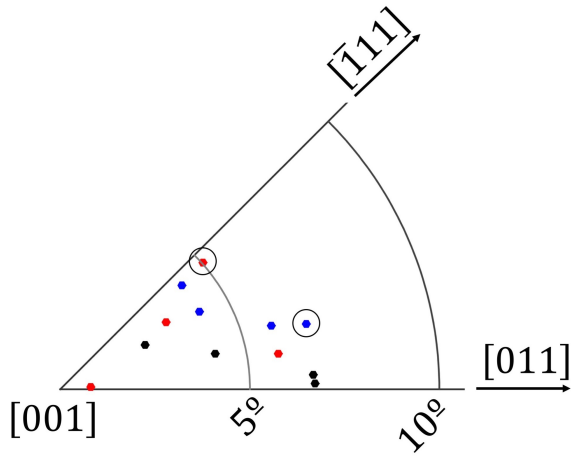

Fig. 5.3 The single-crystal orientational offset measured using Back-Laue reflection for the CMSX-4 test series, the colour of the data points correspond to: 9:3 in black, 18:3 in blue and 27:3 in red.

Using Back-Laue reflection (see Section 3.3.5) the offset of the individual tests was recorded post testing and is plotted as an inverse pole figure in 5.3. Whilst all test pieces were within the allowed tolerances, variation existed between the test samples. The blue and red encircled data points correspond to the above highlighted 2% 18:3 and 0.5% 27:3 tests respectively. The presented figure includes a 2° offset variation from the [001], due to the tolerances of the machining process. However, Matan *et al.* [138] have argued that the orientation dependence decreases at higher temperatures and in the isothermal tertiary creep regime, which is primarily driven by the magnitude of the applied stress. Studies are however required to investigate whether this finding can be translated directly to the high temperature non-isothermal regime.

Table 5.1 illustrates the relationship between the different cycle types and the times spent at base and peak temperature condition, as well as the total number of cycles for each test. The table highlights that, in order to accumulate the same amount of plastic strain, the three tested conditions have undergone very different numbers of cycles and thus spent different lengths of time at the maximum test temperature. The 9:3 test condition underwent the most cycles and thus spent the most time at peak temperature (just above $1/5^{th}$ of the total test

Table 5.1 Comparison of the three test cycle condition times for the CMSX-4 series at peak (1050 °C), base (900 °C) and total number of cycles up to each interrupted stage (single cycle, 0.5%, 1% and 1.8% accumulated plastic strain).

Test cycle / plastic strain		Single cycle	$\sim 0.5\%$	$\sim 1\%$	1.8%
9:3	$t_{peak}[h]$	0.05	4.7	11.35	16.42
9:3	$t_{base}[h]$	0.15	14.1	34.05	49.26
9:3	N_{cycles}	1	94	227	328.40
18:3	$t_{peak}[h]$	0.05	4.15	9.9	11.89
18:3	$t_{base}[h]$	0.30	24.9	59.7	71.31
18:3	N_{cycles}	1	83	198	237.70
27:3	$t_{peak}[h]$	0.05	2.15	7.15	11.13
27:3	$t_{base}[h]$	0.45	19.35	64.35	100.13
27:3	N_{cycles}	1	43	143	222.50

time until 1.8% plastic strain). In comparison, the test with the slowest strain rate and longest creep life, 27:3 spent below $1/10^{th}$ of lifetime at peak temperature. As a result, the 9:3 test has the lowest deformation per cycle but the highest strain rate overall, whilst the 27:3 condition accumulates the most strain per cycle. Similar relationships with varying time at base temperature condition have been published by Raffaitin *et al.* [163] and Giraud *et al.* [77] for thermal cycles to 1150 °C.

5.1.1 Evolution of the microstructure

As the test pieces were machined from the same cast bar a similar microstructure was the starting point for each test condition. Following a single heating cycle, no microscopically visible alteration to the cuboidal microstructure had occurred (see Figure 5.4). With 0.5% plastic strain accumulated in the test pieces, the effects of γ'-rafting and deformation became visible across all three conditions (see Figure 5.4). The progression of rafting is however different between the test conditions. Fully established rafts can be seen for the 9:3 condition only, whilst condition 18:3 is not fully rafted and condition 27:3 even less so. This means that the creep minimum displayed in Figure 5.1b does not coincide with the completion of γ'-rafting, as observed for isothermal creep in CMSX-4 [166]. This suggests that the creep minimum under these non-isothermal conditions is likely to be associated with other effects. Another striking difference from isothermal tests (see [140]) is the disruption to the normal planar rafting process leading to multiple connections between γ'-layers. Evidence of this is that all three conditions exhibit a number of angled side connections, the number increasing with time spent at base condition.

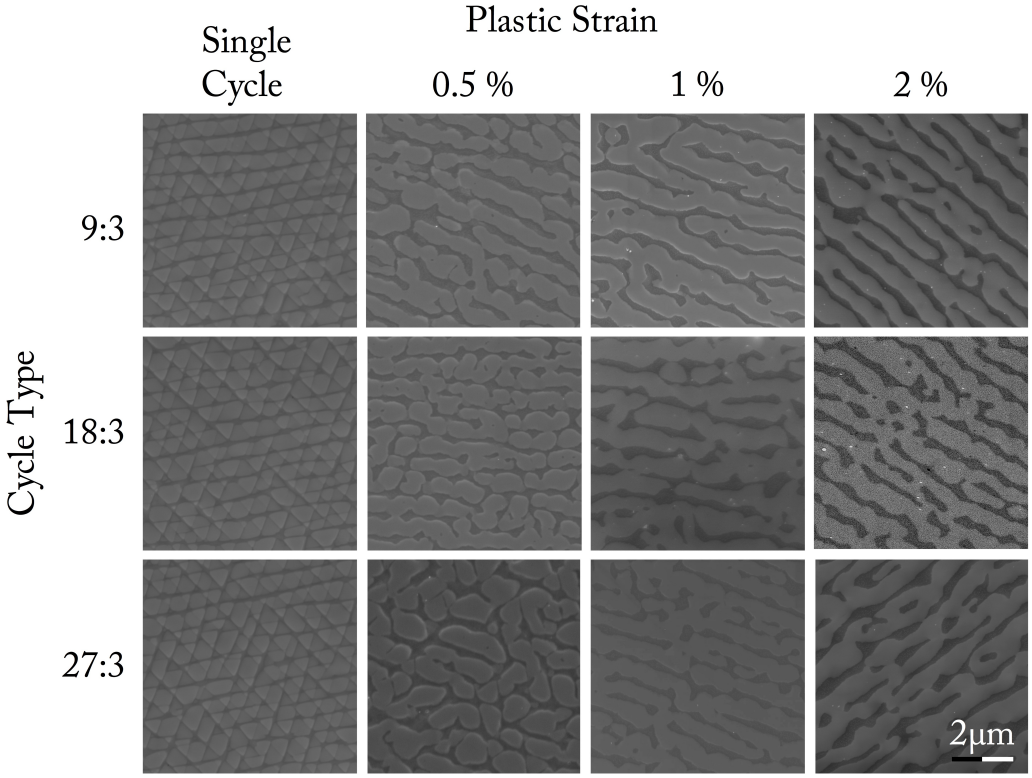

Fig. 5.4 SEM (In-Lens)-micrographs (5kV). TEM-foils cut on the (111)-planes. Figures are arranged by cycle type (9:3, 18:3 and 27:3 top to bottom) and strain accumulated (single cycle, 0.5%, 1% and 2% plastic strain left to right). Dark phases correspond to the γ-matrix and bright ones to γ'-precipitates.

Table 5.2 Special connectivity number for the dendritic (DC) and inter-dendritic (IR) regions of the 1% and 2% strained samples for the three conditions tested of the alloy CMSX-4. See text for further details.

Test condition	Region	$1\% N_A(\gamma')[\mu m^{-2}]$	$2\% N_A(\gamma')[\mu m^{-2}]$
9:3	DC	-0.163	-0.485
9:3	IR	-0.255	-0.460
18:3	DC	-0.085	-0.154
18:3	IR	-0.154	-0.236
27:3	DC	-0.116	-0.505
27:3	IR	-0.113	-0.582

After 1% plastic strain, γ'-rafting is complete for all three conditions. The number of out of plane connections has resulted in islands of γ-matrix indicating the onset of local topological inversion. The level of topological inversion was quantified by Cormier in the joint publication [179], using the approach published by Caron *et al.* [29]. The special

connectivity number $N_A(\gamma')[\mu m^{-2}]$ was calculated from SEM-images of all the three tests interrupted at 1% and 2 % plastic strain, imaged in the inter-dendritic and dendritic region (see Table 5.2). According to Caron *et al.* [29] $N_A(\gamma')$ is equal to the number of connections γ'-precipitates have to the γ-matrix per area. In a fully heat-treated state, the γ-matrix connects predominantly to the γ'-precipitates and the resulting special connectivity number is positive. A negative $N_A(\gamma')$ value then describes a totally interconnected γ'-phase (i.e. topologically inverted). Evidenced by the calculated negative special connectivity numbers, all three test conditions are topologically inverted after 1% plastic strain and have progressed further in the level of topological inversion with 2% plastic strain. Comparing the results between test types, the 27:3 tests exhibit the highest connectivity numbers at both interrupted stages. The connectivity however does not scale with the total test time, as the 18:3 test resulted in the lowest magnitude of connectivity than the two other test cycles. The connectivity thus also depends on the dissolution and precipitation kinetics, which differ between the 9:3 and the longer test conditions (see Section 4.4.1). As discussed in Section 4.4.1, the 9:3 test is exposed to a continuous metastable phase fraction regime, which results in an enhanced connectivity of precipitated tertiaries compared to the longer tests.

5.1.2 Correlating the creep minimum to diffusivity

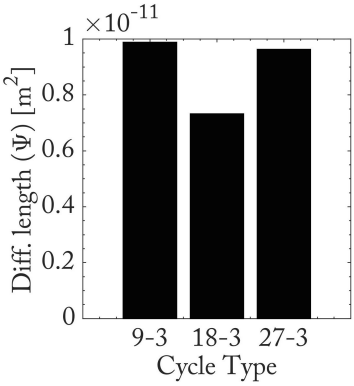

Fig. 5.5 Diffusion lengths to the non-isothermal creep minimum.

To investigate if the experimentally observed strain rate minima in Figure 5.1 could be correlated to diffusion driven mechanisms, these were further investigated.

Using the D_{eff} cycles for all three test conditions and multiplying it by the number of cycles required to reach the creep minimum in each test (from Figure 5.1) the diffusion lengths required to reach the minimum ($\Psi[m^2]$) was calculated and are plotted in Figure 5.5. Despite the different cycles and the different times needed to reach the respective creep

minima, the resulting diffusion lengths are very similar across all three test conditions. The difference between the 9:3 and 27:3 as well as the 18:3 to 27:3 cycles amounts to $\Delta 2.1$ and $\Delta 16.1$ cycles respectively. This calculation highlights, that the creep minima visible in Figure 5.1 are strongly correlated to the effective diffusivity or a diffusion driven mechanism.

5.1.3 Dislocation analysis

To verify the assumptions made for the non-isothermal creep model in Chapter 6, and to understand the implications of varying the cycling rate on a micro-structural level, a dislocation study was undertaken, analysing the deformation structures of the three test cycle types after each interrupted stage (single cycle, 0.5%, 1% and 2% plastic strain).

The single cycle

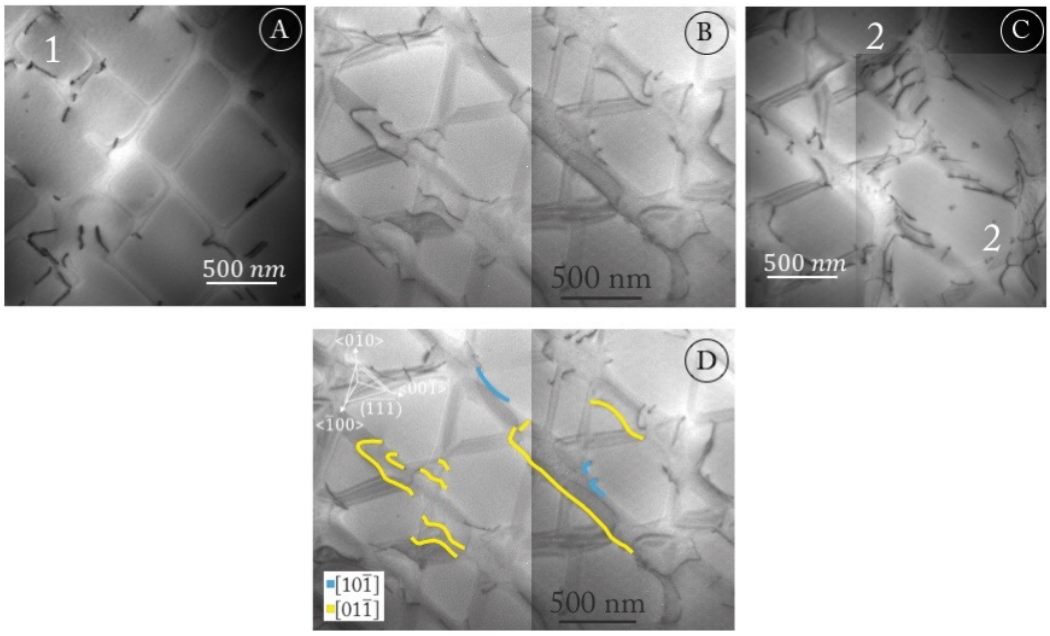

Fig. 5.6 TEM-micrographs imaged after the first heating cycle. a) BF-image of the 9:3 cycle imaged on the (001) zone axis, b) BF-image of the 18:3 cycle imaged on the (111) zone axis, c) BF-image of the 27:3 cycle imaged on the (111) zone axis and d) BF-image from (b) with $\pm 2b/a$ vectors and their corresponding dislocations shown.

Following the first heating cycle, the dislocation activity is localised to areas of low γ'-volume fraction and high interfacial misfit (dendritic cores) and inter-dendritic boundaries (sources of dislocations) as seen in a similar regime by J*á*come *et al.* [6].

Tilting to different imaging conditions and using standard visibility criteria (see [55, 7]) revealed two active slip systems (see Figure 5.6b). Most dislocations were observed to have bowed into the γ-channels, pinned by the γ'-precipitate interfaces (see around marker 1 in Figure 5.6a). The interfacial dislocations of different Burgers vectors (identified in Figure 5.6b as type $\vec{b} = \pm\frac{a}{2}[10\bar{1}]$ and $\vec{b} = \pm\frac{a}{2}[01\bar{1}]$) are further seen to interact, beginning to form interfacial dislocation networks (see southeast of markers 2 in Figure 5.6c). No substantial difference could be observed between the three different cycle types following the first heating cycle.

Dislocation structures in the falling strain rate regime

With further strain accumulation, continuous interfacial dislocation networks are created. Even in the lowest strain rate test condition (27:3) these networks are established throughout the microstructure after 0.5% accumulated strain (see Figure 5.7).

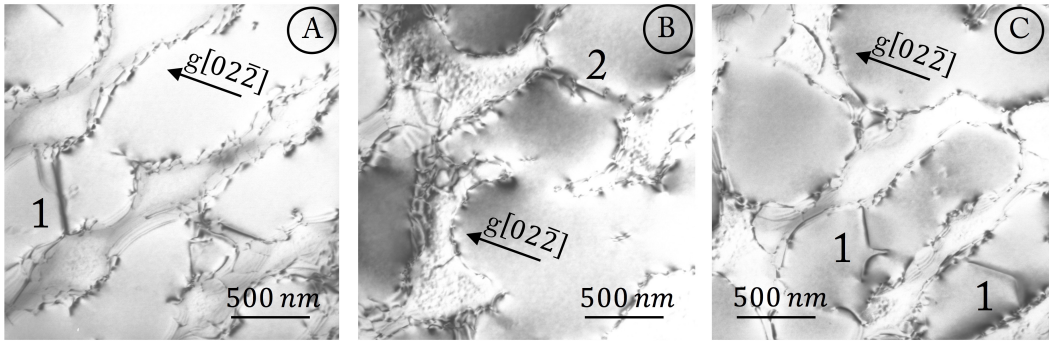

Fig. 5.7 BF-TEM-micrographs of 27:3 test cycle after 0.5% plastic strain imaged on the active (111)-plane in three different regions of the same sample (a,b,c).

Closer inspection of the interfacial dislocation networks under different imaging conditions revealed that two different types of networks are present. In Figure 5.8a west and southeast to position 1, networks of single dislocations along the interfaces can be seen. Tilting the specimens to different two-beam conditions and using standard visibility criteria revealed that these were classical interfacial networks of edge character as shown in Figure 5.18 (see Figure 2.13 taken from Lasalmonie *et al.* [114] for dislocation reactions and Burgers vectors). In the same figure, southeast of position 2 a region of the interfacial network can be seen that consists of a paired dislocation of the same Burgers vector side by side. These dislocation pairs were observed for all test conditions (see Figure 5.8a for the 27:3 and Figure 5.8b and c for the 9:3 test conditions). Using WBDF, the distance between two such

dislocation pairs was estimated from positions such as 1 highlighted in Figure 5.8b, varying between $8-15$nm in width. This proximity suggests, that where the dislocations lie in the γ'-phase an APB-fault between the pairs stabilises the configuration. This will be further discussed in Section 5.3 and the discussion of this chapter.

Such paired interfacial dislocation networks of type $\vec{b} = \pm\frac{a}{2}[1\bar{1}0]$, $\vec{b} = \pm\frac{a}{2}[10\bar{1}]$ and $\vec{b} = \pm\frac{a}{2}[01\bar{1}]$ dislocations have been observed by Ru *et al.* [173] in the single-crystal superalloy IC11B following isothermal creep at 1100 °C and 100 MPa. However, the dislocation configurations observed by Ru *et al.* [173] were identified as pure screw dislocations. However, mixed and screw dislocation do not alleviate the interfacial misfit and are thus not stable on the γ/γ'-interfaces and transform into edge dislocations (see Long *et al.* [128]). The dislocation characterisation and conclusion for the paired screw network formation presented by Ru *et al.* thus goes against the established theory and findings and is thus highly unlikely.

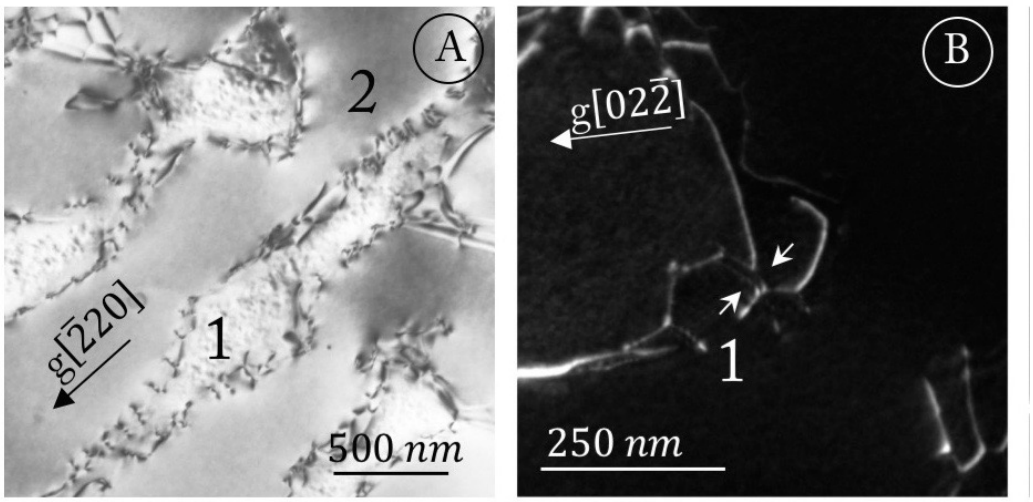

Fig. 5.8 TEM-micrographs of dislocation networks; a) BF-image of 27:3 test cycle after 0.5% plastic strain; b and c) WBDF-images of 9:3 test cycle after 1% plastic strain; imaged on the active (111)-plane.

The 0.5% strained samples have been interrupted just past the creep minimum strain rate (see Figure 5.1b) and exhibit established dislocation networks on all interfaces even for the longest base temperature cycle condition (see Figure 5.7 and 5.8a). In addition to this, a mode of γ'-deformation shown northeast of positions 1 in Figures 5.7a and c appears. Using different imaging conditions (see Figure 5.12a and b), these consist of superdislocation pairs of two dissimilar Burgers vectors. These paired dislocations are two different $\frac{a}{2}\langle 110\rangle$ dislocations with a net Burgers vector of $a\langle 100\rangle$ which remain closely coupled, because they require an APB between them, but with distinct cores. These paired dislocations are

only stable in their tight proximity configuration in the γ'-phase and unzip upon entering the γ-matrix as shown at position 1 in Figure 5.9.

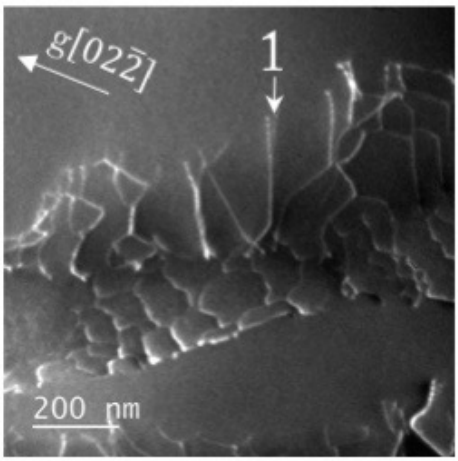

Fig. 5.9 WBDF-TEM-micrograph of a 9:3 test cycle after 2% plastic strain imaged on the active (111)-plane. At position 1 a coupled in γ' is marked that uncouples as soon as it enters the γ-matrix.

The formation and configuration of these dislocation pairs has been extensively studied by Eggeler *et al.* [55] in the superalloy CMSX-6 deformed at 1025 °C and 85 MPa loaded in shear, as well as in CMSX-4 at 1020 °C and 80 MPa by Srinivasan *et al.* [190] and others [174, 110, 58].

The prevalence of different modes of γ'-shearing under isothermal creep at 1020 °C and 160 MPa for the second generation superalloy LEK94 after 2% strain was studied by J*á*come *et al.* [7]. They found, that for [001] creep deformation the principal mode of γ'-deformation was by such $a\langle 100\rangle$ dislocations, with only $3/16$ of all superdislocations in the γ' being of $a\langle 110\rangle$ type.

Regime of the rising strain rate

Past the minimum creep rate, the strain rate increases continuously. Comparing the creep strain with the microstructure evolution in Figure 5.4, this stage seems to be driven by γ'-morphology, i.e. rafting, coarsening and local topological inversion. The process of isothermal γ'-rafting at the peak temperature has been published for this alloy by Reed and Matan *et al.* [166, 140], showing that the creep minimum at 1050 °C and 170 MPa is reached after accumulating 0.4 % strain. Looking at Figure 5.4, the 9:3 test condition has completed rafting under cyclic creep conditions at a comparable accumulated creep strain, whereas the 18:3 and 27:3 conditions complete γ'-rafting at a later time and with more accumulated

strain. Accounting for the time each test condition spent at 1050 °C, it becomes clear that the process of rafting during cyclic creep was completed whilst spending a significantly shorter time in the rafting regime, compared to an isothermal test.

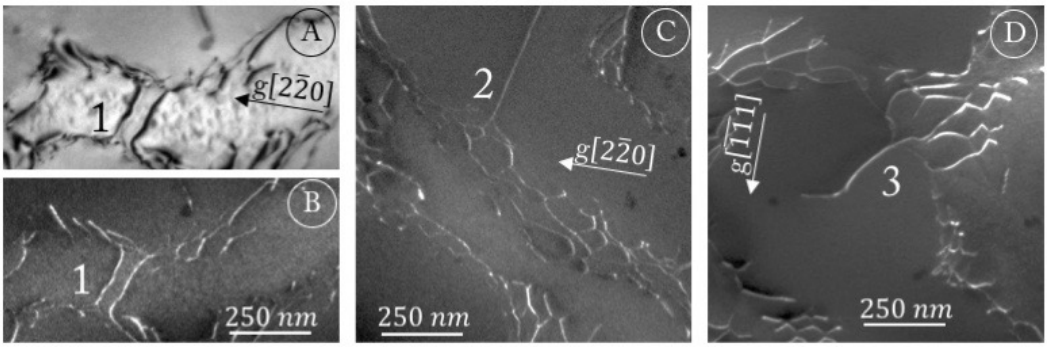

Fig. 5.10 TEM micrographs of the 9:3 test cycle after 1% plastic deformation imaged on the active (111)-plane with a) BF-image and b) WBDF-image of the same region as in a); c) WBDF-image of a new region with the same tilt and d) WBDF-image tilted to a new imaging condition as referenced.

Following the initial incubation time required for the glide-climb formation reaction of Eggeler-type dislocation pairs, these dissimilar Burgers vector pairs can shear the γ'-particles without creating an APB-ribbon (see Eggeler *et al.* [55]). As Eggeler *et al.* pointed out, the formation by climb and glide occurs in the γ-phase prior to shearing. The dislocation pair then consists of two narrowly spaced dislocation cores that can only be distinguished by looking at their separation on the γ/γ'-interface [55]. This can be seen in Figure 5.10a and b, showing most likely two dislocation pairs (four dislocations in total numbered in Figure 5.11) having formed in the γ-matrix east of position 1. As these dislocation pairs were seen from the 0.5% strained samples onwards it is suggested the incubation time for Eggeler-type formation overlaps with the strain necessary to reach the minimum creep rate.

With a net Burgers vector of $a\langle 100\rangle$, these Eggeler-type dislocations are formed from and attached to the $\langle 100\rangle$ and $\langle 010\rangle$ dislocation networks upon shearing through the precipitates (see Figure 5.10c and d positions 2 and 3 respectively). The dislocation motion through the precipitates thus has to overcome the interaction energy between the dislocations and the interfacial networks. Shearing dislocation pairs bound to paired dislocation networks need to remove a single dislocation from each of the different pairs in the 'paired' interfacial network. This requires further energy, such that dislocations not exhibiting the necessary uncoupling energy lie on top of each other (as in the case of 2 pair dislocations at position 3 in Figure 5.10d and at position 2 in 5.12c). When bound to paired networks on both sides of the precipitates, the dislocations exhibit very straight dislocation lines (see position 1 in

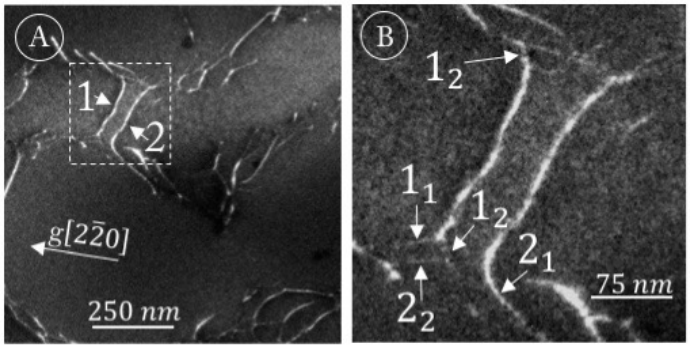

Fig. 5.11 TEM micrographs of the 9:3 test cycle after 1% plastic deformation imaged on the active (111)-plane with WBDF-image of the same region as in 5.10a) magnified. The splitting ends of the dislocations on the γ/γ'-interfaces are referenced.

Figure 5.7a, 2 in Figure 5.10c and 3 in Figure 5.12c) indicating that these dislocation lines have sufficient time to adopt their low energy configuration. Moreover, upon breaking away from the interfacial networks, the γ'-shearing dislocations leave behind a distorted network which, until restored and depending on the dislocations Burgers vector, facilitates easier movement through this area.

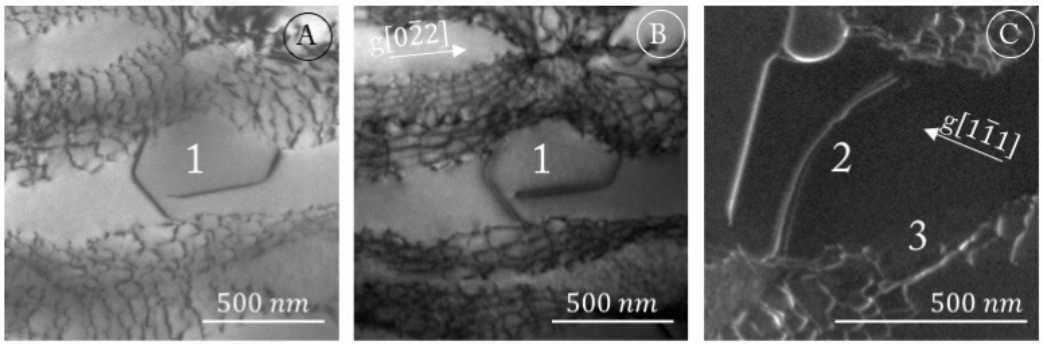

Fig. 5.12 TEM micrographs of the 9:3 tests imaged on the active (111)-plane after 2% accumulated plastic strain. a) BF-image imaged on the (111)-zone axis; b) BF-image of the same region as in a) tilted to the indicated two-beam condition; c and d) WBDF-image of new regions.

After 1% plastic strain, local topological inversion is thought to further add to the creep acceleration, by embedding interfacial dislocation networks into the γ'-phase. An example of this process is shown in Figure 5.7b and 5.12c at positions 2 and 3 respectively. As these absorbed networks are densely packed due to their pairs, the climb distance required to form Eggeler-pairs is small. Thus, these absorbed network dislocations are assumed to be able

to pass through γ' by shear and climb, once they have overcome their binding energy to the networks.

Comparing the three test conditions, the mobility of dislocations in the γ'-phase seems to be proportional to the observed strain rate, with the 9:3 condition showing the highest density of dislocation pairs in γ'. This is evidenced by a number of dislocation interactions forming between different Eggeler-pairs within the γ' for the 9:3 test (see top left of Figure 5.12c). Thus, in line with similar observations by Srinivasan *et al.* [190], γ'-shearing by glide and climb of interfacial dislocations is proposed as the rate determining deformation factor for the conditions studied.

5.2 Investigating the influence of alloy element composition

Three additional non-isothermal creep tests (single cycle, to 0.5% and 2% plastic strain) were performed using the alloy CMSX-10K supplied by *Cannon-Muskegon Corp., USA* with a 18:3 cycle on the same experimental set-up (see Section 3.2). The post-creep orientational offset to the [001] was recoded using Back-Laue reflection (see Section 3.3.5) and the resulting orientational scatter is plotted as an inverse pole figure in 5.13. The light green, yellow and orange datapoints show the single test, 0.5% and 2% strained test respectively. Although a significant scatter exists between the tests (the three samples did not originate from the same castbar), the maximum recorded offset was within the required tolerances.

The resulting creep curves for the 0.5% and 2% strained tests are plotted in Figure 5.14a. In yellow the acquired raw data points are shown for the 0.5% strained test. As outlined in the previous section, the raw data was subsequently processed and approximated with a polynomial function, shown as a dashed orange curve for the 2% strained tests. The dashed orange line shows an initial negative creep regime that was subsequently removed by adding the accumulated strains up, resulting in the solid orange curve. Negative creep is attributed to volumetric changes from initial heating and can result in shrinkage [203]. Where the negative strain reached is small in magnitude ($\sim 0.1\%$), the contribution has been shown not to interact with the creep process, so that the strains due to phase transformations and creep can simply be added (see [189]).

Figure 5.14b compares the accumulated plastic strain over time during the 18:3 non-isothermal creep test using the CMSX-10K alloy (orange curve) to the CMSX-4 test series,

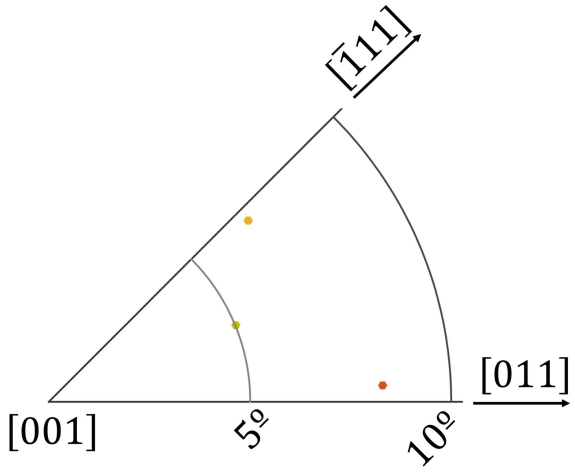

Fig. 5.13 The single-crystal orientational offset measured using Back-Laue reflection for the CMSX-10K tests, colour coded to match the three different test (green for the single cycle, yellow to 0.5 %, orange to 2 % strain).

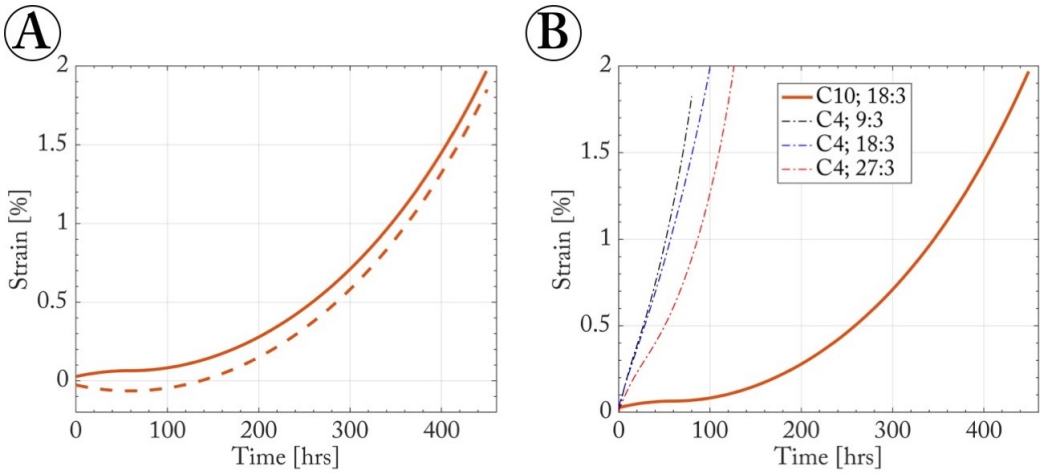

Fig. 5.14 (A) Creep curves for the CMSX-10K tests processed 2 % strain data in original shape (dashed line) and without an initial negative creep regime (solid line); (B) the 2% strain data compared to the CMSX-4 test series (dash-dot lines).

discussed in the previous section. Comparing the 18:3 tests for both alloys, the CMSX-10K test required 4.4× longer times to reach 2% plastic strain, compared to the CMSX-4 test.

This ratio is further reflected in the cycle condition times listed in Table 5.3 when comparing it to those of the 18:3 CMSX-4 tests in Table 5.1.

Comparing the calculated strain rates versus the accumulated plastic strain in Figure 5.15 further highlights the slow strain accumulation for the CMSX-10K tests. Interestingly, Figure 5.15 also shows that the CMSX-10K test exhibited no creep minimum but instead a

Table 5.3 Comparison of the test cycle condition times for the CMSX-10K series at peak (1050 °C), base (900 °C) and total number of cycles up to each interrupted stage (single cycle, 0.5% and 2% accumulated plastic strain).

Test cycle / plastic strain		Single cycle	$\sim 0.5\%$	$\sim 2\%$
18:3	$t_{peak}[h]$	0.05	14.55	56.3
18:3	$t_{base}[h]$	0.30	87.3	337.8
18:3	N_{cycles}	1	291	1126

gradually increasing strain rate in contrast to the CMSX-4 tests. The strain curve for this test is similar to an isothermal creep test in the tertiary creep regime 2.3.3.

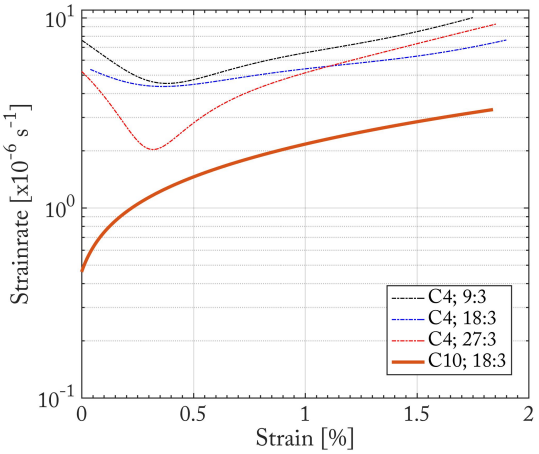

Fig. 5.15 Logarithmic plot of the strain-rate over accumulated plastic strains for the three different CMSX-4 test cycles (dash-dot lines) and the CMSX-10K test (orange curve).

5.2.1 Evolution of the CMSX-10K microstructure

SEM micrographs from the three different tests with CMSX-10K are shown in Figure 5.16. No visible difference was seen between the fully heat-treated microstructure and that following a single heating cycle. The initial microstructure exhibited a greater variation in γ'-cuboidal sizes, compared to CMSX-4 (Figure 5.4), such difference had already been expected, following the rhenium-variant based phase-fraction calculation in Section 4.2 (see Figure 4.10). Following the accumulation of 0.5% plastic strain, the microstructure had fully rafted and continued to evolve by isotropic coarsening with 2% plastic strain.

Analogously to the CMSX-4 tests, the level of topological inversion was quantified by J. Cormier. The special connectivity number $N_A(\gamma')[\mu m^{-2}]$ was calculated from SEM-images

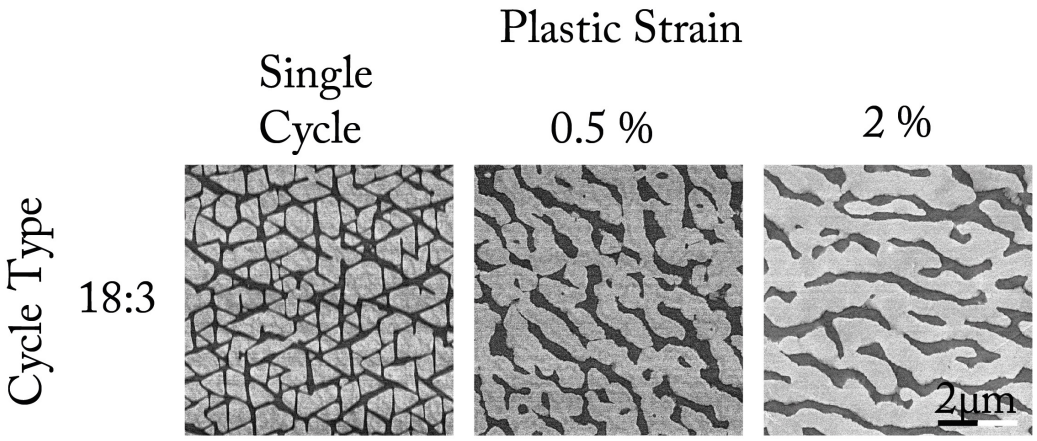

Fig. 5.16 SEM (In-Lens)-micrographs (5kV). TEM-foils cut on the (111)-planes. Figures are arranged by strain accumulated (single cycle, 0.5% and 2% plastic strain left to right). Dark phases correspond to the γ-matrix and bright ones to γ'-precipitates.

of the 2% strained tests, imaged in the inter-dendritic and dendritic region (see Table 5.4). As for the CMSX-4 tests, this also resulted in a topologically inverted microstructure, evidenced by the negative special connectivity numbers. The magnitude of topological inversion and the difference between the values in the DC and IR are however lower than that of the 18:3 CMSX-4 test strained to 2%.

Table 5.4 Special connectivity number for the dendritic (DC) and inter-dendritic (IR) regions of the 2% strained samples for the 18:3 test of the CMSX-10K alloy.

Test condition	Region	$2\%N_A(\gamma')[\mu m^{-2}]$
18:3	DC	-0.126
18:3	IR	-0.132

The rhenium-variant based calculations had revealed that whilst the variation between the DC and IR region based parameters in CMSX-10 is greater than in CMSX-4, the former alloy has a lower standard deviation (see Figures 4.8). The rhenium-variant based parameter calculations for the alloy CMSX-10 further indicated a lower temperature dependence on the evolution of key creep parameters (see Figures 4.11, 4.13, 4.14 and 4.15 in Section 4.2) than CMSX-4. This finding is reflected in the lower strain-rate (Figure 5.15) as well as the lower magnitude in topological inversion (Table 5.4), despite having been exposed to more cycles than the 18:3 CMSX-4 test to accumulate the same plastic strain. The longer time that the CMSX-10 tests are exposed to the peak temperature (Table 5.3) also contributes to the chemical homogenisation of the sample, thereby lowering the difference between the elemental variation in the DC and IR regions.

5.2.2 Dislocation analysis in CMSX-10K

The CMSX-10K tests were investigated after interrupting at three stages (single cycle, 0.5% (real strain 0.55%) and 2% (real strain 1.84%) plastic strain) as previously for CMSX-4. The evolution of the dislocation based deformation is displayed in Figure 5.17 for the three different test cycles and will be laid out in detail in the following subsections.

The single cycle

After the first heating cycle the dislocation activity observed in the CMSX-10K sample was significantly lower and even more localised to the DC, compared to the CMSX-4 alloy (see Figure 5.17a). As a result of the low dislocation density no significant dislocation interaction (i.e. leading to interfacial network creation) could be observed.

Regime of the rising strain rate

Following the accumulation of 0.55% plastic strain, the dislocation activity in the γ-matrix resulted in the formation of paired interfacial dislocation networks (see position 1 in Figure 5.17b). These paired networks are of the same character as observed for the alloy CMSX-4 (see Section 5.1.3). The Burgers vector of these networks was determined by tilting this region of interest (highlighted in Figure 5.18a) to six different two-beam conditions around the active (111)-slip plane. The resulting Burgers vectors of type $\vec{b} = \pm\frac{a}{2}[1\bar{1}0]$, $\vec{b} = \pm\frac{a}{2}[10\bar{1}]$ and $\vec{b} = \pm\frac{a}{2}[01\bar{1}]$ are highlighted in Figure 5.18(1) with the dislocations coloured corresponding to the frames of the two-beam conditions where these are absent according to the visibility Table 3.1. The paired dislocation arrangement is the same as observed for the CMSX-4 samples in the previous section.

Throughout the 0.55% strained micrographs scattered γ'-shearing events by Eggeler-pairs could be observed in the fully rafted microstructure (shown at position 3 in 5.17c). However, the overall dislocation density remained significantly lower than with the CMSX-4 tests strained to the same amount.

Modelling of the interfacial lattice misfit in Section 4.4.7 suggested that CMSX-10 has a significantly lower misfit magnitude. Based on Gabb *et al.* [70] the magnitude of the misfit can be experimentally observed from the interfacial dislocation network spacing, with a wider dislocation network spacing linked to a lower overall magnitude of the interfacial lattice misfit. This can be concluded when comparing the network spacings in both alloys (see Figures 5.18 and 5.30).

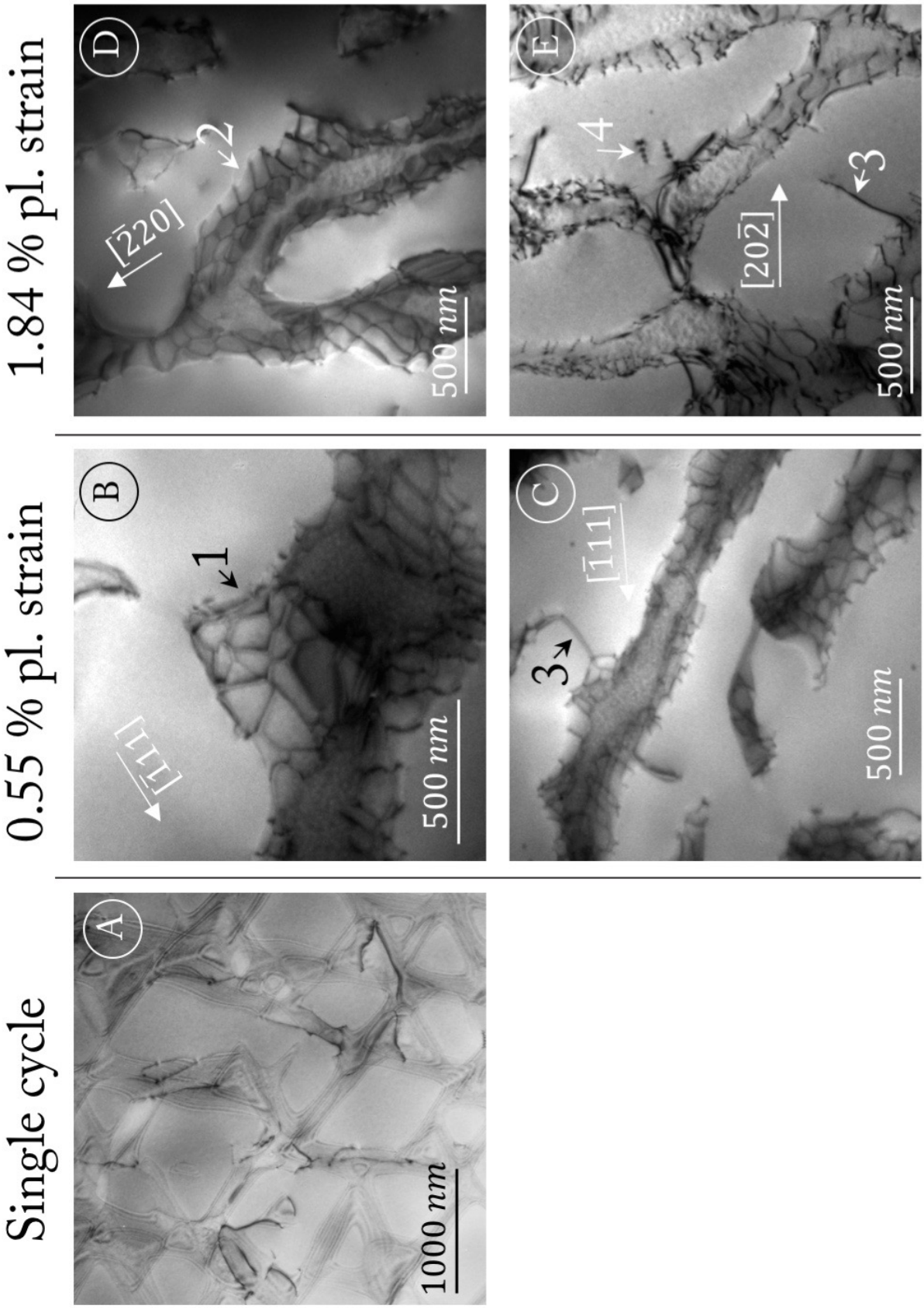

Fig. 5.17 TEM BF micrographs of the alloy CMSX-10K tests interrupted after a single cycle, 0.55% and 1.84% plastic strain (from left to right). Imaged on the active [111]-zone axis for the single cycle and under the displayed g-vectors. See text for further details.

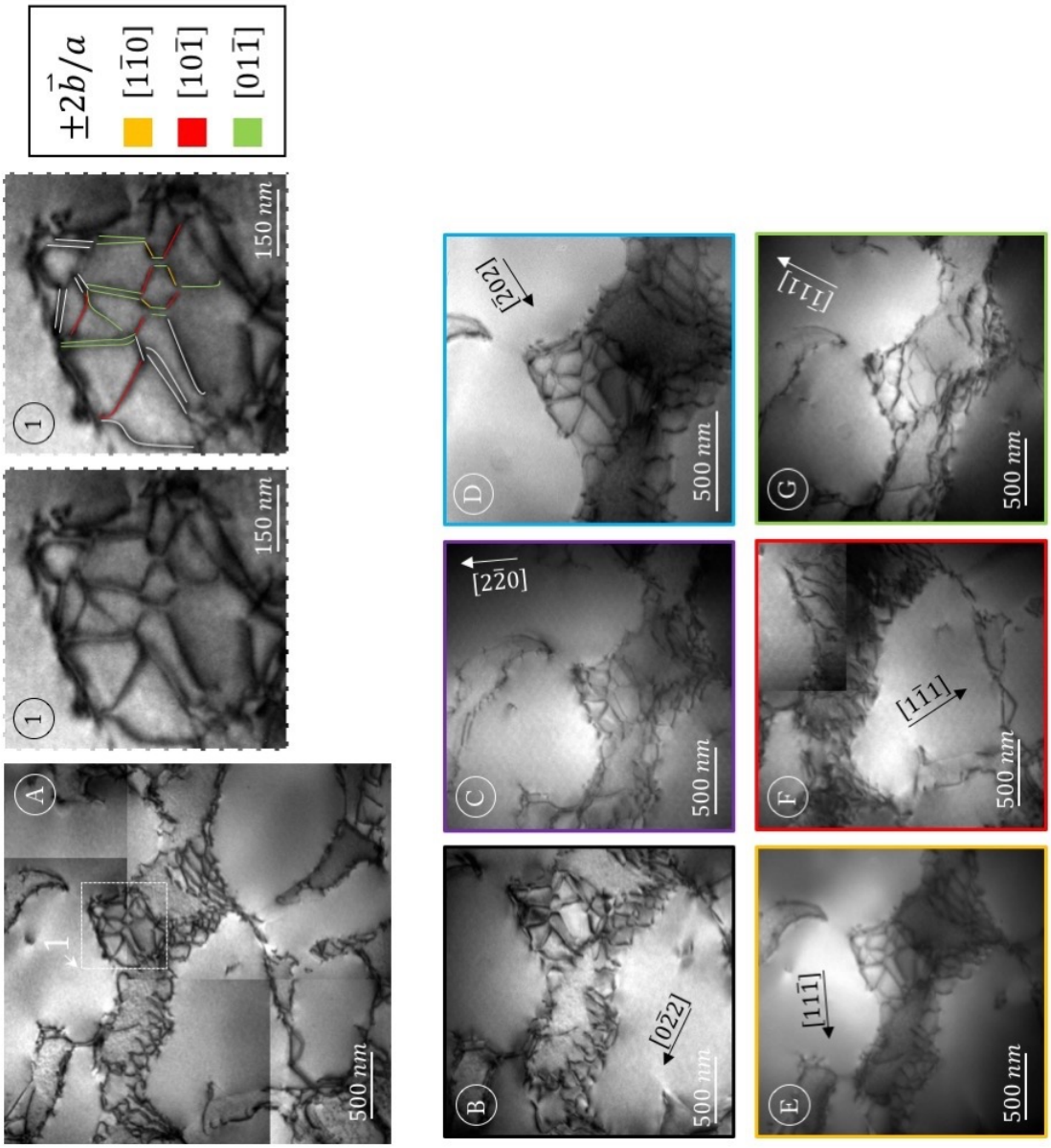

Fig. 5.18 TEM BF-micrographs from the 0.55% strained tests to investigate the interfacial dislocation networks. (a) imaged on the active [111] zone axis with close up of the white boxed region shown in (1). The highlighted dislocations in (1) correspond to the burgers vector colours displayed. The micrographs (b - g) have been tilted to six different two-beam conditions around the [111]-zone axis, indicated by the respective g-vectors. See text for further details.

With the 1.84% strained test, further increase in the dislocation density could be observed, whilst the same Eggeler-type shearing mechanisms remained active (see position 3 in 5.17e). Additionally, some Eggeler-pairs could be seen to climb in the γ'-phase (position 4 in 5.17e). The interfacial dislocation networks could be seen to evolve into more regular and tighter spaced arrangements (see position 2 in Figure 5.17d).

5.3 Topography of the precipitate/matrix interface

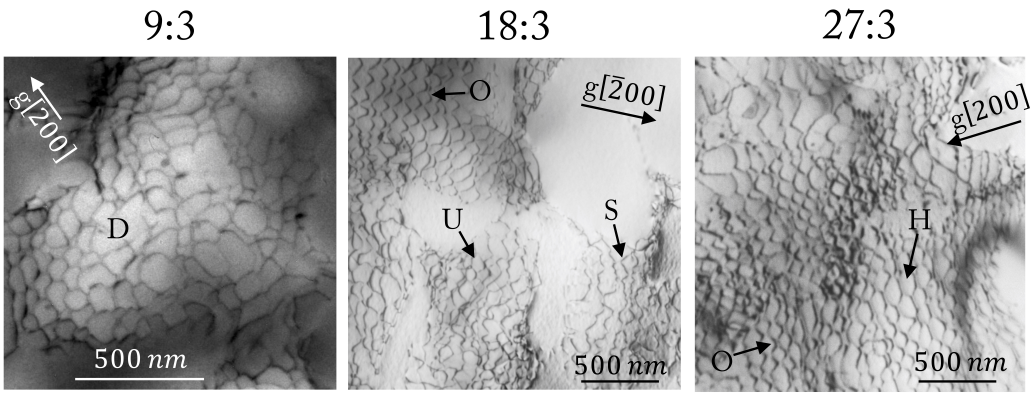

Fig. 5.19 BF-TEM micrographs of the three CMSX-4 test cycles (as labelled) cut on the [001] after $\sim 2\%$ plastic deformation tilted to different two beam conditions around the [001]-zone axis as indicated. See text for further details on the highlighted points.

The prevalence of γ'-shearing can be attributed to the interfacial network regularity (see Section 2.3.2), which varies in relation to the cycling rates. Figure 5.19 displays the interfacial dislocation networks of the CMSX-4 series imaged around the [001] zone axis for the three cycling conditions. The variation in projected dislocation spacing over the images, which is particularly pronounced for the 9:3 cycle, is evidence of the change in interface topography within a single raft. This change in topography is then expected to directly affect the arrangement of the superimposed interfacial dislocations. Looking at the network shapes and regularities in Figure 5.19, it can be concluded that the 9:3 condition results in irregularly spaced double networks (D) around a multifaceted raft. In the case of the 18:3 condition regions of coherent square networks on a (001)-interface are seen (O) as well as regions of single dislocation networks around a sloped interface (S) and irregular networks around a multifaceted part of the raft (U). In addition, the 27:3 condition displays a region of an elongated hexagonal network of paired dislocations on a (111)-interface (H).

This is in contrast to the interfaces observed following the 18:3 tests with CMSX-10K (see Figure 5.17), which resulted in clearer and flatter interfaces.

The following subsections will investigate further the formation of such irregular interfaces, using the mobility database Dictra and then compare this model to experimental results gathered with TEM-EDX. These considerations are then further investigated against isothermal and heat-treated interfaces.

Simulating the transient interface composition using Dictra

Section 4.4.6 simulated the non-isothermal parameter evolution for the experimental thermal cycles. These simulations indicate that during a heating or cooling step the γ/γ'-interface moves by 16 nm and 11.6 nm for CMSX-4 and CMSX-10 respectively. The effect this continuous thermal cycling had on the γ/γ'-microstructure and interfacial topography has been laid out in the previous sections. It remains however unclear, whether the thermal cycling affects the atomic composition on the γ/γ'-interfaces. Furthermore, if the atomic composition is subject to change during thermal cycling would this be on a timescale where a mobile dislocation in the γ-phase could interact with the re-distributing atoms. To answer these questions, the elemental concentration around an interface subjected to a thermal gradient was simulated using *Dictra* with the identical input parameters laid out in Section 4.3.4. As previously, only the six main alloying elements were considered, as the inclusion of the other elements (in particular rhenium) slowed the calculation to an unfeasible extent.

The resulting compositional profiles for four different calculation times are shown in Figure 5.20: yellow (the initial composition profile), red (after 1E-6 seconds), green (after 1E-3 seconds) and purple (after 1 second). The projected interface location is marked above the composition profiles, in the colour corresponding to the time step.

For the calculation of this cooling segment, it was assumed that the initial interface is on the right end of the composition profile. Thus, the disordered matrix phase initially occupied the area up to the dashed vertical yellow line. Adjacent to its right was the ordered precipitate phase. Upon cooling the interface moved from the right to the left-hand side.

The four compositional profiles show the element concentration of cobalt, tungsten, tantalum and aluminium (from top to bottom) in weight percent. Whilst cobalt and tungsten are γ-partitioners, tantalum and aluminium partition to the γ'-phase [200, 216]. As a result, the compositions to the left and right side of the γ/γ'-interface differ accordingly.

Furthermore, the composition profiles indicate the level of atom mobility of the various elements through the lattices. Aluminium shows the fastest diffusion rate, evidenced by the nearly homogeneous concentration profile after one second. Cobalt is faster than tantalum

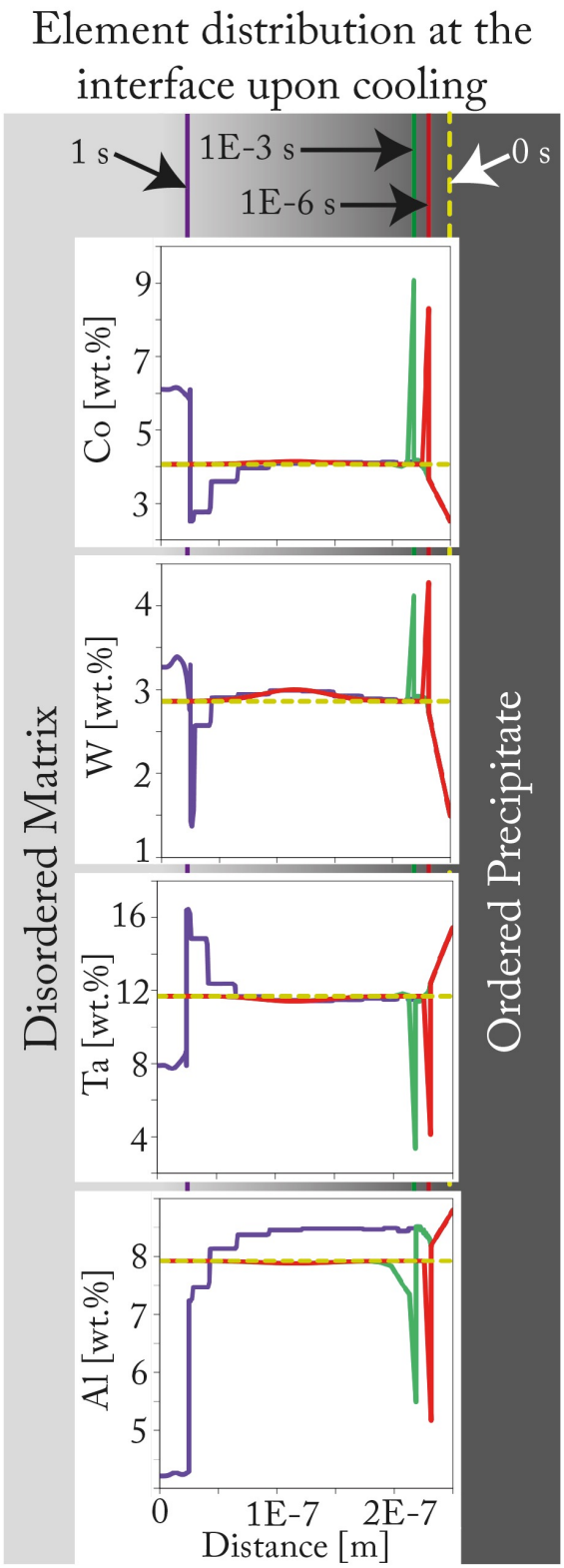

Fig. 5.20 *Dictra* element distribution simulation of the second cooling event using only six major alloying elements of CMSX-4. Showing the composition profiles for the elements cobalt, tungsten, tantalum and aluminium (top to bottom) along with the *Dictra* projected interface position between the disordered matrix phase (left) and the ordered precipitate phase (right). The composition profiles for different calculation times are plotted in yellow (initial profile), red (1E-6 seconds), green (1E-3 seconds) and purple (1 second).

and tungsten is the slowest of the six calculated elements. The diffusion rate and profile for chromium is very similar to the result shown for cobalt. The diffusion rate for rhenium is assumed to be below tungsten, with a steeper compositional difference across the interface, owing to a larger partitioning ratio.

Essentially, in the region over which the γ'-phase has expanded, the composition has acquired an ordered structure by the ingress of aluminium, but largely retains the composition of the other elements as they were in the γ-phase. This calculation thus indicates that this cooling event resulted in an initially metastable compositional profile across the γ/γ'-interface. The following section will thus examine the interfacial composition following a single heating cycle to confirm this simulated result. Furthermore, the calculation indicates that the process of atomic redistribution across the interfaces takes place on a slightly slower timescale compared to the velocity of mobile (of mixed character) dislocations in γ for these temperatures (which is in the region of 4-10 nm s^{-1} according to [168]). Where atomic redistribution is slower than the velocity of the mobile dislocations an interaction between the advancing dislocation and the atomic elements is expected to be traceable through a visible change in the compositional profiles following a single heating cycle. This will also be examined in the following section.

TEM-EDX analysis on the interfaces

The interfaces of a 9:3 CMSX-4 single cycle test sample, cut on the [001]-plane were studied with TEM-EDX using a *FEI Tecnai Osiris FEG-TEM* to examine a potential metastable γ/γ'-interfacial composition profile in a region where the foil thickness was between 50 and 100 nm. The resulting interfaces were formed following a 120 $[\frac{K}{min}]$ cooling from 1050 to 900 °C.

Firstly, a dislocation free segment of the interface was analysed using a 10 $\times$ 40 nm wide box with measuring points spaced 0.5 *nm* apart. The region of interest analysed with TEM-EDX is highlighted with a white box labelled 1 in Figure 5.21. The brighter section corresponds to the γ-matrix and the darker regions to the γ'-precipitates, such that the investigated box changes from a precipitate lattice on the left side of the box to a matrix lattice on the right.

To what extent the interface inside the acquisition box was vertical could not be calculated. Furthermore, as only four different regions were examined using TEM-EDX from this sample, the magnitude of element scatter and experimental scatter could not yet be precisely tracked. Further work is thus required before the results presented in this subsection can be used quantitatively.

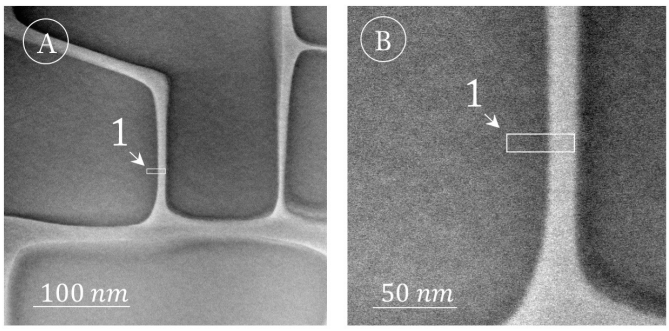

Fig. 5.21 TEM-BF micrograph of CMSX-4 post a single 9:3 cycle showing the dislocation free interface region investigated using TEM-EDX (white box marked with 1, (b) is a close up of the region in (a) with the γ'-precipitates darker and the γ-matrix brighter.

The quantified EDX-maps were then corrected and post-processed, to give the correct compositional distribution of each measuring point. The resulting compositional variation across the interfacial width is plotted in Figure 5.22b for all alloying elements but nickel. The compositional profile displayed uses the mean vertical composition across the quantified box (in Figure 5.22). The degree of interfacial curvature was equal to the datapoint spacing (0.5 *nm*) and further ignored. The interfacial widths and atomic distributions are commonly measured using atom-probe tomography (see [221, 80]). The profiles recorded with Warren *et al.* [221] studying a fully rafted RR 3000 (at 180 MPa and 1050 $^{\circ}C$) alloy found a similar metastable interfacial distribution particularly in the rhenium profile across the cooled interface.

Using TEM-EDX similar metastable interfacial compositions were observed by Ge *et al.* [75, 76, 74] using the single-crystal superalloy DD6. The interfacial widths amounted to 2.2 *nm* following a strong thermal gradient after 1100 °C creep at 140 MPa for 12h [75].

The shape of the interfacial compositional profile corresponds to those modelled using *Dictra* (Section 5.3) with the γ-preferential partitioners (Co, Cr, Re, W, Mo) increasing in content from left to right, whilst those elements partitioning to the γ'-phase decreased (Ta, Al, Ti). To determine the interfacial width from these profiles, a flat ceiling and floor function were defined based on the equilibrium distribution at the right and left ends of the compositional profiles (see Figure 5.23a). For example, the equilibrium composition on the left and right end of the tantalum profile was calculated and is shown as red dashed lines on the top and bottom respectively. The interfacial width (e.g. the distance between the Ta-profile decreasing from left to right) was further calculated and is shown in Figure 5.23b. As the standard deviation across the equilibrium concentration section was around 0.25 wt.%

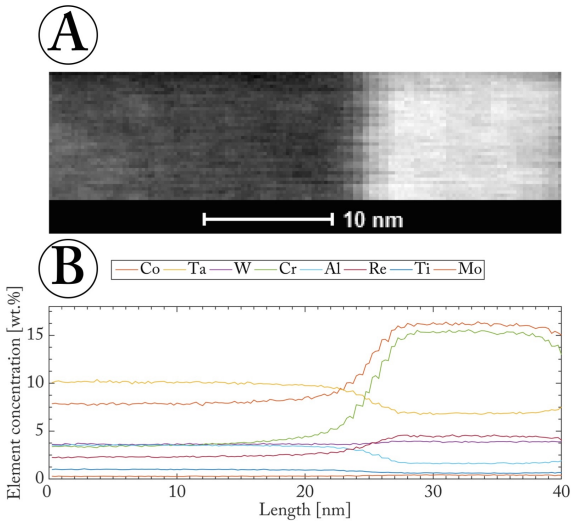

Fig. 5.22 (a) TEM-BF micrograph of the investigated region (highlighted in Figure 5.21), (b) the compositional profiles across the interfacial region in (a) for all alloying elements but nickel.

the interfacial width was calculated once the mean composition had deviated 0.5% from the ceiling or floor function (the exception was rhenium were 0.25 wt.% was taken due to the small compositional difference).

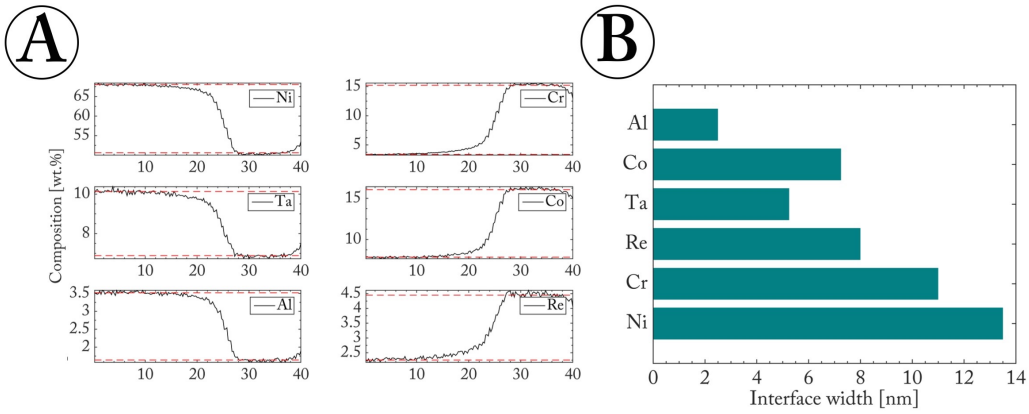

Fig. 5.23 (a) Analysis of the interfacial width in the calculated compositional profiles, (b) computed interfacial widths for the main alloying elements in CMSX-4.

In line with the *Dictra* modelled interfaces, the experimental interfacial widths differ for each alloying element roughly relative to their respective mobilities. Aluminium exhibits the sharpest interfacial profile, whereas the slow diffusing rhenium and tantalum exhibit wider profiles. In contrast to the mobility based *Dictra* model however, the chromium and cobalt profiles were wider than that of tantalum. When comparing the interfacial gradients however,

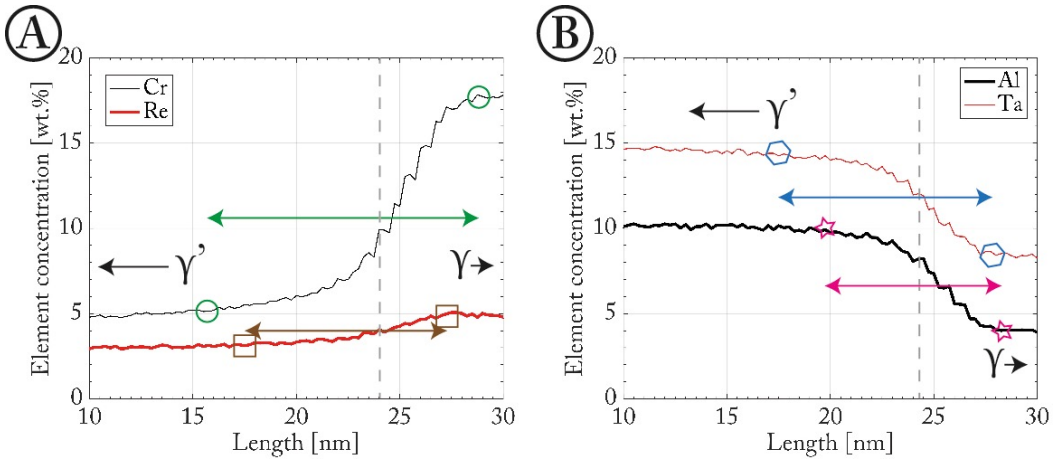

Fig. 5.24 Analysis of the calculated compositional interfacial profiles from Figure 5.22b. (a) Chromium profile (black line) with calculated interfacial width (green arrow) compared to the rhenium profile (bold red line) with calculated interfacial width (brown arrow); (b) aluminium profile (bold black line) with calculated interfacial width (pink arrow) compared to the tantalum profile (red line) with calculated interfacial width (blue arrow). To compare the interfacial gradient between elements a dashed grey line was inserted.

those of aluminium and chromium were slightly higher than that of tantalum and considerably higher than that of rhenium (see Figure 5.24). The larger interfacial width can be attributed to a longer tail on the chromium compositional profile (see Figure 5.24a). The calculated interfacial widths are comparable in their trends and slightly wider than those reported by Goodfellow *et al.* [80] (2-9 *nm*) using atom probe tomography with a polycrystalline model alloy.

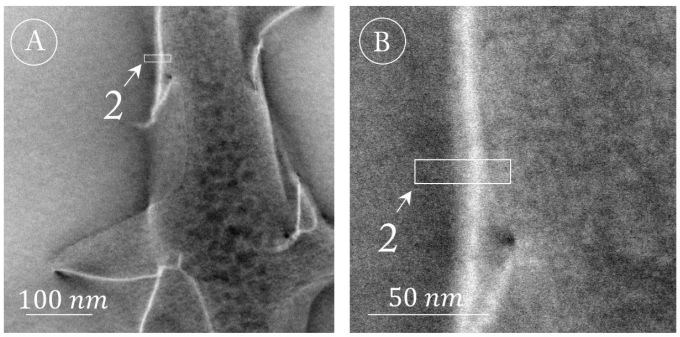

Fig. 5.25 TEM-BF micrograph of CMSX-4 post a single 9:3 cycle showing an interfacial region containing several interfacial dislocations (white lines) and the region investigated using TEM-EDX (white box marked with 2, (b) is a close up of the region in (a) with the γ'-precipitates darker and the γ-matrix brighter.

To investigate how the interfacial profile and corresponding width changes as a result of an interfacial dislocation being present, another region of the same sample was analysed that exhibited interfacial dislocations. The TEM-EDX quantified region of the same size (10×40 *nm*) is shown in Figure 5.25 highlighted by a white box marked 2. An interfacial dislocation can be seen to lie across the γ/γ'-interface (white line in Figure 5.25). The subsequent analysis was performed analogously to the dislocation free interface and the compositional profile is plotted in Figure 5.26 for all alloying elements but nickel.

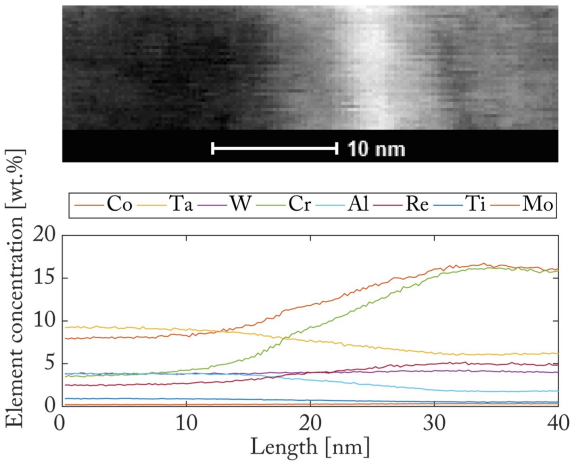

Fig. 5.26 (top) TEM-BF micrograph of the investigated region (highlighted in Figure 5.25), (bottom) the compositional profiles across the interfacial region in (a) for all alloying elements but nickel.

Looking at Figure 5.26, the same compositional trends as in the dislocation-free interface in Figure 5.22 can be seen. In comparison, the transitional region between the matrix and

precipitate regions have visibly broadened. The interfacial width was further calculated and plotted in Figure 5.27. The red and blue bars correspond to the dislocation-containing and -free interfaces respectively.

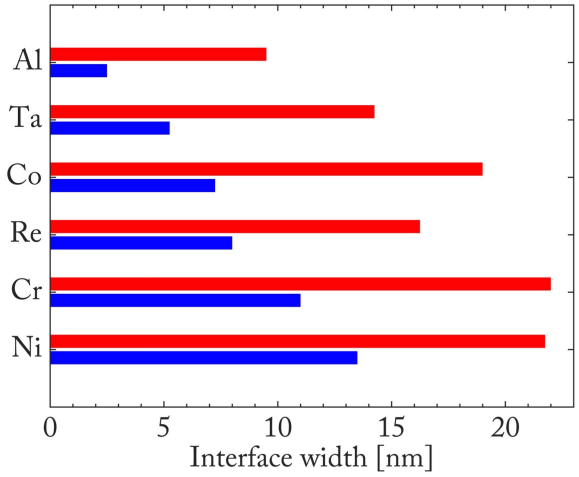

Fig. 5.27 Computed interfacial widths for the main alloying elements in CMSX-4 for the dislocation-free interface (blue) and dislocation-containing (red).

The comparison in Figure 5.27 indicates that the interfacial widths have increased for all major compositional profiles due to the presence of an interfacial dislocation. In relation to the dislocation-free interface, the aluminium interfacial width increased the most by a factor of 3.8 whereas the chromium and cobalt interfacial widths increased most in magnitude by 11 and 11.75 nm respectively. The particularly strong influence of a dislocation line on the local chromium and cobalt atom distribution has been reported by Kontis *et al.* [109] using atom probe tomography with a polycrystalline IN792 alloy.

The influence of the dislocation on the interface differs, depending on whether or not the dislocation next to the interface is mobile. In the case of a sessile interfacial dislocation (pure edge character), Ge *et al.* [76] reported a local re-arrangement of atoms (in particular of rhenium) to result around the dislocation core. This study used the single-crystal superalloy DD6 crept at 140 MPa and 1100 °C for 12h and cooled with a strong thermal gradient. Mobile dislocations (of screw and mixed character) will interact with the pinning forces exerted by the solute atoms on the dislocation line [84] and the dislocation shear will result in a change in atomic distribution around the interfaces as a result of the displacement of slip planes relative to each other (see Section 4.5).

Long *et al.* [128] further make an important connection between the interfacial dislocation of mixed and edge character. The cited study shows that a mobile dislocation of mixed character initially forms interfacial dislocation networks of $\langle 110 \rangle$ diamond shape that

gradually transform into $\langle 100 \rangle$ networks of pure edge character to more efficiently alleviate the interfacial lattice misfit. If the primary driving force for the deposition of interfacial dislocation is the interfacial lattice misfit it is important to clarify where exactly the source of this interfacial lattice misfit is during non-isothermal cycling and how the magnitude of the misfit changes with thermal cycling. Whilst the latter has been modelled in Section 4.4.7 the former will be discussed in more detail at the end of this chapter.

Comparison to isothermal and heat-treated interfaces

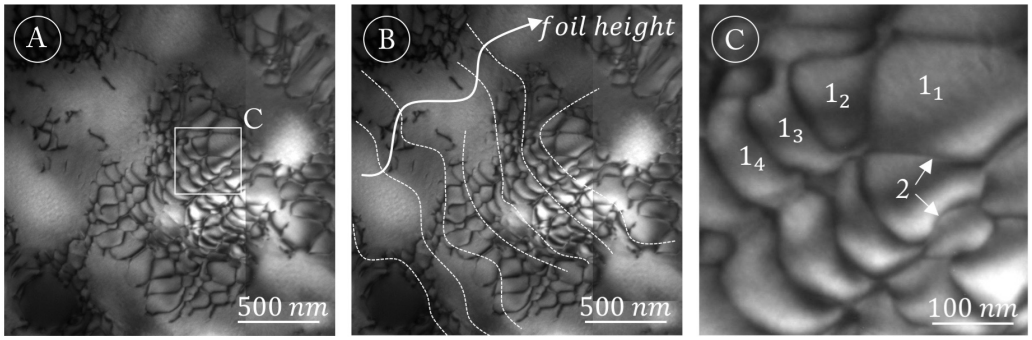

Fig. 5.28 TEM-BF micrograph imaged on a [112]-zone axis showing the interfacial topography in CMSX-4 for a 9:3 1% strained test. The interfacial topography in (a) is plotted with contour lines in (b). The region highlighted in (a) is magnified and plotted in (c). See further details in the text.

As the regularity and arrangement of interfacial dislocation networks is directly related to the topography of the γ/γ'-interface they are attached to, the change of interfacial topography was further investigated in this section. Looking at the non-isothermal creep tests in this study (see Figure 5.28a), the interfaces of the 9:3 tests in CMSX-4 were most irregular. Section 4.4.1 had pointed out that this test resulted in a metastable phase fraction evolution throughout testing. In a thicker region of the microstructure the sloped and terraced nature around the interfacial dislocation networks are highlighted in Figure 5.28b and 5.28c respectively. In Figure 5.28c four levels of protrusions (labelled $1_1 - 1_4$) between the interfacial dislocations (labelled 2) can be seen, taking a terraced shape. Tilting to the [001] zone axis and moving to a thinner region the protrusions between the interfacial dislocation networks remain visible (see Figure 5.29b and e).

To study how additional holding time at the base temperature (900 °C) and a slower cooling rate would impact the interfacial topography, the 9:3 1% strained test was subsequently heat-treated at 905 °C for 2 h and then furnace cooled with a slow cooling rate of 5.8 $\frac{K}{min}$ to 700 °C.

Furthermore, to understand how the topography differs from an isothermal creep test deformed at 1000 °C and 200 MPa a sample of CMSX-4 tested by Matan to failure was cut 1 cm away from the fracture surface and imaged on the [001] zone axis (see Figure 5.29a). The corresponding strain data for this test has been published in [166].

Additionally, Figure 5.30 shows the interfaces of the heat-treated and isothermal tests tilted and imaged on a [112]-zone axis.

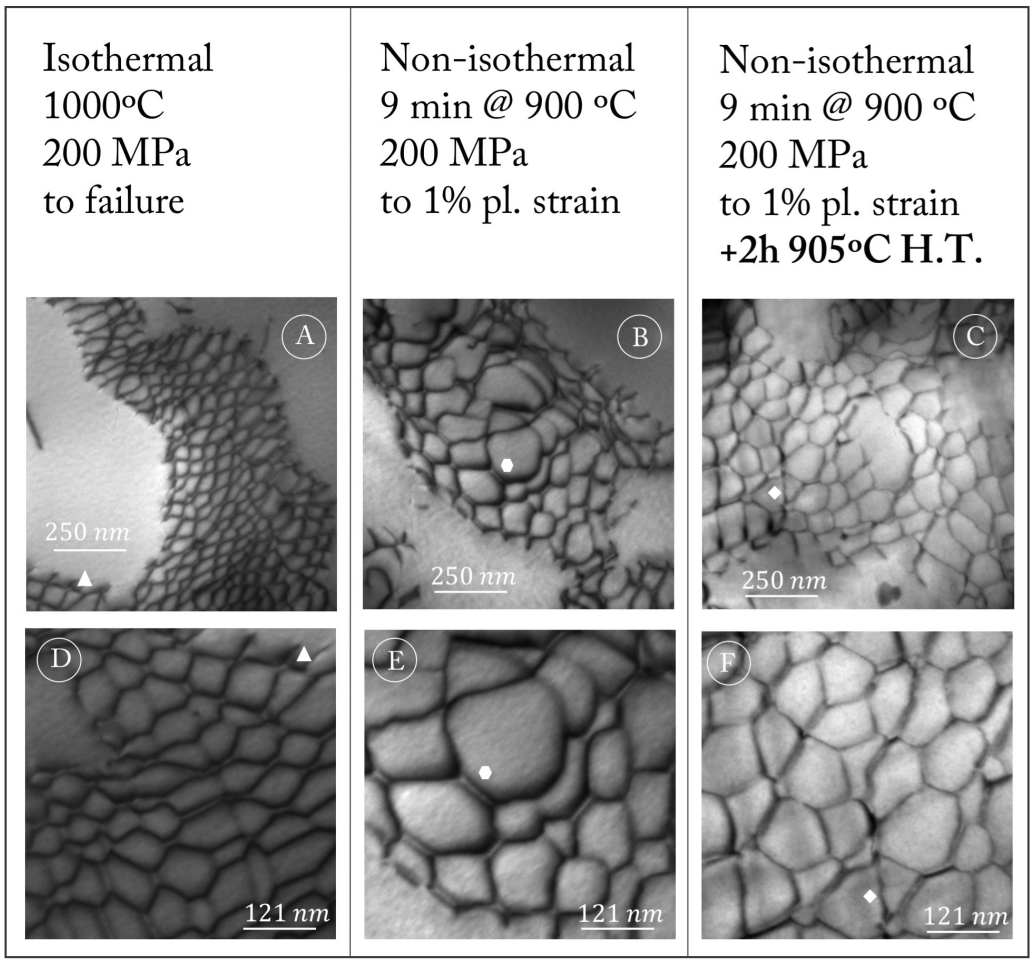

Fig. 5.29 TEM-BF micrographs imaged on the [001]-ZA of the alloy CMSX-4. (a+d) following iso-thermal creep at 1000 °C and 200 MPa until failure, tested by Matan [166]; (b+e) non-isothermal 9:3 test at 200 MPa until 1 % strain and (c+f) the non-isothermal sample further heat-treated at 905 °C for 2h. (d,e,f) are close-ups of (a,b,c) respectively, with the white markers as reference points.

Comparing the non-isothermal 9:3 creep test sample, that has been shown to contain paired dislocation networks (see WBDF images 5.8b and c) before and after the heat-treatment no significant difference can be seen in the character of the network binding. Instead however, the interfacial topography has considerably smoothed as a result of the heat treatment, resulting in a more regular network spacing without any visible protrusions. The network regularity for the heat-treated sample transforms towards the level of regularity observed for the isothermal creep test. This finding further highlights the stability of the paired networks in CMSX-4.

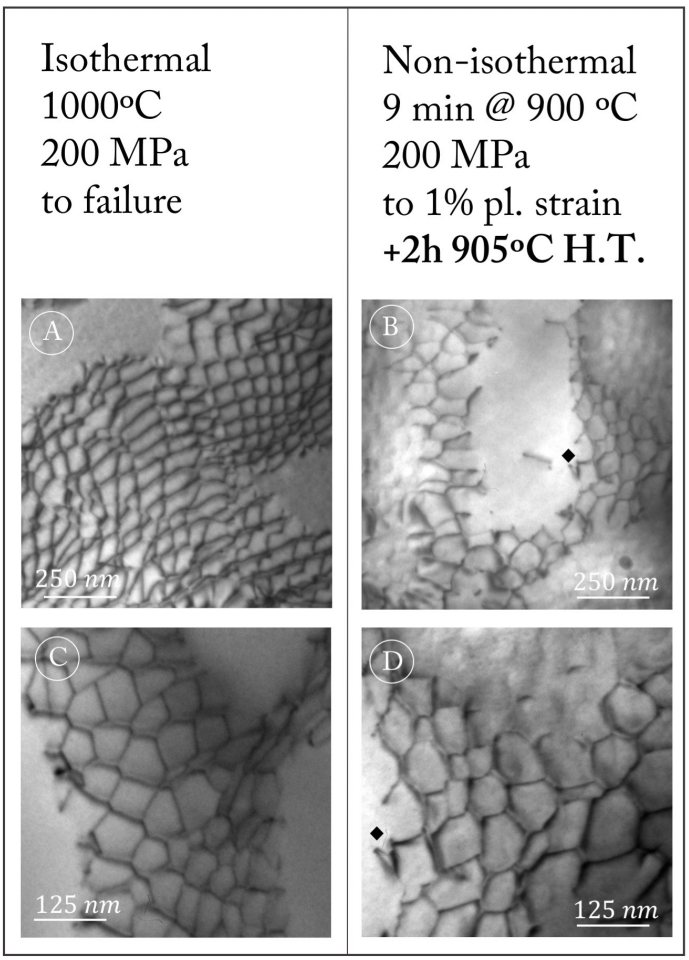

Fig. 5.30 TEM-BF micrographs imaged on a [112]-ZA of the alloy CMSX-4. (a+c) following isothermal creep at 1000 °C and 200 MPa until failure, tested by Matan [166]; (b+d) non-isothermal 9:3 test at 200 MPa until 1% strain subsequently heat-treated at 905 °C for 2h. (c,d) are close-ups of (a,b) respectively, with the black marker as a reference point for (b).

The protrusions created by the paired and regular interfacial networks were further analysed and are shown in Figure 5.31b. The SEM-micrograph imaged on the active (111)-plane of the CMSX-4 27:3 test deformed to 2% plastic strain has been further enhanced using an FFT-Bandpass filter to increase the resolution. Interfacial protrusions resulting from the deposition of interfacial dislocations can be seen southwest of positions marked 2, the white spots southwest of position 1 are γ'-tertiaries. These protrusions and their formation reactions have also been reported in isothermal creep tests in single-crystal superalloys by Huang *et al.* [90].

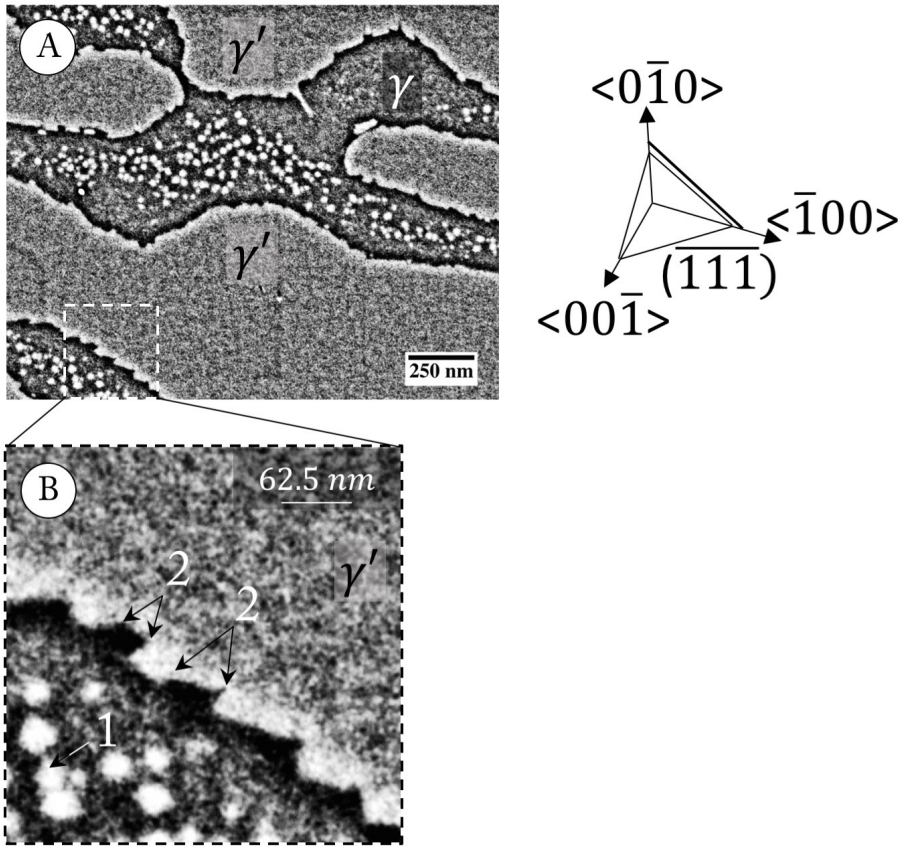

Fig. 5.31 Enhanced SEM-micrograph of the 27:3 deformed to 2% plastic strain with a close-up of the region highlighted in (a) shown in (b). The orientation of the sample is shown on the right. Protrusions and serrations on the interfaces are marked (2) and γ'-tertiaries (1).

5.4 Investigating the presence of tertiary precipitates

High temperature cycling has been shown to increase the amount of γ'-tertiaries in the microstructure (see Section 2.4), which upon precipitation during the cooling segments increase the resistance against γ-glide and push the γ-dislocations towards the interfaces [215]. As γ'-tertiaries precipitate predominantly in wider γ-channels (see Figure 5.32b), they rapidly reduce the effective channel width upon cooling, thereby increasing the Orowan resistance. In this study, the contribution towards the creep resistance by γ'-tertiaries could not be investigated, as the electro-polishing preparation step lifted the γ'-tertiaries out of the γ-matrix for the alloy CMSX-4 (see Figure 5.32). The distortions on the remaining dislocations gliding in the γ-matrix (see Figure 5.32a) can thus not be conclusively attributed to γ'-tertiaries or local solid-solution hardening.

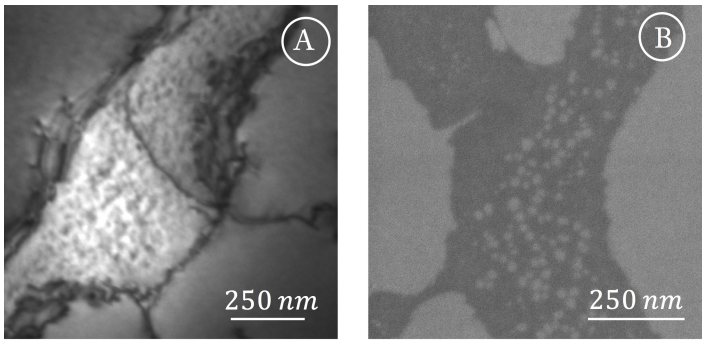

Fig. 5.32 Micrographs of two different regions from the 27:3 test cycle after 2% plastic deformation, imaged on the active (111)-plane using two different microscopes: a) BF-TEM micrograph on the zone axis b) SEM micrograph.

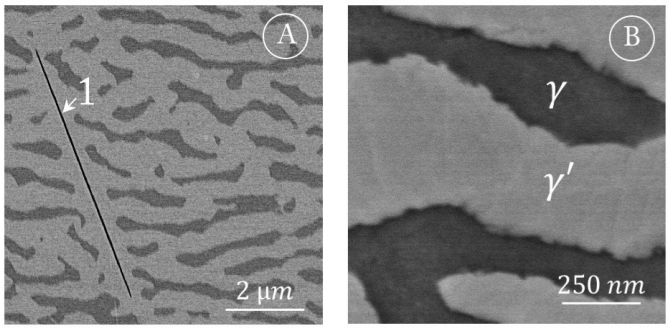

Fig. 5.33 SEM micrographs of the alloy CMSX-10K cycled with 18:3 until 2% plastic strain and subsequently imaged on the active (111)-plane. Region (a) exhibits a TCP phase marked by position 1; a close up of a different region in (b) indicates that no γ'-tertiaries had formed.

The alloy CMSX-10K on the other hand exhibited no γ'-tertiary formation in the wider γ-channels upon cooling as seen in Figure 5.33b. As both alloys were exposed to the same thermal cycling, this difference is attributed to the alloy CMSX-10K having a better high-temperature phase fraction stability, resulting in a smaller phase fraction variation for the same thermal cycles (see Section 4.4.6).

In contrast to the CMSX-4 test series however, topologically closed packed phases (TCPs) were observed after 2% creep in Figure 5.33a, labelled with position 1 (see Reed and Rae [161] for further details on their formation mechanism and role).

5.5 Discussion

As described in Section 5.1, the thermal cycling creep conditions studied deform at a significantly faster rate compared to isothermal tests. As the rate of deformation is driven by dislocations, we can assume a higher dislocation activity to be the driving force behind a faster rafting and interfacial network formation process compared to isothermal creep. The models in Section 4.4 indicate that for the two alloys studied the higher dislocation activity during cyclic creep is facilitated in part by a drop in Orowan backstress in γ, solid-solution hardening resistance in γ and critical resolved shear stress of the γ' during the exposure to 1050 °C. The primary driving force for the added dislocation activity during thermal cycling are the continuously changing misfit stresses [120, 155].

5.5.1 The effect and formation of paired dislocation networks

In comparison to isothermal tests, the interfacial dislocation networks are established more rapidly and surround the precipitates after 0.5% plastic strain. Thus, the process of network completion precedes the completion of γ'-rafting for CMSX-4 (see Section 5.1.1) and is probably reached around the point of the minimum creep rate observed for this alloy (see Figure 5.1b). The association of the minimum creep rate with the completion of effective interfacial networks protecting against γ-glide and γ'-shear equally further helps to explain why in CMSX-4 the creep minimum is reached for all test conditions at roughly the same amount of accumulated creep strain, when the longest cycle (27:3) is the slowest to form well-developed γ'-rafts (see Figure 5.4) with the least time spent in the γ'-rafting regime (see Table 5.1). The networks formed at the γ/γ'-interfaces are a mixture of single and paired edge dislocation networks, forming as a result of the cyclic peak temperature exposure. To the best knowledge of the author, dislocation structures originating from non-isothermal cyclic creep have to date only been studied by Viguier and Hantcherli *et al.* [215, 87]. Their test series on the superalloy MC2 exposed the material to a peak temperature of 1150 °C for 30 minutes and cooled the sample down to room temperature in 25 minutes. In other studies of high temperature (heating to 1050 °C and more) thermal creep cycling [38, 215, 120], the γ'-dissolution was equally large, resulting in a much larger movement of the interface between its peak and base temperature position than in the current study (see Figure 4.20). The larger interface movement resulting in more disruption to the interfacial dislocation is thought to hinder the gradual formation of paired dislocation networks (which were not reported in the cited studies).

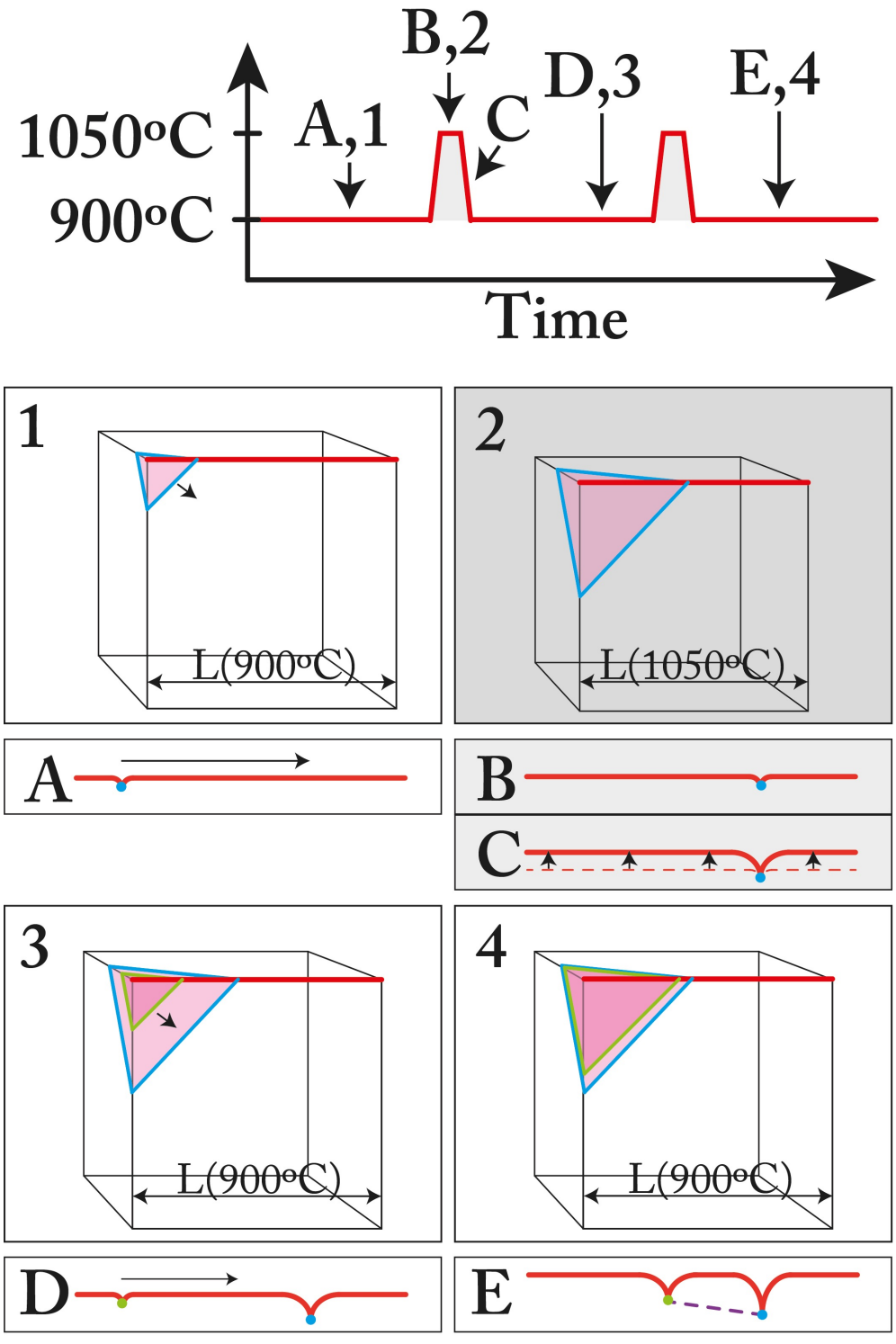

Fig. 5.34 Sketch of the proposed formation mechanism for paired networks. (Top) Temperature profile with marked timestamps of the sketched figures; (1-4) View on a γ'-precipitate with dislocation lines attached to the outsides (blue and green lines); (A-E) close up of the marked (in red) γ'-interface with the position of the attached dislocation cores (blue and green dots). See text for further details.

The reason why these paired dislocation networks form under the test conditions studied seems to be due to the dislocation activity driven by coherency stresses and a certain level of interface mobility. As no fully established paired dislocation network was observed following a single cycle (see Figure 5.6), a gradual formation of the networks can be assumed. To discern the formation mechanism of the paired interfacial networks fully, further work is required with tests interrupted between two cycles and 0.5% strain. In the following a hypothesis of the paired interfacial dislocation formation mechanism is presented based on the experimental evidence collected so far.

Firstly, a single γ'-precipitate with a single blue interfacial dislocation line is assumed to exist in the microstructure. This dislocation can move around the precipitate by dislocation climb, with the hypothetical climb direction marked in Sketches 1 and A of Figure 5.34. During a high temperature exposure to 1050 °C interfacial dislocation climb is enhanced due to higher diffusivity moving the blue dislocation line to the point indicated in Sketches 2 and B of Figure 5.34. As a result of the high temperature exposure the γ'-phase dissolved, reducing the precipitate length to a value of L(1050 °C). Assuming that the force field on the interfacial dislocation line points into the γ'-precipitate, the interfacial dislocation line would track the interface location with its dissolution due to the higher mobility of the dislocation line over the interface position (see Section 5.3).

Upon cooling to the base temperature of 900 °C, the γ'-precipitate expands to a value of L(900°C) due to re-precipitation. The change of the interface location is shown in Sketch C of Figure 5.34, indicating that the position of the dislocation does not change upon cooling. This is assumed to result from the dislocation line remaining to be subjected to the same direction of the force field and due to the deposition of slow diffusing rhenium atoms to the dislocation cores compared to the fast moving γ/γ'-interfaces due to the aluminium diffusion (see Section 5.3). As a result, the lower dislocation core position is assumed to remain stable during the further 900 °C to 1050 °C non-isothermal cycling.

With additional deformation, a further dislocation line (green line in Sketch 3 of Figure 5.34) moves towards the γ'-interface and can again move by interfacial glide and climb into the proximity of the blue dislocation line. With further high temperature cycling the green dislocation core will also create a protrusion as indicated in Sketches 4 and E in Figure 5.34. Between the two protrusions (provided these lie along a (111)-plane) an APB fault (dashed purple line in Sketch E of Figure 5.34) is suggested to give this paired configuration a high temperature stability (see Section 5.3).

Ru *et al.* [173] argued that the paired network configuration forms due to the high interfacial misfit in the alloy IC11B resulting in a dense interfacial network. Network density

has been shown by Gabb *et al.* [70] to exhibit an inverse relationship to the misfit. A higher misfit thus results in a denser interfacial dislocation network in order to resolve the higher coherency stresses. Non-isothermal creep exposures can equally exhibit regimes of high misfit magnitudes even as shown in Figure 4.17 and by le Graverend *et al.* [119, 120]. The high misfit alone, however, cannot explain why during isothermal creep tests (as with Ru *et al.*) dislocation lines would transform from a regular spaced interfacial network configuration into a paired configuration. Interestingly, the paired networks by Ru *et al.* [173] depend on the γ'-phase also in order to stabilise their close proximity arrangement with an APB-fault. However, considerable doubt exists that the coupling and the entire paired network formation would take place inside the γ'-phase as suggested by the authors. Instead, it is more plausible that the interfacial dislocation networks in the study by Ru *et al.* would form upon cooling down the isothermal creep tests from 1100 °C due to protrusions created by the considerable γ'-reprecipitation. However, further isothermal creep tests have to be carried out to conclusively attribute the driving factors for paired network formation as no cooling rates were referenced by Ru *et al.*

5.5.2 The effect of the interfacial misfit during non-isothermal creep

Le Graverend *et al.* [119, 120] verified *in situ* that an increase in misfit magnitude during the high temperature exposures in non-isothermal creep was directly related to an addition in strain accumulation from added dislocation motion. The high temperature excursions thus require additional interfacial dislocations (see Section 4.4.7), whilst simultaneously decreasing the Orowan glide resistance in the γ-matrix (see Figure 4.25) thereby allowing the dislocations to reach their required target quicker. Due to identical heating cycles, the magnitude of the misfit stresses during the high temperature exposures is similar across all CMSX-4 tests and decreases on cooling (compare with [119, 120]).

The frequency of high temperature misfit stress regimes, however, is inversely proportional to the cycle time. As a result, the dislocation activity scales accordingly, evidenced in the 9:3 condition having the highest and 27:3 the lowest creep strain in CMSX-4 (see Figure 5.1b). As a result, the high temperature exposures effectively pump dislocations into the microstructure, facilitating a faster interfacial network completion in comparison to isothermal test conditions.

As the misfit in the alloy CMSX-10K is lower than in CMSX-4 (see Figure 4.36), the network formation resulting from the reduced dislocation activity takes place on a significantly slower timescale (see Figure 5.14). Despite the lower misfit magnitude in

CMSX-10K, paired interfacial networks were observed in this alloy as well, most likely to have formed due to thermal cycling.

5.5.3 The role of interfacial transformation on cyclic creep resistance

The effect of rafting on non-isothermal creep resistance

The microstructure evolution during the test (see Section 5.1.1) shows the establishment of non-planar γ'-rafts. The number of side connections between precipitates results in interfacial networks forming along vertical and horizontal interfaces before the completion of γ'-rafting. Further work is required to understand the driving forces resulting in such a disrupted rafting process. As a result of the continuous precipitate agglomeration (see Figure 5.4) the bulk γ'-area increases, making it easier and quicker for a γ'-pair to shear through the same area. In addition, the interfacial area shrinks requiring fewer interfacial dislocations bound to these interfaces to alleviate the interfacial lattice mismatch. Where these interfacial dislocations have not yet transformed into edge character, the lower interfacial areas free up mobile dislocations of mixed character that can contribute to further plastic accumulation in the γ-matrix by glide and climb. Further the precipitate agglomeration results in some paired dislocation networks being absorbed into the γ' (see Section 5.1.3). These processes are enhanced during cyclic creep conditions since effective interfacial networks have been completed before γ'-rafting. The process of rafting thus contributes to the creep strain acceleration. This agrees with the observations by Giraud *et al.* [77] who observed a similarly detrimental effect of rafting on the high temperature cyclic creep resistance in the 1050-1150 °C regime.

The effect of γ'-shearing by Eggeler-pairs

In the studied 900 °C to 1050 °C regime, the high temperature exposures allow the formation of dissimilar Burgers vector dislocation pairs that do not require the formation of an APB-fault to enter into the γ' [55] and thus only have to overcome the binding energy of the dislocation pair to the interfacial network. This further highlights the importance of network stability to cyclic creep life.

Once a sufficiently large dislocation density in the γ-channels is reached to enable a probable encounter by dislocation glide and climb of dissimilar Burgers vector dislocations these can form Eggeler-type pairs. Section 5.1.3 suggested this point is reached around the minimum strain rate for the CMSX-4 tests (estimated using the diffusion length in Section 4.4.3). The formation of the Eggeler-pairs and their subsequent continuous shearing of the

γ'-precipitates is thus associated with the increase in the observed plastic strain rate (see Sections 5.1.3 and 5.2.2).

In the case of the CMSX-10K tests the 0.55% strained micrographs also revealed γ'-shearing events by Eggeler-pairs. Interestingly, the CMSX-10 tests did not display a visible creep minimum (Figure 5.15). The absence of a visible creep minimum in CMSX-10K is likely to result from the slow rise of the dislocation density paired with the comparatively faster micro-structural transformation (rafting) and onset of γ'-shearing. As a result the microstructure has fully rafted with 0.55% plastic strain in CMSX-10K, whilst exhibiting a lower interfacial dislocation density than the CMSX-4 tests strained to the same amount. As outlined for the CMSX-4 tests, the γ'-shearing mechanism by Eggeler-pairs requires a formation reaction by vacancy assisted dislocation climb in the γ-phase. This diffusion length has been quantified for the CMSX-4 series in Section 4.4.3. Using the same approach, the diffusion length required for Eggeler-type shearing events with the 18:3 CMSX-10K test cycle was quantified at 62.92 cycles. Thus, Eggeler-type shearing is expected to be possible at comparatively lower accumulated plastic strains (<0.1%) than with CMSX-4 ($\sim 0.35\%$). The limiting factor for Eggeler-pair shearing events in CMSX-10K is thus not insufficient vacancy assisted climb to form Eggeler-pairs (as with CMSX-4) but rather the insufficient supply of dislocations. With the γ'-shearing events then depending on the supply of dislocations, such events scale with the accumulated dislocation density. Crucially, the creation of interfacial networks and γ'-shearing happens simultaneously in CMSX-10 rather than after each other thus not resulting in a visible strain-rate minimum. Further tests, interrupted at smaller strains are however required to confirm this hypothesis.

The role of interface topology on non-isothermal creep

The topology of the interfacial networks is deformed by the interface plane it surrounds, which itself depends on the γ'-phase fraction variation. Section 5.3 has laid out how the non-isothermal cycling rate impacts the interface topology, with 9:3 cycles resulting in the most multi-faceted and disrupted interface. A subsequent heat treatment of this test cycle at 905 °C for 2h resulted in a smoother interface with more regular interfacial dislocation spacing (see Section 5.3). Whilst the heat treatment did not break the paired dislocations on the interfaces it did result in an interface topography that was more comparable to the 27:3 cycles which exhibited a significantly lower strain rate. An even lower strain rate was measured for the CMSX-10 tests, for which the cyclic γ'-dissolution was smaller than measured for CMSX-4 (see Section 4.4.6). This highlights the importance of cyclic γ'-phase stability as a design criterion for better non-isothermal creep resistance.

5.6 Summary

In this chapter, the cyclic creep response of the alloys CMSX-4 and CMSX-10K for a tertiary-creep dominated base condition, cycling into the γ'-rafting regime was analysed. It was found that under these conditions the creep strain rate, the onset of γ'-rafting and the formation of interfacial networks is considerably faster than compared to isothermal testing at base temperature.

The creep life under these cyclic conditions is driven by the faster dislocation accumulation (in comparison to isothermal tests) and depends on the formation and stability of interfacial dislocation networks rather than γ'-rafting kinetics. The interfacial networks were found to consist of classical single dislocation networks as well as paired dislocation networks. The paired character resulted from becoming embedded in the outer layer of the γ' due to the repeated exposure to the peak temperature. The interfacial networks were found to contribute to the creep resistance of both alloys studied during non-isothermal exposure. The strain rate acceleration has been linked to the onset of γ'-shearing by dissimilar Burgers vector pairs and a negative impact of rafting during non-isothermal creep exposure. A good cyclic γ'-phase fraction stability was further linked to a higher non-isothermal creep resistance. Lastly, the non-isothermal cycling in CMSX-4 resulted in the formation of γ'-tertiaries, whilst the identical thermal cycling did not precipitate γ'-tertiaries in CMSX-10K.

Chapter 6

Non-isothermal Creep Modelling

This chapter will lay out a dislocation-based non-isothermal creep model that utilizes the dislocation theory presented in Chapter 2, using the non-isothermal parameter modelling presented in Chapter 4.4, and incorporates the experimental observations described in Chapter 5. This chapter is structured into four sections. First, established dislocation-based creep models and their key equations are reviewed to give a general overview of the existing creep models in Section 6.1. The structure of the developed model is described in Section 6.2. Section 6.3 then presents the results of various parameter studies with the developed model. Key results are discussed and compared to synchrotron results in Section 6.4.

6.1 Literature review of creep modelling

Prior to in-depth micro-structural analysis of creep tests using the transmission electron microscope, the high temperature creep deformation was commonly approximated with empirical models. The interested reader is referred to Poirier [150] for an in-depth discussion of such empirical approaches. As the deformation theory in superalloys developed (see Chapter 2), it was possible to not only interpolate between experimental datasets using empirical models but to also develop theoretical and physics-based modelling approaches. The benefit of such physically-based creep models is that they allow quantitative parameter studies and have, to a certain extent, predictive parameter capabilities which can help to reduce development costs of improved alloys.

The principal challenge in physical based modelling lies in capturing the mechanisms, properties and external conditions with adequate formulations to bridge the equations across significant length scale differences (e.g. lattice misfit stresses to macroscopic strains) whilst containing as few fitting parameters as possible. This has been achieved by a number

of dislocation-based, micro-structurally explicit isothermal creep models, each describing deformation in a self-contained code architecture [52, 63, 204, 130, 199]. Additionally, a non-isothermal creep model which is not explicitly based on the microstructure evolution has been proposed by Graverend *et al.* [117].

The core concepts and equations from established models that could best be adapted into a non-isothermal creep framework are reviewed in Section 6.1.1 of this chapter. Section 6.2 presents the code architecture of the model developed. In Section 6.3 the computational results are presented and discussed further.

6.1.1 Dislocation based deformation mechanisms

Chapter 2 laid out that high temperature creep deformation is carried by the motion of dislocations through the γ/γ'-microstructure. The motion and deformation accumulated in the microstructure by individual dislocations can be directly simulated but this requires significant calculation power, time and a number of assumptions (see Yashiro *et al.* [224] and others [91, 213]).

Considering an average dislocation density of $10^{12} - 10^{14}$ $[m^{-2}]$ in superalloys [7, 6, 50], it is computationally more efficient to estimate the dislocation interaction energy and resulting deformation difference rather than to calculate every single dislocation line motion. Therefore, an indirect approach has been implemented by all the creep models cited in Table 6.1.

As the designed creep models are based on experiments performed in specific creep regimes, the models tend to include those mechanisms that are lifetime limiting in the specific creep regime studied experimentally (see Table 6.1).

Dyson and Galindo-Nava consider the γ'-precipitates as non deformable, such that only the dislocation activity in the γ-matrix by climb-glide limits lifetime. This approximation is designed specifically for the tertiary creep regime (see Chapter 2.3.3). To model the mechanical deterioration in glide-climb models that would otherwise describe a continuum vacancy exchange process (*i.e.* steady-state deformation), the calculations rely on a damage parameter description (see models [130, 158, 159]). This damage parameter assumes gradual and continuous weakening, on the grounds that dislocation activity results in void condensation eventually leading to failure by creep porosity [130].

Galindo-Nava *et al.* [73] were able to capture the experimentally observed tertiary creep regime deformation and allowed adaption of the creep deformation in the rafted regime by incorporating effective diffusion lengths based on the evolution of the rafting microstructure.

Table 6.1 Features included (○) and explicitly described (●) in the cited creep models.

Author	γ-glide	γ'-shear	γ-climb	rafting	coarsening
[52] Dyson *et al.*	●		●		○
[73] Galindo-Nava *et al.*	●		●	○	○
[130] Ma *et al.*	●	●	●	○	
[199] Svoboda *et al.*	●	●	●	●	○
[204] Tinga *et al.*	●	●	●	●	○
[63] Fedelich *et al.*	●	●	●	○	○

To the best knowledge of the author, the most comprehensive isothermal creep models to-date have been proposed by Tinga [204, 206, 205], and Svoboda & Lukáš [195–199]. These models include the deformation contribution through γ'-particle shearing as well as a space-resolved description of rafting and coarsening. Both models are based on the morphological evolution of a clearly defined simulated cell domain (see further detail in Section 6.2.1). Svoboda's model in particular has been extensively reviewed and has been proven to give feasible approximations for the isothermal creep deformation of CMSX-4 in the primary, tertiary and rafting regime [199]. The deformation equations in the model by Svoboda and Lukáš are driven by the dislocation density evolution (the strain rate is proportional to the density) in the different regions of the simulated cell that are passed between the otherwise independent code sections. This makes the model easily adaptable to include new mechanisms and thus a good base architecture for a non-isothermal creep model that is also microstructurally explicit. The key equations that allow adaptation into the non-isothermal code architecture have been taken from authors such as Svoboda & Lukáš and will be reviewed and discussed in the following section.

6.2 Overview of the non-isothermal model structure

The computational architecture of the non-isothermal creep model developed here is shown in Figure 6.1. The model is subdivided into three computing steps: physical *constants*, *cyclic* parameters and non-isothermal *dislocation* evolution.

In the first step, the initial physical constants and thermodynamic data are calculated for the applied stress and temperature field in the non-isothermal tests to reduce computation time.

In the second step, the non-isothermal evolution of various creep parameters under thermal cycling is estimated based on the previously computed alloy-specific constants. The

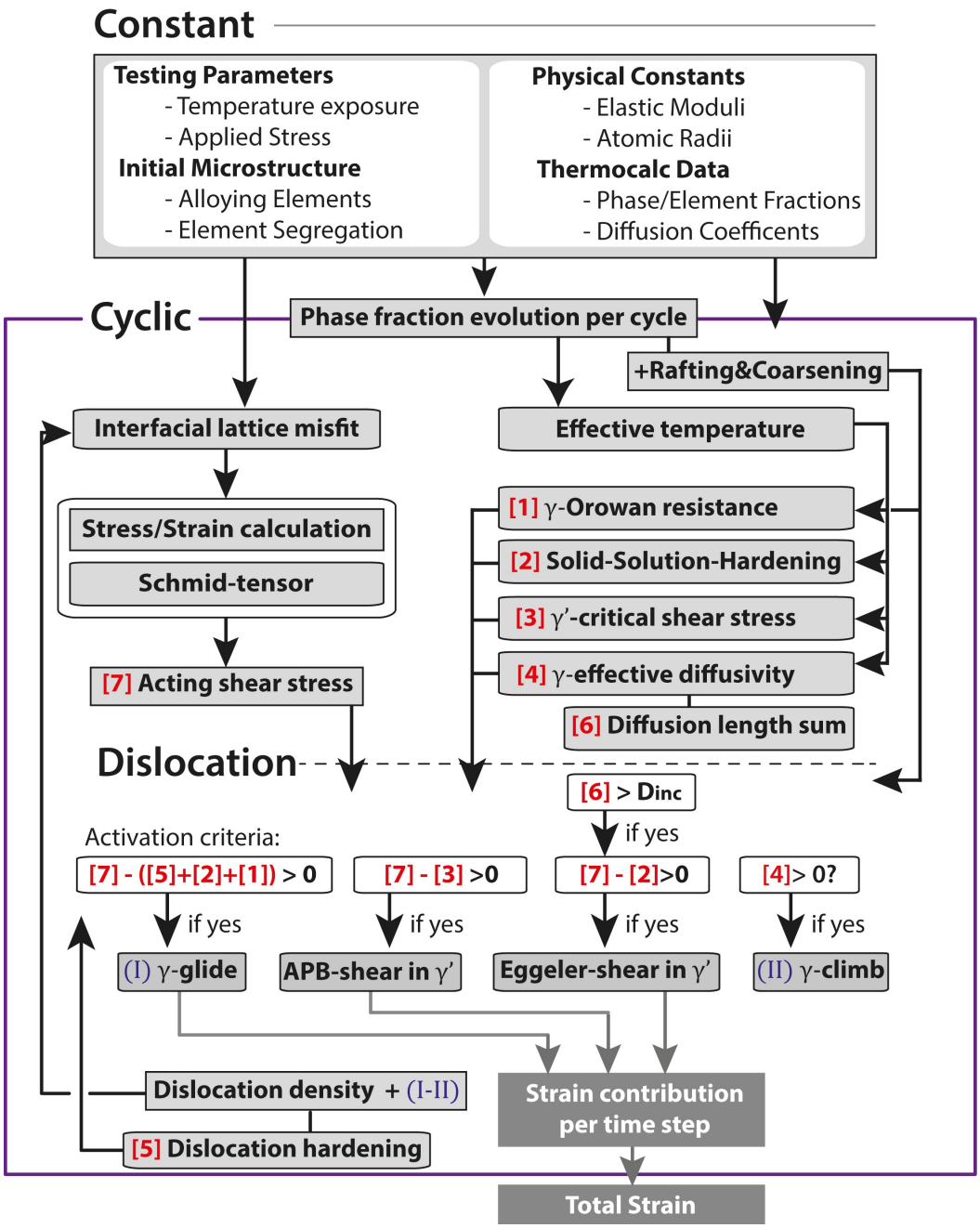

Fig. 6.1 Overview of the devised non-isothermal creep model architecture. The model is organised into three distinct steps: the estimation and read-in of physical constants, quantifying the creep parameters in relation to thermal cycling and the calculation of dislocation mechanisms during said cycling. See text for further details.

equations used to estimate these parameters as well as the specific parameter evolution over the 900 °C - 1050 °C thermal cycling used for the non-isothermal creep experiments (see Section 3.2) are shown in Section 4.4. As Figure 6.1 suggests, the parameter evolution is primarily driven by the non-isothermal phase fraction evolution during a single thermal cycle. As demonstrated in Section 4.4, most cyclic parameter evolutions (e.g. γ-Orowan resistance) are based upon the calculated effective temperature (see Section 4.4.3). The key creep parameters calculated are then numbered in red from 1-7. An exception to this is the calculation of the non-isothermal interfacial lattice misfit evolution which is, according to Section 4.4.7, estimated using the molar volume calculated with ThermoCalc. Using equations further described in Section 6.2.2 the acting shear stresses are then calculated using the current effective interfacial lattice misfit.

In the third step, the previously calculated creep parameters are first used to estimate which of the four modelled dislocation mechanisms might be operative. The activation criteria are displayed in white boxes, referencing the creep parameters and their mathematical relationship required for activation. Whereas most mechanisms depend on a single activation criterion, Eggeler-shear is subject to two activation criteria (these will be described further in Section 6.2.4). Where the activation threshold is exceeded, the dislocation mechanism becomes active and contributes to the modelled strain accumulation (in the case of γ-glide and γ'-shear by APB or Eggeler-pairs) and contributes to the dislocation density accumulated in the microstructure (i.e. γ-glide and γ-climb). The incremental plastic strain, accumulated by each dislocation mechanism on every slip system, is further calculated and added up to estimate the total plastic strain accumulated in the modelled sample (ε^p).

To mimic the constant deformation under creep conditions, the creep model consists of a calculation loop across the *cyclic* and *dislocation* layers (highlighted by a purple line surrounding the cyclic parameter calculations). This cyclic re-calculation of the parameters allows modelling interdependent parameter evolutions, of which three have been included in the model. Firstly, the microstructure evolution subject to rafting and coarsening (outlined in Section 4.4.8) is considered and changes the γ-Orowan resistance over time as well as the dislocation mechanisms (e.g. γ-climb with changing γ-channel volumes). Secondly, the total dislocation density calculated after each cycle step is used to re-calculate the resulting effective interfacial lattice misfit in line with the theory outlined in Section 4.4.7 (this will be further explained in Section 6.2.2). Thirdly, from the accumulated dislocation density the resulting dislocation hardening in the γ-channels is calculated and used as a threshold for the activation of γ-glide and γ'-shear by Eggeler-pairs. Furthermore, the dislocation hardening is used to calculate the strain contributions from each of the contributing parameters. The

dislocation evolution is thus one of the key parameters driving the modelled non-isothermal creep response. To illustrate how the net dislocation density is calculated at each time step, the relationship used in the model is given in Equation 6.1.

$$\rho_{x,K}^{t_2} = \rho_{x,K}^{t_1} + \dot{\rho}_{x,K}^{(glide)} \partial t - \dot{\rho}_{x,K}^{(climb)} \partial t \tag{6.1}$$

In the model, the dislocation evolution on each slip system (K) and in each region of the simulated cell are calculated (see Section 6.2.1). The overall dislocation density at a given time step (ρ^{t_2}) results from the dislocation density at the previous time step (ρ^{t_1}) as well as the sum of all dislocation reactions per time increment (∂t) due to annihilation (resulting from γ-climb) and multiplication events (due to γ-glide), according to Equation 6.1. It is important to point out that the dislocation density in the glide and climb equations have the unit m^{-1} (as used by Svoboda and Lukáš [195–199]), whereas the remaining equations as well as all figures use the conventional unit of m^{-2}.

$$\varepsilon_z = \sum_{K=1}^{12} \varepsilon_{z,K} + \varepsilon_{xz,K}^{(glide)} \partial t + \varepsilon_{yz,K}^{(glide)} \partial t + \varepsilon_{zz,K}^{(glide)} \partial t + \varepsilon_{xz,K}^{(shear)} \partial t + \varepsilon_{yz,K}^{(shear)} \partial t + \varepsilon_{zz,K}^{(shear)} \partial t \tag{6.2}$$

The total strain accumulated in the direction of applied stress (z-direction) results from the sum of all three γ-channel region strain contributions by γ-glide and γ'-shear (either APB or Eggeler-shear if activated) according to Equation 6.2.

6.2.1 The model domain

The term domain here refers to the modelled volume of the microstructure. The domains used in the models of Dyson and Galindo-Nava [52, 73] are not explicitly defined, allowing faster computation.

In the present non-isothermal creep model, a domain is explicitly defined, following the model structure of Fedelich, Tinga, Svoboda and Ma [63, 204, 199, 130]. The benefit of defining a domain explicitly lies in the ability to compute the local stresses and strains in each region of the modelled simulated cell. The dislocation activity in each region of the simulated cell can hence be based upon the stress/strain magnitude in the local region. In the cited models, the γ/γ'-microstructure in a test piece is assumed to consist of identical simulated cells, where the creep deformation is scaled up from a single simulated cell. This greatly reduces complexity and calculation time. The domain defined here is identical to that laid out by Svoboda [199], consisting of one γ'-particle surrounded by γ-matrix channels

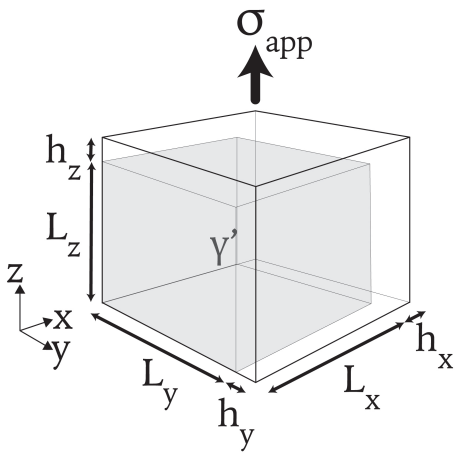

Fig. 6.2 Schematic of a superalloy single-crystal simulated cell domain, consisting of three γ-channels ($h_x - h_z$) around one γ'-precipitate in three dimensions ($L_x - L_z$) shaded in grey.

on three sides (see Figure 6.2). Whilst the γ'-precipitate dimensions are clearly defined by the variables $L_x - L_z$, the dimensions of the γ-channels are less evident. Svoboda and Lukáš [195–199] define the channel regions ambiguously by not defining the corners where two channel regions overlap.

Fedelich [63, 66, 64] resolves this, by defining two cases - one in which all channels are distinctly separate and another in which the the corners common to both channels overlap. Fedelich found that the first case describes octahedral slip in γ, whilst overlapping channels describe cubic slip (enabled by cross-slip). This is due to the difference in stress gradients resulting from the γ/γ'-channel boundary description [63].

Tinga, on the other hand, added additional regions by dividing the interfaces, thus putting more emphasis on the stress gradients located on the γ/γ'-interfaces [204, 206, 205].

However, the domain defined here does not resolve the ambiguity in the Svoboda and Lukáš model, as no significant cross-slip was observed in the microstructures (see Chapter 5) and the approach by Tinga *et al.* would further increase computation time with no obvious benefit.

6.2.2 Stresses and strains modelled

Due to the symmetry of the simulated cell and the direction of the applied load, two sets of equations have to be solved to calculate the resulting 24 stresses and 24 strains in every direction (x, y and z) of every region of the simulated cell (of all three γ-channels and the precipitate). 24 equations result by solving Hooke's Law (see Equation 6.3) for every region

to calculate the stresses and strains contained within each region, 15 equations result from equilibrium conditions and the remaining nine equations are obtained from interfacial contact conditions resulting from the stresses reaching across coherent interfaces [195–199].

$$\sigma_{K,ij} = C_{ijkl} \cdot e_{K,kl} \tag{6.3}$$

$$e_{x,22} - e_{P,22} = \delta_{cpcp} - \frac{b}{\sqrt{2/3}} \sum_{K=1}^{12} \rho_{x,K} \cdot m_{K,22} \tag{6.4}$$

As an example, the γ/γ'-contact condition in the x-channel in y-direction across all twelve slip systems (K) is shown in Equation 6.4. The contact condition according to Svoboda and Lukáš [199] is a function of the interfacial strain difference in the γ-channel ($e_{x,22}$) and γ'-precipitate ($e_{P,22}$). This strain difference results from the initial constrained interfacial misfit (δ_{cpcp}), the product of the deposited dislocation density in this region ($\rho_{x,K}$) and the Schmid factor in this region ($m_{K,22}$).

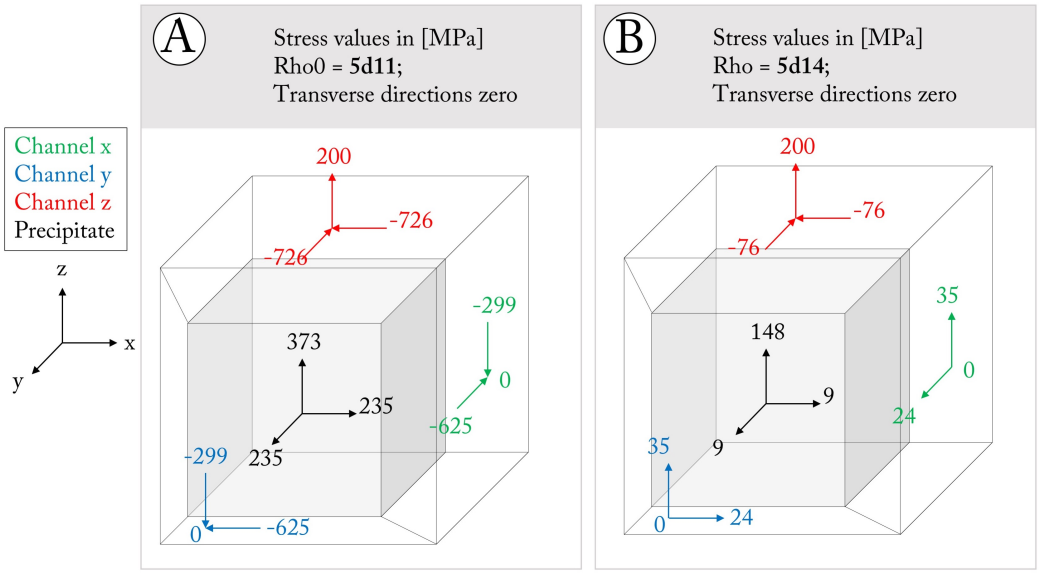

Fig. 6.3 γ/γ'-coherency stresses in the three different γ-matrix channels and precipitate of an ideal simulated cell (values in MPa) in relation to the contained dislocation density: (a) with a dislocation density of $\rho = 5 \cdot 10^{11}[m^{-2}]$ and (b) $\rho = 5 \cdot 10^{14}[m^{-2}]$.

The assumption is that the applied stresses, the initial constrained misfit and the deposited interfacial dislocations are interdependent on one another (see Chapter 4.4.7). Due to the contact conditions defined, the magnitude of the stresses in all four regions of the simulated cell change in relation to the dislocation density deposited on the γ/γ'-interfaces (referred

to as ρ). This is further illustrated in Figure 6.3 that displays a calculation of the resulting stresses in each region of the simulated cell under an applied external stress of 200 MPa in $\langle 001 \rangle$-direction. Using the interfacial misfit stresses at base temperature (900 °C), the resulting stresses were calculated for a dislocation density of $\rho = 5 \cdot 10^{11} [m^{-2}]$ in Figure 6.3a which represents a fully-heat treated microstructure and $\rho = 5 \cdot 10^{14} [m^{-2}]$ which represents a heavily deformed microstructure in Figure 6.3b.

The increase in dislocation density and the assumption that the accumulated dislocations become interfacial dislocations of mixed character (see [199]) thus results in a significant reduction in local stresses of the microstructure. This is particularly pronounced for the γ-channel stresses on the coherent interfaces, which change from areas of large compressive stresses into areas of low compressive and tensile stresses.

The notion that all interfacial dislocations are of mixed character disagrees with the calculation by Long *et al.* [128], where it was shown that a gradual transformation of interfacial dislocations from mixed to edge type takes place across the interfaces. Incorporating this effect directly into the model would require experimental data on the transformation time between both dislocation types in relation to applied stresses and temperatures. However, it is assumed that this effect is captured indirectly in the model already, as the dislocation hardening effect described in Equation 6.7 accounts for the hardening effect that a gradual dislocation transformation has on the creep response.

Furthermore, should the creep model incorporate the effect of element alloy scatter by using rhenium-based variants (described in Chapter 4.2), the stress-strain equations would have to be re-tested for high γ'-volume fractions as seen in the inter-dendritic regions, as the current equations published by Svoboda [199] and Tinga [204] are only valid within the boundary conditions of a near-average CMSX-4 simulated cell.

6.2.3 Describing dislocation glide

Dislocation glide according to Svoboda and Lukáš

The Orowan equation (Equation 2.2 in Chapter 2.3.1) is commonly the basis of a dislocation slip description. Svoboda and Lukáš [199] adapted the equation by substituting the velocity with the shear stress difference (see Equation 6.5), such that the slip rate on a glide plane ($\dot{\gamma}_K$) is proportional to the acting shear stress on each glide system (τ_K) and the resistance to dislocation glide (τ_{K_0}). The units and scaling in the model published by Svoboda [199] were balanced and fitted to experimental isothermal creep data of CMSX-4 from Lukáš, by using a scaling parameter W_1 that took a value of $W_1 \simeq 2 \times 10^{-21} [\frac{m}{sPa}]$ for γ-dislocation glide. The

exponent n in the model was similarly fitted to the experimental dataset and subsequently set at $n = 1$ for dislocation glide. According to Svoboda and Lukáš [199] the deposition rate for interfacial dislocations ($\dot{\rho}_K^{glide}$) by γ-slip then follows in Formula 6.5.

$$\dot{\rho}_{K_x}^{glide} = \dot{\gamma}_{K_x} \frac{\sqrt{2/3}}{b} \quad | \quad \dot{\gamma}_{K_x} = W_1 \cdot \rho_{Kx} (\tau_{K_x} - \tau_{K_{0,x}})^n \tag{6.5}$$

According to Svoboda [199], the total plastic strain rate results by adding up the strain increments from all active slip systems in a matrix region, according to Formula 6.6.

$$\dot{\varepsilon}_{ij} = \sum_{K=1}^{12} \dot{\gamma}_{K,x} \cdot m_{K,ij} \tag{6.6}$$

According to Equation 6.6, the plastic strain deformation on each slip system ($\dot{\varepsilon}_{ij}$) at each time step results from the slip rate on the respective slip system times the Schmid factor of that slip system ($m_{K,ij}$). This assumes an identical slip length from all mobile dislocations in the γ-phase.

The resistance towards γ-dislocation glide in the x-channel $\tau_{K_{0,x}}$ is based upon the Orowan resistance and dislocation hardening that also incorporates the interaction between neighbouring slip planes and is laid out in the publication by Svoboda and Lukáš [199] and the parameters are reviewed in Section 2.3.2.

Dislocation hardening is modelled by a linear multiplication factor (2.2×10^{-8}) and results from approximating the line energies of screw and mixed dislocation (see equations outlined in the appendix of Svoboda and Lukáš [199] for the derivation of the equation).

To adapt the glide equations to the non-isothermal model all temperature dependent parameters were calculated for the studied temperature field. The temperature dependent parameters of the Orowan resistance include the shear modulus and effective channel width and these were estimated in Section 4.4.2. In addition, the glide resistance due to solid solution hardening in the γ-phase ($\tau_{\gamma-SSH}$) was added and the resulting overall resistance to γ-dislocation glide was calculated according to Equation 6.7. The non-isothermal quantification of the solid-solution resistance used for this model has been laid out in Section 4.4.4.

$$\tau_{K_0} = \sqrt{\frac{2}{3}} \frac{Gb}{h} (1 + 2.2 \times 10^{-8} \cdot \rho_K) + \tau_{\gamma-SSH} \tag{6.7}$$

The channel width (h) in Equation 6.7 is not only subject to continuous dissolution and re-precipitation due to the non-isothermal cycling but further evolves due to rafting and coarsening (see Section 4.4.8). The third factor of influence on the evolution of the channel

width is the precipitation dynamics of γ'-tertiaries, which have been observed in the alloy CMSX-4 (see Section 5.4). The impact of the effective channel width (the net distance between γ and γ'-phase including γ'-tertiaries) on the modelled creep response is further laid out in Section 6.3.2.

Adapting the dislocation glide equations

The descriptions of dislocation hardening and dislocation generation were adapted upon implementation in the non-isothermal model to better reflect experimental findings on the dislocation evolution and stabilise the dislocation equations.

To reflect the higher dislocation hardening contribution from γ/γ'-interfacial networks, which initially form square lattices that gradually transform in shape according to Field *et al.* [67]), the dislocation contribution (2.2×10^{-8}) was squared in this model (resulting in 4.84 $\times 10^{-16}$).

The dislocation generation according to Equation 6.5 is proportional to strain rate and estimates an addition of dislocations four orders of magnitude higher than the dislocation activity resulting from γ'-shear and γ-climb (see results section of this chapter). Whilst dislocation glide is seen as a key driving force for creep deformation, the experimental results shown in the Chapter 5 indicated a slower and more gradual dislocation evolution. Furthermore, the analysis of the recorded strain rates (Figure 5.1) in the previous chapter pointed out that the onset of γ'-shear is a key contributor to the strain rate acceleration and thus γ-glide and γ'-shear contributions would likely accumulate similar strain rates. To slow and stabilise the dislocation generation to a level that correlated to the order of magnitude of the dislocation activity by γ'-shear the equation was changed to 6.8. With the fitting parameter S harmonising the dislocation density and scaling the result with a value of $1.27 \cdot 10^{-9}$.

$$\dot{\rho}_{K_x}^{glide} = \frac{\sqrt{2/3}}{b} \cdot S \cdot exp(-\dot{\gamma}_{K_x}) \tag{6.8}$$

The result section of this chapter will show that this dislocation evolution results in a balanced glide-climb interaction that is in line with the mechanisms observed experimentally.

6.2.4 Describing dislocation shearing

The non-isothermal creep model depends on two different modes of γ'-deformation. The classical shearing by a pair of dislocations of similar Burgers vectors (APB-shearing activated by a sufficiently high stress to form an APB-fault) as outlined in Section 2.3.1 and the shearing

by dissimilar Burgers vector pairs (Eggeler-pairs, formed by the glide and climb of dissimilar Burgers vector dislocations), observed in Chapter 5.1.3 and 5.2.2.

Modelling APB-shearing

Svoboda and Lukáš describe slip through γ'-precipitates analogously to γ-slip (see Equation 6.9) [199]. This allows an estimate of characteristic particle shear stresses as well as the critical shear stress in every channel region of the simulated cell for γ'-glide of a dislocation pair separated by an APB-fault.

$$\dot{\rho}_{K_x}^{shear} = \dot{\gamma}_{K_x} \frac{\sqrt{2/3}}{b} \quad | \quad \dot{\gamma}_{K_x} = W_1 \cdot \rho_{Kx} (\tau_{K_x} - \tau_{K_{0,x}})^n \tag{6.9}$$

However, the advances made in studying high-temperature creep in superalloys (see Chapter 2.3.1) since Svoboda and Lukáš published their isothermal creep model result in three aspects of the γ'-shearing model theory requiring reworking. Firstly, the shearing exponent (n in Equation 6.9) was chosen by Svoboda to be in line with visco-plastic flow models at $n = 3$ [199]. This effectively means that, according to Svoboda, over time the contribution by γ'-shear becomes significantly more important to the micro-structural degradation than γ-glide. This higher exponent for γ'-shear was chosen by Svoboda and Lukáš in order to model a rising creep rate that resembles the tertiary creep stage (see [181]) because, in their model, the primary creep stage is driven by γ-glide. Furthermore, according to Svoboda every shearing dislocation resulted in an annihilation event thus decreasing the overall dislocation density. A third shortcoming of the isothermal model by Svoboda is that the resistance to γ'-shearing ($\tau_{K_{0,P}}$) is not particle-size dependent.

The dislocation theory outlined in Section 2.3.1 assumes that γ'-shearing depends on the entry of dislocation pairs from the γ-matrix. So far there is no indication for γ'-shear to result in the formation of new dislocations in the γ'-phase. The higher exponent for γ'-shear (suggesting self multiplication) therefore seems unjustified and in the current model the shearing exponentials for γ-glide and γ'-shear are identical at $n = 1$. The faster strain accumulation associated with the multiplication of γ'-shearing by APB-pairs in the tertiary creep stage does not result from a higher exponential factor of the activated mechanism but rather due to the decreasing resistance of growing γ'-rafts (modelled in Section 4.4.8) to shearing (modelled in Section 4.4.5). The respective rafting and critical resolved shear stress equations in the cited chapters have further been adapted to the experimental thermal cycles.

The impact γ'-shearing events have on the overall dislocation density are not yet fully understood. It is however unlikely, that all shearing events result in a decrease of dislocation

density as suggested by Svoboda and Lukáš [199] or Tinga [204]. The ratio of γ-glide to γ'-shear and the impact of potential dislocation density reduction due to dislocation γ'-shear will thus be further investigated in Section 6.3.4. In the default model presented the dislocation density will not be impacted by γ'-shearing dislocations (see Equation 6.1), as shearing dislocations are thought to originate from the γ-phase and, due to the very low diffusivity in the γ'-phase (see Chapter 4.1.3), are expected to not have sufficient time to climb onto a new slip plane whereon an annihilation reaction would be facilitated upon exiting the γ'-phase.

Modelling Eggeler-shearing

The dislocation analysis presented in Chapter 5.1.3 for CMSX-4 and Chapter 5.2.2 for CMSX-10 revealed that the primary mode of dislocation motion through the γ'-phase was by dislocation pairs of dissimilar Burgers vectors (referred to as Eggeler-pairs in this thesis). Dlouhy *et al.* [49] outlined two scenarios for the motion of Eggeler-pairs. Using high-resolution TEM Srinivasan *et al.* [190] could show that both dislocations exhibit distinct cores and that thus the glide-climb mechanism outlined by Dlouhy *et al.* would be the most likely method for the dislocation motion. Srinivasan *et al.* further argued that because the glide-climb Dlouhy configuration would require the continuous exchange of vacancies between the leading and trailing dislocation to facilitate γ'-shear, the mechanism would be rate dependent on diffusion driven climb. Srinivasan *et al.* approximated the strain rate attributed to the γ'-shear of Eggeler-pairs in Equation 6.10. The equation is based on the Orowan equation and is primarily driven by the climb velocity of $\frac{a}{2}\langle 110\rangle$ dislocations (given by $v_{CED}^{\langle 110\rangle}$. $D_{\gamma' s}$ is the self-diffusion coefficient in the γ'-phase, b_e the Burgers vector of the edge component, d_{CED} is the mean separation distance between individual $\frac{a}{2}\langle 110\rangle$ dislocations (set at 25 Å based on HRTEM work), Ω is the atomic volume, k is the Boltzmann constant and $\frac{F_c}{L}$ is the total climb force per unit length on the dislocation.

$$\dot{\gamma} = 0.5 \cdot b \cdot \rho \cdot v_{CED}^{\langle 110\rangle} \quad | \quad v_{CED}^{\langle 110\rangle} = \frac{2 \cdot \Pi \cdot D_{\gamma' s}}{b_e^{\langle 110\rangle} ln(d_{CED}/2 \cdot b)} \left[exp\left(\frac{F_c \cdot \Omega}{L \cdot b_e \cdot k \cdot T} \right) - 1 \right] \tag{6.10}$$

Using Equation 6.10, Srinivasan *et al.* [190] calculated an overall climb velocity of $v_{CED}^{\langle 110\rangle} = 4 \times 10^{-8} ms^{-1}$ at 1293 K and a secondary creep rate of $\dot{\gamma} = 4.9 \times 10^{-7} s^{-1}$, which was close to that observed for the isothermal creep tests performed for the alloy CMSX-6 at this temperature.

The equations by Srinivasan *et al.* are fitted to a steady-state secondary creep regime (see [190]). Therefore the model is based on the assumption that all deposited dislocations

have the potential to form Eggeler-pairs from the beginning. Whilst this simplification is possible in an isothermal framework, it is unfeasible to replicate in non-isothermal tests. Due to the continuous thermal cycling, only a fraction of all γ-dislocations have undergone the glide-climb formation mechanism required in the γ-phase to form Eggeler-pairs [55] and shear the γ'-phase in a Dlouhy configuration [49] (by a self-fed glide-climb mechanism). The variable $\rho_{K_x}^{D_{inc}}$ in Equation 6.11 describes the dislocation density of shear activated dislocations and is calculated at each time step (around 14 % of all γ-dislocations exhibit shearing potential at the point of initial activation). The experimental analysis indicated that the minimum strain-rate observed in the CMSX-4 test series overlaps with the onset of γ'-shearing by Eggeler-pairs. Relating the strain-rate minimum for the CMSX-4 test series to the mean diffusivity and resulting diffusion length revealed a strong correlation (see Chapter 4.4.3). Based on the experimental analysis, an activation threshold was estimated amounting to a mean diffusion length coefficient of $D_{inc} > 9.76 \cdot 10^{-12}$ [m s^{-2}] required to start dislocation shearing by Eggeler-pairs in the non-isothermal creep model (this is the first activation criterion for this mechanism shown in Figure 6.1).

A further point to consider when using Equation 6.10 proposed by Srinivasan *et al.*, is that the equation is primarily driven by the diffusivity in the γ'-phase. Srinivasan *et al.* approximated this parameter with the self-diffusivity of nickel in the γ'-phase ($D_{\gamma' s}$). To determine the temperature dependence of the γ'-interdiffusivity, the experimental dataset published by Frank *et al.* [68] was taken.

Using the effective temperature approach outlined in Section 4.4.3, the evolution of the diffusivity in the γ'-phase during a 27:3 non-isothermal cycle was estimated and is plotted in Figure 6.4A together with the effective diffusivity in the γ-phase (D_{effm}, shown in Figure 4.26B). Comparing the two plots, it is apparent that the γ-inter-diffusivity is substantially faster (by over one order of magnitude) than in the γ'-phase.

Using the γ'-diffusivity the velocity of $\frac{a}{2}\langle 110 \rangle$ dislocations is calculated using Equation 6.10 and the resulting evolution during a 27:3 non-isothermal test cycle is plotted in Figure 6.4B. The dislocation density reflects the change in diffusivity with temperature and thus shows an increase by a factor of 10 at the peak temperature compared to the diffusivity measured at the base temperature hold.

Unlike the dislocation climb velocity outlined in Equation 6.13, the velocity for the γ'-glide and climb of Eggeler-pairs in Equation 6.10 is not dependent on the applied stress. Srinivasan *et al.*[190] argued that as the γ'-interdiffusion is very low, this parameter would be the rate limiting for this mechanism and thus no stress dependence would be needed. This however results in the activation of dislocation shearing from all slip systems and entry of

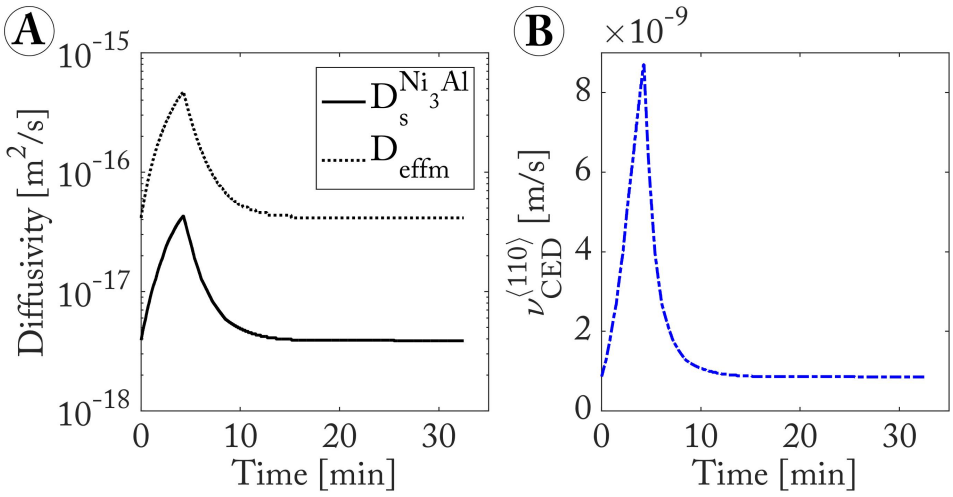

Fig. 6.4 (a) γ-interdiffusivity (dotted curve) and γ'-interdiffusivity (solid curve), (b) dislocation velocity of the Dlouhy-configuration in γ' (blue dash-dotted curve).

dislocations into the γ'-phase from all three γ-channels. With the progression of rafting, the vertical channels are gradually lost. To capture this dependency, a second activation criterion (a threshold stress) was introduced ($\tau_{K_{P,x}} - \tau_{K_{SSP,x}} > 0$) that is driven by the acting shear stress and solid solution hardening in the precipitate phase (see Figure 6.1). The non-isothermal evolution of the latter parameter has been modelled in Section 4.4.4.

The non-isothermal shear rate contribution from the Eggeler-shear mechanism used in this model is then estimated using Equation 6.11.

$$\dot{\gamma}_{K_x} = m_K \cdot b \cdot \rho_{K_x}^{D_{inc}} \cdot \nu_{CED}^{\langle 110\rangle} \tag{6.11}$$

It is important to note here that the equation currently does not take into account the Burgers vector diversity of the activated slip systems. This would be important when using the model to calculate the creep response with an applied stress not in the [001]-direction, as the Eggeler-pairs require two different yet compatible Burgers vectors to form (see Eggeler *et al.* [55]).

The parameter description and its implications on the modelled creep rate is further analysed in Section 6.3.4.

6.2.5 Describing dislocation climb

Dislocation climb is a non-conservative dislocation motion (see Section 2.3.1) and thus the rate of climbing edge dislocation segments is proportional to the volumetric change of

the system. The change in volume of each region of the simulated cell is driven by the total energy of the system which is proportional to the plastic deformation, the exchange of vacancies and the micro-structure transformation due to rafting and coarsening. Under isothermal and constant stress conditions the total energy of the system seeks to reach a minimum *i.e.* thermodynamic equilibrium. This process has been described by Svoboda and Lukáš [199], modelling the climb rate as a diffusion driven function proportional to the sum of the dislocation, elastic and potential energies of the system.

When considering non-isothermal tests a number of additional points have to be considered. Non-isothermal tests do not evolve towards a single thermodynamic equilibrium, instead including local minima (during each temperature cycle) and a global minimum. Trial calculations with the model by Svoboda and Lukáš [199] revealed that the model only returned feasible results using near optimum γ'-phase-fractions ($\sim 70\%$). However, in non-isothermal calculations the phase fractions change significantly and continuously. Furthermore, the non-isothermal tests displayed a significantly faster rafting and coarsening rate than observed previously for isothermal tests. For these reasons, the current energy dissipation rate model would require reworking to describe non-isothermal creep, requiring additional experimental datasets of single and multi-cycle non-isothermal creep tests of different alloys and non-isothermal cycling conditions. As this could not be achieved in the scope of this thesis, the micro-structural evolution is not driven by the reduction of the total energy of the system. Rafting and coarsening are instead based on experimentally fitted equations presented in Chapter 4.4.8.

An alternative climb model has been described by Dyson *et al.* [52]. In the cited study it is argued that dislocation glide and climb mechanism are coupled. Such that vacancies are absorbed by dislocations facilitating climb and emitted by γ-gliding dislocations. The interdependency suggests that a steady-state between both mechanisms is achieved, an approximation that holds well under certain isothermal test conditions (in which diffusion rates and shear rates are similar and the plastic deformation is low) and thus avoids the necessity to calculate the energy dissipation rate of the total system under these conditions.

However, under non-isothermal test conditions it is expected that high temperature exposures result in excess vacancies that allow a significant dislocation recovery which in turn enables a higher dislocation activity at every high temperature exposure (see Viguier *et al.* [215] le Graverend *et al.* [119] and Jacques *et al.* [97]). This hypothesis thus requires a model with a diffusion controlled γ-climb rate independent of the γ-glide rate.

The rate of height change of a channel ($\frac{dh_\gamma}{\partial t}$) due to the climb of dislocations in the γ-channels is approximated in Equation 6.12 by analogy to equations 7 and 8 in [199]. To

simplify the problem it is assumed that all vacancies generated per time step have sufficient time to be absorbed into the force field of edge dislocation segments, which are assumed to be the primary vacancy sinks.

$$\frac{dh_\gamma}{\partial t} = \rho_{mc} \cdot v_c \quad with \quad \rho_{mc} = \frac{N_c \cdot l_c}{V_\gamma} \tag{6.12}$$

The dislocation density in the γ-channels that has been activated to climb by vacancies is given by ρ_{mc}. This parameter depends on the number of climb dislocations (N_c) the average length of the edge character dislocation segments that climb (l_c) per volume of the γ-channel (V_γ).

The climb velocity of extended edge dislocations (v_c) was modelled according to the equations proposed by Argon and Moffat [11] quoted here in Equation 6.13.

$$v_c = \left[\frac{\sigma \cdot \Omega \cdot D_{eff}}{b \cdot k \cdot T}\right] \cdot A \cdot c_j \left(\frac{\chi}{G \cdot b}\right)^2 \tag{6.13}$$

The equation depends on the applied stress (σ) and the mean atomic volume of the alloy mixture (Ω). The latter parameter along with the total temperature (T) and the effective diffusivity (D_{eff}) change with the non-isothermal cycling and are thus estimated for each time step of the thermal cycle in layer two of the creep model. The second term of Equation 6.13 depends on a numerical constant A related to the Poisson's ratio of the material (set at 1050 °C for $\nu = 0.3$), the jog concentration (c_j) and the stacking fault energy (χ).

The recovery rate due to dislocation climb ($\dot{\rho}_{x,K}^{(climb)}$) is further assumed to be given by the height change of the channels ($\frac{dh_\gamma}{\partial t}$) divided by the Burgers vector of the edge dislocation segments (b_e that climbed) according to Equation 6.14.

$$\dot{\rho}_{x,K}^{(climb)} = \frac{dh_\gamma}{\partial t} \cdot \frac{1}{b_e} \tag{6.14}$$

Substituting Equation 6.12 and 6.13 into 6.14 results in Equation 6.15.

$$\dot{\rho}_{x,K}^{(climb)} = \left[\frac{\sigma \cdot \Omega \cdot D_{eff}}{V_\gamma \cdot b \cdot k \cdot T}\right] \cdot P \quad | \quad with \quad P = \frac{N_c \cdot l_c \cdot A \cdot c_j}{b_e} \cdot \left(\frac{\chi}{G \cdot b}\right)^2 \tag{6.15}$$

The rate of recovery due to dislocation climb is thus inversely proportional to the volume of the γ-channels. For a constant flux of vacancies through a gradually rafting and coarsening microstructure, a gradual reduction of the recovery rate then results. Furthermore, equation 6.15 is sorted into two parts, a term in brackets that consists largely of parameters that have

been determined previously and a term summarised with the parameter P that depends on parameters that have not yet been studied non-isothermally (excluding the Burgers vectors which are assumed constant). Furthermore, parameters such as the jog concentration (c_j) and stacking fault energy (χ) are commonly fitting parameters due to insufficient experimental data. Rather than fitting the variables contained in P without experimental verification, for simplification a constant value was assumed. The change in dislocation climb due to thermal cycling is therefore driven by the non-isothermal evolution of the effective diffusivity, temperature and γ-channel volume. The impact of changing the parameter P to reflect a higher dislocation climb ratio was further investigated in Section 6.3.3.

Summary of the dislocation equations

The dislocation density and slip rate descriptions implemented in the non-isothermal creep model for the three key dislocation mechanisms are summarised in Table 6.2.

Table 6.2 Summary of equations used to describe the dislocation density and slip rate contributions from the three defined dislocation mechanisms in the non-isothermal creep model.

Mechanism	γ-glide	γ'-Eggeler-shear	γ-climb
Disl. density ($\dot{\rho}_{K_x}$)	$\frac{\sqrt{2/3}}{b} \cdot S \cdot exp(-\dot{\gamma}_{K_x})$	/	$\left[\frac{\sigma \cdot \Omega \cdot D_{eff}}{b \cdot k \cdot T \cdot V_\gamma}\right] \cdot P$
Slip rate ($\dot{\gamma}_{K_x}$)	$\mathrm{W}_1 \cdot \rho_{K_x}(\tau_{K_x} - \tau_{K_{0,x}})$	$\mathrm{m}_K \cdot b \cdot \rho_{K_x}^{D_{inc}} \cdot \nu_{CED}^{\langle 110 \rangle}$	/

6.3 Results of non-isothermal modelling

The following subsection presents results calculated using the non-isothermal creep model laid out in the previous sections.

Firstly, the influence of different thermal cycles were estimated with the non-isothermal model and are presented in Section 6.3.1. Section 6.3.2 analyses the influence of γ'-tertiaries in combination with rafting and coarsening on the overall creep response. Section 6.3.3 examines the sensitivity of the model to changes in the climb ratio. Section 6.3.4 examines how adapting the Eggeler-type shearing model in the γ'-phase impacts the overall plastic response. Lastly, Section 6.3.5 calculates the creep deformation using the parameters estimated for the alloy CMSX-10 and as such examines the influence of alloy composition on non-isothermal creep.

6.3.1 The influence of the cycling rate

The non-isothermal creep tests performed on the alloy CMSX-4 in this study consisted of three temperature cycles that differed only by the holding time at the base temperature, which were 9, 18 and 27 minutes (see Figure 3.2 in Chapter 3.2). The three different test conditions are thus further referred to as 9:3, 18:3 and 27:3.

To study how well the developed creep model incorporates the influence of the cycling rate on the overall creep deformation, the model simulated 400 cycles of each of the three temperature cycles.

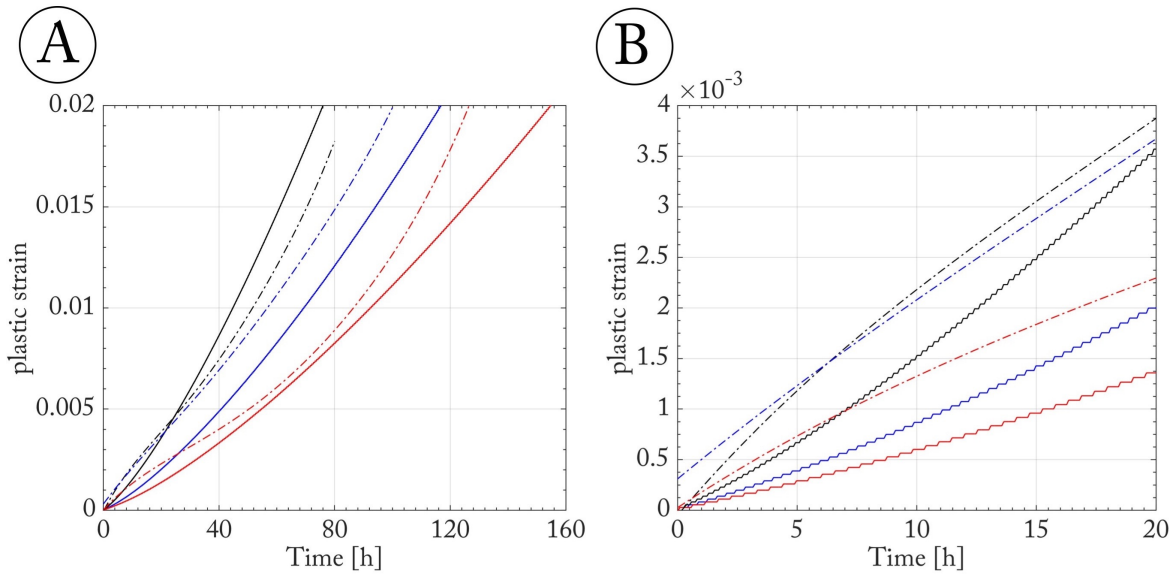

Fig. 6.5 (a) Calculated strain accumulation for the three test cycles (solid lines) compared against the experimentally observed accumulation (dash-dotted lines) with the colours corresponding to black line (9:3), blue (18:3) and red (27:3); (b) close-up of the initial 20 h of the tests.

Figure 6.5 plots the resulting accumulated creep strains for the three different temperature cycles over the test time (solid curves). These calculations are compared to the experimental data previously presented in Figure 5.1A of Section 5.1 (plotted as dash-dotted curves).

Looking at the Figures it is evident that whilst the model can predict the impact of the cycling rate on the creep response at the right order of magnitude the modelled creep curves evolve differently from the experimental results. Whereas, the experimental results suggest a non-monotonic rise in strain rate evolution (see Section 5.1), the modelled strain rates increase monotonically.

As seen in the experiments, the 9:3 calculations show the fastest creep strain accumulation and 27:3 shows the lowest. However, the three experimental results are more similar to each

other than the simulation predicted. In the initial primary creep stage (roughly the initial 20h plotted in Figure 6.5B) the experimental creep strains are larger than simulated. The figure further illustrates how cyclic the strain accumulation is in the non-isothermal model. Segments with virtually no strain addition (base temperature regimes) can be seen for all three simulated test cycles (solid lines) followed by sharp spikes in strain accumulation (high temperature regimes). The step sizes correspond to the cycling rates for the three cycling rates simulated.

Simulation of the non-isothermal strain accumulation

To illustrate the cyclic strain accumulation further, Figure 6.6 plots the calculated strain rate for the 9:3 test (black curves) in the 90 h to 91 h time frame and is compared against the calculated strain rates for the 18:3 (blue) and 27:3 (red) tests at the 5412 minute (90.2 h) mark. A white background in the figure indicates the base temperature regimes (900 °C). Figure 6.6 shows that no significant strain is accumulated in the base temperature regimes and that significant activity takes place only in the high temperature segments. The heating, high temperature hold and cooling to base temperature stages are all highlighted with a grey background. In the plotted time range the 9:3 test exhibits the highest strain rates at peak temperature and the 27:3 test the lowest. Additionally, the high strain rate regime broadens with cycle time resulting in the longest high strain regime for the 27:3 cycle. Another interesting observation in Figure 6.6 is that, upon reaching base temperature, a retardation in the strain rate evolution is visible, but the strain rate does not automatically drop to its base temperature value. The retardation scales with cycle time and amounts to 0, 36 s and 72 s for for the 9:3, 18:3 and 27:3 cycles respectively.

Whilst the retardation time does not change significantly over the test time, the maximum strain rate gradually increases. Comparing the 20 h to 21 h time frame plotted on a linear axis in Figure 6.7 to the 90 h to 91 h time frame in Figure 6.8 the gradual increase becomes evident. The maximum strain rate increases from $\sim 2.1 \cdot 10^{-7} s^{-1}$ to $\sim 5.5 \cdot 10^{-7} s^{-1}$ in the time frame. The strain rate thus increases monotonically and is inversely proportional to the cycle time, increasing fastest for the 9:3 cycle (see Figure 6.9).

Simulation of the non-isothermal dislocation density evolution

The strain accumulation in this model is linked to the evolution of the dislocation density (see Equation 6.1 in Section 6.2). To better understand this we consider the non-isothermal evolution of the three dislocation motions: γ-glide, γ-climb and γ'-shear. The impact and

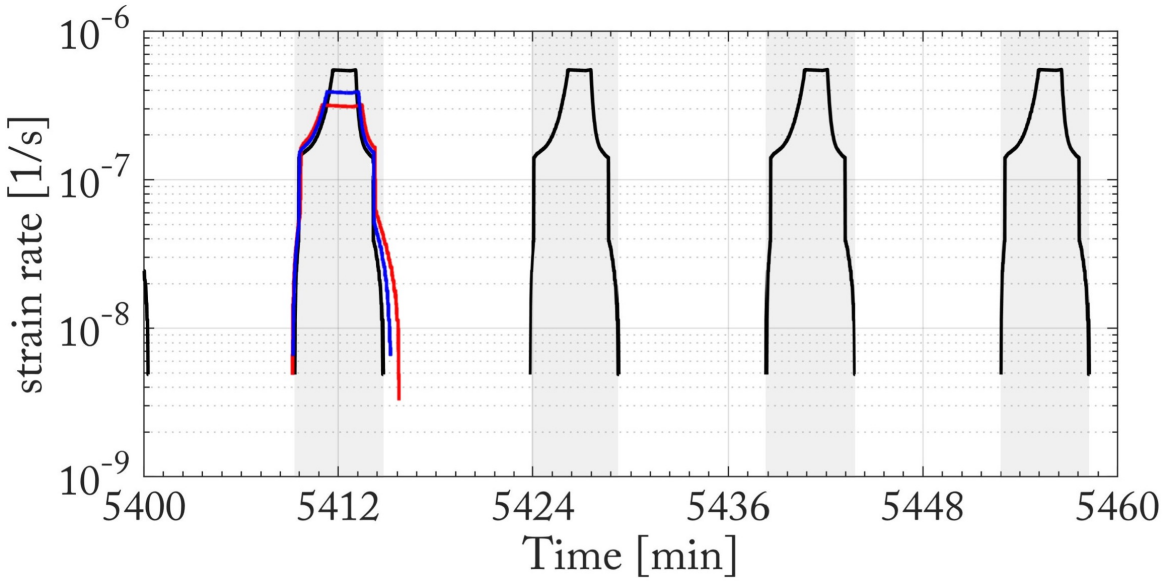

Fig. 6.6 Log-scale plot of the calculated strain rates for the three test cycles: black curves (9:3), blue (18:3) and red (27:3) over the test time. The grey background indicates temperatures above the base temperature.

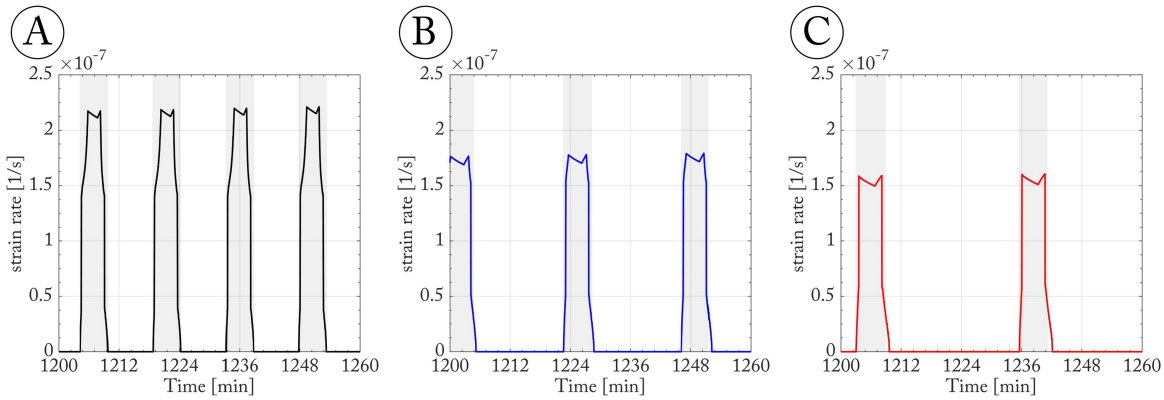

Fig. 6.7 Linear-scale plot of the calculated strain rates from 20h to 21h for the three test cycles: black curves (9:3), blue (18:3) and red (27:3) over the test time. The grey background indicates higher than base temperatures.

evolution of these three mechanisms is further analysed for the 9:3 temperature cycle in the following paragraphs.

At peak temperature eight of the twelve $\pm\frac{a}{2}\langle 110\rangle\{111\}$ - slip systems are activated in the microstructure and contribute to dislocation multiplication by γ-glide (see Figure 6.10). In contrast to the dislocation generation by γ-glide, γ-climb reduces the overall dislocation density, such that over the duration of a single cycle the effective dislocation density evolves in two steps (see Figure 6.11). Regime 1 in Figure 6.11 sees a reduction of dislocation density

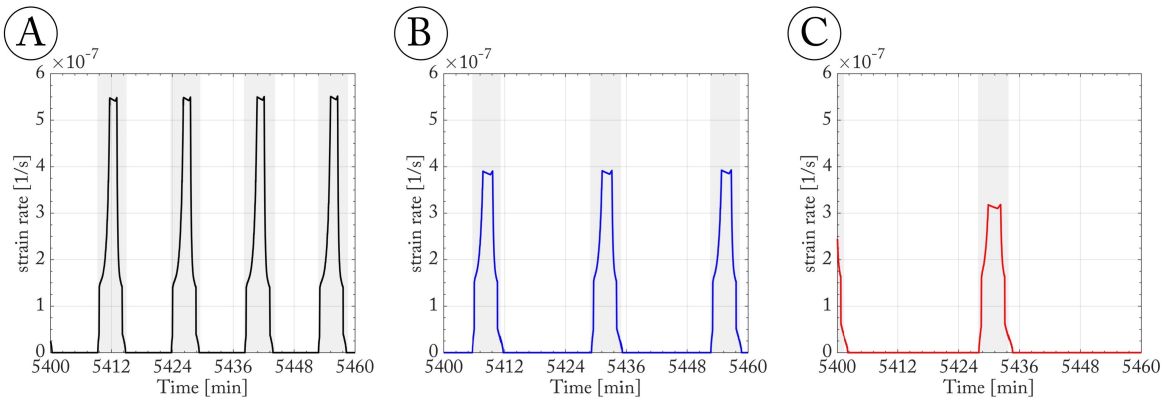

Fig. 6.8 Linear-scale plot of the calculated strain rates from 90 h to 91 h for the three test cycles: black curves (9:3), blue (18:3) and red (27:3) over the test time. The grey background indicates higher than base temperatures.

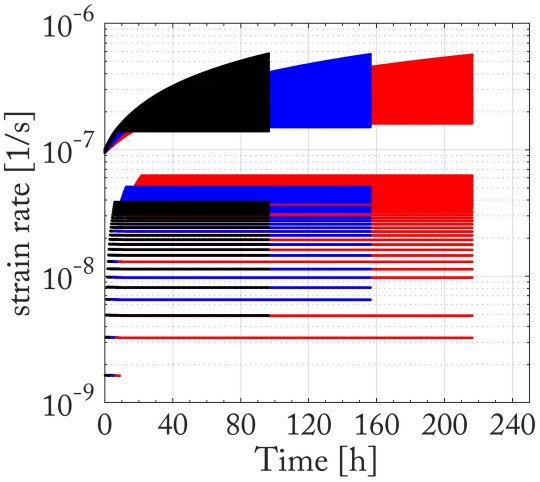

Fig. 6.9 Log-scale plot of the strain rates calculated for the three temperature cycles in CMSX-4 over the test times: black (9:3), blue (18:3) and red (27:3).

due to the dominant dislocation climb in γ, whilst in regime 2 γ-glide prevails resulting in a net increase in dislocation density (see Figure 6.12). Whilst the dislocation accumulation is only limited to the high temperature exposures, dislocation climb in γ is activated throughout the test cycles and increases during heating. Hence, longer cycles experience more climb related recovery and thus exhibit a lower strain rate due to an overall lower dislocation density. Longer cycles however, have a longer strain rate tail which increases overall strain per cycle.

Longer cycle times enable more dislocation climb at base temperature and thus exhibit a slower dislocation accumulation per cycle and an overall lower dislocation density. As a result, the net dislocation contribution per cycle differs for the three non-isothermal cycling conditions and evolves over test time (see Figure 6.13) with close-ups of the 20-21 h and

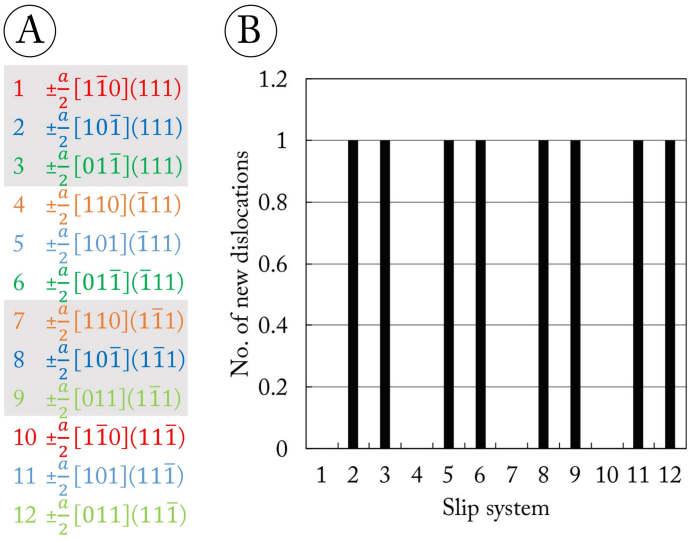

Fig. 6.10 $\pm\frac{a}{2}\langle 110\rangle\{111\}$ Slip systems considered in the model (A). Activated slip systems in the creep test at peak temperature (black) and at base temperature (blue) where the x-axis labels correspond to the slip system in (A).

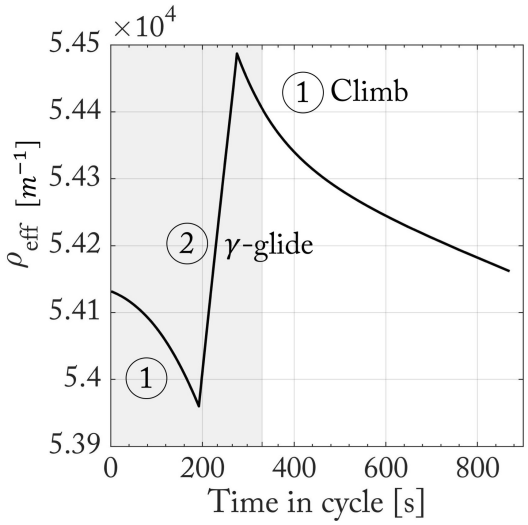

Fig. 6.11 Dislocation density evolution for one slip system and in one region of the simulated cell during a single 9:3 temperature cycle.

90-91 h regime plotted in Figure 6.12. In Figure 6.13 the dislocation density on every glide system and in every region of the microstructure was added up at each time step of the calculation for each of the three calculated creep cycles. The dislocation density increases from the default starting value of ρ_0 to a level that corresponds to the systems dislocation saturation level calculated in Chapter 4.4.7 (in the order of magnitude of $\rho \simeq 10^{14}$ $[m^{-2}]$, which corresponds to a mean dislocation spacing of ~ 100 nm).

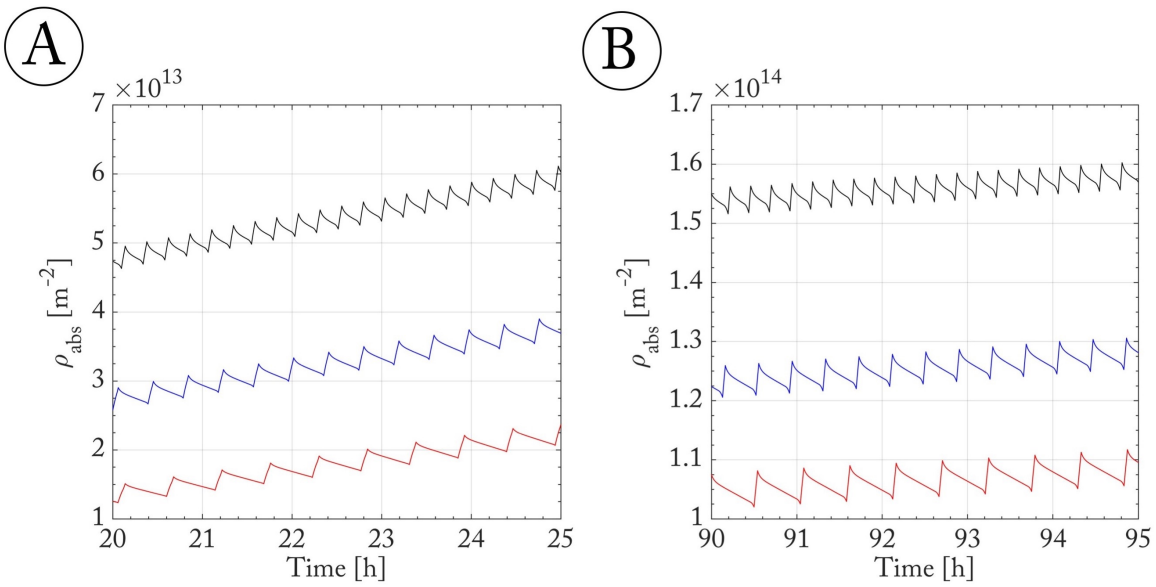

Fig. 6.12 Overall dislocation density evolution for the three non-isothermal cycles: 9:3 (black), 18:3 (blue) and 27:3 (red) for the 20-21 h (A) and 90-91 h timeframe (B).

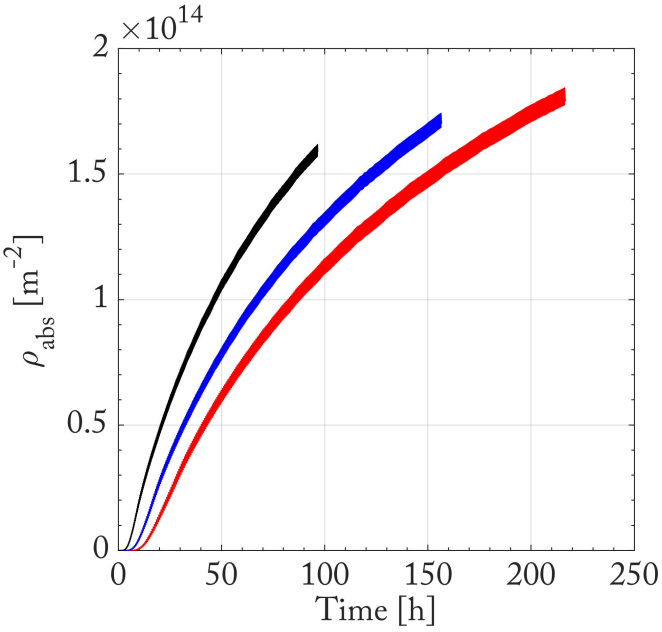

Fig. 6.13 Overall dislocation density evolution for the three non-isothermal tests using CMSX-4: 9:3 (black), 18:3 (blue) and 27:3 (red).

Simulation of the activated dislocation mechanisms

In this creep model, new dislocations are generated by dislocation glide in the γ-matrix and reduced by dislocation climb in γ, with dislocation shear in γ' only adding to the overall

strain accumulation (see Equation 6.1). These three mechanisms are all individually activated in each of the regions of the simulated cell domain. Figure 6.14 and Figure 6.15 show which mechanisms are activated at what time step and with what contribution to the overall dislocation number per calculated time step.

The dislocation contributions by the three dislocation mechanisms in the 9:3 test between 20-21 h test time are shown in Figure 6.14 for γ-glide (6.14A), γ'-shear (6.14B) and γ-climb (6.14C) respectively. With eight activated slip systems (and a maximum Schmid-factor of 0.5) the net addition in the microstructure amounts to four slip systems contributing per time step during the high temperature regimes (Figure 6.14A). The γ'-shearing also shows strong thermal activation, increasing significantly during the high temperature exposures but crucially not decreasing to zero at base temperature (Figure 6.14B). A similar trend is observed for γ-climb (Figure 6.14C).

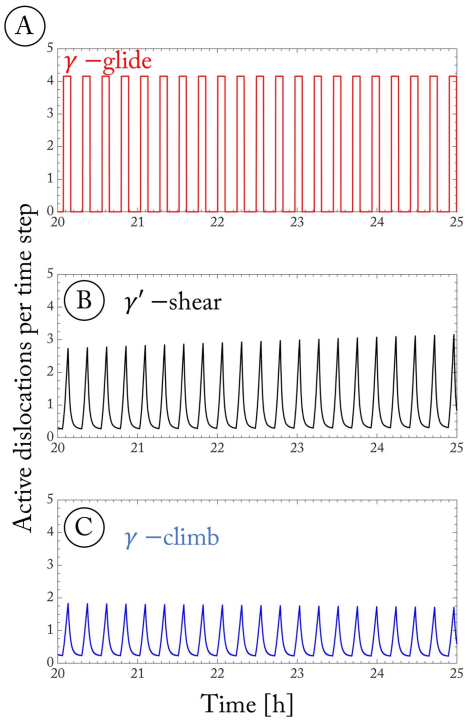

Fig. 6.14 Active dislocation mechanisms contributing to the creep response at every time in CMSX-4 for 9:3 test cycle between 20 h and 21 h: (A) γ-glide, (B) γ'-shear and (C) γ-climb.

Figure 6.15 reveals how the dislocation contributions from each of the three mechanisms evolve over the simulated test time, showing a continuous and stable γ-glide contribution (Figure 6.15A), a gradually increasing γ'-shear contribution once activated (Figure 6.15B) and a continuously decreasing γ-climb contribution resulting from the effects of coarsening and rafting (i.e. due to the closing of vertical channels, see Figure 6.15C).

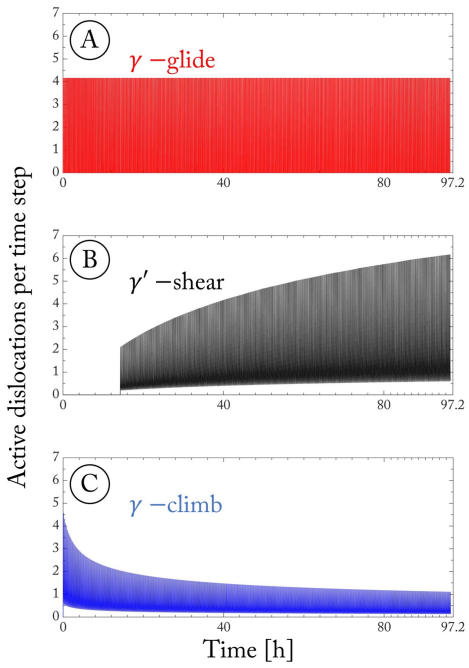

Fig. 6.15 Active dislocation mechanisms contributing to the creep response at every time in CMSX-4 for 9:3 test cycle: (A) γ-glide, (B) γ'-shear and (C) γ-climb.

In this model, the net dislocation density in the microstructure (which is assumed to be an interfacial dislocation density) directly impacts the magnitude of the interfacial lattice misfit according to the contact equations outlined in Equation 6.4. In Figure 6.16, the evolution of the misfit (plotted on z-axis) resulting from the changing dislocation density is plotted over the number of calculated cycles (x-axis) as well as within a single thermal creep cycle (y-axis).

The calculated misfit evolution starts with a large negative value and decreases in magnitude with the accumulation of interfacial dislocations. After 400 simulated cycles the interfacial misfit is in the same order of magnitude as the unconstrained lattice misfit (see Section 4.4.7).

Dislocation glide can occur in all three γ-channels (see Figure 6.2) but as Figure 6.17 shows, only in the z-channels of the simulated cell domain the shear stresses are sufficiently high to activate γ-glide (yellow indicates a mechanism is active and blue inactive). Dislocation shear and climb on the other hand are active in all three γ-channels. The shearing mechanism activated throughout this simulation is not the APB-shearing mechanism but rather the Eggeler-pair mechanism which becomes active once the diffusion length criterion is fulfilled (see Section 6.2.4). Due to the very low dislocation density in the x and y channels, very little climb and shear contribution is made from these regions. In Figure 6.17 the spacings

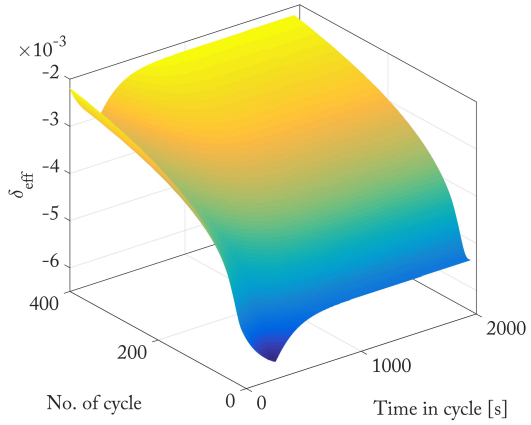

Fig. 6.16 Resulting effective interfacial lattice misfit (δ_{eff}) for a 9:3 test cycle at each calculation step.

between high temperature glide segments appear to be irregularly spaced, a plotting artefact with the software used (Matlab), as the calculated spacings do not change over the simulation time.

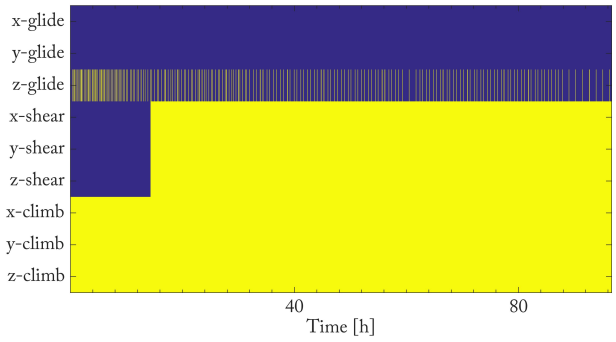

Fig. 6.17 Dislocation mechanisms activated (in yellow) and not active (in blue) for the three test cycles over the test times, 9:3 in (a), 18:3 in (b) and 27:3 (c); Mechanisms on y-axis: dislocation glide in x-channel, y-channel, z-channel; dislocation shear in x-direction, y-direction, z-direction; dislocation climb in x-channel, y-channel and z-channel.

To examine the dislocation activity trends further, the contributions of each of the three dislocation mechanisms were summed up at each time step during the 9:3 test and then plotted as normalised contributions to deformation in Figure 6.18. The yellow area corresponds to the fraction of dislocation climb in γ, blue to dislocation glide in γ and green to dislocation shear in γ'. The increasing γ'-shear rate and decreasing γ-climb shift the constant contribution of γ-glide to lower contribution fractions over the simulation time.

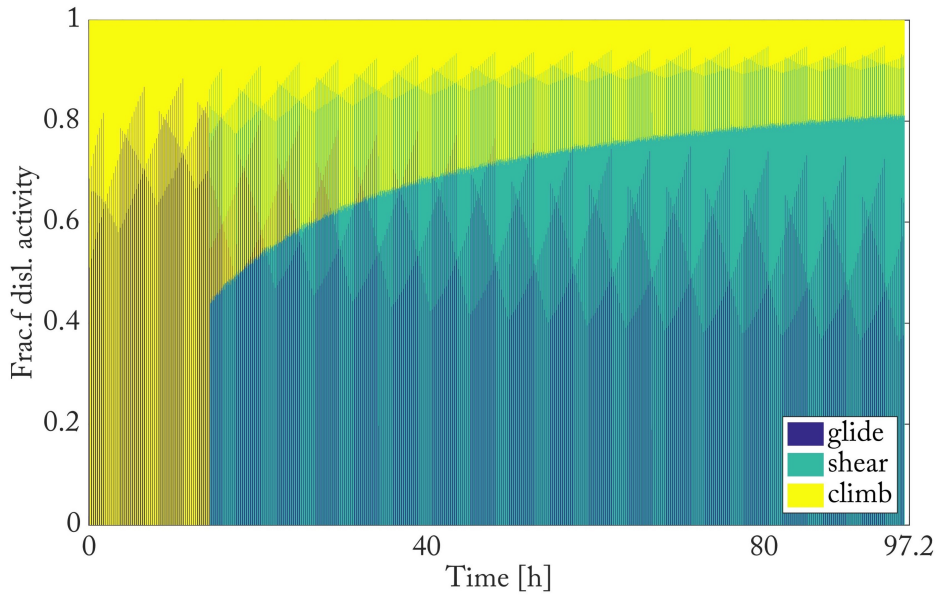

Fig. 6.18 Fraction of the activated dislocation based creep mechanisms calculated for the 9:3 test cycle in CMSX-4 simulated for 400 cycles. Yellow area for dislocation climb, blue for dislocation glide and green for dislocation shear.

Figures 6.19A-C plot the dislocation activity in the 9:3, 18:3 and 27:3 tests respectively. The time window in all three figures was chosen so that the point of Eggeler-type shearing activation is visible. On the left side of the figures a base temperature regime is plotted in which the dislocation activity is only driven by dislocation climb, predominantly in the z-channels. With heating to the high temperature regime, the dislocation activity changes towards a large dislocation glide contribution (activated by the decreasing Orowan resistance due to γ-expansion, see Figure 4.4.2). The dislocation climb activity also increases in number (although decreasing in total share) and continues to do so until reaching the peak effective temperature (see Chapter 4.4.3). This trend is similar across all three test conditions and only the spacing between the high temperature glide segments changes in accordance to the time exposure at base temperature.

In Section 5.1.2 it was argued that the point of the observed creep minimum in the tests would serve as an indicator for the activation of γ'-shearing by Eggeler-pairs. As a result, the diffusion length required to reach the creep minimum was used to activate this shearing mechanism. As the diffusion length criterion is primarily driven by the number of peak temperature regimes, the criterion is reached faster for the 9:3 cycle and more slowly for the cycles with longer base temperature time. The activation times calculated and shown in Figure 6.19 exhibit a reasonable agreement with the experimental analysis, where the creep minimum was activated for the 9:3, 18:3 and 27:3 tests at 18.8 h, 20 h and 31 h

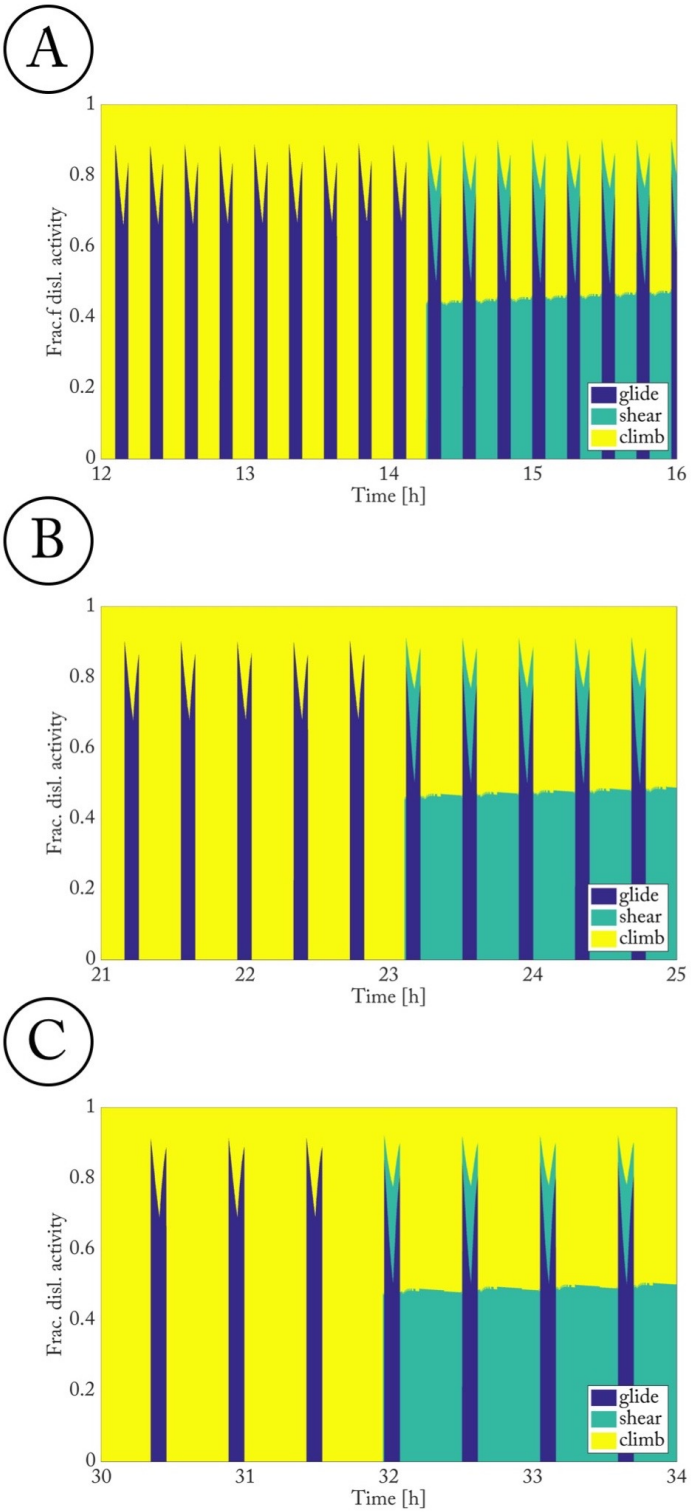

Fig. 6.19 Fraction of the activated dislocation based creep mechanisms calculated for the three temperature cycles in CMSX-4: (a) 9:3, (b) 18:3 and (c) 27:3. Yellow area for dislocation climb, blue for dislocation glide and green for dislocation shear.

respectively. Past the activation threshold, the plastic strain accumulation intensifies. During base temperature segments the dislocation activity is limited to γ-climb and γ'-shear with the latter mechanism gradually increasing in share, eventually becoming the dominant base temperature mechanism (see Figure 6.18). During high temperature exposures, the share of γ'-shear and γ-climb decrease as the share of γ-glide spikes.

Conclusions on simulating the cycling rate

A number of key assumptions made following the microstructure analysis in Chapter 5 could be translated into the non-isothermal creep model. Most importantly, the significantly higher creep rate of these non-isothermal test cycles compared to linear combinations of isothermal tests could be reproduced using the equations outlined above. This was achieved through the cyclic contributions of the three dislocation mechanisms. Furthermore, the dislocation density evolution reflects the experimental observations outlined in Chapter 5, where the dislocation density has not reached an equilibrium and is inversely proportional to the cycle time.

Overall, the calculated creep tests deviate from the experimental dataset to a degree that lies within the scatter observed in experimental creep data (see Chapter 5.1) and the parameters used to obtain these calculations (see Table 6.3) were set as the default or base line values to which the calculations in the following sections are compared. These base line values include the scaling parameter used for the microstructure evolution (see ξ in Section 4.4.8). Table 6.3 further references the following sections where the impact and role of the individual fitting parameters will be examined in more detail.

Table 6.3 Default fitting parameters for the non-isothermal creep model.

Parameter	Value & Unit	Analysis presented in
∂t	1 [s]	
ρ_0	$5 \cdot 10^9 [m^{-2}]$	
P	2.1 [/]	Section 6.3.3
ξ_{eff}	1 [/]	Section 6.3.2
ξ_{raft}	15 [/]	
W_1^{γ}	$3 \cdot 10^{-16} [\frac{m}{sPa}]$	
$W_2^{\gamma'}$	$3 \cdot 10^{-16} [\frac{m}{sPa}]$	

6.3.2 The influence of the effective channel width

In addition to the micro-structure evolution due to coarsening and rafting (see Section 4.4.8), experimental observations in Section 5.4 revealed that temperature cycling results in the precipitation of γ'-tertiaries upon cooling. The presence of γ'-tertiaries in the γ-channel changes the mean separation distance between the γ and γ'-phase and thus changes the back-stress to dislocation bowing in the γ-matrix.

To include the impact of γ'-tertiaries in the model, the channel width (h) used in Equation 6.7 was scaled with a different coarsening constant (ξ) to a value that reflects the experimentally measured mean distance between the γ'-precipitates (primary or tertiary) and the γ-matrix. This modified channel width in Equation 6.7 is further referred to as the 'effective channel width'. The effective γ-channel width is calculated by changing the scaling parameter ξ in Equation 4.20. The other channel widths used in the remaining equations (e.g. for γ-climb) of the model remain unchanged and thus continue to represent the distance between the γ-channel and primary γ'-precipitates and their separation distance changes with rafting and coarsening.

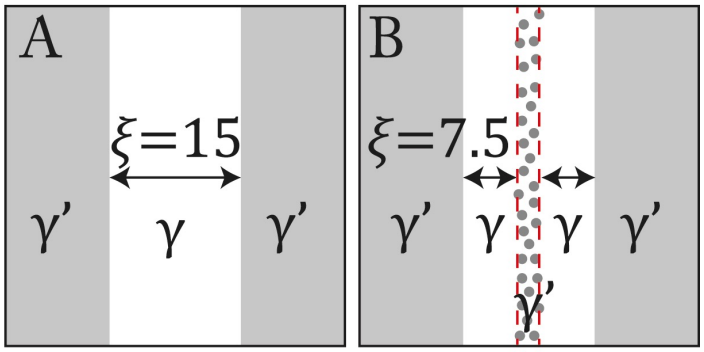

Fig. 6.20 Sketch demonstrating how the effective channel width parameter is calculated (a) a strongly rafting microstructure and no γ'-tertiaries forming in the γ-channels resulting in a length $\xi = 15$ (black arrow); (b) gradually rafting microstructure with γ'-tertiaries forming in the middle of the γ-channels resulting in $\xi = 1$ (black arrow).

To study the impact of the effective γ-channel width, three calculations with different ξ values are presented. Firstly, a value of $\xi = 15$ was chosen, implying a total absence of γ'-tertiaries (see Figure 6.20a) since the effective channel width increases at the same rate as the growing h_z-channel due to rafting and coarsening (as shown in Section 4.4.8). Secondly, a value of $\xi = 7.5$ was chosen to model an effective channel width growing slower due to the precipitation of γ'-tertiaries reduces the effective channel width (see dashed black line in Figure 4.39). Lastly, a simulation with a value of $\xi = 1$ is shown where the effective channel

width grows at the rate of isothermal creept CMSX-4 due to the abundant precipitation of γ'-tertiaries (see dash-dot black line in Figure 4.39). The last case was chosen for the default calculations presented in the previous section.

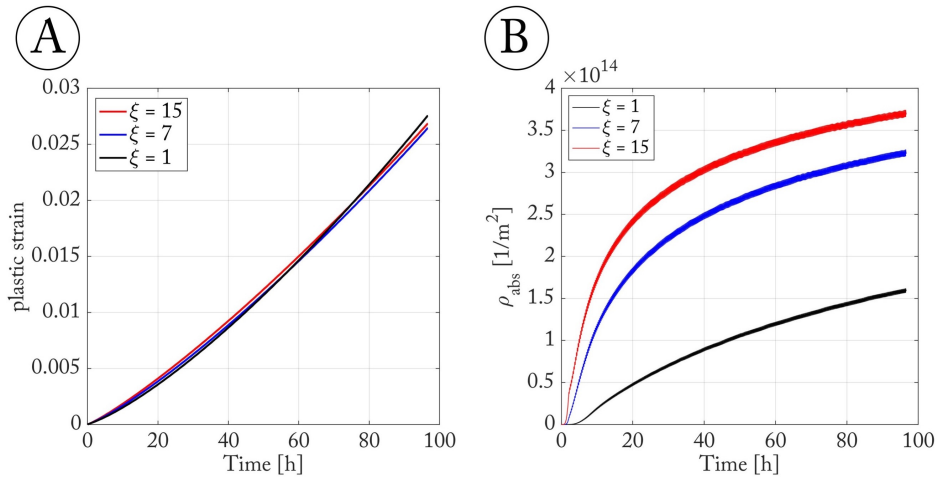

Fig. 6.21 (A) Modelled strain accumulation for an 9:3 CMSX-4 non-isothermal cycle with three different effective channel widths: black line $\xi = 1$, blue line $\xi = 7.5$, and red line $\xi = 15$; (B) dislocation density evolution for the simulated effective channel widths in (A).

The precipitation of γ'-tertiaries occurs in the centre of wide γ-channels (Figure 5.4), such that the distance between the γ'-primary and γ'-tertiaries (approximated by a dashed red line) is reduced (shown in Figure 6.20B).

The presence of tertiaries reduces the dislocation density accumulation (see Figure 6.21B), marginally lowering the strain accumulation per time step (Figure 6.21A). This effect is driven by the increase in Orowan resistance resulting from a smaller effective γ-channel width. After around 60 h however, this effect is no longer the primary driving force for strain accumulation (see Figure 6.21A). Due to the higher dislocation density in the simulation without γ'-tertiaries (red curve), further strain accumulation is limited by the increasing dislocation hardening resistance, although this effect is also small. This parameter then lowers the strain accumulation for the $\xi = 15$ curve (red) below that of the black curve $\xi = 1$.

Plotting the resulting strain rates for the different effective channel widths in Figure 6.22 shows that upon cooling to the base temperature the time lag increases with increasing effective channel width, such that for $\xi = 15$ the time lag of decreasing strain accumulation spans the entire base temperature regime. The much longer regime of strain accumulation facilitates the faster dislocation density evolution. Crucially, the lower dislocation density for the $\xi = 1$ condition enables a high temperature and high strain rate increase which eventually drives the faster strain accumulation for a lower effective channel width.

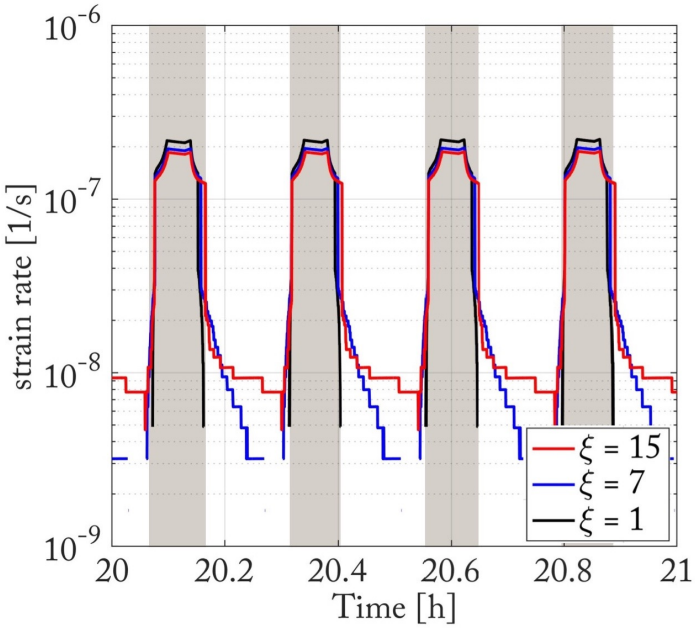

Fig. 6.22 Modelled strain rate accumulation for an 18:3 CMSX-4 non-isothermal cycle with three different effective channel widths: black dots $\xi = 0$ and red dots $\xi = 15$.

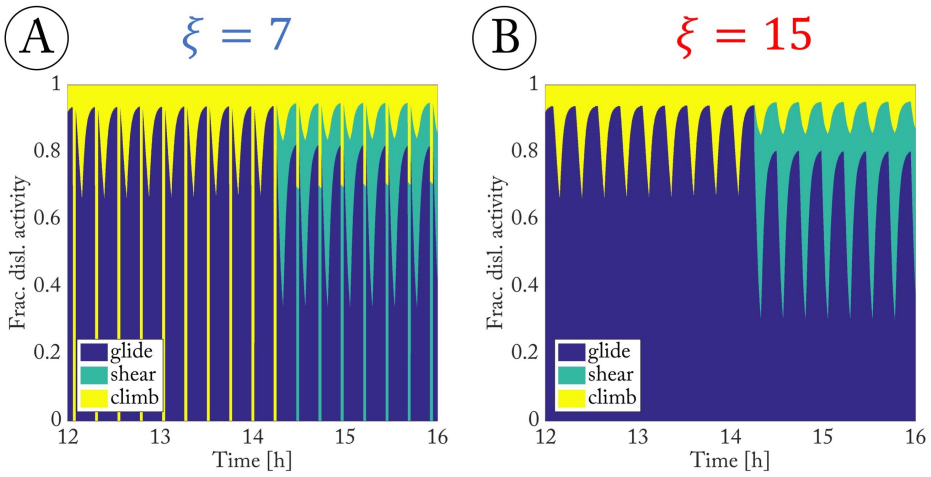

Fig. 6.23 Fraction of the activated dislocation based creep mechanisms calculated for different effective channel widths: (a) $\xi = 0$ and (b) $\xi = 15$. Yellow area for dislocation climb, blue for dislocation glide and green for dislocation shear.

Comparing the fraction of activated creep mechanisms in Figure 6.23 and Figure 6.19A (for the 9:3 $\xi = 1$ condition) reveals which mechanisms drive the strain rate evolution for the different effective channel widths. Looking at Figure 6.23, the dislocation glide segments extend to the base temperature regimes except for the $\xi = 1$ simulation. The dislocation glide share of dislocation activity decreases upon the activation of Eggeler-shearing.

In conclusion, a larger effective channel width (less γ'-tertiary precipitates) initially increases the strain accumulation driven by dislocation γ-glide. The easier glide is facilitated by a lower Orowan resistance. Eventually, the higher dislocation density limits further strain accumulation via dislocation hardening in γ. However, the effect of these changes on the macroscopic strain accumulations are small.

6.3.3 The sensitivity of the model to the climb ratio

Dislocation climb and the resulting recovery of the material is largely diffusion driven and thus a key parameter in the high temperature creep regime. The dislocation climb description in this model depends on a number of variables that are summarised in a parameter P which scales the dislocation climb contribution (see Section 6.2.5). To understand how sensitive the presented model is to changes in this parameter and what model trends result from a lower or higher dislocation climb to glide ratio, three calculations with values of P = 1.05, 2.10 and 4.20 are compared in this chapter (*ceteris paribus*). In addition to the default value used, P was thus halved and doubled to reflect a lower and higher jog concentration.

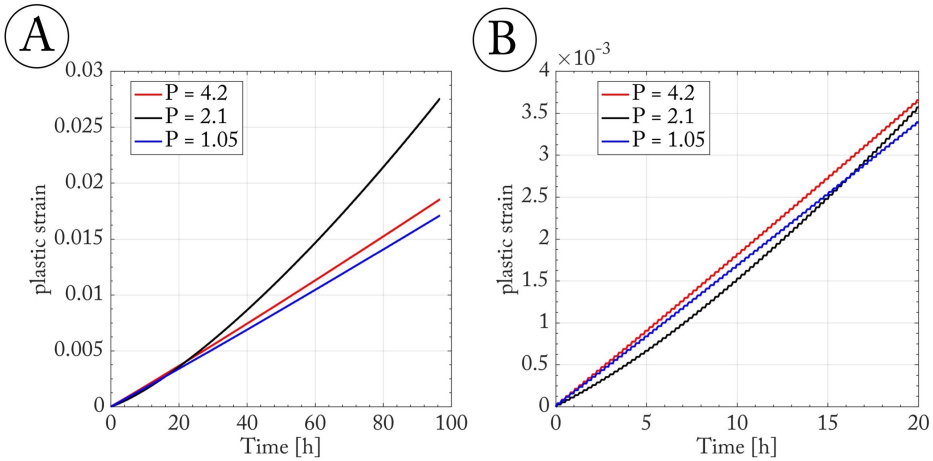

Fig. 6.24 Plastic strain modelled for an 9:3 CMSX-4 non-isothermal cycle; (A) using three different climb fitting parameters (P): 1.05 (blue line), 2.10 (black line) and 4.20 (red line); (B) close-up of the first 20 h of simulation time.

A higher climb rate expressed through a larger parameter P results in a faster accumulation of plastic strain as seen in Figure 6.24a and a slower dislocation density accumulation (see Figure 6.25). On the other hand, a higher dislocation density results in a larger dislocation hardening effect which limits the accumulation of plastic strain. Dislocation hardening (see Equation 6.7) and softening (via γ-climb, see Equation 6.1) then dominate for a case of P = 1.05 and P = 4.20 respectively, such that a slower and near linear strain accumulation

results (see Figure 6.24). For a value of P = 2.1 both effects are in balance thus marking a regime where dislocation climb and glide are interdependent, resulting in an exponential strain accumulation. To understand why the regime of interdependent glide-climb is only visible around a P value of 2.1, the role of dislocation hardening and softening is further analysed.

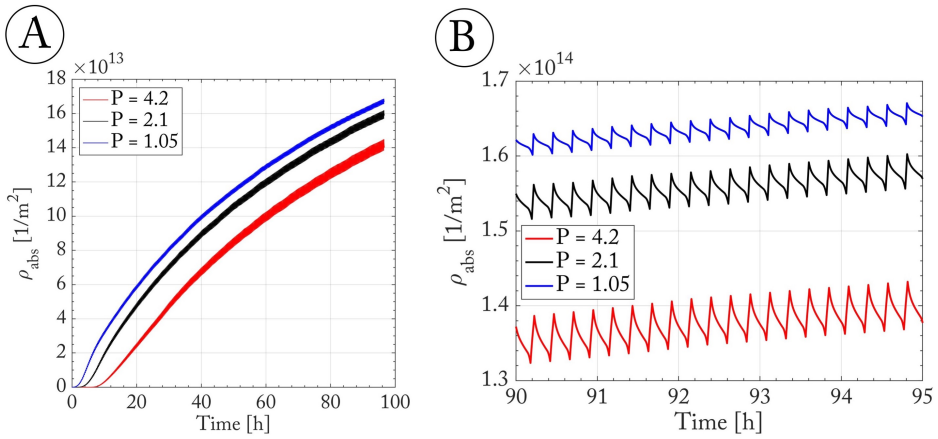

Fig. 6.25 (A) Total dislocation density (ρ_{abs}) evolution for CMSX-4 for three different climb fitting parameters (P): 1.05 (blue line), 2.1 (black line) and 4.2 (red line). (B) close-up of the dislocation density evolution between 90-95 h.

With a higher climb factor, the oscillation in dislocation density accumulation increases (see Figure 6.25B), such that a higher dislocation annihilation due to γ-climb facilitates more dislocation addition due to γ-glide. The oscillation indicates that the dislocation mobility in the microstructure increases with climb rate. A higher dislocation mobility then results in a higher strain rate per time step and thus a faster strain accumulation. However, the net strain contribution is smaller due to the overall lower dislocation density with a higher climb rate. To understand the strain accumulation better as a function of a changing climb factor the results are plotted in Figure 6.26A and 6.26B for the 2-3 h and 20-21h simulation times respectively.

Three key observations can be made by comparing the results plotted in Figure 6.26A and 6.26B. Firstly, the initial strain rates are proportional to the climb factor but after 20 h the black curves (P = 2.1) have increased beyond the levels observed for the highest climb factor modelled (P = 4.2), which has stayed almost constant. Secondly, the time lag (high strain rate observed after cooling to base temperature) increases significantly over time for P = 4.2. Thirdly, for the lowest climb rate an initial spike to a high strain rate of constant magnitude is observed on heating.

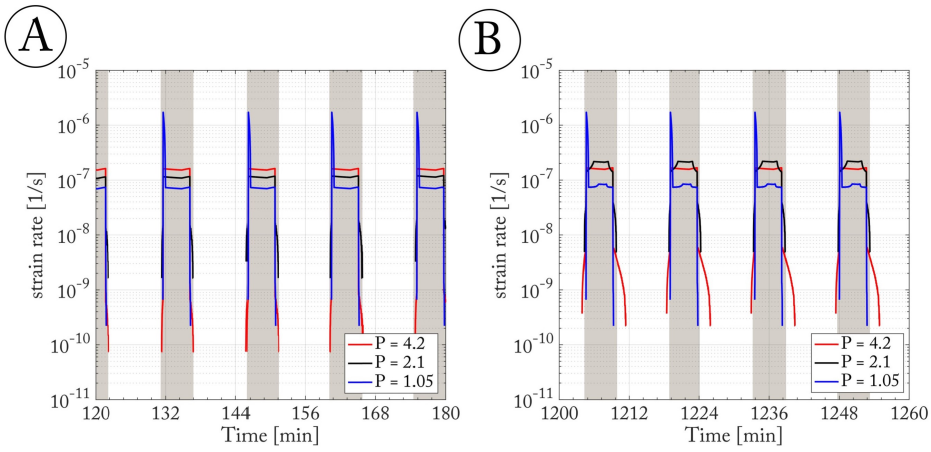

Fig. 6.26 Log-scale plot of strain rates modelled for a 9:3 CMSX-4 non-isothermal cycle with different climb fitting parameters (P): 1.05 (blue lines), 2.1 (black lines) and 4.2 (red lines). A white background highlights base temperature regimes. (A) from 2-3 h and (B) 20-21 h.

Due to the lower dislocation density evolution with a higher climb factor (resulting from higher dislocation annihilation) a higher effective interfacial lattice misfit persists in the microstructure compared to the simulation with a lower climb factor. This larger magnitude in misfit means that the higher climb factor calculation exhibits a higher driving force for dislocation generation at the later stages of the calculation times, whereas the simulations with a lower climb factor display a dislocation density which has relaxed the misfit with interfacial dislocations more rapidly.

A higher climb factor also increases the dislocation annihilation in the base temperature segment which reduces the dislocation density and thus decreases the dislocation hardening resistance, thereby allowing a regime of higher strain rate accumulation to persist in the base temperature regime (strain rate time lag).

When simulating a heating cycle with a climb factor of P = 1.05 an initial spike in strain rate is visible that remains unchanged in magnitude and spike length throughout simulation time. The spike indicates a constant high strain increment caused by dislocation glide in γ upon heating, enabled by the rapid reduction in Orowan backstress due to γ'-dissolution (see Figure 4.25). The effect rapidly stops as dislocation hardening increases due to the new dislocations generated.

On the other hand, a climb factor of P = 2.1 results in a glide-climb interdependency, in which the strain rate accumulation rapidly increases, resulting in a continuously increasing strain rate.

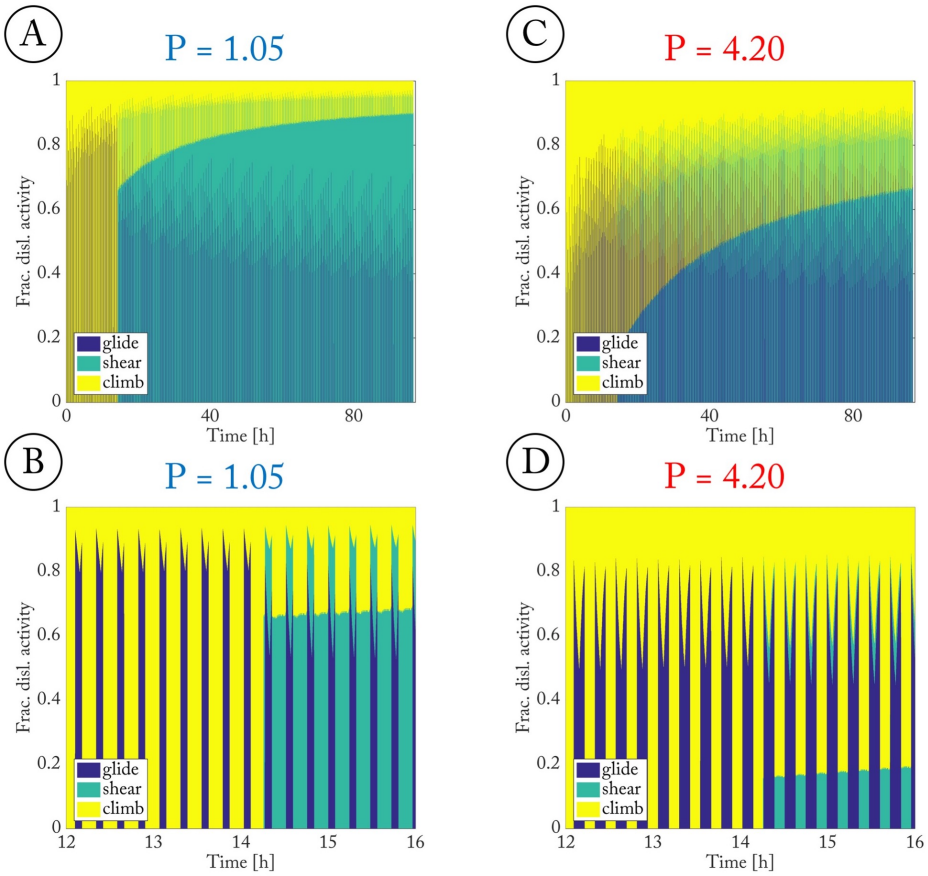

Fig. 6.27 Fraction of the activated dislocation based creep mechanisms calculated for different climb rates: (A) P = 1.05 overview, (B) P = 1.05 between 12-16 h, (C) P = 4.2 overview and (D) P = 4.2 between 12-16 h. Yellow area for dislocation climb, blue for dislocation glide and green for dislocation shear.

Plotting the dislocation mechanism contribution fractions in Figure 6.27 highlights that the longer strain rate segments seen for larger climb factors are primarily driven by longer segments of dislocation glide accumulation (see Figure 6.27D). Furthermore, the higher climb factor also annihilates γ'-shearing dislocations thereby resulting in an overall lower γ'-shearing contribution and slower shearing evolution. The higher shearing activity seen for the lower climb factor (see Figure 6.27C) almost balances the higher glide activity seen for a higher climb factor (see Figure 6.27D) which results in a very similar and almost linear strain accumulation.

6.3.4 The influence of precipitate shearing

Section 6.2.4 outlined a new approach to model Eggeler-pair shearing events. The calculations presented are based on the assumption that the Eggeler-pairs that enter the γ'-precipitates from the γ-channels will shear the former phase without hinderance and return to the γ-channels. When assuming that a shearing events requires significantly less time than the time step used in the model (∂t, see Table 6.3), the γ-channel dislocation density remains unchanged and no net reduction of dislocations in the γ-phase results.

According to the model by Svoboda and Lukáš [199], shearing by APB-separated dislocation pairs reduces the dislocation density in the γ-channels (see Section 6.2.4). The underlying assumption is that γ'-shearing dislocations are either locked up in the γ'-precipitates or annihilate interfacial γ-dislocations upon exiting the precipitates. Whilst the latter assumptions could not be investigated in this thesis, the dislocation analysis in Chapter 5.1.3 indicated that γ'-shearing dislocations can be so immobile that shearing dislocation lines adapt their lowest energy position (evidenced by straight dislocation lines in Figure 5.12c). The resulting dislocation density in the γ-channels would then be reduced due to shearing.

To model the impact of such locking events during γ'-shearing on the creep model response the dislocation density description was changed to Equation 6.16.

$$\rho_{x,K}^{t_2} = \rho_{x,K}^{t_1} + \dot{\rho}_{x,K}^{(glide)}\partial t - \dot{\rho}_{x,K}^{(climb)}\partial t - \aleph \cdot \dot{\rho}_{x,K}^{(shear)}\partial t \tag{6.16}$$

According to Equation 6.16, the mobile dislocation density was reduced by the shearing dislocations multiplied by a locking ratio ($\aleph$). A ratio of $\aleph$ = 0.1 (10 % locking) means that every tenth shearing dislocation is expected to be locked in the γ'-phase, resulting in a reduction of dislocation density in the γ-channels and the overall mobile density by the number of shearing dislocations at every time step. To show the influence of this parameter, a locking ratio of 0.1 was chosen. Additionally, a case of γ-channel dislocation addition by γ'-shearing dislocations is shown as a comparison. In this case, the sign preceding $\aleph$ is positive, such that $\aleph = -0.1$. So far, no dislocation multiplication event has been observed inside the γ'-precipitates, such that this simulation is not based on physical findings. However, it is useful to show how the model equations would reflect such a simulation to understand the role of the dislocation density variable.

The strain accumulation for a CMSX-4 9:3 non-isothermal test using three different locking ratios is shown in Figure 6.28A. In black, the default calculation is re-plotted from Figure 6.5 in red, a simulation assuming a 10% locking rate; and in blue, a 10% addition

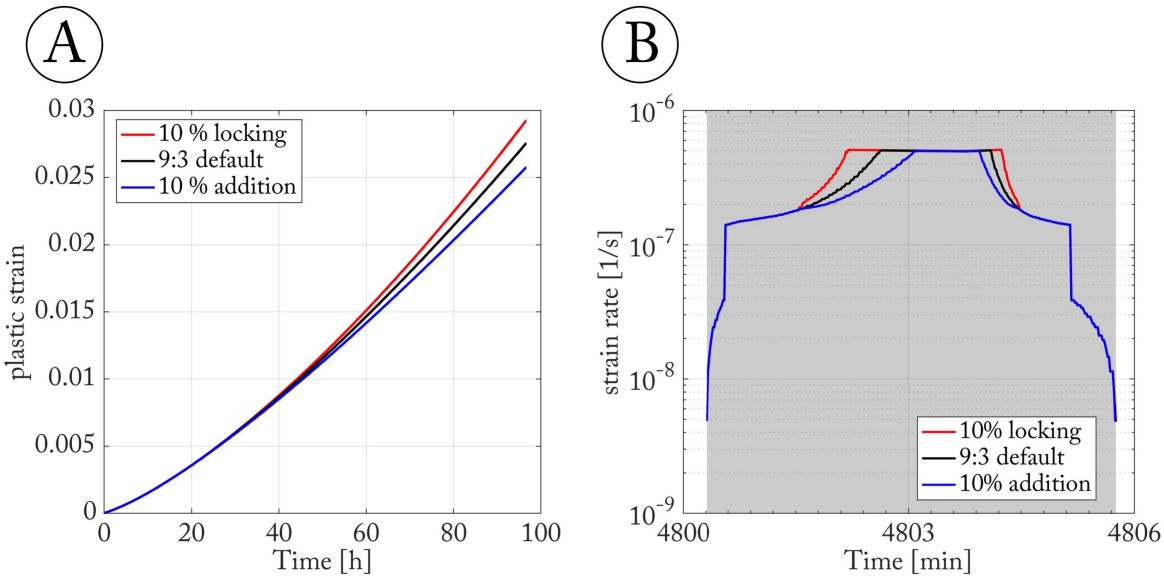

Fig. 6.28 Impact of shear locking and shear addition in CMSX-4 for a 9:3 non-isothermal cycle: (A) on the plastic shear accumulation: 10% locking (red), default parameters (black), 10% addition (blue); (b) strain rates between 80 - 80.1 h of the test time for 10% locking (red), default parameters (black), 10% addition (blue).

rate is shown. Varying the locking rate only impacts the creep response once the shearing mechanism is activated (after $\sim 14h$).

The change in strain accumulation dynamic due to locking by shearing events is similar to the impact that a higher climb rate has in γ-channels (see Section 6.3.3), resulting in a faster strain accumulation. In Figure 6.28B, the strain rate accumulation for different locking ratios are compared for single cycles after 80 h simulation time with different locking ratios. The higher strain accumulation for a 10% locking ratio is then driven by a gradual expansion of the high temperature strain regime, such that past the 80 h simulation time the high temperature strain regime increases by $\sim$ 36 s upon heating (see Figure 6.28B), whilst a 10% addition ratio decreases the high temperature strain regime by the same amount. Furthermore, from the results displayed in this figure it can be concluded that the high strain plateau at the high temperature exposure is partially driven by γ'-shearing.

The driving force behind the change in strain evolution due to different locking ratios in the model is then due to the effect of dislocation hardening in the γ-channels.

Impact of the scaling factor W

The activation volumes for both phases ($W_1^{\gamma} = 3 \cdot 10^{-16}[\frac{m}{sPa}]$ and $W_2^{\gamma'} = 3 \cdot 10^{-16}[\frac{m}{sPa}]$, see Table 6.3) are scaling parameters that are required to increase the strains calculated for a single simulated cell to the macroscopic strain levels observed experimentally.

Svoboda and Lukáš [199] used similar scaling parameters for CMSX-4 in their equations to model isothermal creep for calculations at 1000 °C. Their cited scaling parameters were $W_1 = 2.9 \cdot 10^{-19}[mPa^{-1}s^{-1}]$ for the γ-matrix and $W_2 = 4 \cdot 10^{-39}[mPa^{-3}s^{-1}]$ for the γ'-phase respectively. As the scaling parameters of both phases differ by an exponent of twenty (to match the experimental results), this effectively means that the authors thought γ-glide was the dominant contribution to the primary creep stage. As the dislocation evolution equations were changed (see Equation 6.8), larger scaling parameters in this model do not mean an overall faster strain evolution. The strain rates calculated with the adapted equations result in strain rates that are in the same order of magnitude as those calculated by Svoboda and Lukáš [199] for CMSX-4 at 1000 °C. This agrees with the finding presented in Figure 5.2 of the previous chapter where the isothermal strain evolution at 1000 °C was shown to be in the same order of magnitude as that for the non-isothermal creep tests.

However, further datasets are required to accurately fit the scaling parameter and its alloy dependence. Accuracy of the parameter is particularly important when considering adapting a multi-cellular creep model in which the individual cells represent specific rhenium based variants (see Section 4.2).

6.3.5 The influence of alloy composition

In this subsection, the influence of alloy composition is examined by comparing the modelled creep response in CMSX-4 and CMSX-10 resulting from calculations of identical temperature cycles (18:3). However, it is important to remember that two alloy specific parameters are not yet properly described. Firstly, as described in Section 4.4.7, the initial constrained lattice misfit (δ_{cpcp}) could not be calculated using ThermoCalc and instead was estimated using the alloy-specific unconstrained lattice misfit (δ_{cpcm}, estimated with ThermoCalc) and the predefined maximum dislocation density (identical to that calculated for CMSX-4). Secondly, the coarsening and rafting coefficient ($\breve{k}$, see Section 4.4.8) could not be determined from the limited tests carried out for the alloy CMSX-10. Therefore, the CMSX-4 rafting and coarsening fitting parameter ξ was chosen and the only difference with the CMSX-4 calculation according to Equation 4.20 arose from using the alloy specific γ-interdiffusion parameter (D_{eff}). CMSX-4 however rafts and coarsens significantly faster than CMSX-10

(by about one order of magnitude) which can be seen by comparing the SEM images acquired post testing in Figures 5.4 and 5.16.

The remaining alloy-dependent creep parameters for CMSX-10 have been calculated and presented in Section 4.4.6, indicating a higher non-isothermal stability of CMSX-10 compared to CMSX-4 (e.g. the γ'-phase fraction varied significantly less during the same 18:3 cycling for the alloy CMSX-10). This could be verified experimentally and is shown in Section 5.2.

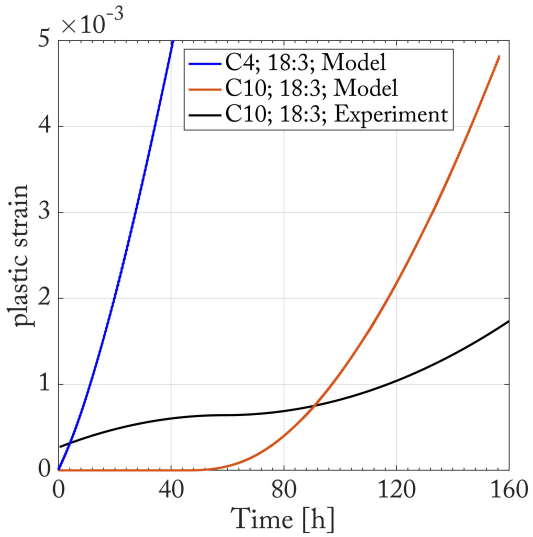

Fig. 6.29 Strain accumulation calculated for 18:3 tests: of the alloy CMSX-10 (orange curve), the experimental dataset of CMSX-10 (black curve) and a model of CMSX-4 (blue curve).

The modelled creep strain accumulation for CMSX-10 (orange curve) and CMSX-4 (blue curve) are compared in Figure 6.29 against the experimental dataset acquired for CMSX-10 (black curve). These calculations were obtained using the default fitting parameters described in Table 6.3. Comparing the modelled results, it is apparent that the maximum strain rate for CMSX-10 is several orders of magnitude lower than that of CMSX-4 up to the 80 h mark (see Figure 6.29b). A close-up of the strain rate accumulation plotted between 50-51 h in Figure 6.30 highlights how the maximum strain rate in CMSX-10 is not only over one order of magnitude lower but also the plastic strain regime is much shorter, such that no strain accumulation can be seen for CMSX-10 at the base temperature and for much of the high temperature hold regime. Eventually the γ-phase yields and strain is accumulated for 1.2 minutes, a process which ceases rapidly with the cooling to base temperature and no strain rate retardation on cooling is observed for CMSX-10.

The strain accumulation plotted in Figure 6.29 results in an initially lower strain accumulation than observed experimentally, before it rises rapidly past the 80 h mark to the order

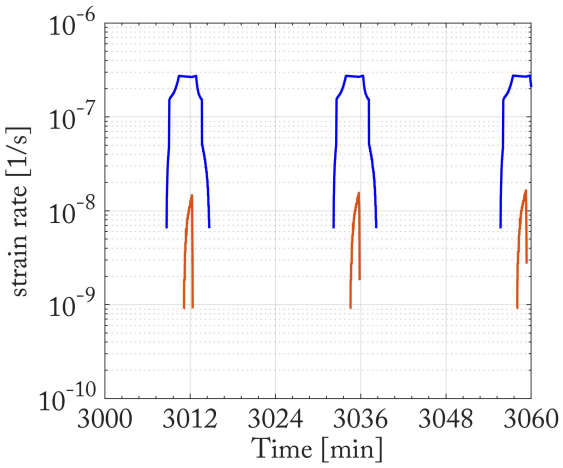

Fig. 6.30 Close-up log-scale plot between 50 and 51h for 18:3 CMSX-4 test (blue) and 18:3 CMSX-10 test (orange).

of magnitude seen in CMSX-4. The gradual rafting and coarsening of the microstructure continuously lowers the Orowan resistance due to a widening γ-channel (the z-channel widens whilst the vertical channels close up) until the point where frequent dislocation multiplication is possible. The rapid rise past the 80 h mark, which is far beyond the rates seen experimentally, results from using the microstructure evolution constants derived for CMSX-4 in the current model for CMSX-10.

Nevertheless, the calculation below the 80 h mark highlights two findings. Firstly, the alloy dependent creep parameters derived (except for coarsening and rafting) result in an initial strain accumulation that is similar to that seen experimentally. Secondly, the activation of γ'-shear in the creep model follows the experimental evidence which will be discussed further here.

The share of activated dislocation mechanisms in CMSX-10 is plotted in Figure 6.32. In comparison to the calculation for the 18:3 CMSX-4 cycle in Figure 6.19B, it is evident that significant differences exist between the activated dislocation mechanisms between both alloys. Firstly, prior to Eggeler-type shearing activation the dislocation γ-glide in CMSX-4 is active throughout the whole high temperature regime, visible as a thick blue bar. Despite being subjected to the same heating cycles, dislocation glide in CMSX-10 is only active for a small fraction of the high temperature exposure due to a generally higher Orowan resistance. As a result, the dislocation annihilation due to dislocation climb is so pronounced that only a very small overall dislocation addition results from each non-isothermal cycle.

Eggeler type shearing is assumed to be operative in CMSX-10 after 63 completed cycles, which corresponded to 0.1 % plastic strain or 24.6 h (see Section 5.5.3). The cited section

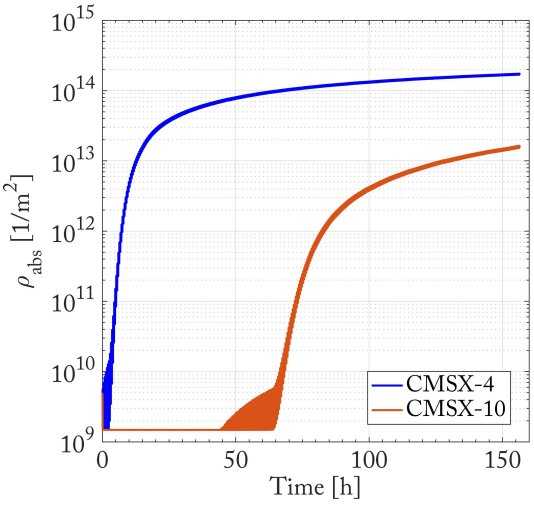

Fig. 6.31 (a) Total dislocation density (ρ_{abs}) evolution for CMSX-4 (blue) and CMSX-10 (orange); (b) Resulting effective interfacial lattice misfit (δ) for a 18:3 test cycle of CMSX-10 at each calculation step.

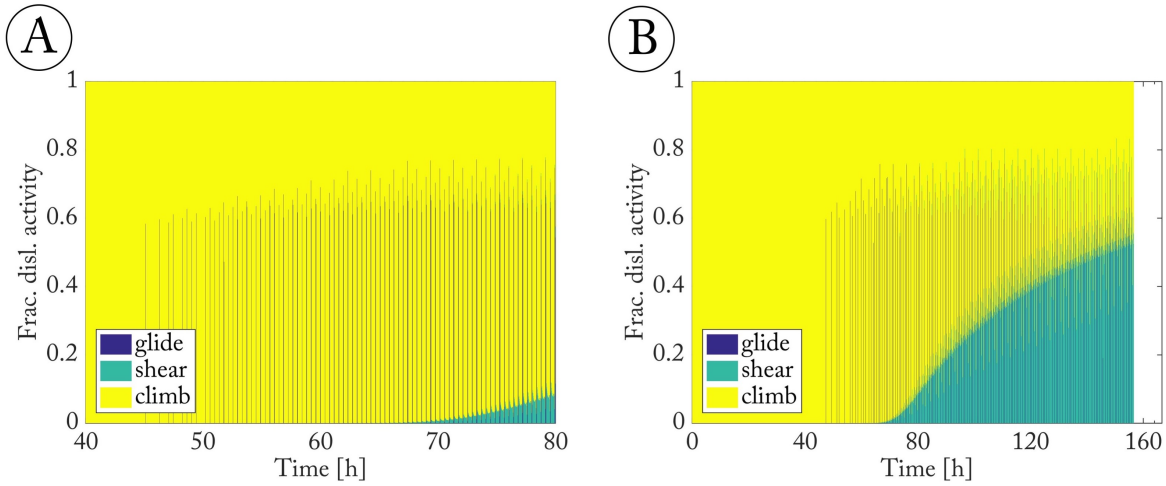

Fig. 6.32 Fraction of the activated dislocation based creep mechanisms calculated for different stages of the creep test for CMSX-10: (a) 40-80 h, (b) total simulation time.

further argued that despite the possible activation no strain rate effect is visible due to the comparatively low dislocation density in the CMSX-10 microstructure.

According to the model, Eggeler-type shearing becomes active after 67 h (see Figure 6.32A) and has limited impact initially due to the low dislocation density. The modelled strain reached at activation, however, is below 0.1 % strain. The modelled gradual onset of shearing results from the description of Eggeler-type shearing in Equation 6.11 The equation is proportional to the number of dislocations that have the potential to climb sufficiently to

form Eggeler-pairs ($\rho^{D_{inc}}$). The number of such dislocations in CMSX-10 is very low, as the overall dislocation density is low. Past the 80 h mark, the rapid microstructure evolution coupled with the low interfacial misfit and dislocation density (both strong dislocation multiplication driving forces) results in an exponential dislocation density accumulation (see Equation 6.8), such that significantly more dislocations are accumulated than are lost due to recovery mechanisms (see Figure 6.32B). The glide and shear mechanisms remain active for longer times and the latter remains active throughout parts of the base temperature regime (see Figure 6.32B). After around 130 h the shearing mechanism is the primary mode of deformation in the CMSX-10 microstructure.

Amongst other findings, this section highlighted how strongly the micro-structure evolution impacts the creep response during non-isothermal cycling and thus future work has to be done to describe the alloy-dependent variation of this parameter due to rafting and coarsening.

6.4 Discussion

The results from the non-isothermal creep model (see Section 6.3) have given new insights into the parameter interdependencies and ability of the model to reflect the experimental observations presented in the literature and in Chapter 5. The accuracy of the modelled trends are further discussed in this section and further potential for optimisations are laid out.

6.4.1 Optimising the model fit

The above outlined creep model has been able to accurately reflect key observations gathered from non-isothermal creep experiments (see Section 6.4.2) depending largely on the non-isothermal evolution of published creep parameters. The model requires six scaling or fitting parameters that can be grouped into three different categories: (1) physical based parameters, (2) parameters based on physics but requiring more validation and (3) scaling and fitting parameters without physical basis. The majority of these parameters have a significant influence on the modelled creep response, as is common amongst creep models that exist within exponential functions (see strain rate descriptions in Table 6.2).

1. Category: $\partial t, \rho_0$
2. Category: P, ξ_{eff}, ξ_{raft}
3. Category: $W_1^{\gamma}, W_2^{\gamma'}$

In isothermal creep models, increasing the time differential allows to significantly reduce computation time of the calculation. Due to the significant temperature gradients in the non-isothermal experiments a single time-step was chosen that is a good compromise between computational efficiency whilst representing the thermal gradients correctly ($\partial t = 1[s]$). In this model, the computational speed was thus further optimised in other ways. The role of the initial dislocation density can be inferred from the dislocation density graphs displayed in the previous section. According to the current model, a higher dislocation density (including the initial density) results in a higher dislocation hardening contribution and thus a lower strain rate.

The second category includes the climb scaling parameter P, as well as the microstructure evolution parameters for the effective channel width (ξ_{eff}) and the overall microstructure evolution due to rafting and coarsening (ξ_{raft}). These parameters are based on physical evidence (the observation of climb and the micro-structure transformation). To verify the magnitude of these four parameters and their dependence on alloy chemistry, further interrupted non-isothermal creep tests with different alloy compositions are required.

The parameters W_1^{γ} and $W_2^{\gamma'}$ are necessary to scale the deformation estimated from a single simulated cell up to a macroscopic deformation and to harmonise the units of the equations. Both parameters do not have a physical basis and are of a similar order of magnitude as the fitting parameters published by Svoboda.

With the adaptation of a multi-cellular creep model that reflects the parameter variation in a fully heat treated alloy (see Section 4.2), the influence of these fitting parameters is thought to decrease as the contribution fraction per simulated cell and time step to the total strain increment would decrease with a higher number of modelled cells. Beyond verifying the fitting parameters as outlined in the previous section a number of additional optimisations can be made in order to enhance the predictive capabilities of the model. These improvements will be presented below in increasing order of expected impact on the model optimisation.

To correctly reflect the impact of interfacial dislocation networks in this model, the transformation from mixed to edge character dislocations on the interfaces could be included. This would change the ratio of mobile to immobile dislocations in both phases as well as the interfacial lattice misfit. The impact on the overall model optimisation is however expected to be limited, as the impact seen by changing the ratio of mobile to immobile dislocations in the γ'-precipitate phase had a low impact on the creep response (see Section 6.3.4).

Accounting for the variation in composition across different regions of the microstructure (see Chapter 2.1.2) and the interconnectivity between γ'-particles (see Figure 2.18) could improve the predictive modelling capabilities significantly and increase its accuracy. Includ-

ing the former effect would allow an investigation of the effectiveness of heat-treatments on alloy performance. Including the interconnectivity between γ'-particles would mean that instead of unconnected simulated cells, representative microstructures with their actual stress/strain responses could be modelled. Both effects would result in optimised W_1^{γ} and $W_2^{\gamma'}$ fitting parameters, and new insights into the non-isothermal parameter evolution in different regions of the microstructure. Chapter 4.2 laid out an approach to include the elemental alloy scatter summarised in Figure 4.16. The influence of the precipitate interconnectivity could on the other hand only be investigated qualitatively in Chapter 4.5. However, further work is required until both contributions can be included into a future model in a computationally efficient way.

To correctly reflect the alloy dependent creep response in the non-isothermal secondary and tertiary creep stages it is important to include an accurate rafting and coarsening description. This microstructure evolution should eventually be based on alloy dependent equations that then allow predictive capabilities to model a wide range of alloy compositions. This study should furthermore include an in-depth analysis of the effective channel width evolution in relation to different thermal creep cycles. This would optimise the model significantly in that it would be possible to model the cyclic creep response for a range of different compositions and temperature cycles.

6.4.2 Comparing the model to synchrotron results

The modelled results have so far been compared to the experimental results displayed in Chapter 5. In addition to this *post mortem* analysis it is particularly interesting to compare the modelled results to an *in-situ* synchrotron analysis. Such *in-situ* non-isothermal creep study can be found with le Graverend *et al.* [120] where the alloy AM1 was used. The key findings of their study will be briefly summarised here:

- During low and moderate temperature excursions, the γ-phase remains close to the mechanical equilibrium with a von Mises stress slightly above the Orowan stress.
- During very high-temperature excursions, the γ'-phase yields, the γ-phase cannot strain fast enough to remain at equilibrium, the constrained lattice misfit ($\delta_{\perp}$) of the γ/γ'-interface plane saturates at -4.3×10^{-3} and the von Mises stress within γ'-rafts can exceed the Orowan stress by several tens of MPa.
- During cooling of the specimens at the end of the excursions, plastic strain stops within the γ-phase, but goes on within the γ'-phase until the dislocations present there

annihilate at the end of γ'-rafts. This results in an increase of $\delta_{\perp}$, whose amplitude will determine the stress state and the further behaviour of the material.

- The analysis of the experimental data highlighted that one of the rate-limiting mechanisms of the γ'-raft plasticity is probably the entry of dislocations with $a_{\gamma'}$ [1 0 0] and $a_{\gamma'}$ [0 1 0] Burgers vectors which are sensitive to the internal stress and to the osmotic stress due to the supersaturation of vacancies within the γ'-phase.

- Citing the work by Touratier *et al.* [210], where the dislocation velocity at 1150 °C was estimated at 0.22 [nm s^{-1}], le Graverend *et al.* [120] further argued that dislocation γ'-shear by $a_{\gamma'}$ [0 0 1] dislocations due to the abundance of dislocation climb and the easy supply of dislocations could not be rate-limiting.

In this study, the dissolved γ'-fraction at the high temperature hold was close to its mechanical equilibrium and thus the non-isothermal cycling performed can be classified as a moderate temperature excursion according to the definition by le Graverend *et al.* [120]. As observed *in situ* with le Graverend *et al.* [120], the temperature excursion does result in a softening of both phases, enabling enhanced γ-channel glide but not resulting in a yielding of the γ'-phase by APB-shear.

Furthermore, the model correctly reflects that upon cooling the plastic strain decreases and eventually ceases within the γ-phase resulting in no further dislocation glide in the channels. The driving force behind the dislocation multiplication in the model is the effective interfacial lattice misfit as suggested by le Graverend *et al.* [120].

The deformation of the γ'-precipitate phase below the yield point is however slightly different as suggested by le Graverend *et al.* [120]. In their study, the samples were pre-rafted at 1050 $^{\circ}C$ and 150 MPa for 24 h prior to non-isothermal testing. Pre-rafting under these conditions would have most likely resulted in the activation of Eggeler-pair γ'-shearing prior to starting the non-isothermal tests (in the CMSX-4 test series this mechanism was observed after 0.5% strain and 2.15 - 4.7 h at 1050 °C, see Table 5.1).

Le Graverend *et al.* [120] concluded that shearing would not be rate-limiting for $a_{\gamma'}$ [0 0 1] but for $a_{\gamma'}$ [1 0 0] and a_{γ} [0 1 0] Burgers vectors which in this study could not be reproduced since the three Burgers vector combinations are not interdependent in their formation and the latter two cease in importance with the rapid closing of the vertical γ-channels due to accelerated rafting and coarsening under thermal cycling conditions. Thus, the conclusions cannot be compared directly as the pre-rafting performed by le Graverend *et al.* significantly increased the dislocation density in the microstructure under isothermal conditions before exposing it to a non-isothermal test regime.

6.5 Conclusion

The outlined non-isothermal creep model in its current form is able to correctly reflect the majority of key experimental trends and findings on the non-isothermal dislocation driven response correctly, despite the outlined limitations and need for further improvements. This chapter further clarified that thermal cycling results in a time lag between the high temperature and base temperature strain rate regime. This time lag is primarily driven by the phase fraction and microstructure evolution during non-isothermal cycling conditions and thus highlights that in order to obtain a non-isothermal creep resistant alloy a high temperature phase fraction stability, a low inter-diffusivity and a slow rafting and coarsening kinetics are all required.

Chapter 7

Conclusions and Further Work

7.1 Conclusions

The thermal cycling of CMSX-4 and CMSX-10 for a tertiary-creep dominated base condition, with short exposures into the γ'-rafting regime under a constant applied load was analysed experimentally and modelled using dislocation theory.

Non-isothermal creep testing

The strain curves for the three different test conditions studied were remarkably similar despite having been subjected to very different cycle times. For example the 9:3 (9 minutes at 900 °C and 3 minutes at 1050 °C) test condition underwent the most cycles and thus spent the most time at peak temperature (16 h) which corresponded to just above $\frac{1}{5}^{th}$ of the total test time until 1.8 % plastic strain. In comparison, the test with the slowest strain rate and longest creep life, 27:3 (27 minutes at 900 °C and 3 minutes at 1050 °C) spent 11 h at peak temperature which is below $\frac{1}{10}^{th}$ of the total test time until 1.8 % plastic strain. As a result, the 9:3 test has the lowest deformation per cycle but the highest strain rate overall, whilst the 27:3 condition accumulates the most strain per cycle. These trends are very similar to those published for thermal cycles at significantly higher temperatures of 1150 °C [77, 163].

Comparing the microstructure evolution using the SEM, three important distinctions to isothermal creep became apparent. Firstly, the progression of rafting is different in each of the test conditions. Fully established rafts can be seen after 0.5 % plastic strain accumulation for the 9:3 condition only. This means, that the creep minimum seen at 0.35 % strain does not coincide with the completion of γ'-rafting, as observed for isothermal creep in CMSX-4. This suggests, that the creep minimum under these non-isothermal conditions is likely to

be associated with other effects. Secondly, unlike the planar rafting process in isothermal rafting the non-isothermal cycling results in disrupted non-planar rafts leading to multiple connections between γ'-layers. Evidence of this is that all three conditions exhibit a number of angled side connections, the number increasing with time spent at base condition. Thirdly, the process of rafting is completed having spent less time at the peak temperature condition than during isothermal creep but with a different amount of plastic strain.

The falling strain rate regime under non-isothermal creep conditions was linked to the filling of γ-channels, the creation of interfacial networks and the subsequent increase in dislocation hardening. The interfacial networks in the non-isothermal microstructures were found to consist of classical single edge dislocation networks as well as paired edge dislocation networks.

The eventual strain rate acceleration in the non-isothermal tests was linked to the onset of γ'-shearing by dissimilar Burgers vector pairs (as observed previously by Eggeler and Dlouhy). Shearing by dislocation pairs separated by an APB-fault were absent in this test regime.

The non-planar and faster rafting process under non-isothermal conditions compared to isothermal creep resulted in a faster completion of topological inversion. After 1% plastic strain all test conditions exhibited a microstructure that was topologically inverted. However, the level of topological inversion did not scale with the cycling time. Exploring this anomaly further, the exceptionally fast topological inversion for the 9:3 test was linked to different precipitation and dissolution dynamics. The phase fraction modelling revealed that only the 9:3 test was exposed to a continuous metastable phase fraction regime, which resulted in an enhanced connectivity of precipitated γ'-tertiaries compared to the longer tests.

Non-isothermal creep parameter modelling

The non-isothermal γ'-phase fraction evolution was modelled based on a synchrotron dataset. The data revealed that the γ'-phase fraction evolution does not track the thermal cycling profile. Comparing the modelled γ'-phase fraction evolution for the three cycles it is apparent, that the phase fractions for the 9:3 test cycle continually change, whereas the 18:3 and 27:3 tests end in segments of equilibrium volume fraction of 9 minutes and 18 minutes respectively.

To estimate the effect of thermal cycling and calculate the evolution of key creep parameters the modelled γ'-phase fraction evolution was used to calculate an effective temperature that relates the phase fraction to its equivalent equilibrium temperature. Using this approach, it was found that some parameters show no considerable thermal cycling dependence, such

as solid-solution hardening, whereas other parameters changed significantly. The parameters driving non-isothermal creep were identified as the γ-interdiffusion, γ'-phase fraction dissolution, interfacial lattice misfit and Orowan backstress. The dislocation activity in the γ-matrix is then hindered in particular by stronger dislocation hardening contributions due to a faster dislocation density accumulation in the microstructure coupled with the formation and stability of interfacial dislocation networks.

Non-isothermal creep modelling

Using the estimated creep parameter evolutions in a non-isothermal creep model, it was possible to reflect the majority of key experimental trends and findings on the dislocation driven response under thermal cycling conditions. In particular, the acceleration in creep rate brought about by thermal cycling and lower dependence on thermal cycling rates can be modelled correctly.

The model highlighted that thermal cycling results in a time lag between the high temperature and base temperature strain rate regime. This time lag is primarily driven by the phase fraction and microstructure evolution during non-isothermal cycling conditions. The modelled trends suggest, that in order to obtain a non-isothermal creep resistant alloy a stable high temperature phase fraction, a low inter-diffusivity and a slow rafting and coarsening kinetics are all required.

Comparison to conventional strain rate models

To date, the non-isothermal strain rates in the turbine are frequently approximated using the isothermal strain rates at each temperature exposure multiplied by their respective exposure times. However, the experimental results presented in this thesis show that such an approach underestimates the non-isothermal strain rates significantly whilst simultaneously overestimating the influence of the respective cycling rates. It is thus recommended to incorporate non-isothermal testing into lifing methodologies.

Estimating alloy element segregation

Using EPMA the alloy element segregation was mapped for a fully heat-treated sample of CMSX-4 and CMSX-10. Based on the composition analysis the variation in creep parameters was estimated in different regions of the microstructure (dendrite cores and inter-dendritic region). The parameter modelling showed that even in fully γ'-solution heat treated samples the creep parameters can differ between the dendrite cores and inter-dendritic segregation

regions by as much as the mean alloy parameters differ for a first (e.g. CMSX-6) and sixth generation superalloy (e.g. TMS-238). This study highlights that the distribution of alloy element additions in different regions of the microstructure is a crucial factor in determining the creep response of an alloy and that effective γ'-solution heat treatments are essential.

Influence of the microstructure arrangement on deformation

Deforming CMSX-4 micro-pillars at room temperature in compression it was found, that the three dimensional microstructure arrangement of γ'-precipitates and γ-matrix resulted in a different strain hardening response, which was driven by the dislocation activity on the activated slip systems.

7.2 Further work

Exploring a new test regime

The non-isothermal creep tests were performed for turbine blades that cycle between the tertiary and rafting creep regime. Based on the significantly faster strain rates observed under these test conditions, it would be interesting to see if similar trends would be observed for thermal cycling between the primary and tertiary creep regime (lower temperatures and higher applied stresses). Such study would also provide the experimental results required to verify the model for application at these stress and temperatures.

Including the element segregation effect in the creep model

To further enhance the accuracy and predictive capabilities of the creep model, the rhenium-based variant approach developed by using the alloy element segregation maps (EPMA maps) should be included into the creep model. Including the effect of alloy element segregation would allow the effectiveness of heat treatments and alloying element additions in relation to the thermal cyclic creep response of the studied alloys to be estimated.

Non-isothermal rafting kinetics

As the non-isothermal rafting and coarsening kinetics are significantly faster than under isothermal conditions (by a factor of 15), it is crucial to revisit the γ'-precipitate evolution theory in order to derive a physics based rafting and coarsening model that is applicable to non-isothermal conditions.

Examining the interfacial composition gradients further

Examining the non-isothermal creep tests, it was found that the element concentration gradients varied considerably across the γ/γ'-interfaces. Fast diffusing elements such as aluminium showed a sharp interfacial composition profile and slow diffusing elements such as rhenium a much broader interfacial width. The interfacial composition profile further widens in the proximity of an interfacial dislocation. Further work is proposed to investigate how pronounced this interfacial widening effect is for an alloy with a higher non-isothermal phase fraction stability (CMSX-10).

Testing sixth generation superalloys

Comparing the two alloys examined under non-isothermal conditions it is suggested that a mixture of three key creep parameters trends contribute to a higher non-isothermal creep performance: a low γ-interdiffusivity, a high and temperature stable γ'-volume fraction and a moderate γ/γ'-interfacial lattice misfit. In particular the moderate misfit is at odds with the alloy development direction currently taken in the TMS series by the NIMS group. Thus, it would be beneficial to compare the non-isothermal creep performance of two of the latest generation alloys, TMS-238 (with a high negative misfit) and CMSX-4Plus (designed to have a more moderate interfacial misfit).

Further examining the impact of the 3D microstructure on the local stress/strain distribution

The impact of the local γ/γ'-microstructure arrangement on the slip band spacing and source of slip bands could not be investigated in this study but could be acquired when using the same settings as outlined and sectioning the micro-pillars with a more stable FiB-tomography software.

Examining the role of tertiaries in non-isothermal creep

As the non-isothermal creep tests were interrupted at the same point of the thermal cycle, the contribution of γ'-tertiaries to the Orowan resistance in the γ-channels could not be investigated. The creep model in its current form assumes that the γ'-tertiary contribution is small and thus it would be interesting to compare this result with a detailed TEM study examining the hardening contribution by γ'-tertiary precipitation following non-isothermal exposures.

References

[1] (2015). IATA. Airlines to Welcome 3.6 Billion Passengers in 2016 http://goo.gl/Gyl2d0 - last Accessed 01-07-2015.

[2] (2015). Rolls-Royce plc. How does a jet engine work? http://goo.gl/XijFTH - last Accessed 15-06-2015.

[3] (2015). Shakal, C. Trent 900 Turbofan, https://goo.gl/JkTaug, last Accessed 01-06-2018.

[4] (2015). Thermocouples in Gas Turbines; Scervini, http://goo.gl/XAxCxi, last Accessed 01-06-2015.

[5] (2015). UK Civil Aviation Authority. Engine type certificate data sheet No. 1051 https://goo.gl/0tEPGb - last Accessed 06-06-2015.

[6] Agudo Jácome, L., Nörtershäuser, P., Heyer, J. K., Lahni, A., Frenzel, J., Dlouhy, A., Somsen, C., and Eggeler, G. (2013). High-temperature and low-stress creep anisotropy of single-crystal superalloys. *Acta Materialia*, 61(8):2926–2943.

[7] Agudo Jácome, L., Nörtershäuser, P., Somsen, C., Dlouhy, A., and Eggeler, G. (2014). On the nature of γ' phase cutting and its effect on high temperature and low stress creep anisotropy of Ni-base single crystal superalloys. *Acta Materialia*, 69:246–264.

[8] Ardell, A. J. (1972). The effect of volume fraction on particle coarsening: theoretical considerations. *Acta Metallurgica*, 20(1):61–71.

[9] Ardell, A. J. (1985). Precipitation Hardening. *Metallurgical Transactions A*, 16(12):2131–2165.

[10] Ardell, A. J. (2011). A1-L12 interfacial free energies from data on coarsening in five binary Ni alloys, informed by thermodynamic phase diagram assessments. *Journal of Materials Science*, 46(14):4832–4849.

[11] Argon, A. S. and Moffatt, W. C. (1981). Climb of extended edge dislocations. *Acta Metallurgica*, 29(2):293–299.

[12] Arsenlis, A. (2004). On the evolution of crystallographic dislocation density in non-homogeneously deforming crystals. *Journal of the Mechanics and Physics of Solids*, 52(6):1213–1246.

[13] Avrami, M. (1941). Granulation, Phase Change, and Microstructure Kinetics of Phase Change. III. *The Journal of Chemical Physics*, 9(2):177–184.

[14] Baluc, N., Schäublin, R., and Hemker, K. J. (1991). Methods for determining precise values of antiphase boundary energies in Ni_3Al. *Philosophical Magazine Letters*, 64(5):327–334.

[15] Barba, D., Alabort, E., Pedrazzini, S., Collins, D. M., Wilkinson, A. J., Bagot, P. A. J., Moody, M. P., Atkinson, C., Jérusalem, A., and Reed, R. C. (2017). On the microtwinning mechanism in a single crystal superalloy. *Acta Materialia*, 135:314–329.

[16] Bentley, R. E. (1998). *Handbook of Temperature Measurement Vol. 3*. The Theory and Practice of Thermoelectric Thermometry. Springer Science & Business Media.

[17] Biermann, H., Strehler, M., and Mughrabi, H. (1996). High-temperature measurements of lattice parameters and internal stresses of a creep-deformed monocrystalline nickel-base superalloy. *Metallurgical and Materials Transactions A*, 27(4):1003–1014.

[18] Boittin, G., Locq, D., Rafray, A., Caron, P., Kanouté, P., Gallerneau, F., and Cailletaud, G. (2012). Influence of γ' Precipitate Size and Distribution on LCF Behavior of a PM Disk Superalloy. *Superalloys 2012*, pages 167–176.

[19] Brooks, H. (1952). *Theory of Internal Boundaries, In "Metal Interfaces"*. American Society of Metals.

[20] Brückner, U., Epishin, A. I., Link, T., and Dressel, K. (1998). The influence of the dendritic structure on the γ/γ'-lattice misfit in the single-crystal nickel-base superalloy CMSX-4. *Materials Science and Engineering: A*, 247(1-2):23–31.

[21] Brunetti, G., Settefrati, A., Hazotte, A., Denis, S., Fundenberger, J. J., Tidu, A., and Bouzy, E. (2012). Determination of γ–γ' lattice misfit in a single-crystal nickel-based superalloy using convergent beam electron diffraction aided by finite element calculations. *Micron*, 43(2-3):396–406.

[22] Bruno, G., Schönfeld, B., and Kostorz, G. (2003a). Lattice misfit in CMSX4-like nickel-base superalloys and its temperature dependence. *Zeitschrift für Metallkunde*, 94(1):12–18.

[23] Bruno, G., Schumacher, G., Pinto, H. C., and Schulze, C. (2003b). Measurement of the lattice misfit of the nickel-base superalloy SC16 by high-energy synchrotron radiation. *Metallurgical and Materials Transactions A: Physical Metallurgy and Materials Science*, 34(2):193–197.

[24] Buffiere, J. Y. and Ignat, M. (1995). A dislocation based criterion for the raft formation in nickel-based superalloys single crystals. *Acta metallurgica et materialia*, 43(5):1791–1797.

[25] Bürgel, R. (2013). *Handbuch Hochtemperatur-Werkstofftechnik*. Grundlagen, Werkstoffbeanspruchungen, Hochtemperaturlegierungen. Springer-Verlag.

[26] Campbell, C. E., Boettinger, W. J., and Kattner, U. R. (2002). Development of a diffusion mobility database for Ni-base superalloys. *Acta Materialia*, 50(4):775–792.

[27] Caron, P. (2000). High γ' solvus new generation nickel-based superalloys for single crystal turbine blade applications. *Superalloys 2000*, pages 737–746.

[28] Caron, P., Ohta, Y., Nakagawa, Y. G., and Khan, T. (1988). Creep Deformation Anisotropy in Single Crystal Superalloys. *Superalloys 1988*, pages 215–224.

[29] Caron, P., Ramusat, C., and Diologent, F. (2008). Influence of the γ' fraction on the γ/γ' topological inversion during high temperature creep of single crystal superalloys. In *Proceedings of the International Symposium on Superalloys*, pages 159–167. ONERA - The French Aerospace Lab, Chatillon, France.

[30] Carroll, L. J., Feng, Q., and Pollock, T. M. (2008). Interfacial Dislocation Networks and Creep in Directional Coarsened Ru-Containing Nickel-Base Single-Crystal Superalloys. *Metallurgical and Materials Transactions A*, 39(6):1290–1307.

[31] Chen, W. and Immarigeon, J. P. (1998). Thickening behaviour of gamma' precipitates in nickel base superalloys during rafting. *Scripta Materialia*, 39(2):167–174.

[32] Cheng, K. Y., Jo, C. Y., Jin, T., and Hu, Z. Q. (2010). Influence of applied stress on the γ' directional coarsening in a single crystal superalloy. *Materials and Design*, 31(2):968–971.

[33] Clement, N., Couret, A., and Caillard, D. (1991). An in situ study of cube glide in the γ'-phase of a superalloy. *Philosophical Magazine A*, 64(3):669–695.

[34] Collins, D. M. and Stone, H. J. (2014). A modelling approach to yield strength optimisation in a nickel-base superalloy. *International Journal of Plasticity*, 54(C):96–112.

[35] Cormier, J., Jouiad, M., Hamon, F., Villechaise, P., and Milhet, X. (2010). Very high temperature creep behavior of a single crystal Ni-based superalloy under complex thermal cycling conditions. *Philosophical Magazine Letters*, 90(8):611–620.

[36] Cormier, J., Milhet, X., Champion, J. L., and Mendez, J. (2008a). Simulation of Very High Temperature Overheating During Isothermal Creep of Single Crystal Ni-Base Superalloy. *Advanced Engineering Materials*, 10(1-2):56–61.

[37] Cormier, J., Milhet, X., and Mendez, J. (2007a). Effect of very high temperature short exposures on the dissolution of the γ' phase in single crystal MC2 superalloy. *Journal of Materials Science*, 42(18):7780–7786.

[38] Cormier, J., Milhet, X., and Mendez, J. (2007b). Non-isothermal creep at very high temperature of the nickel-based single crystal superalloy MC2. *Acta Materialia*, 55(18):6250–6259.

[39] Cormier, J., Milhet, X., Vogel, F., and Mendez, J. (2008b). Non-Isothermal Creep Behavior of a Second Generation Ni-Based Single Crystal Superalloy: Experimental Characterization and Modeling. In *Superalloys 2008*, pages 941–949. TMS.

[40] Coujou, A., Benyoucef, M., Clement, N., and Priester, L. (1996). Interactions between dislocations and γ/γ' interfaces in superalloys. *Interface Science*, 4(3-4):317–327.

[41] Crudden, D. J., Mottura, A., Warnken, N., Raeisinia, B., and Reed, R. C. (2014). Modelling of the influence of alloy composition on flow stress in high-strength nickel-based superalloys. *Acta Materialia*, 75:356–370.

[42] Cumpsty, N. A. (2003). *Jet propulsion a simple guide to the aerodynamic and thermodynamic design and performance of jet engines*. Cambridge University Press, Cambridge.

[43] Daymond, M. R., Preuss, M., and Clausen, B. (2007). Evidence of variation in slip mode in a polycrystalline nickel-base superalloy with change in temperature from neutron diffraction strain measurements. *Acta Materialia*, 55(9):3089–3102.

[44] Debiaggi, S. B., Decorte, P. M., and Monti, A. M. (1996). Diffusion by vacancy mechanism in Ni, Al, and Ni_3Al: Calculation based on many-body potentials. *Physica Status Solidi (B) Basic Research*, 195(1):37–54.

[45] Di Gioacchino, F. and Clegg, W. J. (2014). Mapping deformation in small-scale testing. *Acta Materialia*, 78(C):103–113.

[46] Dimiduk, D. M., Thompson, A. W., and Williams, J. C. (1993). The compositional dependence of antiphase-boundary energies and the mechanism of anomalous flow in Ni_3Al alloys. *Philosophical Magazine A*, 67(3):675–698.

[47] Dirand, L. (2011). *Fluage à haute température d'un superalliage monocristallin: expérimentation in situ en rayonnement synchrotron (PhD Thesis)*. PhD thesis, Université de Nancy.

[48] Dirand, L., Cormier, J., Jacques, A., Chateau-Cornu, J.-P., Schenk, T., Ferry, O., and Bastie, P. (2013). Measurement of the effective γ/γ' lattice mismatch during high temperature creep of Ni-based single crystal superalloy. *Materials Characterization*, 77(C):32–46.

[49] Dlouhy, A. and Eggeler, G. (1997). On the formation and motion of < 010>—dislocations during high temperature low stress creep of superalloy single crystals. *Materials Science and Engineering: A*.

[50] Dubiel, B. and Czyrska-Filemonowicz, A. (2012). TEM Analyses of Microstructure Evolution in Ex-Service Single Crystal CMSX-4 Gas Turbine Blade. *Solid State Phenomena*, 186:139–142.

[51] Durand-Charre, M. (1998). *The Microstructure of Superalloys*. CRC Press.

[52] Dyson, B. F. (2009). Microstructure based creep constitutive model for precipitation strengthened alloys: theory and application. *Materials Science and Technology*, 25(2):213–220.

[53] Dyson, B. F. and McLean, M. (1983). Particle-coarsening, $\sigma 0$ and tertiary creep. *Acta Metallurgica*, 31(1):17–27.

[54] Ecob, R. C., Ricks, R. A., and Porter, A. J. (1982). The measurement of precipitate/matrix lattice mismatch in nickel-base superalloys. *Scripta Metallurgica*, 16(9):1085–1090.

[55] Eggeler, G. and Dlouhy, A. (1997). On the formation of <010>-dislocations in the gamma'-phase of superalloy single crystals during high temperature low stress creep. *Acta Materialia*, 45(10):4251–4262.

[56] Epishin, A. I., Brückner, U., Portella, P. D., and Link, T. (2003). Influence of small rhenium additions on the lattice spacing of nickel solid solution. *Scripta Materialia*, 48(4):455–459.

[57] Epishin, A. I., Klingelhöffer, H., Link, T., Fedelich, B., Brückner, U., and Portella, P. D. (2009). New technique for characterization of microstructural degradation under creep: Application to the nickel-base superalloy CMSX-4. *Materials Science and Engineering: A*, 510-511:262–265.

[58] Epishin, A. I. and Link, T. (2004). Mechanisms of high-temperature creep of nickel-based superalloys under low applied stresses. *Philosophical Magazine*, 84(19):1979–2000.

[59] Epishin, A. I., Link, T., Brückner, U., Fedelich, B., and Portella, P. (2004). Effects of segregation in nickel-base superalloys: Dendritic stresses. In *Proceedings of the International Symposium on Superalloys*, pages 537–543. Federal Institute for Materials Research and Testing Berlin, Berlin, Germany.

[60] Epishin, A. I., Link, T., Brückner, U., and Portella, P. D. (2001). Kinetics of the topological inversion of the γ/γ'-microstructure during creep of a nickel-based superalloy. *Acta Materialia*, 49(19):4017–4023.

[61] Epishin, A. I., Link, T., Noltze, G., Svetlov, I. L., Bokshtein, B. S., Rodin, A. O., Salivan-Neumann, R., and Oder, G. (2014). Diffusion processes in multicomponent nickel-base superalloy-nickel system. *The Physics of Metals and Metallography*, 115(1):21–29.

[62] Epishin, A. I., Link, T., and Nolze, G. (2007). SEM investigation of interfacial dislocations in nickel-base superalloys. *Journal of microscopy*, 228(2):110–117.

[63] Fedelich, B. (2002). A microstructural model for the monotonic and the cyclic mechanical behavior of single crystals of superalloys at high temperatures. *International Journal of Plasticity*, 18(1):1–49.

[64] Fedelich, B., Epishin, A. I., Link, T., Klingelhöffer, H., Künecke, G., and Portella, P. D. (2012a). Experimental characterization and mechanical modeling of creep induced rafting in superalloys. *Computational Materials Science*, 64:2–6.

[65] Fedelich, B., Epishin, A. I., Link, T., Klingelhöffer, H., Künecke, G., and Portella, P. D. (2012b). Rafting during High Temperature Deformation in a Single Crystal Superalloy: Experiments and Modeling. In *Superalloys 2012*, pages 491–500, Hoboken, NJ, USA. Federal Institute for Materials Research and Testing Berlin, Berlin, Germany, John Wiley & Sons, Inc.

[66] Fedelich, B., Künecke, G., Epishin, A. I., Link, T., and Portella, P. (2009). Constitutive modelling of creep degradation due to rafting in single-crystalline Ni-base superalloys. *Materials Science and Engineering: A*, 510-511:273–277.

[67] Field, R. D., Pollock, T. M., and Murphy, W. H. (1992). The Development of γ/γ' Interfacial Dislocation Networks during Creep in Ni-Base Superalloys . In *Superalloys 1992 (Seventh International Symposium)*, pages 557–566. TMS.

[68] Frank, S., Södervall, U., and Herzig, C. (1997). Self- and Impurity Diffusion of Ni, Ga, Ge, Ti, Nb and B in the L12-Type Intermetallic Compounds Ni_3Al. *Defect and Diffusion Forum*, 143-147:245–250.

[69] Fu, C. L., Kremar, M., Reed, R., and Janotti, A. (2004). On the Diffusion of Alloying Elements in the Nickel-Base Superalloys. In *Superalloys 2004 (Tenth International Symposium)*, pages 867–876. TMS.

[70] Gabb, T. P., Draper, S. L., Hull, D. R., MacKay, R. A., and Nathal, M. V. (1989). The Role of Interfacial Dislocation Networks in High-Temperature Creep of Superalloys. *Materials Science and Engineering: A*, 118:59–69.

[71] Gale, W. F. and Totemeier, T. C. (2003). *Smithells Metals Reference Book*. Butterworth-Heinemann.

[72] Galindo-Nava, E. I., Connor, L. D., and Rae, C. M. F. (2015). On the prediction of the yield stress of unimodal and multimodal γ' Nickel-base superalloys. *Acta Materialia*, 98:377–390.

[73] Galindo-Nava, E. I. and Rae, C. M. F. (2014). Modelling creep of single–crystal superalloys: II. Primary and tertiary creep. *unpublished*, pages 1–38.

[74] Ge, B., Luo, Y., Li, J., and Zhu, J. (2010a). Study of γ/γ' Interfaces in Nickel-Based, Single-Crystal Superalloys by Scanning Transmission Electron Microscopy. *Metallurgical and Materials Transactions A*, 42(3):548–552.

[75] Ge, B., Luo, Y., Li, J., Zhu, J., Tang, D., and Gui, Z. (2012). Study of γ/γ' interfacial width in a nickel-based superalloy by scanning transmission electron microscopy. *Philosophical Magazine Letters*, 92(10):541–546.

[76] Ge, B. H., Luo, Y. S., Li, J. R., and Zhu, J. (2010b). Distribution of rhenium in a single crystal nickel-based superalloy. *Scripta Materialia*, 63(10):969–972.

[77] Giraud, R., Cormier, J., Hervier, Z., Bertheau, D., Harris, K., Wahl, J., Milhet, X., Mendez, J., and Organista, A. (2012a). Effect of the Prior Microstructure Degradation on the High Temperature/Low Stress Non-Isothermal Creep Behavior of CMSX-4® Ni-Based Single Crystal Superalloy. *Superalloys 2012*, pages 265–274.

[78] Giraud, R., Hervier, Z., Cormier, J., Saint-Martin, G., Hamon, F., Milhet, X., and Mendez, J. (2012b). Strain Effect on the γ' Dissolution at High Temperatures of a Nickel-Based Single Crystal Superalloy. *Metallurgical and Materials Transactions A*, 44(1):131–146.

[79] Goehler, T., Schwalbe, C., Svoboda, J., Affeldt, E., and Singer, R. F. (2016). Discussing the effect of gamma prime coarsening on high temperature low stress creep deformation with respect to the role of refractory elements. In *Proceedings of the International Symposium on Superalloys*, pages 655–664. MTU Aero Engines GmbH, Munich, Germany.

[80] Goodfellow, A. J., Galindo-Nava, E. I., Christofidou, K. A., Jones, N. G., Martin, T., Bagot, P. A. J., Boyer, C. D., Hardy, M. C., and Stone, H. J. (2017). Gamma Prime Precipitate Evolution During Aging of a Model Nickel-Based Superalloy. *Metallurgical and Materials Transactions A*, 49(3):718–728.

[81] Goswami, K. N. and Mottura, A. (2014). Can slow-diffusing solute atoms reduce vacancy diffusion in advanced high-temperature alloys? *Materials Science and Engineering: A*, 617:194–199.

[82] Grosdidier, T., Hazotte, A., and Simon, A. (1998). Precipitation and dissolution processes in gamma/gamma' single crystal nickel-based superalloys. *Materials Science and Engineering: A*, 256(1-2):183–196.

[83] Guha, A. (2015). Cooling Systems in a Turbine Blade http://goo.gl/bSv1qB - last Accessed 15-06-2015.

[84] Gypen, L. A. and Deruyttere, A. (1977). Multi-component intrinsic solid solution softening and hardening. *Journal of the Less Common Metals*, 56(1):91–101.

[85] Gypen, L. A. and Deruyttere, A. (1981). The Combination of Atomic Size and Elastic-Modulus Misfit Interactions in Solid-Solution Hardening. *Scripta Metallurgica*, 15(8):815–820.

[86] Hafez Haghighat, S. M., Eggeler, G., and Raabe, D. (2013). Effect of climb on dislocation mechanisms and creep rates in γ'-strengthened Ni base superalloy single crystals: A discrete dislocation dynamics study. *Acta Materialia*, 61(10):3709–3723.

[87] Hantcherli, M., Pettinari-Sturmel, F., Viguier, B., Douin, J., and Coujou, A. (2012). Evolution of interfacial dislocation network during anisothermal high-temperature creep of a nickel-based superalloy. *Scripta Materialia*, 66(3-4):143–146.

[88] Hemker, K. J. and Mills, M. J. (1993). Measurements of antiphase boundary and complex stacking fault energies in binary and B-doped Ni_3Al using TEM. *Philosophical Magazine A*, 68(2):305–324.

[89] Hobbs, R. A., Tin, S., Rae, C. M. F., Broomfield, R. W., and Humphreys, C. J. (2004). Solidification characteristics of advanced nickel-base single crystal superalloys. In *Proceedings of the International Symposium on Superalloys*, pages 819–825. TMS.

[90] Huang, M., Cheng, Z., Xiong, J., Li, J., Hu, J., Liu, Z., and Zhu, J. (2014). Coupling between Re segregation and γ/γ' interfacial dislocations during high-temperature, low-stress creep of a nickel-based single-crystal superalloy. *Acta Materialia*, 76:294–305.

[91] Huang, M., Zhao, L., and Tong, J. (2012). Discrete dislocation dynamics modelling of mechanical deformation of nickel-based single crystal superalloys. *International Journal of Plasticity*, 28(1):141–158.

[92] Hull, D. and Bacon, D. J. (2011). Introduction to dislocations. Elsevier.

[93] Humphreys, F. J. and Hatherly, M. (1995). *Recrystallization and Related Annealing Phenomena*. Elsevier.

[94] Husseini, N. S., Kumah, D. P., Yi, J. Z., Torbet, C. J., Arms, D. A., Dufresne, E. M., Pollock, T. M., Wayne Jones, J., and Clarke, R. (2008). Mapping single-crystal dendritic microstructure and defects in nickel-base superalloys with synchrotron radiation. *Acta Materialia*, 56(17):4715–4723.

[95] Inden, G., Bruns, S., and Ackermann, H. (1986). Antiphase boundary energies in ordered f.c.c. alloys. *Philosophical Magazine A*, 53(1):87–100.

[96] Jacques, A. and Bastie, P. (2003). The evolution of the lattice parameter mismatch of a nickel-based superalloy during a high-temperature creep test. *Philosophical Magazine*, 83(26):3005–3027.

[97] Jacques, A., Trehorel, R., and Schenk, T. (2018). High-Temperature Dislocation Climb in the γ' Rafts of Single-Crystal Superalloys: The Hypothesis of a Control by Dislocation Entry into the Rafts. *Metallurgical and Materials Transactions A*, pages 1–16.

[98] Jaroszewicz, J., Matysiak, H., Michalski, J., Matuszewski, K., Kubiak, K., and Kurzydlowski, K. J. (2011). Characterization of single-crystal dendrite structure and porosity in nickel-based superalloys using X-ray micro-computed tomography. In *Advanced Materials Research*, pages 66–71. Politechnika Warszawska, Warsaw, Poland.

[99] Jena, A. K. and Chaturvedi, M. C. (1984). The Role of Alloying Elements in the Design of Nickel-Base Superalloys. *Journal of Materials Science*, 19(10):3121–3139.

[100] Jones, R. D., Di Gioacchino, F., Lim, H., Edwards, T. E. J., Schwalbe, C., Battaile, C. C., and Clegg, W. J. (2018). Reduced partitioning of plastic strain for strong and yet ductile precipitate-strengthened alloys. *Scientific Reports*, 8(1):361.

[101] Jouiad, M., Ghighi, J., Cormier, J., Ostoja-Kuczynski, E., Lubineau, G., and Mendez, J. (2012). 3D Imaging Using X-Ray Tomography and SEM Combined FIB to Study Non Isothermal Creep Damage of (111) Oriented Samples of γ / γ ' Nickel Base Single Crystal Superalloy MC2. *Materials Science Forum*, 706-709:2400–2405.

[102] Kakehi, K. (1999). Influence of secondary precipitates and crystallographic orientation on the strength of single crystals of a Ni-based superalloy. *Metallurgical and Materials Transactions A*, 30(5):1249–1259.

[103] Kakehi, K. (2000). Effect of primary and secondary precipitates on creep strength of Ni-base superalloy single crystals. *Materials Science and Engineering: A*, 278(1-2):135–141.

[104] Kamaraj, M., Serin, K., Kolbe, M., and Eggeler, G. (2001). Influence of stress state on the kinetics of γ-channel widening during high temperature and low stress creep of the single crystal superalloy CMSX-4. *Materials Science and Engineering: A*, 319-321:796–799.

[105] Karunaratne, M. S. A., Rae, C. M. F., and Reed, R. C. (2001). On the microstructural instability of an experimental nickel-based single-crystal superalloy. *Metallurgical and Materials Transactions A*, 32(10):2409–2421.

[106] Karunaratne, M. S. A. and Reed, R. C. (2003). Interdiffusion of the platinum-group metals in nickel at elevated temperatures. *Acta Materialia*, 51(10):2905–2919.

[107] Kawagishi, K., Yeh, A. C., Yokokawa, T., Kobayashi, T., Koizumi, Y., and Harada, H. (2012). Development of an Oxidation-Resistant High-Strength Sixth-Generation Single-Crystal Superalloy TMS-238. In *Superalloys 2012*, pages 189–195, Hoboken, NJ, USA.

National Institute for Materials Science Tsukuba, Tsukuba, Japan, John Wiley & Sons, Inc.

[108] Koizumi, Y., Osawa, M., Kobayashi, T., Yokokawa, T., Zhang, J., Harada, H., Aoki, Y., and Arai, M. (2004). Development of Next-Generation Ni-Base Single Crystal Superalloys. In *Superalloys 2004 (Tenth International Symposium)*, pages 35–43. TMS.

[109] Kontis, P., Li, Z., Collins, D. M., Cormier, J., Raabe, D., and Gault, B. (2018). The effect of chromium and cobalt segregation at dislocations on nickel-based superalloys. *Scripta Materialia*, 145:1–5.

[110] Kostka, A., Mälzer, G., Eggeler, G., Dlouhy, A., Reese, S., and Mack, T. (2007). L12-phase cutting during high temperature and low stress creep of a Re-containing Ni-base single crystal superalloy. *Journal of Materials Science*, 42(11):3951–3957.

[111] Kozar, R. W., Suzuki, A., Milligan, W. W., Schirra, J. J., Savage, M. F., and Pollock, T. M. (2009). Strengthening Mechanisms in Polycrystalline Multimodal Nickel-Base Superalloys. *Metallurgical and Materials Transactions A*, 40(7):1588–1603.

[112] Kuhn, H. A., Biermann, H., Ungar, T., and Mughrabi, H. (1991). An X-ray study of creep-deformation induced changes of the lattice mismatch in the γ'-hardened monocrystalline nickel-base superalloy SRR 99. *Acta metallurgica et materialia*, 39(11):2783–2794.

[113] Kundin, J., Mushongera, L., Goehler, T., and Emmerich, H. (2012). Phase-field modeling of the γ'-coarsening behavior in Ni-based superalloys. *Acta Materialia*, 60(9):3758–3772.

[114] Lasalmonie, A. and Strudel, J. L. (1975). Interfacial dislocation networks around γ' precipitates in nickel-base alloys. *Philosophical Magazine*, 32(5):937–949.

[115] le Graverend, J. B., Cormier, J., Gallerneau, F., and Kruch, S. (2014a). Highly non-linear creep life induced by a short close γ'-solvus overheating and a prior microstructure degradation on a nickel-based single crystal superalloy. *Materials and Design*, 56:990–997.

[116] le Graverend, J.-B., Cormier, J., Gallerneau, F., and Paulmier, P. (2011). Dissolution of Fine γ' Precipitates of MC2 Ni-Based Single-Crystal Superalloy in Creep-Fatigue Regime. *Advanced Materials Research*, 278:31–36.

[117] le Graverend, J. B., Cormier, J., Gallerneau, F., Villechaise, P., Kruch, S., and Mendez, J. (2014b). A microstructure-sensitive constitutive modeling of the inelastic behavior of single crystal nickel-based superalloys at very high temperature. *International Journal of Plasticity*, 59:55–83.

[118] le Graverend, J. B., Cormier, J., Jouiad, M., Gallerneau, F., Paulmier, P., and Hamon, F. (2010). Effect of fine γ' precipitation on non-isothermal creep and creep-fatigue behaviour of nickel base superalloy MC2. *Materials Science and Engineering: A*, 527(20):5295–5302.

[119] le Graverend, J.-B., Dirand, L., Jacques, A., Cormier, J., Ferry, O., Schenk, T., Gallerneau, F., Kruch, S., and Mendez, J. (2012). In Situ Measurement of the γ/γ' Lattice Mismatch Evolution of a Nickel-Based Single-Crystal Superalloy During Non-isothermal Very High-Temperature Creep Experiments. *Metallurgical and Materials Transactions A*, 43(11):3946–3951.

[120] le Graverend, J.-B., Jacques, A., Cormier, J., Ferry, O., Schenk, T., and Mendez, J. (2015). Creep of a nickel-based single-crystal superalloy during very high-temperature jumps followed by synchrotron X-ray diffraction. *Acta Materialia*, 84:65–79.

[121] Li, X., Saunders, N., and Miodownik, A. P. (2002). The coarsening kinetics of γ' particles in nickel-based alloys. *Metallurgical and Materials Transactions A: Physical Metallurgy and Materials Science*, 33(11):3367–3374.

[122] Lifshitz, I. M. and Slyozov, V. V. (1961). The kinetics of precipitation from supersaturated solid solutions. *Journal of Physics and Chemistry of Solids*, 19(1-2):35–50.

[123] Link, T., Epishin, A. I., Brückner, U., and Portella, P. (2000). Increase of misfit during creep of superalloys and its correlation with deformation. *Acta Materialia*, 48(8):1981–1994.

[124] Link, T., Epishin, A. I., Klaus, M., Brückner, U., and Reznicek, A. (2005). 100 Dislocations in nickel-base superalloys: Formation and role in creep deformation. *Materials Science and Engineering: A*, 405(1-2):254–265.

[125] Link, T. and Feller-Kniepmeier, M. (1992). Shear mechanisms of the γ' phase in single-crystal superalloys and their relation to creep. *Metallurgical Transactions A*, 23(1):99–105.

[126] Liss, K. D., Royer, A., Tschentscher, T., Suortti, P., and Williams, A. P. (1998). On High-Resolution Reciprocal-Space Mapping with a Triple-Crystal Diffractometer for High-Energy X-rays. *Journal of synchrotron radiation*, 5(2):82–89.

[127] Liu, X. L., Shang, S.-L., Hu, Y.-J., Wang, Y., Du, Y., and Liu, Z.-K. (2017). Insight into γ-Ni/γ'-Ni_3Al interfacial energy affected by alloying elements. *Materials and Design*, 133(C):39–46.

[128] Long, H., Wei, H., Liu, Y., Mao, S., Zhang, J., Xiang, S., Chen, Y., Gui, W., Li, Q., Zhang, Z., and Han, X. (2016). Effect of lattice misfit on the evolution of the dislocation structure in Ni-based single crystal superalloys during thermal exposure. *Acta Materialia*, 120:95–107.

[129] Lukáš, P., Čadek, J., Šustek, V., and Kunz, L. (1996). Creep of CMSX-4 single crystals of different orientations in tension and compression. *Materials Science and Engineering: A*, 208(2):149–157.

[130] Ma, A., Reed, R. C., and Dye, D. (2008). A model for the creep deformation behaviour of single-crystal superalloy CMSX-4. *Acta Materialia*, 56(8):1657–1670.

[131] MacKay, R. A. and Ebert, L. J. (1985). The development of γ-γ' lamellar structures in a nickel-base superalloy during elevated temperature mechanical testing. *Metallurgical Transactions A*, 16(11):1969–1982.

[132] MacKay, R. A., Gabb, T. P., and Nathal, M. V. (2013). Microstructure-sensitive creep models for nickel-base superalloy single crystals. *Materials Science and Engineering: A*, 582(C):397–408.

[133] MacKay, R. A. and Nathal, M. V. (1990). γ' coarsening in high volume fraction nickel-base alloys. *Acta metallurgica et materialia*, 38(6):993–1005.

[134] Madison, J., Spowart, J. E., Rowenhorst, D. J., Fiedler, J., and Pollock, T. M. (2008). Characterization of Three-Dimensional Dendritic Structures in Nickel-Base Single Crystals for Investigation of Defect Formation. In *Superalloys 2008*, pages 881–888. TMS.

[135] Maldini, M., Harada, H., Koizumi, Y., Kobayashi, T., and Lupinc, V. (2000). Tertiary creep behaviour of a new single crystal superalloy at 900 °C. *Scripta Materialia*, 43(7):637–644.

[136] Malygin, G. A. (1990). Dislocation density evolution equation and strain hardening of fcc crystals. *physica status solidi (a)*, 119(2):423–436.

[137] Masoumi, F., Shahriari, D., Jahazi, M., Cormier, J., and Devaux, A. (2016). Kinetics and Mechanisms of γ' Reprecipitation in a Ni-based Superalloy. *Scientific Reports*, 6(1):841.

[138] Matan, N., Cox, D. C., Carter, P., Rist, M. A., Rae, C. M. F., and Reed, R. C. (1999a). Creep of CMSX-4 superalloy single crystals: effects of misorientation and temperature. *Acta Materialia*, 47(5):1549–1563.

[139] Matan, N., Cox, D. C., Carter, P., Rist, M. A., Rae, C. M. F., and Reed, R. C. (1999b). Creep of CMSX-4 superalloy single crystals: effects of misorientation and temperature. *Acta Materialia*, 47(5):1549–1563.

[140] Matan, N., Cox, D. C., Rae, C. M. F., and Reed, R. C. (1999c). On the kinetics of rafting in CMSX-4 superalloy single crystals. *Acta Materialia*, 47(7):2031–2045.

[141] Milhet, X., Arnoux, M., Cormier, J., Mendez, J., and Tromas, C. (2012). On the influence of the dendritic structure on the creep behavior of a Re-containing superalloy at high temperature/low stress. *Materials Science and Engineering: A*, 546:139–145.

[142] Miller, J. D., Tschopp, M. A., Oppedal, A. L., and Solanki, K. N. (2013). Characterizing the Local Primary Dendrite Arm Spacing in Directionally Solidified Dendritic Microstructures. *Metallurgical and Materials Transactions A*, 45(1):426–437.

[143] Mishima, Y., Ochiai, S., Hamao, N., Yodogawa, M., and Suzuki, T. (1986). Solid Solution Hardening of Nickel - Role of Transition Metal and B-subgroup Solutes. *Transactions of the Japan Institute of Metals*, 27(9):656–664.

[144] Mishima, Y., Ochiai, S., and Suzuki, T. (1985). Lattice-Parameters of Ni(Gamma), Ni_3Al(Gamma') and Ni_3Ga(Gamma') Solid-Solutions with Additions of Transition and B-Subgroup Elements. *Acta Metallurgica*, 33(6):1161–1169.

[145] Murakumo, T., Kobayashi, T., Koizumi, Y., and Harada, H. (2004). Creep behaviour of Ni-base single-crystal superalloys with various γ' volume fraction. *Acta Materialia*, 52(12):3737–3744.

[146] Nabarro, F. R. N. (1996). Rafting in Superalloys. *Metallurgical and Materials Transactions A*, 27(3):513–530.

[147] Nathal, M. V., MacKay, R. A., and Garlick, R. G. (1985). Temperature dependence of γ-γ' lattice mismatch in nickel-base superalloys. *Materials Science and Engineering*, 75(1-2):195–205.

[148] Neumeier, S., Ang, J., Hobbs, R. A., Rae, C. M. F., and Stone, H. J. (2011). Lattice Misfit of High Refractory Ruthenium Containing Nickel-Base Superalloys. *Advanced Materials Research*, 278:60–65.

[149] Pinto, H. C. and Bruno, G. (2003). Formation and relaxation of coherency strain in the nickel-base superalloy SC16. *Journal of synchrotron radiation*, 10(2):148–153.

[150] Poirier, J.-P. (1985). *Creep of Crystals*. High-Temperature Deformation Processes in Metals, Ceramics and Minerals. Cambridge University Press.

[151] Pollock, T. M. and Argon, A. S. (1992). Creep resistance of CMSX-3 nickel base superalloy single crystals. *Acta metallurgica et materialia*, 40(1):1–30.

[152] Pollock, T. M. and Argon, A. S. (1994). Directional Coarsening in Nickel-Base Single-Crystals with High-Volume Fractions of Coherent Precipitates. *Acta metallurgica et materialia*, 42(6):1859–1874.

[153] Pollock, T. M. and Tin, S. (2006). Nickel-based superalloys for advanced turbine engines: Chemistry, microstructure, and properties. *Journal of Propulsion and Power*, 22(2):361–374.

[154] Porter, D. A. and Easterling, K. E. (1992). *Phase Transformations in Metals and Alloys*. Springer US, Boston, MA.

[155] Prakash, A. and Bitzek, E. (2017). Idealized vs. Realistic Microstructures: An Atomistic Simulation Case Study on γ/γ' Microstructures. *Materials*, 10(1):88–18.

[156] Probst-Hein, M. (2001). Dislocation interactions in y-channels between y'-particles of superalloy single crystals . *Materials Science and Engineering*, pages 1–4.

[157] Pyczak, F., Devrient, B., Neuner, F. C., and Mughrabi, H. (2005). The influence of different alloying elements on the development of the γ/γ' microstructure of nickel-base superalloys during high-temperature annealing and deformation. *Acta Materialia*, 53(14):3879–3891.

[158] Qi, W. and Bertram, A. (1998). Damage modeling of the single crystal superalloy SRR99 under monotonous creep. *Computational Materials Science*, 13(1-3):132–141.

[159] Qi, W. and Bertram, A. (1999). Anisotropic continuum damage modeling for single crystals at high temperatures. *International Journal of Plasticity*, 15(11):1197–1215.

[160] Quested, P. N. and McLean, M. (1984). Solidification morphologies in directionally solidified superalloys. *Materials Science and Engineering*, 65(1):171–180.

[161] Rae, C. M. F. and Reed, R. C. (2001). The precipitation of topologically close-packed phases in rhenium-containing superalloys. *Acta Materialia*, 49(19):4113–4125.

[162] Rae, C. M. F. and Reed, R. C. (2007). Primary creep in single crystal superalloys: Origins, mechanisms and effects. *Acta Materialia*, 55(3):1067–1081.

[163] Raffaitin, A., Monceau, D., Crabos, F., and Andrieu, E. (2007). The effect of thermal cycling on the high-temperature creep behaviour of a single crystal nickel-based superalloy. *Scripta Materialia*, 56(4):277–280.

[164] Reed, R. C. (2006). *The Superalloys*. Fundamentals and Applications. Cambridge University Press.

[165] Reed, R. C., Cox, D. C., and Rae, C. M. F. (2007). Kinetics of rafting in a single crystal superalloy: effects of residual microsegregation. *Materials Science and Technology*, 23(8):893–902.

[166] Reed, R. C., Matan, N., Cox, D. C., Rist, M. A., and Rae, C. M. F. (1999). Creep of CMSX-4 superalloy single crystals: Effects of rafting at high temperature. *Acta Materialia*, 47(12):3367–3381.

[167] Reed, R. C., Tao, T., and Warnken, N. (2009). Alloys-By-Design: Application to nickel-based single crystal superalloys. *Acta Materialia*, 57(19):5898–5913.

[168] Rehman, H., Durst, K., Neumeier, S., Sato, A., Reed, R., and Göken, M. (2017). On the temperature dependent strengthening of nickel by transition metal solutes. *Acta Materialia*, 137:54–63.

[169] Ricks, R. A., Porter, A. J., and Ecob, R. C. (1983). The growth of γ' precipitates in nickel-base superalloys. *Acta Metallurgica*, 31(1):43–53.

[170] Roth, H. A., Davis, C. L., and Thomson, R. C. (1997). Modeling solid solution strengthening in nickel alloys. *Metallurgical and Materials Transactions A: Physical Metallurgy and Materials Science*, 28(6):1329–1335.

[171] Roy, I., Balikci, E., Ibekwe, S., and Raman, A. (2005). Precipitate growth activation energy requirements in the duplex size γ' distribution in the superalloy IN738LC. *Journal of Materials Science*, 40(23):6207–6215.

[172] Royer, A., Jacques, A., Bastie, P., and Veron, M. (2001). The evolution of the lattice parameter mismatch of nickel based superalloy: an in situ study during creep deformation. *Materials Science and Engineering: A*, 319:800–804.

[173] Ru, Y., Li, S., Zhou, J., Pei, Y., Wang, H., Gong, S., and Xu, H. (2016). Dislocation network with pair-coupling structure in 111 γ/γ' interface of Ni-based single crystal superalloy. *Scientific Reports*, 6.

[174] Sarosi, P. M., Srinivasan, R., Eggeler, G. F., Nathal, M. V., and Mills, M. J. (2007). Observations of a010 dislocations during the high-temperature creep of Ni-based superalloy single crystals deformed along the [001] orientation. *Acta Materialia*, 55(7):2509–2518.

[175] Sato, A., Harada, H., Yeh, A. C., Kawagishi, K., Kobayashi, T., Koizumi, Y., Yokokawa, T., and Zhang, J. X. (2008). A 5th Generation SC Superalloy with Balanced High Temperature Properties and Processability. In *Superalloys 2008 (Eleventh International Symposium)*, pages 131–138. TMS.

[176] Schenk, T., Jacques, A., le Graverend, J.-B., and Cormier, J. (2015). Real Time In Situ X-Ray Diffraction Study of the High Temperature Mechanical Behavior of a Rafted Single Crystal Superalloy. In *TMS2015 Supplemental Proceedings*, pages 1289–1298. John Wiley & Sons, Inc., Hoboken, NJ, USA.

[177] Schneider, W., Hammer, J., and Mughrabi, H. (1992). Creep Deformation and Rupture Behaviour of the Monocrystalline Superalloy CMSX-4: A Comparison with the Alloy SRR 99. In *Superalloys 1992 (Seventh International Symposium)*, pages 589–598. TMS.

[178] Schulze, C. and Feller-Kniepmeier, M. (2000). Transmisson electron microscopy of phase composition and lattice misfit in the Re-containing nickel-base superalloy CMSX-10. *Materials Science and Engineering: A*, 281(1-2):204–212.

[179] Schwalbe, C., Cormier, J., Jones, C. N., Galindo-Nava, E., and Rae, C. M. F. (2018a). Investigating the Dislocation-Driven Micro-mechanical Response Under Non-isothermal Creep Conditions in Single-Crystal Superalloys. *Metallurgical and Materials Transactions A*, pages 1–15.

[180] Schwalbe, C., Jacques, A., Galindo-Nava, E., Jones, C. N., Rae, C. M. F., and Cormier, J. (2018b). In situ measurement of the precipitate volume fraction and interfacial lattice misfit during non-isothermal creep in the superalloy cmsx-4. *Materials Science and Engineering: A*, 740-741:182–186.

[181] Schwalbe, C. W. M. (2014). Verifizierung des Kriechmodells nach Svoboda und Lukas im Hinblick auf die Vergroeberungsdynamik von einkristallinen Nickel-basis-superlegierungen der ersten und zweiten Generation. Master's thesis, TU Berlin.

[182] Schwalbe, C. W. M., Jacques, A., Galindo-Nava, E. I., Jones, N. C., Rae, C. M. F., and Cormier, J. (2018c). Quantifying the mechanisms controlling non-isothermal creep in single-crystal superalloys . *under review*.

[183] Shah, D. M. (1983). Orientation dependence of creep behavior of single crystal γ' (Ni_3Al). $ScriptaMetallurgica, 17(8) : 997 - -1002$.

[184] Shang, S. L., Kim, D. E., Zacherl, C. L., Wang, Y., Du, Y., and Liu, Z. K. (2012). Effects of alloying elements and temperature on the elastic properties of dilute Ni-base superalloys from first-principles calculations. *Journal of Applied Physics*, 112(5):053515.

[185] Siebörger, D., Knake, H., and Glatzel, U. (2001). Temperature dependence of the elastic moduli of the nickel-base superalloy CMSX-4 and its isolated phases. *Materials Science and Engineering: A*, 298(1-2):26–33.

[186] Singh, A. K., Louat, N., and Sadananda, K. (1988). Dislocation network formation and coherency loss around gamma-prime precipitates in a nickel-base superalloy. *Metallurgical Transactions A*, 19 A(12):2965–2973.

[187] Smith, T. M., Unocic, R. R., Deutchman, H., and Mills, M. J. (2016). Creep deformation mechanism mapping in nickel base disk superalloys. *Materials at High Temperatures*, 33(4-5):372–383.

[188] Sonderegger, B. and Kozeschnik, E. (2010). Interfacial Energy of Diffuse Phase Boundaries in the Generalized Broken-Bond Approach. *Metallurgical and Materials Transactions A*, 41(12):3262–3269.

[189] Sondhi, S. K., Dyson, B. F., and McLean, M. (2004). Tension–compression creep asymmetry in a turbine disc superalloy: roles of internal stress and thermal ageing. *Acta Materialia*, 52(7):1761–1772.

[190] Srinivasan, R., Eggeler, G. F., and Mills, M. J. (2000). γ'-cutting as rate-controlling recovery process during high-temperature and low-stress creep of superalloy single crystals. *Acta Materialia*, 48(20):4867–4878.

[191] Steuer, S., Hervier, Z., Thabart, S., and Castaing, C. (2014a). Creep behavior under isothermal and non-isothermal conditions of AM3 single crystal superalloy for different solutioning cooling rates. *Materials Science and Engineering: A*, 601:145–152.

[192] Steuer, S., Hervier, Z., Thabart, S., Castaing, C., Pollock, T. M., and Cormier, J. (2014b). Creep behavior under isothermal and non-isothermal conditions of AM3 single crystal superalloy for different solutioning cooling rates. *Materials Science and Engineering: A*, 601:145–152.

[193] Sugui, T., Huihua, Z., Jinghua, Z., Hongcai, Y., Yongbo, X., and Zhuangqi, H. (2000). Formation and role of dislocation networks during high temperature creep of a single crystal nickel-base superalloy. *Materials Science and Engineering: A*, 279(1-2):160–165.

[194] Suortti, P. and Tschentscher, T. (1995). High energy scattering beamlines at European Synchrotron Radiation Facility. *Review of Scientific Instruments*, 66(2):1798–1801.

[195] Svoboda, J. and Lukáš, P. (1996). Modelling of kinetics of directional coarsening in Ni-superalloys. *Acta Materialia*, 44(6):2557–2565.

[196] Svoboda, J. and Lukáš, P. (1997a). Activation energy of creep in 001-oriented superalloy CMSX-4 single crystals. *Materials Science and Engineering: A*, 234-236:173–176.

[197] Svoboda, J. and Lukáš, P. (1997b). Modelling of recovery controlled creep in nickel-base superalloy single crystals. *Acta Materialia*, 45(1):125–135.

[198] Svoboda, J. and Lukáš, P. (1998). Model of creep in < 001>-oriented superalloy single crystals. *Acta Materialia*, 46(10):3421–3431.

[199] Svoboda, J. and Lukáš, P. (2000). Creep deformation modelling of superalloy single crystals. *Acta Materialia*, 48(10):2519–2528.

[200] Szczotok, A. and Chmiela, B. (2013). Effect of Heat Treatment on Chemical Segregation in CMSX-4 Nickel-Base Superalloy. *Journal of Materials Engineering and Performance*, 23(8):2739–2747.

[201] Tabrizi, N. (2014). *Optimizing The Microstructure of Single Crystal Ni-Base Superalloys*. PhD thesis, University of Cambridge.

[202] Tian, S., Su, Y., Qian, B., Yu, X., Liang, F., and Li, A. (2012). Creep behavior of a single crystal nickel-based superalloy containing 4.2 pct. Re. *Materials and Design*, 37(C):236–242.

[203] Timmins, R., Greenwood, G. W., and Dyson, D. F. (1986). Negative creep in a nickel-base superalloy. *Scripta Metallurgica*, 20(1):67–70.

[204] Tinga, T. (2009). *Multiscale modelling of single crystal superalloys for gas turbine blades*. PhD thesis, Technische Universiteit Eindhoven.

[205] Tinga, T., Brekelmans, W. A. M., and Geers, M. G. D. (2008). Incorporating strain gradient effects in a multiscale constitutive framework for nickel-base superalloys. *Philosophical Magazine*, 88(30-32):3793–3825.

[206] Tinga, T., Brekelmans, W. A. M., and Geers, M. G. D. (2009). Directional coarsening in nickel-base superalloys and its effect on the mechanical properties. *Computational Materials Science*, 47(2):471–481.

[207] Tinga, T., de Wolf, W. B., Visser, W. P., and Woldendorp, S. (2001). Integrated Lifing Analysis of a Film-Cooled Turbine Blade. In *RTO-AVT Symposium on Monitoring and Management of Gas Turbine Fleets for Extended Life and Reduced Costs*, Manchester, UK.

[208] TMS The Minerals, M. M. S. (2007). Composition of Typical Cast Superalloys.

[209] Toda-Caraballo, I. and Rivera-Díaz-del Castillo, P. E. J. (2015). Modelling solid solution hardening in high entropy alloys. *Acta Materialia*, 85:14–23.

[210] Touratier, F., Viguier, B., Siret, C., Lesterlin, S., and Andrieu, E. (2011). Dislocation Mechanisms during High Temperature Creep Experiments on MC2 Alloy. *Advanced Materials Research*, 278:7–12.

[211] Tsuno, N., Shimabayashi, S., Kakehi, K., Rae, C. M. F., and Reed, R. C. (2008). Tension/Compression Asymmetry in Yield and Creep Strengths of Ni-Based Superalloys. In *Superalloys 2008*, pages 433–442. TMS.

[212] Vamsi, K. V. and Karthikeyan, S. (2012). Effect of Off-Stoichiometry and Ternary Additions on Planar Fault Energies in Ni_3Al. In *Superalloys 2012*, pages 521–530, Hoboken, NJ, USA. Indian Institute of Science, Bangalore, Bangalore, India, John Wiley & Sons, Inc.

[213] Vattré, A., Devincre, B., and Roos, A. (2009). Dislocation dynamics simulations of precipitation hardening in Ni-based superalloys with high gamma' volume fraction. *Intermetallics*, 17(12):988–994.

[214] Vattré, A., Devincre, B., and Roos, A. (2010). Orientation dependence of plastic deformation in nickel-based single crystal superalloys: Discrete–continuous model simulations. *Acta Materialia*, 58(6):1938–1951.

[215] Viguier, B., Touratier, F., and Andrieu, E. (2011). High-temperature creep of single-crystal nickel-based superalloy: microstructural changes and effects of thermal cycling. *Philosophical Magazine*, 91(35):4427–4446.

[216] Volek, A., Pyczak, F., Singer, R. F., and Mughrabi, H. (2005). Partitioning of Re between γ and γ' phase in nickel-base superalloys. *Scripta Materialia*, 52(2):141–145.

[217] Völkl, R., Glatzel, U., and Feller-Kniepmeier, M. (1998). Measurement of the lattice misfit in the single crystal nickel based superalloys CMSX-4, SRR99 and SC16 by convergent beam electron diffraction. *Acta Materialia*, 46(12):4395–4404.

[218] Wagner, C. (1961). Theorie der Alterung von Niederschlägen durch Umlösen (Ostwald-Reifung). *Berichte der Bunsengesellschaft für physikalische Chemie*, 65(7-8):581–591.

[219] Wang, T., Wang, X., Zhao, Z., and Zhang, Z. (2016). Dissolution behaviour of the γ' precipitates in two kinds of Ni-based superalloys. *Materials at High Temperatures*, 33(1):51–57.

[220] Wang, W., Lee, P. D., and McLean, M. (2003). A model of solidification microstructures in nickel-based superalloys: predicting primary dendrite spacing selection. *Acta Materialia*, 51(10):2971–2987.

[221] Warren, P. J., Cerezo, A., and Smith, G. D. W. (1998). An atom probe study of the distribution of rhenium in a nickel-based superalloy. *Materials Science and Engineering: A*, 250(1):88–92.

[222] Wilson, B. and Fuchs, G. (2008). Primary creep: Secondary gamma prime and the rhenium effect. *JOM*, 60(7):43–48.

[223] Yang, C., Liu, L., Zhao, X., Li, Y., Zhang, J., and Fu, H. (2012). Dendrite morphology and evolution mechanism of nickel-based single crystal superalloys grown along the <001> and <011> orientations. *Progress in Natural Science: Materials International*, 22(5):407–413.

[224] Yashiro, K., Kurose, F., Nakashima, Y., Kubo, K., Tomita, Y., and Zbib, H. M. (2006). Discrete dislocation dynamics simulation of cutting of γ' precipitate and interfacial dislocation network in Ni-based superalloys. *International Journal of Plasticity*, 22(4):713–723.

[225] Zacherl, C. L., Shang, S. L., Kim, D. E., Wang, Y., and Liu, Z. K. (2012). Effects of Alloying Elements on Elastic, Stacking Fault, and Diffusion Properties of Fcc Ni from First-Principles: Implications for Tailoring the Creep Rate of Ni-Base Superalloys. In *Superalloys 2012*, pages 455–461. Pennsylvania State University, University Park, United States.

[226] Zhang, J., Wang, J., Harada, H., and Koizumi, Y. (2005). The effect of lattice misfit on the dislocation motion in superalloys during high-temperature low-stress creep. *Acta Materialia*, 53(17):4623–4633.

[227] Zhang, J. X., Harada, H., Koizumi, Y., and Kobayashi, T. (2009). Dislocation motion in the early stages of high-temperature low-stress creep in a single-crystal superalloy with a small lattice misfit. *Journal of Materials Science*, 45(2):523–532.

[228] Zhang, J. X., Murakumo, T., Harada, H., and Koizumi, Y. (2003a). Dependence of creep strength on the interfacial dislocations in a fourth generation SC superalloy TMS-138. *Scripta Materialia*, 48(3):287–293.

[229] Zhang, J. X., Murakumo, T., Koizumi, Y., Kobayashi, T., and Harada, H. (2003b). Slip geometry of dislocations related to cutting of the γ' phase in a new generation single-crystal superalloy. *Acta Materialia*, 51(17):5073–5081.

[230] Zhang, X., Deng, H., Xiao, S., Li, X., and Hu, W. (2013). Atomistic simulations of solid solution strengthening in Ni-based superalloy. *Computational Materials Science*, 68(C):132–137.

[231] Zhu, Z., Basoalto, H., Warnken, N., and Reed, R. C. (2012). A model for the creep deformation behaviour of nickel-based single crystal superalloys. *Acta Materialia*, 60(12):4888–4900.

[232] Zitara, M., Kruk, A., Gruszczyński, A., and Czyrska-Filemonowicz, A. (2014). FIB–SEM tomography of 4th generation PWA 1497 superalloy. *Materials Characterization*, 87:143–148.

Appendix A

Additional Data

A.1 Alloy compositions

Table A.1 Selected average alloy compositions cited in this thesis [wt.%] taken from [164, 175, 110], * contains 0.05 wt. %Y [173]

	Cr	Co	Mo	W	Al	Ti	Ta	Nb	Re	Ru	Ni
AM1	7.0	8.0	2.0	5.0	5.0	1.8	8.0	1.0			Bal.
CMSX-4	6.5	9.6	0.6	6.4	5.6	1.0	6.5		3.0		Bal.
CMSX-6	10.0	5.0	3.0		4.8	4.7	6.0				Bal.
CMSX-10	2.0	3.0	0.4	5.0	5.7	0.2	8.0		6.0		Bal.
*IC*11*B**	2.2		7.0		7.7		3.0		1.0		Bal.
LEK 94	6.0	7.5	2.1	3.5	6.5	1.0	2.3		2.5		Bal.
MC2	8.0	5.0	2.0	8.0	5.0	1.5	6.0				Bal.
MC-NG	4.0	<0.2	1.0	5.0	6.0	0.5	5.0		4.0	4.0	Bal.
PWA 1480	10.0	5.0		4.0	5.0	1.5	12.0				Bal.
PWA 1497	2.0	16.5	2.0	6.0	5.55		8.25		5.95	3.0	Bal.
Rene N4	9.0	8.0	2.0	6.0	3.7	4.2	4.0	0.5			Bal.
Rene N5	7.0	8.0	2.0	5.0	6.2		7.0		3.0		Bal.
Rene N6	4.2	12.5	1.4	6.0	5.75		7.2		5.4		Bal.
TMS-75	3.0	12.0	2.0	6.0	6.0		6.0		5.0		Bal.
TMS-138	2.9	5.9	2.9	5.9	5.9		5.6		4.9	2.0	Bal.
TMS-138A	3.2	5.8	2.8	5.6	5.7		5.6		5.8	3.6	Bal.
TMS-162	2.9	5.8	3.9	5.8	5.8		5.6		4.9	6.0	Bal.
TMS-238	4.6	6.5	1.1	4.0	5.9		7.6		6.4	5.0	Bal.

A.2 Physical constants

Table A.2 Alloy element specific parameters. Taken from [18] a_i the Goldschmidt atomic radius, G_i the shear modulus. Taken from [27]: the Vegard coefficients for the γ and γ'-phases.

	a_i $[\times 10^{-10} m]$	G_i [GPa]	V_γ	$V_{\gamma'}$
Cr	1.28	115.3	0.110	-0.004
Co	1.26	82	0.0196	-0.004
Mo	1.40	125.6	0.478	0.208
W	1.41	160.6	0.444	0.194
Al	1.43	26.2	0.179	/
Ti	1.47	45.6	0.422	0.258
Ta	1.47	69.2	0.7	0.5
Nb	1.47	170.3	0.7	0.46
Re	1.38	181	0.441	0.262
Ru	1.34	173	0.3125	0.1335
Ni	1.25	76	3.524	3.57

Appendix B

Supplemental Experimental Data

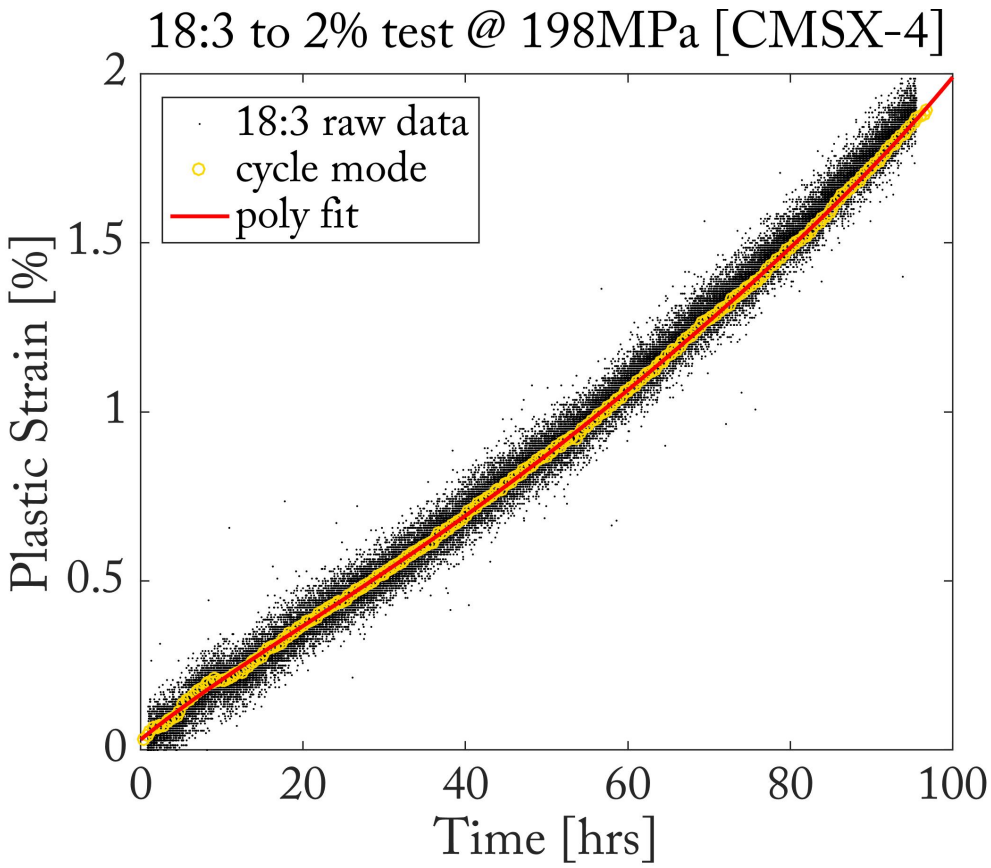

Fig. B.1 CMSX-4 18:3 test data to 2% plastic strain acquired raw data (black datapoints), calculated mean elongation per cycle step at base temperature (yellow circles) and polynomial best fit to mean elongation (red curve)

B.1 Correction to the phase fraction model

Following the peer-review of the γ'-phase fraction model presented in Section 4.3 this model was derived differently to better reflect diffusion dynamics. Following the corrections, the re-submitted approach is presented here.

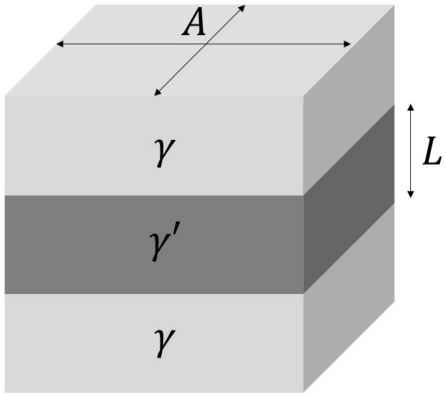

Fig. B.2 Sketch of the fully rafted γ/γ'-microstructure *ideal sandwich* cell with a precipitate thickness of L and cell surface area of A

It is assumed that following the pre-rafting an ideally rafted *sandwich structure* is present throughout the microstructure in which the γ'-phase is now a raft between two γ-matrix channels (see Figure B.2). The interested reader is referred to [146] for a review of the factors contributing to microstructural transformation known as rafting. The γ'-volume of a given fully rafted ideal sandwich is given by Equation B.1. Where L is the precipitate width and the γ'-raft area.

$$V^{\gamma'} = L \cdot A \tag{B.1}$$

The γ'-volume fraction then follows in Equation B.2.

$$f^{\gamma'} = \frac{V^{\gamma'}}{V^{tot}} \tag{B.2}$$

During thermal cycling the microstructure dimensions changes due to the γ'-precipitation (upon cooling) and the γ'-dissolution (due to heating). These effects result in an expansion and shrinkage of the γ'-volume respectively. This change in volume ($V_P^{\gamma'}$) can be expressed with Equation B.3.

$$V_P^{\gamma'} = V^{\gamma'} \cdot N_0 = \frac{dL}{dt} A \cdot N_0 \tag{B.3}$$

Where the number density of precipitates is given by the variable N_0. Due to the fully rafted sandwich microstructure during the non-isothermal creep tests, no significant change in area A is assumed such that this variable is a constant. Considering that the specimen was pre-rafted under an applied load, it is assumed that the number of nucleation sites (*i.e.* dislocations) are sufficiently high upon starting the non-isothermal excursions, to further assume a full saturation of potential precipitation sites such that N_0 is constant during a single thermal cycle. The specific influence of the applied stress on the phase fraction dissolution and re-precipitation gradients can be neglected as the applied stress was held constant and the phase fraction model was only applied to the post-rafted dataset (see Giraud *et al.* [78]). The overall change in the -precipitate phase fraction evolution is modelled using an approach similar to the Johnson-Mehl-Avrami (JMA) equation [154, 93, 13]. The rate of γ'-change resulting from thermal variation is then given by Equation B.4

$$dV^{\gamma'} = dV_P^{\gamma'}(P_{FE} - \frac{V^{\gamma'}}{V^{tot}}) \tag{B.4}$$

where the constant P_{FE} is given by the equilibrium phase fraction at the final temperature of the heating / cooling step. Solving the previous equation, with initial equilibrium phase-fraction P_{IE},$the\gamma'$-volume fraction results in Equation B.5.

$$f^{\gamma'} = \frac{V^{\gamma'}}{V^{tot}} = P_{FE} + (P_{IE} - P_{FE}) \cdot exp(-A \cdot L \cdot N_0) \tag{B.5}$$

The change of the precipitate width during a heating or cooling event is further assumed to be driven primarily by the inter-diffusion of γ'-ordering elements through the γ-matrix. The resulting diffusion length then is given by Equation B.6 with the molar gas constant R, T the absolute temperature prior to the thermal gradient and the activation energy (Q).

$$L = (D \cdot t)^{1/2} \quad with \quad L = (D_0)^{1/2} \cdot exp(-\frac{Q}{2RT}) \cdot t^{1/2} \tag{B.6}$$

Ultimately, the γ'-volume fraction at a given time (t) subjected to a thermal gradient results in Equation B.7. The pre-exponential constants are summarised in the constant β (see Equation B.8).

$$f^{\gamma'}(t) = P_{FE} + (P_{IE} - P_{FE}) \cdot exp(-\beta \cdot exp(-\frac{Q}{2RT}) \cdot t^{1/2}) \tag{B.7}$$

$$\beta = A \cdot N_0 \cdot {D_0}^{1/2} \tag{B.8}$$

The model constants were determined by first subdividing the experimental dataset into its respective heating and cooling segments. Each dataset was fitted with the software *Igor Pro* to an exponential function of the type ($y = c + a \cdot exp(-bx^{1/2})$) to determine the activation energy (Q) for the phase dissolution and re-precipitation. The activation energy for the single-crystal superalloy CMSX-4 was approximated to 300 [kJ/mol] (95% confidence bounds were 955 [kJ/mol] and -475.6 [kJ/mol]). This value is in the order of the self-diffusion activation energy for pure Nickel (279.7 [kJ/mol] [154]) and equal to that determined for the self-diffusion activation for the ordered Ni_3Al(301.6[kJ/mol] [68]). Compared to the literature the value lies between those published for the precipitation events in polycrystalline superalloys by Masoumi *et al.* [137] (396 [kJ/mol] for alloy AD730), Roy *et al.* [171] (50-350 [kJ/mol] for IN738LC). Roy *et al.* examined the activation energies for precipitate growth in a duplex microstructure (large and small precipitate sizes of equal volume fraction) following different holding temperatures. Concluding that small precipitates exhibit a higher activation energy, whereas larger precipitates exhibited lower energy values. Further Roy *et al.* concluded that a higher prior annealing temperature and a longer holding time at this annealing temperature would decrease the activation energy. Wang *et al.* [219] examined the dissolution kinetics of the polycrystalline superalloy IN100 publishing an activation energy of 367-467 [kJ/mol]. According to Wang *et al.* the dissolution activation energy increased with a longer high temperature dwell time.

In this study, the activation energy for dissolution and precipitation is held constant to reflect that the overall alloy composition remains largely unchanged during the thermal cycling and instead the pre-exponential factor (β) is fitted to the specific datasets (see Figure B.3A). As outlined in Equation B.8, β depends on the precipitate surface area A, the number of precipitates (for dissolution events) and the number of nucleation sites (for precipitation events) via N_0 and the diffusion constant $D_0^{1/2}$. As the experimentally examined three cooling and heating events were performed in sequence these depend on each other. The precipitation events (II, IV and VI in Figure B.3B) followed high temperature exposures under constant load, resulting in a lower number of nucleation sites (N_0). Such that the resulting best fit for precipitation events was obtained when using a factor of $\beta = 4 \cdot 10^{-8} s^{-1}$ (see Figure B.3B). The dissolution segments were performed following cooling cycles, during which a significant number of -tertiaries were formed. As the number and impact of γ'-tertiaries as a share of the phase dissolution and re-precipitation increases with temperature (and thus here with each heating cycle) [191, 82, 35], the constant N_0 increases. A best fit for the dissolution events is found for $\beta = 9 \cdot 10^{-8} s^{-1}$ and $\beta = 3 \cdot 10^{-7} s^{-1}$, for the I and III dissolution segments respectively (see Figure B.3B). A specific fit for section V was not determined as this dataset

only contained three data points. Furthermore, as sample failure occurred during the fourth heating step, the γ'-tertiary size distribution and number density during the prior segments is unclear and could not be used to discretise the magnitudes of the contributing constants to β. A summary of the best fit functions compared against the experimental data (black x-data points) for the different cooling and heating regimes is shown in Figure B.3B. This figure highlights, that the fit for the precipitation events is much better than that derived for the dissolution events. The model-fit overestimates the initial dissolution speed for segments I and III in particular.

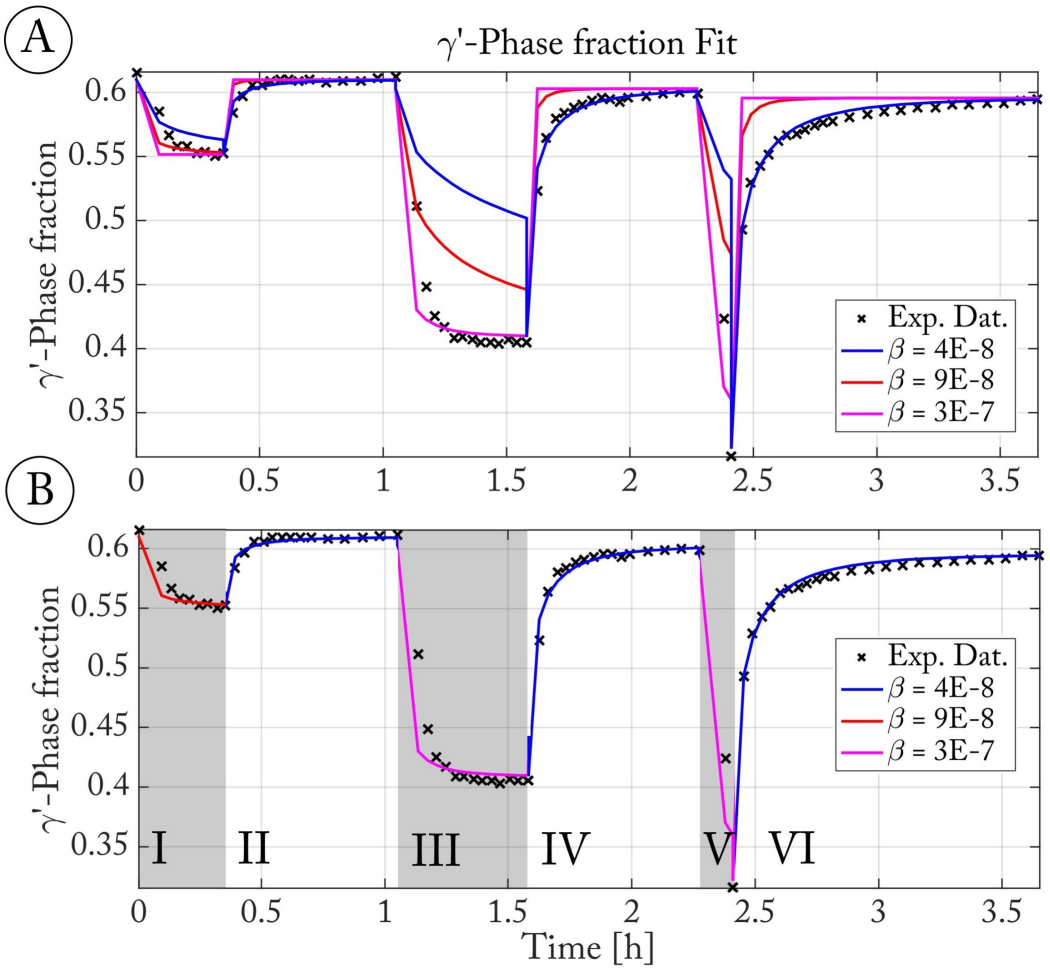

Fig. B.3 (A) Comparison of the experimentally measured γ'-phase fraction during heating and cooling regimes (black crosses) with three fitting functions obtained for values of: $\beta = 4 \cdot 10^{-8}$ (blue), $\beta = 9 \cdot 10^{-8}$ (red), $\beta = 3 \cdot 10^{-7}$ (magenta); (B) Combination of best model fit functions in six (I-VI) regimes. See text for further details.